Classical and quantum dynamics of optical frequency conversion

By

Andrew G. White

A THESIS SUBMITTED FOR THE DEGREE OF
DOCTOR OF PHILOSOPHY
OF THE AUSTRALIAN NATIONAL UNIVERSITY

DEPARTMENT OF PHYSICS
28TH MARCH, 1997

Typeset in Palatino by TEX and LATEX 2ε.

To my parents

Who encouraged me to find out about dinosaurs

Declaration

This thesis is an account of research undertaken in the Department of Physics, Faculty of Science, Australian National University and the Fakultät für Physik, Universität Konstanz, Germany, between March 1991 and October 1996.

Except where acknowledged in the customary manner, the material presented in this thesis is, to the best of my knowledge, original and has not been submitted in whole or part for a degree in any university.

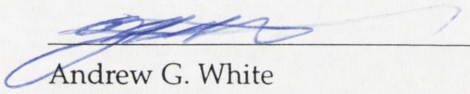

Andrew G. White
Friday 28th March, 1997

EXAMINER'S VERSION

Abstract

A second harmonic generator is constructed to investigate the power and noise behaviour of optical frequency conversion.

Strong squeezing of the second harmonic is demonstrated. It is found that pump noise critically affects the squeezing, with attenuation of the pump noise significantly improving the squeezing. A modular modelling approach is used to describe and quantify this effect, and excellent agreement is found between theory and experiment.

Two methods of SHG are possible, passive (occurs external to a laser) and active (occurs within a laser). Theoretically exploring the possible squeezing regimes, the effect of laser noise on both methods is considered. It is concluded that active SHG is not feasible, as the high dephasing of practical lasers totally destroys the squeezing.

It is shown that the second harmonic generator can simultaneously support multiple, interacting, second order nonlinear processes. Two categories of interaction are identified: competing, where the interacting processes do not share all of the modes; and cooperating, where they do.

Competing nonlinearities are evident in the system as triply resonant optical parametric oscillation (TROPO): where second harmonic generation (SHG) and non-degenerate optical parametric oscillation (NDOPO) occur simultaneously. Power clamping of the second harmonic and nondegenerate frequency production in both the visible and infrared are observed and explained, again obtaining good agreement between theory and experiment. Design criteria are given that allow TROPO to be avoided in future efficient SHG systems.

The second harmonic squeezing is observed to be degraded by TROPO, with a maximum value occurring just before the onset of TROPO – in contrast to predictions for closely related systems. A model is developed that shows this is due to two effects: a noise eating effect related to the second harmonic clamping; and low frequency noise added by the additional TROPO modes.

A model of cooperating nonlinearities is developed that shows a wide variety of third order effects, including cross- and self phase modulation (Kerr effects) and two photon and Raman absorption, are in principle possible in the second harmonic generator. A strong third order effect is demonstrated experimentally: the system is phase mismatched and optical bistability is observed that is shown to be due to the Kerr effect.

Arguments are presented to prove that, in principle, the system acts as a Kerr medium even at the quantum level. A model of Kerr squeezing is developed that allows consideration of the effect of pump noise: it is shown that the predicted squeezing is sensitive to both the amplitude and phase quadratures of the pump. Strong classical noise reduction (but no squeezing) is observed on light reflected from the cavity. It is speculated that the squeezing is masked by excess phase noise from the laser.

Due to the quantitative and qualitative agreement between experiment and theory, and the experimental reliability of the system, it is concluded that SHG is now a well understood and practical source of squeezed light. The potential for future systems, given the availability of new nonlinear materials, is discussed.

Papers by author

Accepted papers resulting from work in this thesis

- A. G. White, P. K. Lam, M. S. Taubman, M. A. M. Marte, S. Schiller, D. E. McClelland and H.-A. Bachor. *Classical and quantum signatures of competing $\chi^{(2)}$ nonlinearities*. To appear Physics Review A, 1997

- S. Schiller, R. Bruckmeier, and A. G. White. *Classical and quantum properties of the subharmonic-pumped parametric oscillator*. To appear Optics Communications, 1997

Published papers resulting from work in this thesis

- A. G. White, T. C. Ralph, H.-A. Bachor. *Comment on "Noiseless amplification in cavity based optical systems with an internal two-photon process"*. Submitted to Journal of Modern Optics, May 1996; accepted September 1996

- A. G. White, M. S. Taubman, T. C. Ralph, P. K. Lam, D. E. McClelland, H.-A. Bachor. *Experimental test of modular noise propagation theory for quantum optics*. Physics Review A, **54**, no. 4, p. 3400 - 3404, 1996

- A. G. White, J. Mlynek and S. Schiller. *Cascaded second-order nonlinearity in an optical cavity*. Europhysics Letters, **35**, no. 6, pp. 425 - 430, 1996

- A. G. White, T. C. Ralph, H.-A. Bachor. *Active versus passive squeezing via second harmonic generation*. Journal of the Optical Society of America B, **13**, no. 7, pp. 1337 - 1346, 1996

- H.-A. Bachor, T. C. Ralph, M. S. Taubman, A. G. White, C. C. Harb, D. E. McClelland. *Progress in the search for the optimum light source: squeezing experiments with a frequency doubler*. Journal of Quantum and Semiclassical Optics, 7, pp. 715 - 726, 1995

- T. C. Ralph, M. S. Taubman, A. G. White, D. E. McClelland, and H.-A. Bachor. *Squeezed light from second harmonic generation: experiment versus theory*. Optics Letters, **20**, no. 5, pp. 1316 - 1318, 1995

- T. C. Ralph and A. G. White. *Retrieving squeezing from classically noisy light*. Journal of the Optical Society of America B, **12**, no. 5, pp. 833 - 839, 1995

Published papers resulting from work in Honours thesis

- N. R. Heckenberg, R. McDuff, C. P. Smith, and A. G. White. *Generation of optical phase singularities by computer-generated holograms*. Optics Letters, **17**, no. 3, pp. 221 - 223, 1992

- A. G. White, C. P. Smith, N. R. Heckenberg, H. Rubinsztein-Dunlop, R. McDuff, C. O. Weiss, and Chr. Tamm. *Interferometric measurements of phase singularities in the output of a visible laser*. Journal of Modern Optics, **38**, no. 12, pp. 2531 - 2541, 1991

Other published papers

- A. E. Stuchbery, A. G. White, G. D. Dracoulis, K. J. Schiffer, and B. Fabricius. *Gyromagnetic ratios of low-lying rotational states in* Gd^{156}, Gd^{158}, Gd^{160}. Zeitschrift für Physik A - Atomic Nuclei, **338**, no. 2, pp. 135 - 138, 1991

Acknowledgements

It is not so much our friends' help that helps us as the confident knowledge that they will help us

Epicurus

I have been gifted with the friendship and support of a great number of people during the course of this thesis, and now is my chance, in ever so humble a way, to thank them.

Firstly I wish to thank Dianna Gould, who has endured my stress and our separation due to this thesis, and responded with understanding and loving company. Thank you, you made it all worthwhile.

To my family – mum, dad, nanna, pa, Damian and Natalie – your unstinting love and support has been my crutch in the lean times, and I cannot think how to repay you, except maybe to try and see you much more often (oh, OK, and to get my nose out of a book occasionally while I'm there!).

To paraphrase Rumpole, a number of my friends from Queensland have gone on to "join the legions of those I like, but never see". Tracey and James, Jacinta and Mark, thank you for your understanding and regular Christmas cards. A special thank you to Matthew Molineux, whose continued efforts to stay in touch have kept our friendship alive and well across several continents despite my habit of regularly losing his contact address (well, you will move so often).

To the old gang from uni: Margaret Wegener, Alan Monaghan, Sam Meyer, Bradley Ellis, (and the others I've forgotten because it's 4 o'clock in the morning, but you know who you are) thank you for continuing phone calls, emails, and hurried dinners at Christmas. A special thank you to Craig Smith (who was my laboratory partner in Honours), for both the regular, sanity inducing, contact, and for reminding me of the important things in life. For their friendship and for acting as a mirror to my soul when required, thank you to Rebecca Farley and Steven Siller (*atque in perpetuum, frāter, avē atque valē*).

Thank you to Wayne and Pippa Rowlands and Joe and Janet Hope for their welcome and for restoring my faith in humanity - it was appreciated guys!

Being a student in a town far from my home state, I have been in more rental houses than I care to think about. The thing that has made this not only tolerable, but absolutely enjoyable, has been my wonderful housemates. I'd like to thank the Fisher gang: Simon "Simpsons" Watt, Robert "Anzac bikkie"Gulley, Brett "TV and mirror" Brown, Darryn "live in the lounge" Schneider, and Simon "warm beer" Schwarz, whose collective emphasis on bodily humour, sport, and strangely, Star Trek, made for a text book bachelor existence. I'd also like to thank the Banjine bunch for introducing me to adult group housing (in the luxury of inner Canberra): Darryn (again), Tim Ralph, Helen Smith, and Dianna. And finally I'd like to thank my Jarrah St housemates, Dianna and Leanne McDonald, who provided me with a wonderfully creative and energising household in my stressful last year of the thesis (and so clean!). I'd also like to heartily thank those who generously (and it must be said, bravely) provided housing for me (and associated housemates I confess) when we needed it most – Hans and Connie, Mal and Jeannie, Craig and Denise – I've enjoyed it every time.

My stay in Germany was immeasurably enriched by the Europahaus gang. To my *mitbewohnerin* Şenay Azak and Berndt Brinkamp, thank you for the music, tea, presents, and laughter - it recharged my batteries at the end of every day. To the rest of the gang:

Suzanne Zelasny, Felix Kluge, Barbara Hughes, Mario, and most especially, Tamara Weterings, thank you for the friendship, the singing, the toast, and the support. I'd also like to thank Chris and Gretchen Ekstrom, who kindly invited me into their family (and let me watch Simpson videos!) which made me feel more at home than I would have thought possible.

The PhD is the last vestige of the apprenticeship system: nowhere else can one find such a close and lengthy relationship between student and teacher. I have been fortunate indeed to have had two supervisors, Prof. Hans Bachor and Assoc. Prof. David McClelland who are not only passionately concerned with the development of the craft, but of the student as well. Gentleman, for your advice, encouragement, enthusiasm, patience (sorely tested at times I'm sure) and faith, a tremendous thank you. I suspect I won't fully appreciate the thanks I owe you unless I one day supervise a student of my own.

To my most talented lab partners and office mates, Matthew Taubman ("Hare Krishna, Hare Krishna ...ting!") and Ping Koy Lam ("manumanup") from whom I have learned much – thank you for the many hours of your company (from reconstructing labs, to experiments, to writing papers). I am forever grateful that we share a sense of the absurd. I'd also like to thank my other long-term office mate, Bruce Stenlake, who introduced me to the Dark Side of the Force (game? what game?).

A big thank you also to Charles Harb, Timothy Ralph, and Mal Gray who have always been available for discussions (physics or otherwise) and long lunches. And thank you to the other students and postdocs in the department who have guaranteed an interesting working enviroment, Darren Sutton, Andrew Stevenson, Ian Littler, Joseph Hope (see, I did finish!), Glenn Moy, Dan Gordon, and Geoff Erickson (a special thanks to Geoff and Ping Koy for their last minute help with the thesis).

The physics department has proved to be a pleasant and congenial enviroment in which to work. I'd like to thank Drs Craig Savage, Mark Andrews, Frank Houwing and Heather Kennet for their advice and insights during the course of my PhD. A special thank you to Felicity Davy who has steamrolled innumerable bumps in the highway of university administration (and for the quality gossip!).

This PhD could not have been completed without the technical expertise of Brett Brown, who built innumerable vital, need-it-yesterday, type components with the maximum of fuss and good cheer. For their likewise invaluable help with electronics, from finding components to the Secret of Design, I'd like to thank David Cooper, Alex Eades, Doug Crawford, and Walter Goydych.

I was privileged to spend a year at Universität Konstanz in Germany during my PhD. Thank you to Prof Jürgen Mlynek for considering my application, and to Dr Stephan Schiller for his enthusiasm and intellectual generosity - his example taught me much. I'd also like thank Sylvania Pereira, Matthew Collett, and Monika Marte for sharing their insights, on physics and otherwise.

A final thank you, to my fellow Konstanz students, Gerd Breitenbach, Robert Bruckmeier, Stefan Seel, Rafael Storz, Raid Al-Tahtamoundi, Sigmund Kohler, Thomas Müller, Klaus Schneider and Christian Kurtsiefer. They showed me that quality physics can involve bottles of port, Monty Python, darts, beer, strolls through Amsterdam, bike rides to small festivals, musical instruments, beer again, and roller skates. Compared to all that, the many stimulating physics conversations were an unexpected, but appreciated, bonus.

Contents

List of Figures

List of Tables

Chapter 1

Introduction

Science and technology are separate, but forever intertwined, disciplines. At their best they are enabling, with advances in one opening up new vistas for both: the electrical basis of modern society can be traced to esoteric 18th and 19th century science; conversely, a straight intellectual line can be drawn from the mechanical clock to General Relativity. The laser is a prime example of an enabling technology, with many new sciences and technologies resulting from its development. In this thesis we examine the interaction of two such fields that owe their existence to the laser: quantum optics and optical frequency conversion.

Optical frequency conversion was first demonstrated in 1961 by Franken and colleagues [1], just one year after the first demonstration of the laser [2]. They doubled the frequency of a pulsed helium neon laser (694.3nm to 347.2nm) with a conversion efficiency of one millionth of a percent. Throughout the 1960's there were theoretical and experimental advances, with the realisation that any frequency manipulation that could be performed at radio frequencies, could, in principle at least, be performed at optical frequencies. Further technological advances were limited by the performance of available nonlinear materials, and during the 1970's the field lost much of its impetus as the tunable dye laser became seen as the solution to wideband optical frequency production. However dye lasers did have considerable experimental disadvantages (mechanically complicated, require separate pump laser) and the field once again gained impetus in the 1980's with the introduction of a suitable optical sources in the form of narrow linewidth, solid state lasers (notably the Nd:YAG nonplanar ring oscillator, or NPRO), and the commercial availability of good nonlinear materials. In the last few years both strong up and down conversion sources have been developed (second harmonic generation and optical parametric oscillation, respectively). At the inception of this thesis, conversion efficiencies of 10-40% had been reported and were regarded as impressively high; currently, figures of 60-80% are regarded as standard. With the rapid development of such efficient sources, previously neglected effects, such a simultaneous up and down conversion, have taken on a new significance.

In principle, quantum optics could have been developed as a coherent field any time after the final synthesis of quantum mechanics in the 1930's. However, lacking the laser, there was no strong impetus to do so, nor a suitable experimental system against which to test the theory. Theoretical work began soon after the development of the laser, and continued throughout the 1960's and 70's. Wider attention was focussed on the field when Caves [3] suggested that the sensitivity of interferometers (in particular, interferometers to detect gravitational waves) could be improved via the use of *squeezed states*. These are states of light where one quadrature is quieter than the standard quantum limit (SQL). Experimentally, the SQL is seen as a flat noise floor on the photocurrent spectrum of the detected light, and is thus also known as quantum noise. Squeezing was first demonstrated in 1985 by Slusher et. al [4]; this was also the year that the input/output formalism was developed, which allowed theoretical predictions of quantum noise spectra that could be tested against experiment [5]. At the inception of this thesis several bright

continuous-wave squeezed sources had been demonstrated, but none had achieved their predicted potential.

In this thesis we examine the classical and quantum dynamics of optical frequency conversion. In particular, we focus on the steady state behaviour of continuous wave cavity systems, the system is thus in the linearisable limit. In this limit, the concern of classical dynamics is the origin, destination, and frequency behaviour of the optical power; similarly the concern of quantum dynamics becomes the origin, destination, and frequency behaviour of the quantum noise.

The primary aim of the thesis is to understand what happens to quantum noise in second harmonic generation (SHG), where light is produced at twice the frequency of the original light. We build and analyse a SHG experiment to address the following questions – where is squeezing generated? how much? what limits it? and how reliable can it be made? There has been much previous theoretical and experimental work on these questions , which is described in detail at the beginnings of Chapters 4 & 6. To briefly summarise previous results: there are two forms of SHG, passive (external to a laser) and active (internal to a laser). In principle either form can provide strong squeezing. Experimentally, SHG is an attractive source of squeezing as it can be made very stable and reliable, and only requires one nonlinear stage. However in practice squeezing has only been observed in passive systems, and it has always been less than predicted. We aim to explain these results, demonstrate strong squeezing in agreement with theory, find what limits the squeezing, and recommend steps to avoid these limits.

As a consequence, a secondary aim of the thesis is to explore the power behaviour of an efficient SHG system. SHG is a second order optical effect (where first order effects are standard linear optics). As reviewed in Chapters 2, 7 & 8, in recent years there has been investigation into a number of curious optical effects in second-order systems that are due to two or more second-order processes occurring simultaneously. Depending on the nature of the interaction, the final behaviour can effectively be either second-order or third-order in nature. Previously, strong second-order effects due to interacting processes have been demonstrated in efficient continuous wave systems (such as nondegenerate frequency production around the fundamental in SHG); however no strong third order effects have been demonstrated. We aim to explore which of these effects can and do occur in our experiment, and detail their experimental signatures. Further, we aim to understand the effect these higher order interactions have on the quantum noise behaviour of the system.

1.1 Thesis plan

In the first part of Chapter 2 we give an overview of second order optical processes. In the second part we model classical second harmonic generation, and discuss the doubly vs singly resonant limits. The third part introduces the idea of interacting nonlinearities. In the fourth we present and contrast a classical model for second harmonic generation (SHG) interacting with simultaneous nondegenerate optical parametric oscillation (TROPO) and predict power clamping in addition to nondegenerate frequency production. In the fifth part we look at the interaction of SHG with itself, and introduce equations that shows this can lead to a number of third order effects, notably the Kerr effect which we consider in some detail.

The first part of Chapter 3 is an introduction to quantum theory (readers already familiar with this material may wish to skip this section, but are advised to read the

discussion of the sideband picture); the second part looks at the two core methods for modelling quantum systems, and the third part is a detailed exposition of the method favoured in this thesis (the Heisenberg approach) for the case of an empty cavity.

At the beginning of Chapters 4, 6, 7, & 8, there is an appropriate review of previous research. In Chapter 4 the limits to squeezing in both active and passive second harmonic generation are explored via a Schrödinger approach – this is the only place in the thesis where the Heisenberg approach is not used, and comparison between the two shows the strong advantages of the Heisenberg approach. The first and second parts of the chapter introduce the model and numerical parameters, respectively. In the third part, the limits to squeezing are explored graphically, with intuitive interpretations provided to explain the predicted behaviour.

Chapter 5 is a very detailed discussion of the design and construction of the experiment. The first three parts discuss the laser and modecleaner, and optical path. The fourth section concerns the doubling cavity, with particular emphasis placed on design considerations. The last two parts discuss the locking system and detection systems.

Chapters 6,7, & 8 contain the bulk of the experimental results. The first part of Chapter 6 presents a quantum model of singly resonant frequency doubling, and predicts squeezing of the second harmonic. The second part presents the concept of a modular approach to noise propagation. The third part presents the experimental squeezing data. Pump noise is found to degrade the squeezing; attenuating this noise improves it significantly. Using the results of the first two parts of the chapter, excellent agreement is found between theory and experiment.

Chapter 7 explores the classical and quantum signatures of TROPO. Data is presented in the first part of the chapter that shows nondegenerate frequency generation in both the visible and the infrared; in the second part power clamping of the second harmonic is demonstrated. In the third part a model is developed for the effect on the second harmonic noise, and data is presented that confirms the dual effects of noise eating and additional low frequency noise.

Chapter 8 considers and explores the classical and quantum behaviour of the Kerr effect. The first part explores the nonideal phase matching of our experiment, the second part reports significant optical bistability, which demonstrates that large third order effects are possible in practical, continuous wave, second order systems. The third part introduces a quantum theory of the Kerr effect, and highlights the sensitivity of the Kerr effect to both quadratures of the pump noise. The fourth part reports noise reduction (of 1.5-1.8 dB) on the beam reflected from a doubler run as a Kerr cavity.

Chapter 9 briefly summarises the results, discusses future research, and highlights a number of concepts for general consideration, including removing the effect of pump noise via optical cancellation. Appendix 1 contains an brief analysis of optical cancellation in SHG, using the Heisenberg approach.

The thesis has been written both as a report and as pedagogical document. It also encompasses a fair amount of conceptual ground. Given this, it is natural that many readers will only be interested in a selection of the thesis topics. Accordingly, as far as was possible, the thesis has been written in a modular fashion. If the reader is chiefly interested in classical frequency conversion, the key components are Chapters 2 and the relevant experimental results presented in Chapters 6 & 7. If instead the reader's interest is quantum optics theory, then the key components are Chapters 3 & 4 and the relevant theoretical sections of Chapters 6, 7, & 8. Experimentally minded readers can find the nuts and bolts of the experimental design in Chapter 5, and the experimental squeezing and noise reduction results in Chapters 6, 7, & 8.

Chapter 1 bibliography

[1] P. A. Franken, A. E. Hill, C. W. Peters and G. Weinreich, Physical Review Letters, **7**, no. 4, p. 118, 1961. *Generation of optical harmonics*. Note that the second harmonic is so faint that the spectrometer output at 347.2nm did not reproduce well, and cannot be seen in the actual journal article!

[2] T. H. Maiman, Nature, **187**, p. 493, 1960. *Stimulated Optical Radiation in Ruby Masers*

[3] C. M. Caves, Physical Review D, **23**, no. 8, p. 1693, 1981. *Quantum-mechanical noise in an interferometer*

[4] R. E. Slusher, L. W. hollberg, B. yurke, J. C. Mertz, and J. F. Valley, Physical Review Letters, **55**, no. 22, p. 2409, 1985. *Observation of Squeezed States Generated by Four-Wave Mixing in an Optical Cavity*

[5] M. J. Collett and D. F. Walls, Physics Review A, **32**, no. 5, p. 2887, 1985. *Squeezing spectra for nonlinear optical systems*

Chapter 2

Classical nonlinear optics

When an electromagnetic (em) wave passes through a dielectric material, the electrons of the constituent atoms or molecules are disturbed. As the valence electrons are displaced from their normal orbits by the em wave, temporary dipoles are formed in the material. The dipoles thus form a *polarisation* wave in the material. This wave reradiates an em field.

For low em field strengths the polarisation wave mimics the incoming em wave. The reradiated em wave thus matches the incident em wave. This regime is the province of linear optics, for example, light passing through glass. At higher field strengths the dipole response is distorted. The reradiated wave contains new frequency components that depend on higher orders of the field. This is the province of nonlinear optics [1].

The induced macroscopic polarisation, P, is a function of the applied electric and magnetic fields, E, B. P can be expanded in a convergent power series:

$$P = \chi^{(1)}E + \chi^{(2)}E^2 + \chi'^{(2)}E.B + \chi^{(3)}E^3 + \dots \tag{2.1}$$

where $\chi^{(1)}$ is the linear susceptibility, and $\chi^{(2)}$ and $\chi^{(3)}$ are weaker, higher order nonlinearities in the dielectric response. The $\chi^{(1)}$ term describes linear effects, including the electrooptic and photoelastic effects. For the case of an applied DC magnetic field, the $\chi'^{(2)}$ term describes the Faraday effect. The $\chi^{(3)}$ term describes third order optical effects, such as Four Wave Mixing (FWM), third harmonic generation (THG), self phase modulation (optical Kerr effect), cross phase modulation (optical cross-Kerr effect), applied field phase modulation (electronic Kerr effect), 2 photon absorption (2PA), and Raman processes.

In this thesis we consider *optical* $\chi^{(2)}$ processes. That is, both electric fields are due to the optical em field. (For the case of an applied DC electric field, the $\chi^{(2)}$ term describes the Pockel effect). As intensity is proportional to the square of the electric field, all optical $\chi^{(2)}$ processes are intensity dependent.

2.1 Overview of optical $\chi^{(2)}$ processes

Optical $\chi^{(2)}$ processes fall into one of two complementary categories: *upconversion*, where 2 low frequency photons are converted into one high frequency photon; or *downconversion*, where one high frequency photon is converted into two low frequency photons. Note that optical $\chi^{(2)}$ processes are always explicitly 3 photon processes. Fig. 2.1 is a schematic overview of possible $\chi^{(2)}$ processes. Optical fields are shown incident onto a lossless $\chi^{(2)}$ material. New fields are generated inside the material, and are shown exiting from the material along with possible residual input fields. The residual fields are either from fields not directly involved in the $\chi^{(2)}$ process, or are due to less than perfect nonlinear conversion. To emphasise again that $\chi^{(2)}$ processes are explicitly 3 photon pro-

[1] The discussion in these two paragraphs is basically that given in Koechner [1, Ch. 10].

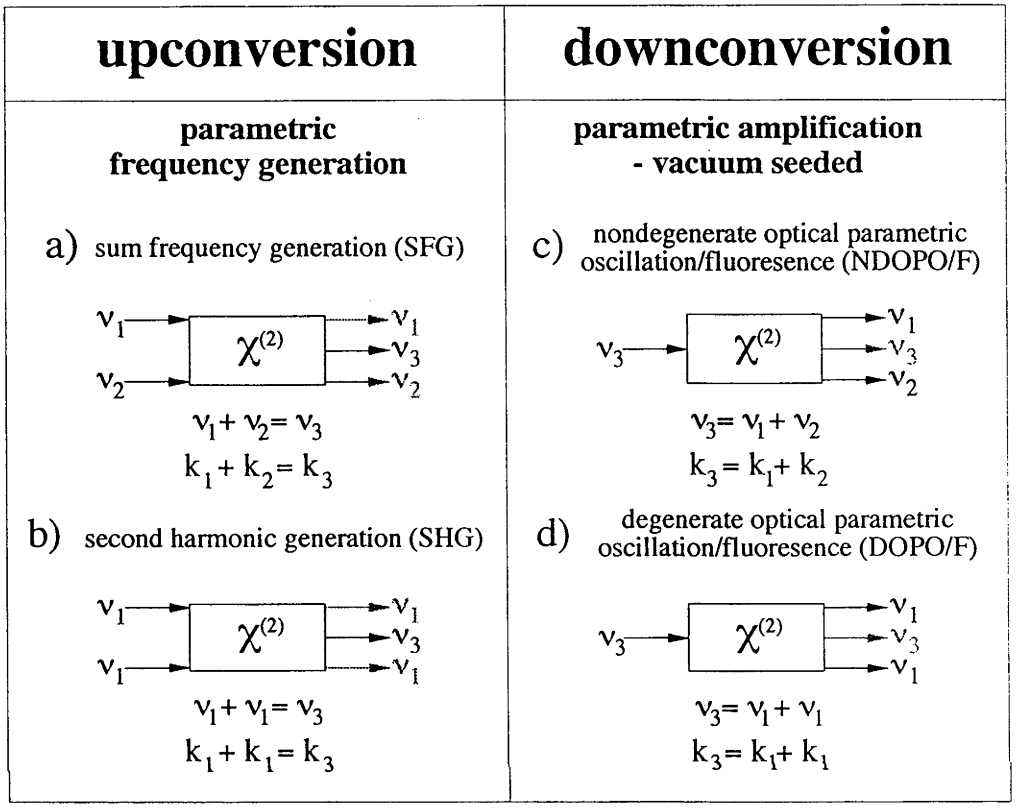

Figure 2.1: Schematic overview of basic $\chi^{(2)}$processes. Fields explicitly involved in the $\chi^{(2)}$process are shown in black. Possible residual fields are in grey. Vacuum inputs are not displayed. *upconversion: parametric frequency generation.* a) sum frequency generation (SFG): nondegenerate. b) second harmonic generation (SHG): degenerate. *downconversion: parametric amplification - seeded by vacuum.* In a cavity system these interactions lead to oscillation, in a travelling wave system they lead to parametric fluorescence. c) nondegenerate optical parametric oscillation / fluorescence (NDOPO/F). d) degenerate optical parametric oscillation / fluorescence (DOPO/F).

cesses, the fields that explicitly involve the 3 photons are shown in black. Residual fields are shown in grey.

The top half of Fig. 2.1 shows the four basic $\chi^{(2)}$ processes. The processes on the left hand side of the figure are complementary to the those on the right. Fig. 2.1 (a) shows Sum Frequency Generation (SFG), where two fields at ν_1, ν_2 are summed to form a frequency ν_3. SFG is implemented in frequency chains, and in detection of weak signals low optical frequencies (by upconverting to higher optical frequencies that can be detected with high efficiency). Second Harmonic Generation (SHG) is obviously the degenerate case of SFG, Fig. 2.1 (b). However it is of special interest as the two incoming photons can come from the same field. Due to this relative simplicity it is a very widespread tool for generating high optical frequencies. the low frequency field is known as the *fundamental*, the high frequency as the *second harmonic*. As two low frequency photons are required to produce one high frequency photon the second harmonic field and residual fundamental field tend to be anti-correlated.

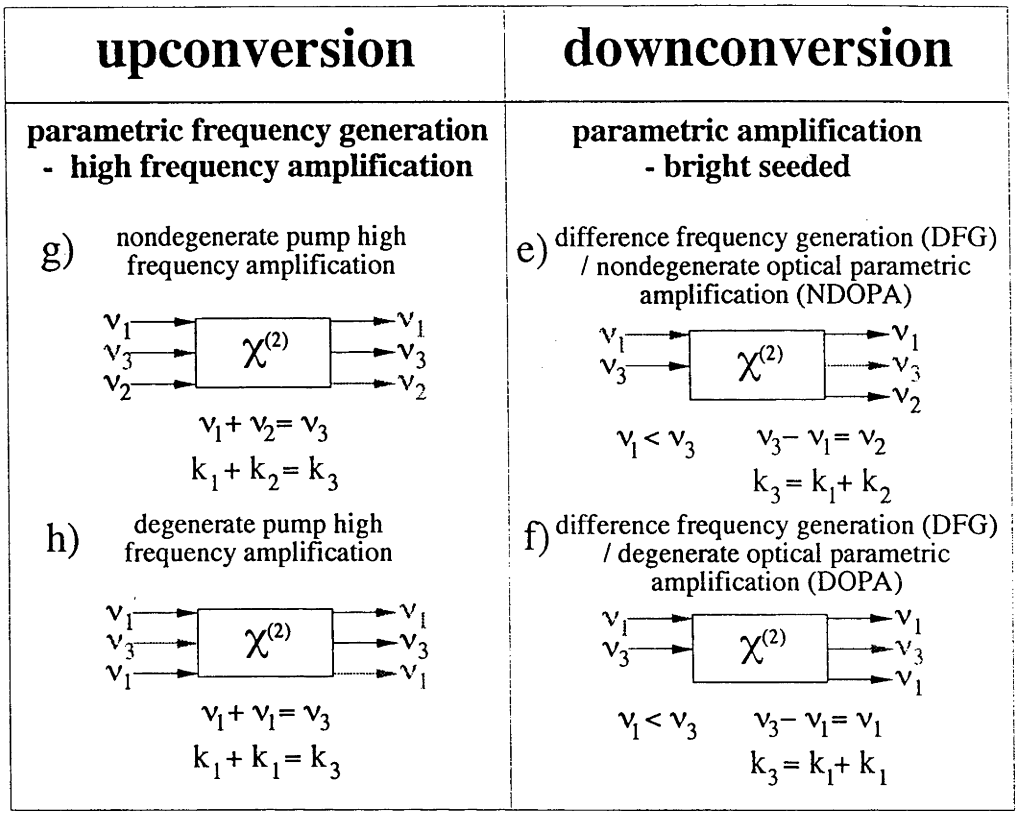

Figure 2.1: Schematic overview of basic $\chi^{(2)}$ processes, part 2. e) difference frequency generation (DFG) / nondegenerate optical parametric amplification (NDOPA). f) difference frequency generation (DFG) / degenerate optical parametric amplification (DOPA). *upconversion: high frequency amplification* g) nondegenerate pump high frequency amplification. h) degenerate pump high frequency amplification.

Note that in both cases the quantum noise in the generated field, ν_3, is influenced by the vacuum noise at ν_3 incident on the crystal. To keep Fig. 2.1 uncluttered the incident vacuum fields are not shown. Please keep in mind however, that whenever a field is generated (right hand side of each $\chi^{(2)}$ block), there is an incident vacuum field at that frequency (left hand side of $\chi^{(2)}$ block, unshown).

Downconversion processes are also known as parametric amplification processes. They can be categorised as: *vacuum seeded*, where only the high frequency pump field is incident on the system; and *bright seeded*, where there is an additional low frequency field. If the vacuum seeded downconversion takes place in a travelling wave system (no optical feedback) it is known as Optical Parametric Fluorescence (OPF). If there is optical feedback, i.e. the material is inside a cavity, then the the process is known as Optical Parametric Oscillation (OPO). In the nondegenerate case (NDOPO/F) the field splits into two low frequency fields, ν_1, ν_2, where $\nu_3 = \nu_1 + \nu_2$, Fig. 2.1 (c). This is the complementary process to SFG. The high frequency field is known as the *pump* field, the low frequency fields as the *signal* and *idler* fields. Unlike the upconversion processes, where the degree of degeneracy is set by the input fields, in downconversion it is set by the *phase-matching* of the crystal (see section 2.1.1 below). In the degenerate case (DOPO/F) the field is frequency halved, $\nu_3 = 2\nu_1$, Fig. 2.1 (c). The low frequency field is known

as the *subharmonic*. DOPO is obviously complementary to SHG. Note that the $\chi^{(2)}$ material is acting as a parametric amplifier of the vacuum field at ν_1. For both DOPO and NDOPO the signal and idler fields are perfectly correlated to each other, as each pair of low frequency photons is produced by the one high frequency photon.

If we take either DOPO or NDOPO and seed it with a bright field at, say, ν_1, we induce Difference Frequency Generation (DFG) as shown in Figs 2.1 (e) & (f). The seed field is not directly involved in the $\chi^{(2)}$ process, it acts solely as a catalyst causing the pump field to downconvert so that one of the low frequencies matches the seed frequency. DFG is often referred to as Optical Parametric Amplification (OPA), as in the limit of perfect nonlinear conversion two photons (nondegenerate) or three photons (degenerate) at ν_1 are produced for every one incident. DFG most often finds application in frequency chains.

The complementary processes, which are equivalent to SFG or SHG with an additional pump field at ν_3, are rarely considered and have no widely accepted name, Figs 2.1 (g) & (h). Unlike the seeded downconversion processes, the frequency of the seed field does not influence the frequency of the generated wavelengths, which is set only by the phasematching conditions. However, if the seed field and the upconverted field(s) are the same frequency, then the system acts as an amplifier of the seed field. In the limit of perfect nonlinear conversion, for either case, two high frequency photons are produced for every incident high frequency photon.

The first four cases are limiting cases of the last four when the seed fields go to zero power. In these descriptive sketches we have neglected more complex issues such as the effect of unequal field intensities or phases.

2.1.1 Phase matching

Obviously for all the described $\chi^{(2)}$ processes both energy and momentum of the interacting photons must be conserved. If we use the indices 1, 2, for the low frequency fields and the index 3 for the high frequency field, then energy conservation is expressed simply in terms of the the relevant photon frequencies, $\nu_1 + \nu_2 = \nu_3$. Momentum conservation is expressed in terms of the optical wavevector, k, i.e. $k_1 + k_2 = k_3$. When this holds exactly the system is said to be *phase matched*. To deal with situations where the momentum matching does not hold exactly, we define the *phase mismatch*, $\Delta k \equiv k_3 - (k_1 + k_2)$. In $\chi^{(2)}$ materials, the wavevector, k, is related to the refractive index of the material, n, via the relation (from Yariv [2]):

$$k(\nu, \Pi) = \nu\sqrt{\mu\varepsilon_0}\, n(\nu, \Pi) \tag{2.2}$$

Note that the refractive index is a function of both wavelength, ν, and polarisation, Π, and thus so is the wavevector. For a certain set of polarisation conditions, the phase matching condition becomes:

$$\nu_1 n(\nu_1) + \nu_2 n(\nu_2) = \nu_3 n(\nu_3) \tag{2.3}$$

If $n(\nu_1) = n(\nu_2)$, this reduces to:

$$n(\nu_1) = n(\nu_3) \tag{2.4}$$

That is, the refractive index must be the same for the high and low frequencies. Physically this phase matching condition can be understood as follows. The phase velocity and wavelength of the polarisation wave that is established is determined by $n(\nu_1)$. The phase velocity and wavelength of the generated em wave is determined by $n(\nu_3)$. Thus, for efficient transfer of energy from the polarisation wave to the em wave, $n(\nu_1) \simeq n(\nu_3)$.

In crystalline materials the refractive index is normally polarisation dependent. This

polarisation dependence offers a degree of freedom to achieve reasonable phase matching. There are currently three methods for achieving phase matching in crystalline systems:

• *Type I phase-matching*. The refractive indices are equal when the two low frequency fields are of the same polarisation and the high frequency field has orthogonal polarisation. This can be achieved by orienting the crystal to a certain angle, setting the crystal to a certain temperature, or both. If the refractive indices are matched for light propagating at 90° to the optical axis the crystal is said to be *noncritically* phase matched. It is noncritical in the sense that the light may propagate in any direction within the xy plane (where z is the optical axis) and the phase matching is more robust with respect to changes in temperature.

• *Type 2 phase-matching*. The refractive indices are equal when the two low frequency fields have orthogonal polarisations and the high frequency field has the same polarisation as one of the low frequency fields. Again, this can be achieved by orienting the crystal to a certain angle, setting the crystal to a certain temperature, or both.

• *Quasi-phase-matching (QPM)* If no particular effort is made to match the refractive indices via Type I or II phase matching then, in general, after some relatively short distance (the coherence length, see eqn 2.17) the undesired complementary process begins to occur (e.g. downconversion instead of upconversion). At twice the coherence length there is no net nonlinear effect. In QPM materials the $\chi^{(2)}$ medium is periodically inverted every coherence length, so that the undesired process in suppressed and the desired process continues for that coherence length. Arbitrarily long pieces of material can be phase matched in this manner. This is difficult in practice, as non-Type I,II coherence lengths are typically very short (a few microns) and best results are obtained only when the medium is totally and sharply inverted.

All three phase matching methods were first proposed in the 1960's. The first two are mature, in that there are several materials commercially available that span a range of optical frequencies. The third method only began to reach its full potential in 1996 [3, 4]. In this thesis, all experiments were carried out via Type I noncritical phase matching in magnesium oxide doped lithium niobate (see Chapters 5-8).

2.2 Second Harmonic Generation, SHG

2.2.1 Deriving the equations of motion

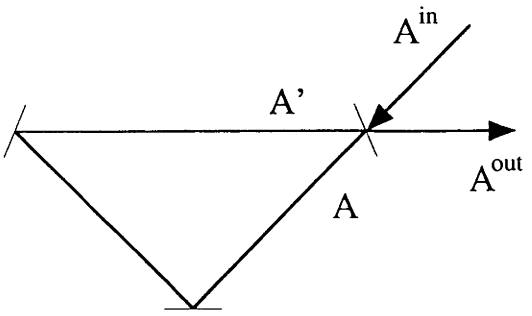

Figure 2.2: Schematic overview of a ring cavity. Coupling mirror has reflectivity r, transmittivity, t.

Consider a field at a field of frequency ν_1, A_1, and field of frequency $\nu_2 = 2\nu_1$, A_2.

The fields are defined such that the optical power is given by the absolute square, i.e $P_i = A_i^* A_i$. The two fields interact in a $\chi^{(2)}$ crystal of length Z. In the slowly varying envelope approximation (SVEA), the interaction is described by [2, p. 399]:

$$\begin{aligned} \frac{dA_1(z)}{dz} &= -i\kappa' A_3(z) A_1^*(z) f'^*(\Delta kz) \\ \frac{dA_3(z)}{dz} &= -i\kappa' A_1^2(z) f'(\Delta kz) \end{aligned} \tag{2.5}$$

where κ' is the nonlinear coupling parameter. The phase mismatch function, $f'(\Delta kz)$, also describes the effect of focussing for Gaussian waves:

$$f'(\Delta kz) = \frac{e^{+i\Delta kz}}{1 + i\frac{z}{z_R}} \tag{2.6}$$

In the rest of this chapter we will consider only plane waves, $z_R \to \infty$, so that.

$$f(\Delta kz) = e^{+i\Delta kz} \tag{2.7}$$

Assuming the fields interact weakly, then after the length Z the fields become (integrating eqn 2.5):

$$\begin{aligned} A_1(Z) &= A_1(0) - i\kappa' Z\, A_3(0)\, A_1^*(0)\, g(\Delta kZ) \\ A_3(Z) &= A_3(0) - i\kappa' Z\, A_1^2(0)\, g(\Delta kZ) \end{aligned} \tag{2.8}$$

Where the function $g(\Delta kZ)$ is [5]:

$$\begin{aligned} g(\Delta kZ) &= \frac{1}{Z}\int_0^Z f(\Delta kz)dz \\ &= \frac{e^{+i\frac{\Delta kZ}{2}} - 1}{+i\Delta kZ} \\ &= \mathrm{sinc}(\tfrac{\Delta kZ}{2})\, e^{+i\frac{\Delta kZ}{2}} \end{aligned} \tag{2.9}$$

Now consider the ring cavity shown in Fig. 2.2. A field A^{in} is incident on a mirror of reflectivity r, transmittivity, t. The field just inside the cavity is A, after one round trip the field becomes A'. The output field is A^{out}. The boundary conditions for the cavity are:

$$\begin{aligned} A &= rA' + tA^{in} \\ A^{out} &= -rA^{in} + tA' \end{aligned} \tag{2.10}$$

We require self-consistency, that is after one round-trip of time τ the cavity boundary conditions are fulfilled. So from eqn 2.10:

$$A(0, t+\tau) = rA(z, t) + tA^{in}(t) \tag{2.11}$$

Using the Taylor expansion, $f(x+\delta x) = f(x) + \dot{f}(x)\delta x + \ldots$, this becomes:

$$\frac{\partial A(0,t)}{\partial t}\tau + A(0,t) = rA(Z,t) + tA^{in}(t) \tag{2.12}$$

Rewriting $\mathrm{A}(z, \mathrm{t}+\tau) \equiv \mathrm{A}(z)$:

$$\frac{\partial \mathrm{A}(0)}{\partial \mathrm{t}} = \frac{r}{\tau}\mathrm{A}(\mathrm{Z}) - \frac{1}{\tau}\mathrm{A}(0) + \frac{t}{\tau}\mathrm{A}^{\mathrm{in}} \tag{2.13}$$

In practice, the mean field assumption (MFA), is satisfied, which implies that the amplitudes vary little along one round trip. Substituting eqn 2.8 into eqn 2.13 gives equations of motion for the scaled fields, α_i:

$$\begin{aligned} \dot{\alpha}_1 &= -\gamma_1\alpha_1 + \kappa\alpha_3\alpha_1^* + \sqrt{2\gamma_1}\mathrm{A}_1^{\mathrm{in}} \\ \dot{\alpha}_3 &= -\gamma_3\alpha_3 - \frac{\kappa}{2}\alpha_1^2 + \sqrt{2\gamma_3}\mathrm{A}_3^{\mathrm{in}} \end{aligned} \tag{2.14}$$

where we have used the scalings:

$$\begin{aligned} &\mathrm{A}_1 = \sqrt{h\nu_1}\sqrt{\frac{r_1}{\tau_1}}\alpha_1 \quad \mathrm{A}_3 = i\sqrt{h\nu_3}\sqrt{\frac{r_3}{\tau_3}}\alpha_3 \quad \kappa = \kappa' \mathrm{Z}\frac{r_1}{\tau_1}\sqrt{\frac{r_3}{\tau_3}}\sqrt{2\,h\nu_1}\; g(\Delta \mathrm{kZ}) \\ &\mathrm{A}_1^{\mathrm{in}} = \sqrt{h\nu_1}\sqrt{r_1}\mathrm{A}_1^{\mathrm{in}} \quad \mathrm{A}_3^{\mathrm{in}} = i\sqrt{h\nu_3}\sqrt{r_3}\mathrm{A}_3^{\mathrm{in}} \quad \gamma_i = \frac{T_i}{2\,\tau_i} \end{aligned} \tag{2.15}$$

and, as $r \simeq 1$, the approximation:

$$T = 1 - r^2, \quad (1-r) = \frac{T}{(1+r)} \simeq \frac{T}{2} \tag{2.16}$$

The scalings are such that, α_i, is dimensionless. The factor of one half that appears in the nonlinear term of the second harmonic equation of motion appears directly due to the frequency dependence of the scalings.

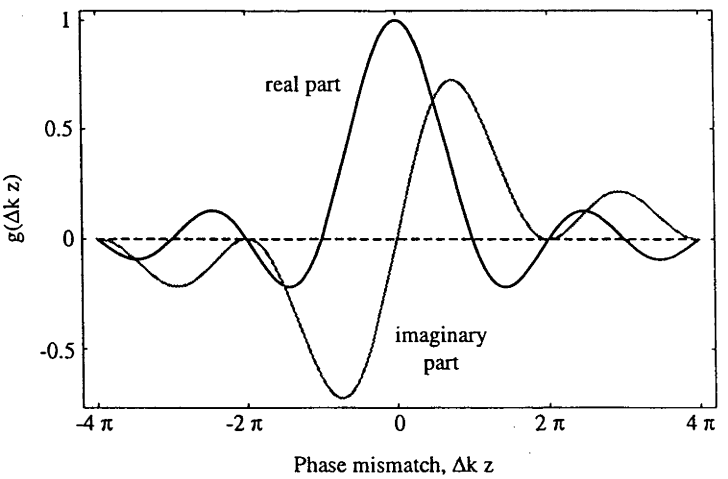

Figure 2.3: Plot of $g(\Delta \mathrm{kZ})$ vs $\Delta \mathrm{kZ}$, where $g(\Delta \mathrm{kZ}) = \mathrm{sinc}(\frac{\Delta \mathrm{kz}}{2})\, \mathrm{e}^{-i\frac{\Delta \mathrm{kZ}}{2}}$. Black line = real part; gray line = imaginary part.

The nonlinear coupling, κ, varies as as function of $\Delta \mathrm{k}$ & Z via the function $g(\Delta \mathrm{kZ})$. As shown in Fig. 2.3, $g(\Delta \mathrm{kZ})$ has both real and imaginary components. For perfect phase matching, $\Delta \mathrm{k} = 0$, $g(\Delta \mathrm{kZ})$ is purely real. At $\Delta \mathrm{k}Z = n\pi$, where $n = 1, 2, 3, \ldots$ both the real and imaginary components of $g(\Delta \mathrm{kZ})$ disappear: at these values there is no nonlinear interaction whatsoever. As will be shown in section 2.2.3, the nonlinear conversion

efficiency is dependent on the absolute value of κ. Fig. 2.4 plots $Z^2|g(\Delta kZ)|^2$, the phase mismatch dependent part of $|\kappa|^2$, for several values of Δk. When $\Delta k = 0$ the nonlinear coupling increases linearly with increasing interaction length. For $\Delta k = \pi/(2)$ the nonlinear coupling reaches a maximum at $Z = 2$, i.e. the length where $\Delta kZ = \pi$. This characteristic length is known as the *coherence length*, l_c:

$$l_c \equiv \frac{\pi}{\Delta k} \tag{2.17}$$

If the phase mismatch is increased further, both the maximum possible nonlinear coupling and the coherence length decrease accordingly. In practice it is impossible to achieve perfect phase matching; practical materials also suffer appreciable loss. To maximise nonlinear interaction and minimise loss it is best to design a system so that the crystal length is, at most, equal to the coherence length.

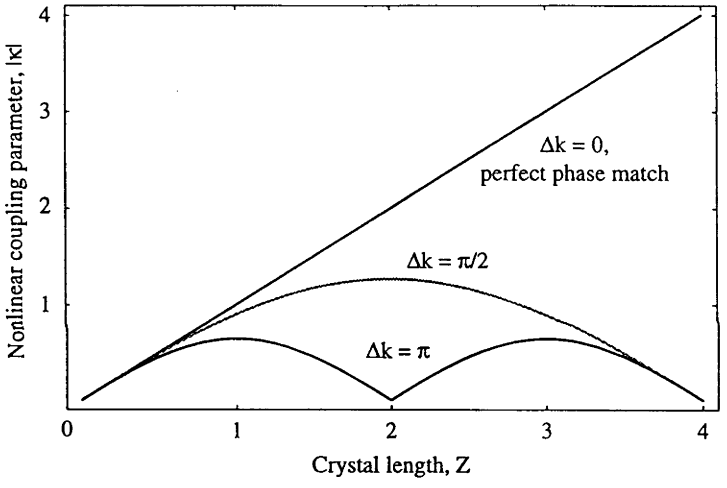

Figure 2.4: Nonlinear coupling parameter, $|\kappa|$ versus crystal length, Z. a) $\Delta k = 0$ b) $\Delta k = \pi/2$ c) $\Delta k = \pi$.

2.2.2 Decay rate of an optical cavity

There are several possible definitions of the decay rate, γ, of an optical cavity. For a cavity in the steady state, we assume that the field varies smoothly over the length of the cavity, with no appreciable change in amplitude. This is known as the mean field assumption (MFA). Given the MFA, the field retained in the cavity after each mirror interaction can be described by a function that varies smoothly in time:

$$A(t) = r^{t/\tau} = R^{\frac{t}{2\tau}} \tag{2.18}$$

where τ is the cavity round trip time, $\tau = c_0/np$; c_0 is the speed of light *in vacuo*; n is the refractive index; and p is the physical cavity perimeter. The free spectral range (FSR) of the cavity is the frequency spacing between cavity resonances, and is defined as $1/\tau$. The intracavity field amplitude can modelled by an exponential decay:

$$A(t) = e^{-\gamma t} \tag{2.19}$$

Remembering that $r = \sqrt{R}$, simple algebra gives:

$$\gamma_\ell = \frac{1}{\tau} \ln r = \frac{1}{2\tau} \ln R \tag{2.20}$$

Note that γ_ℓ diverges as R→0. However using the Taylor expansion:

$$\ln(1+x) \to x, \text{ for small x} \tag{2.21}$$

we can rewrite eqn 2.20 so that:

$$\text{for } x = r - 1, \quad \gamma_m = \frac{1}{\tau}(1-r) = \frac{1}{\tau}(1-\sqrt{R}) \tag{2.22}$$

$$\text{for } x = R - 1, \quad \gamma_n = \frac{1}{2\tau}(1-R) \tag{2.23}$$

Note that eqn 2.23 is equivalent to that given in eqn 2.15. So from eqns 2.20, 2.22, 2.23, we now have 3 possible definitions of γ. How suitable are these? We can estimate this by considering what happens before the steady state is reached. Assume that intracavity power loss occurs only at the mirror, in a stepwise fashion (this is the opposite of the MFA). There are then two ways of modelling the intracavity power. We define these as P_a (make a round trip of cavity, then lose power at mirror), and P_b (lose power at mirror, then make a round trip of cavity). That is:

$$P_a = R^{\text{round(t)}} \tag{2.24}$$

$$P_b = R^{\text{round(t)}} + 1 \tag{2.25}$$

where $\text{round}(x)$ means "round to the nearest integer value of x". P_a & P_b can be considered as bounds, in some sense, to the power loss from the cavity. In Fig. 2.5 these bounds are plotted, as are the power decay curves predicted using each definition of γ, $P = e^{-2\gamma t}$. For R=0.99, Fig. 2.5(a), it is not possible to distinguish between the definitions of γ: they agree with each other and lie between the stepwise bounds. For moderate reflectivities, such as R=0.70, γ_ℓ gives the best fit to the stepwise bounds, Fig. 2.5(b). At low reflectivities, such as R=0.15, where we expect the mean field approximation to break down, γ_ℓ still gives a surprisingly good fit to the stepwise bounds. However in the limit R→0, γ_m is the better fit, as γ_ℓ predicts that photons leave the cavity instantaneously, which is physically unlikely given that in a standing wave cavity half the photons make one round trip, of duration τ. As is clear from Fig. 2.5(b-d), for any but high reflectivities γ_n is a poor estimate of the cavity decay rate.

Inherent in this discussion is the assumption that the the cavity supports a single resonance of the field ("a mode"). The break down of γ_ℓ as R→0 reflects the fact that this assumption breaks down. As a rule of thumb, when the linewidth of a resonance starts to approach the FSR then the cavity can no longer be said to be resonant ("a single mode"): it instead supports a field. Thus the explicit model of a resonance with a certain decay rate, no longer suffices. (A suitable definition of γ can be obtained by retaining all the terms of the Taylor expansion when deriving the equations of motion via self consistency, so that eqn 2.12 contains a term that is the infinite sum of the Taylor terms [6].)

To summarise, for high reflectivities the definitions of γ are equally valid. For moderate reflectivities γ_ℓ is the best definition, however as R→0 it breaks down. In this regime γ_m is quite an acceptable definition. As in this thesis we we consider a wide range of

reflectivities we will favour γ_m to maintain consistency.

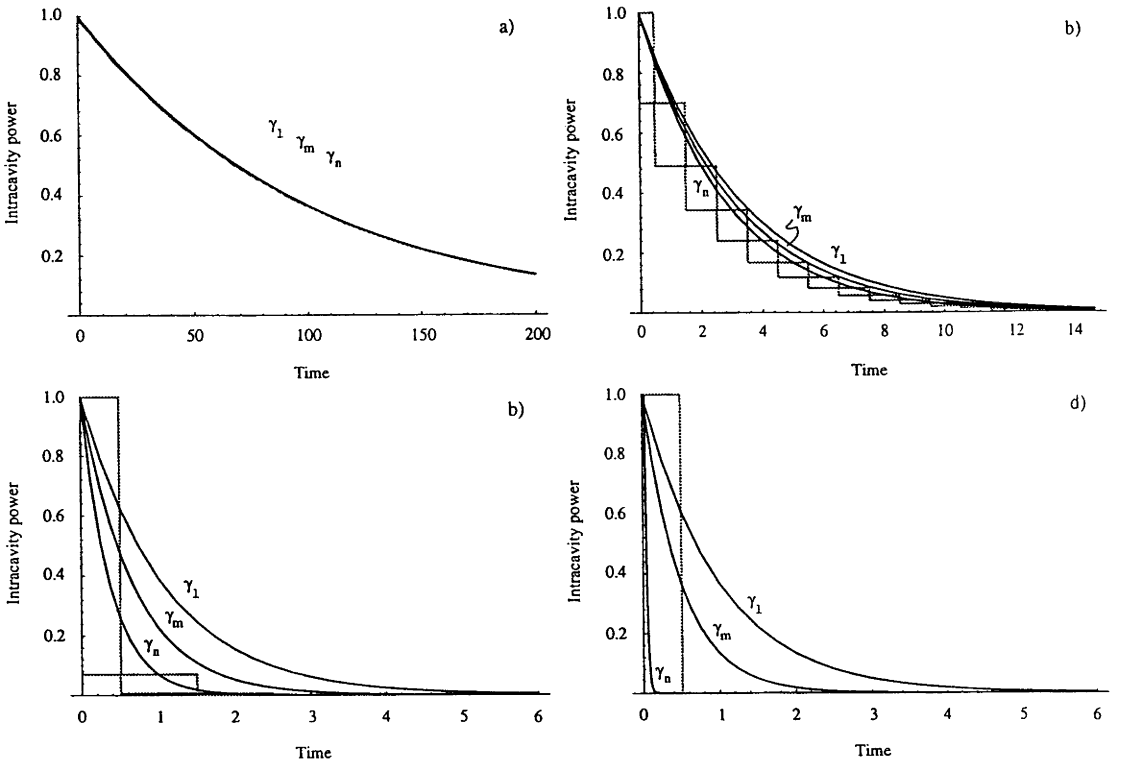

Figure 2.5: Decay of intracavity power versus time. Step functions are calculated as discussed in text. Smooth curves are plotted using various definitions of γ. a) R = 0.99 b) R = 0.70 c) R = 0.15 d) R→0.

2.2.3 Doubly vs singly resonant SHG

In section 2.2.1 we derived the equations of motion for a doubly resonant cavity, where both the fundamental and second harmonic modes are simultaneously resonant. Remembering that for simple SHG, $A_3^{in} = 0$, we recast eqn 2.14 to define the equations of motion as [2]:

$$\begin{aligned} \dot{\alpha}_1 &= -(\gamma_1 + i\Delta_1)\,\alpha_1 + \kappa\alpha_3\alpha_1^* + \sqrt{2\gamma_1^c}\mathcal{A}_1^{\text{in}} \\ \dot{\alpha}_3 &= -(\gamma_3 + i\Delta_3)\,\alpha_3 - \frac{\kappa^*}{2}\alpha_1^2 + \sqrt{2\gamma_3^c}\mathcal{A}_3^{\text{in}} \end{aligned} \tag{2.26}$$

where Δ_i is the detuning for each mode, the losses are related by:

$$\gamma_i = \gamma_i^c + \gamma_i^{other} \tag{2.27}$$

where γ_i is the total decay rate for mode i; γ_i^c is the decay rate through the coupling mirror; and γ_i^{other} are decay rates due to internal losses, other mirrors, etc.

[2] The equations of motion 2.14 & 2.26 are effectively those first given in Drummond et. al. [7], except that the coupling follows the input/output formalism.

We define the term $(\gamma_i + i\Delta_i)$ as the *effective decay rate* of the cavity. To see why, consider the following argument. Without loss of generality, we can assume that the pump rates, $\mathcal{A}_i^{\text{in}}$ are real. If all detunings, Δ_i, are zero then the field values, α_i are real. In this limit it is clear that the values of α_i are limited by the total decay rates γ_i: if γ_i are large then the absolute values of α_i will be small. If the detunings are not zero, then the values of α_i are complex, and their values are limited by both the decay rates, γ_i *and* the detunings, Δ_i. If the detunings, Δ_i are very large, then, even if γ_i are small, the absolute values of α_i will be small. Thus the detuning effectively increases the decay rate of the cavity.

The pump rates, $\mathcal{A}_i^{\text{in}}$, are related to the pump power, P_1^{in}, by:

$$\mathrm{P}_1^{\text{in}} = h\nu_1 |\mathcal{A}_i^{\text{in}}|^2 \tag{2.28}$$

The power through a cavity port, j, for a mode, i, is given by:

$$\mathrm{P}_i^j = 2h\nu_i \gamma_i^{(j)} |\alpha_i|^2 \tag{2.29}$$

Cavity ports include the outcoupling mirror, internal loss, and other cavity mirrors. The intracavity or circulating power of a mode i is given by:

$$\mathrm{P}_i^{\text{circ}} = \frac{h\nu}{\tau} |\alpha_i|^2 \tag{2.30}$$

The boundary conditions for the cavity are:

$$\mathcal{A}_1^{\text{out}} = \sqrt{2\gamma_1^c}\alpha_1^{\text{ss}} - \mathcal{A}_1^{\text{in}} \tag{2.31}$$

$$\mathcal{A}_3^{\text{out}} = \sqrt{2\gamma_3^c}\alpha_3^{\text{ss}} - \mathcal{A}_3^{\text{in}} \tag{2.32}$$

where α_i^{ss} is the steady state value of mode i; $\mathcal{A}_i^{\text{in}}$ is the incident field for mode i; and $\mathcal{A}_i^{\text{out}}$ is the reflected field for mode i.

The singly resonant case, where only the fundamental is resonant, can be derived using a similar argument as that given in section 2.2.1. Alternatively, we can use eqn 2.26 directly. The advantage of this approach is that it makes the connection between the doubly and singly resonant cases transparent. In the singly resonant case the dynamics of the second harmonic field are much quicker than those of the fundamental. Thus, on the time scale of the fundamental field, the second harmonic is constant, letting us set $\dot{\alpha}_3 = 0$. As discussed in section 2.5.3, we can set $\Delta_3 = 0$. Solving for $\dot{\alpha}_3 = 0$, and assuming $\gamma_3^c = \gamma_3$ we find:

$$\alpha_3^{\text{ss}} = \frac{-\kappa}{2\gamma_3} |\alpha_1|^2 + \frac{\sqrt{2}\mathcal{A}_3^{\text{in}}}{\sqrt{\gamma_3}} \tag{2.33}$$

Substituting this into eqn 2.26 we obtain the singly resonant equation of motion:

$$\dot{\alpha}_1 = -(\gamma_1 + i\Delta_1)\,\alpha_1 - \mu|\alpha_1|^2\alpha_1 + 2\sqrt{\mu}\mathcal{A}_3^{\text{in}}\alpha_1^* + \sqrt{2\gamma_1^c}\mathrm{A}_1^{\text{in}} \tag{2.34}$$

where the nonlinear interaction, μ, is:

$$\mu = \frac{\kappa^2}{2}\frac{(\gamma_3 - i\Delta_3)}{(\gamma_3^2 + \Delta_3^2)} \tag{2.35}$$

For SHG, there is no power input at the second harmonic, so $\mathcal{A}_3^{\text{in}} = 0$ and the third term disappears.

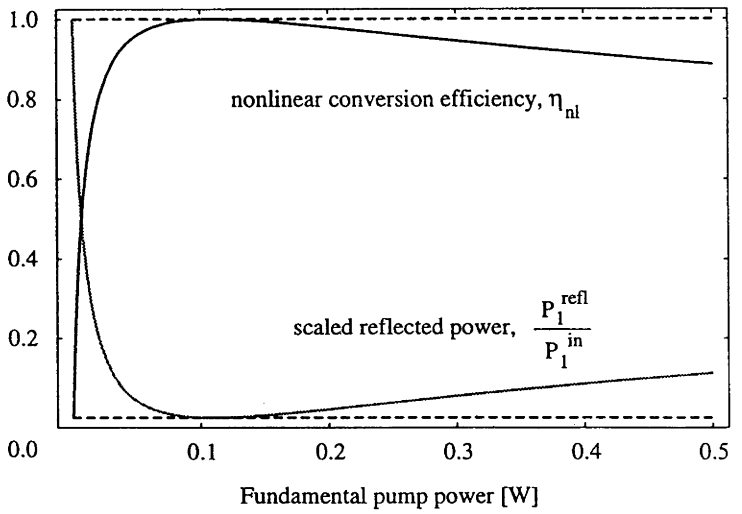

Figure 2.6: Nonlinear conversion efficiency, η_{nl}, and scaled reflected power, P_1^{refl}/P_1^{in}, versus incident power. Values used are: $\mu = .002$; $R = 0.991$; $\gamma_1^c = \gamma_1$; $\tau = 1.863\ 10^{-10}$ s; $\lambda = 1064$ nm.

Thus the first term of equation 2.34 represents linear loss and linear detuning, the second term, represents nonlinear loss, and if $\Delta_3 \neq 0$, nonlinear detuning [7], whilst the third term is linear gain. ($\Delta_3 = 0$ is the case given in Paschotta et. al. [8]). The nonlinear loss leads to power broadening of the cavity linewidth.

In singly resonant SHG, $\gamma_3^c = 1/\tau$ and Δ_3 can be ignored (see 2.5.3). Using eqns 2.35 & 2.33 the boundary condition for the second harmonic becomes:

$$\alpha_3^{out} = \sqrt{\mu}|\alpha_1^{ss}|^2 \tag{2.36}$$

Equation 2.34 is a cubic in alpha. We obtain the steady state solution:

$$\alpha_1^{ss} = \frac{\sqrt{2\gamma_1^c}A_1^{in}}{(\gamma_1 + \gamma_{nl} + i\Delta_1)^2} \tag{2.37}$$

where $\gamma_{nl} = \mu|\alpha_1^{ss}|^2$. The generated second harmonic power is:

$$\begin{aligned} P_3 &= h\nu_3|\alpha_3^{out}|^2 \\ &= h2\nu_1\mu|\alpha_1^{ss}|^2|\alpha_1^{ss}|^2 \\ &= 4h\nu_1|A_1^{in}|^2\frac{\gamma_{nl}\gamma_1^c}{(\gamma_1 + \gamma_{nl} + i\Delta_1)^2} \end{aligned} \tag{2.38}$$

From eqns 2.28 & 2.38, we can calculate the nonlinear conversion efficiency, η_{nl}:

$$\eta_{nl} = \frac{4\gamma_1^c\gamma_{nl}}{(\gamma_1 + \gamma_{nl} + i\Delta_1)^2} \tag{2.39}$$

The reflected fundamental power is given by:

$$\frac{P_1^{refl}}{P_1^{in}} = 1 - \frac{4\gamma_1^c(\gamma_{nl} + [\gamma_1 - \gamma_1^c])}{(\gamma_1 + \gamma_{nl} + i\Delta_1)^2}$$

$$= 1 - \eta_{\rm nl} - \frac{4\gamma_1^c(\gamma_1 - \gamma_1^c)}{(\gamma_1 + \gamma_{\rm nl} + i\Delta_1)^2} \tag{2.40}$$

For zero detuning, $\Delta_1 = 0$, Fig. 2.6 plots the nonlinear conversion efficiency and the ratio of reflected to incident power as a function of incident power. The maximum conversion efficiency, $\eta_{\rm nl}^{\rm max}$, occurs at, $\gamma_{\rm nl} = \gamma_1$, with a value:

$$\eta_{\rm nl}^{\rm max} = \frac{\gamma_1^c}{\gamma_1} \tag{2.41}$$

(For $\gamma_1^c = \gamma_1$, perfect conversion occurs, i.e. $\eta_{\rm nl}^{\rm max} = 1$). The pump power at which the maximum conversion efficiency occurs, is:

$$\mathrm{P}_1^{\rm max\ conv} = 2h\nu_1 \frac{\gamma_1^3}{\mu\gamma_1^c} \tag{2.42}$$

Small fundamental decay rates, large outcoupling ratios (γ_1^c/γ_1) and large nonlinear couplings minimise the power at which maximum conversion occurs.

When the reflected power is zero the cavity is said to be *impedance matched*. For zero detuning this occurs at:

$$\gamma_{\rm nl}^{imp} = 2\gamma_1^c - \gamma_1, \ \text{ for } \gamma_1^c \geq \gamma_1/2 \tag{2.43}$$

If $\gamma_1^c < \gamma_1/2$ then there is no power at which the cavity is impedance matched. (Note that when $\gamma_1^c = \gamma_1$, $\gamma_{\rm nl}^{imp} = \gamma_1$.) The impedance matching power, P_1^{imp} is given by:

$$\mathrm{P}_1^{imp} = 2h\nu_1 \frac{\gamma_1^c(2\gamma_1^c - \gamma_1)}{\mu}, \ \text{ for } \gamma_1^c \geq \gamma_1/2 \tag{2.44}$$

2.3 Introducing: Interacting $\chi^{(2)}$ nonlinearities

In recent years there has been investigation into a wide number of optical effects in second order systems: nonlinear phase shifts; optical bistability; power limiting; efficient and broadband frequency generation. All these effects can be considered as due to one of the basic $\chi^{(2)}$processes, as considered at the beginning of the chapter, cascaded with at least another basic $\chi^{(2)}$process, for example SHG followed by OPO. Hence they are often refereed to as *cascaded* nonlinearities.

As we shall see, the problem with this appellation is its generality. Very different effects have been labelled as cascaded effects (e.g.. dynamics of simultaneous SHG and NDOPO; nonlinear optical phase shift due to phase mismatched SHG; etc) but this name does not specify the actual mechanism that causes the effect. To clarify the situation, we introduce the concept of *interacting nonlinearities*. Interacting nonlinearities can be categorised as *cooperating* and *competing*. Cooperating nonlinearities are those where all the downconversion and upconversion processes share the same modes, e.g. $\nu \rightleftharpoons 2\nu$ or $\nu \pm \Delta_1 \rightleftharpoons 2\nu$. Competing nonlinearities are those where all the downconversion and upconversion processes do not share the same modes, e.g. $\nu \rightleftharpoons 2\nu \rightleftharpoons \nu \pm \Delta_2$, or, $\nu \pm \Delta_1 \rightleftharpoons 2\nu \rightleftharpoons \nu \pm \Delta_2$. We restrict the term "cascading" to describing situations where several different competing or cooperating nonlinearities occur simultaneously (for example, see section 7.1).

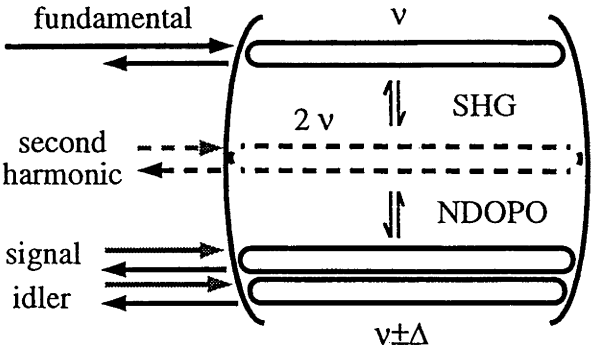

Figure 2.7: Conceptual layout of competing SHG & NDOPO. Gray lines represent vacuum inputs, i.e zero average power.

2.4 Competing $\chi^{(2)}$ nonlinearities

Systems of competing nonlinearities have been mainly investigated for their potential as frequency tunable sources of light. Systems considered include: intracavity SFG and NDOPO [10, 11]; intracavity DFG and NDOPO [12]; and intracavity SHG and NDOPO [9, 13, 14, 15, 16, 17, 19]. In these systems the $\chi^{(2)}$processes have been considered as occurring in separate nonlinear media or as occurring simultaneously in the one medium.

2.4.1 Competing SHG and NDOPO

In this section we will focus on competition between SHG and NDOPO. Consider a cavity system in which SHG and NDOPO occur simultaneously. Fig. 2.7 shows the conceptual layout. A frequency doubler, resonant at and pumped by a frequency ν, produces a resonant field of frequency 2ν. The second harmonic can either downconvert back to the original mode, or act as the pump for the NDOPO. For the latter to occur the signal & idler modes ($\nu_{s,i} = \nu \pm \Delta$) must be simultaneously resonant with the mode ν. With sufficient power in the 2ν field the NDOPO can be above threshold, otherwise the system is below threshold and acts as an amplifier of the vacuum modes. By inspection (adding appropriate terms to 2.26) we can write the equations of motion as [9]:

$$\begin{aligned}
\dot{\alpha}_1 &= -(\gamma_1 + i\Delta_1)\,\alpha_1 + \kappa_1\alpha_3\alpha_1^* + \sqrt{2\gamma_1^c}A_1^{\text{in}} \\
\dot{\alpha}_3 &= -(\gamma_3 + i\Delta_3)\,\alpha_3 - \frac{\kappa_1^*}{2}\alpha_1^2 - \kappa_2^*\alpha_s\alpha_i \\
\dot{\alpha}_{s,i} &= -(\gamma_{s,i} + i\Delta_{s,i})\,\alpha_{s,i} + \kappa_2\alpha_3\alpha_{i,s}^*
\end{aligned} \tag{2.45}$$

where α_1, α_2, α_s , α_i are the fundamental, second harmonic, signal, and idler field amplitudes, respectively; and κ_1 and κ_2 are the respective nonlinear interaction rates for SHG and NDOPO. All four modes are resonant, so this system has been labelled Quadruply Resonant Optical Parametric Oscillation (QROPO). The quantum properties of this system have been modelled and several new nonclassical features are predicted [18]: this will be discussed further in Chapter 7.

We are particularly interested in the case where the second harmonic is not resonant.

Adiabatically eliminating the second harmonic gives [19]:

$$\begin{aligned}\dot{\alpha}_1 &= -(\gamma_1 + i\Delta_1)\,\alpha_1 - 2\sqrt{\mu_1\mu_2}\alpha_1^*\alpha_s\alpha_i - \mu_1|\alpha_1|^2\alpha_1 + \sqrt{2\gamma_1^c}A_1^{in} \\ \dot{\alpha}_{s,i} &= -(\gamma_{s,i} + i\Delta_{s,i})\,\alpha_{s,i} - \sqrt{\mu_1\mu_2}\alpha_1^2\alpha_{i,s}^* - 2\mu_2|\alpha_{i,s}|^2\alpha_{s,i}\end{aligned} \tag{2.46}$$

where the nonlinear interactions for SHG & NDOPO are respectively:

$$\begin{aligned}\mu_1 &= \frac{\kappa^2}{2(\gamma_3 + i\Delta_3)} \\ \mu_2 &= \frac{\kappa'^2}{2(\gamma_3 + i\Delta_3)}\end{aligned} \tag{2.47}$$

For simplicity, we will consider the case where all detunings are set to zero. The threshold power for the NDOPO, and thus competition, is then given by:

$$P_1^{thr} = h\nu_1 \frac{\bar{\gamma}}{\gamma_1^c}\frac{\gamma_1^2}{\sqrt{\mu_1\mu_2}}\frac{1}{2}\left(1 + \mathcal{R}\frac{\bar{\gamma}}{\gamma_1}\right)^2 \tag{2.48}$$

where we introduce the cumulative decay rate for the low frequencies of the NDOPO, $\bar{\gamma}$, and the scaled total nonlinearity, $\mathcal{R}$:

$$\begin{aligned}\bar{\gamma} &= \sqrt{\gamma_s\gamma_i} \\ \mathcal{R} &= \sqrt{\mu_1/\mu_2}\end{aligned} \tag{2.49}$$

The scaled power, N, is defined with respect to the TROPO threshold as:

$$N = \frac{P_1}{P_1^{thr}} \tag{2.50}$$

The threshold power can be altered by changing either the value of the nonlinearities or the signal & idler resonance conditions. The former is achieved via the phase matching. The latter is achieved via *dispersion matching*, i.e. altering the dispersion (by changing the laser frequency or cavity length), so that the signal & idler are unable to be resonant with the fundamental. As discussed in section 2.2.3, a mode that is so detuned from the optimum resonance condition is lossy, and can be considered to have an increased decay rate which previously labelled the effective decay rate.

For the likely experimental optimum of equal losses and nonlinearities:

$$\gamma_s = \gamma_i = \gamma_1, \quad \mu_1 = \mu_2 \tag{2.51}$$

we define a minimum threshold power:

$$P_1^{min} = h(2\nu_1)\frac{\gamma_1^2}{\eta\mu_1} \tag{2.52}$$

where the cavity escape efficiency, η is given by:

$$\eta = \frac{\gamma_1^c}{\gamma_1} \tag{2.53}$$

Note that this expression is identical to that for the threshold power of a normal DOPO cavity where the second harmonic is double-passed, but not resonant. The conversion

efficiency at TROPO threshold is defined as:

$$\epsilon = \frac{P_2}{P_1^{\text{thr}}} \tag{2.54}$$

Note that the minimum threshold, P_1^{min}, is the impedance matching point for the cavity, and thus the point of maximum conversion efficiency, $\epsilon = \eta$.

The obvious signature that the cavity is above threshold is production of the signal and idler modes. However another, somewhat surprising, signature of competition exists: clamping of the second harmonic power. From 2.46 we find that for $P_1 > P_1^{\text{thr}}$ (N > 1), the second harmonic power is:

$$P_2 = h2\nu\frac{\bar{\gamma}^2}{\mu_2} \tag{2.55}$$

i.e above threshold the generated second harmonic power is constant, and is clamped to its threshold value. "Excess" fundamental pump power is not converted to second harmonic, but instead is reflected or converted to signal and idler. (Clamping has also been predicted for QROPO [9])

Similar behaviour has been predicted for the *optical limiter* [21]. Fig. 2.8 shows the conceptual layout of both the optical limiter and the TROPO cavity. The limiter is a standing wave DOPO cavity resonant at the subharmonic, ν, which is single-pass pumped at 2ν. (Note that the following argument works equally well for a NDOPO cavity). At threshold, the 2ν field is converted to the subharmonic as it propagates along the cavity so that at the end of the cavity it is depleted to some value. As the power of the 2ν field is increased, it's value at the end of the cavity does not change: "excess" power is downconverted to the subharmonic field. In turn the backward component of the standing wave subharmonic partially upconverts to the pump (an example of cooperating nonlinearities) so that a backward travelling wave at 2ν is generated: the remaining power exits the cavity as subharmonic. Far above threshold, the reflection at 2ν predominates, with very little power exiting the cavity at the subharmonic. From the point of view of the incident 2ν field then, the limiter is effectively a nonlinear mirror: at low powers it transmits all of the 2ν field; above threshold it is limited to passing the threshold power, excess power is reflected back from the cavity as fields at 2ν or the subharmonic. Note that within the cavity the 2ν field has a very strong spatial dependence.

The TROPO system is obviously analogous to the limiter in that the 2ν field in both cases sees three input and three output ports. For the limiter two of the ports are cavity ports (input and output mirrors for the pump field) and one is a nonlinear port (interaction with the subharmonic). For the TROPO system only one of the ports is a cavity port (the input/output port for the second harmonic), the other two ports are nonlinear (interaction with the fundamental, interaction with the subharmonic/signal & idler). Without the extra nonlinear port that competition provides, clamping could not occur. As with the limiter the second harmonic field has a strong spatial dependence. However unlike the optical limiter no additional 2ν field is generated: the excess second harmonic power is either downconverted to the signal & idler modes, or downconverted back to the fundamental mode.

2.4.2 Competition and phase matching

In the systems considered in refs [10, 11, 12, 15] the competing nonlinear processes

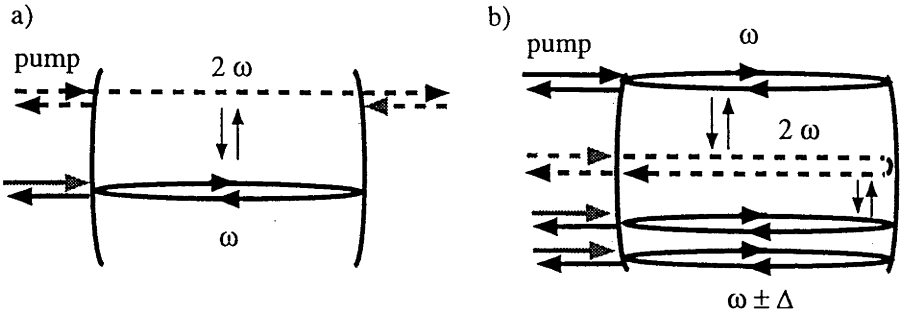

Figure 2.8: Conceptual layouts of: a) *Optical limiter*, a standing wave (N)DOPO resonant at the subharmonic ν, which is single-pass pumped at 2ν. Only the DOPO case is shown here. Clamping of the transmitted 2ν (pump) field occurs due to cooperating nonlinearities. b) *TROPO*, Triply Resonant Optical Parametric Oscillator. Fundamental, signal & idler modes are resonant, second harmonic executes a double pass through crystal. Clamping of the generated 2ν (second harmonic) field occurs due to competing nonlinearities. Gray lines represent vacuum inputs, i.e. zero average power.

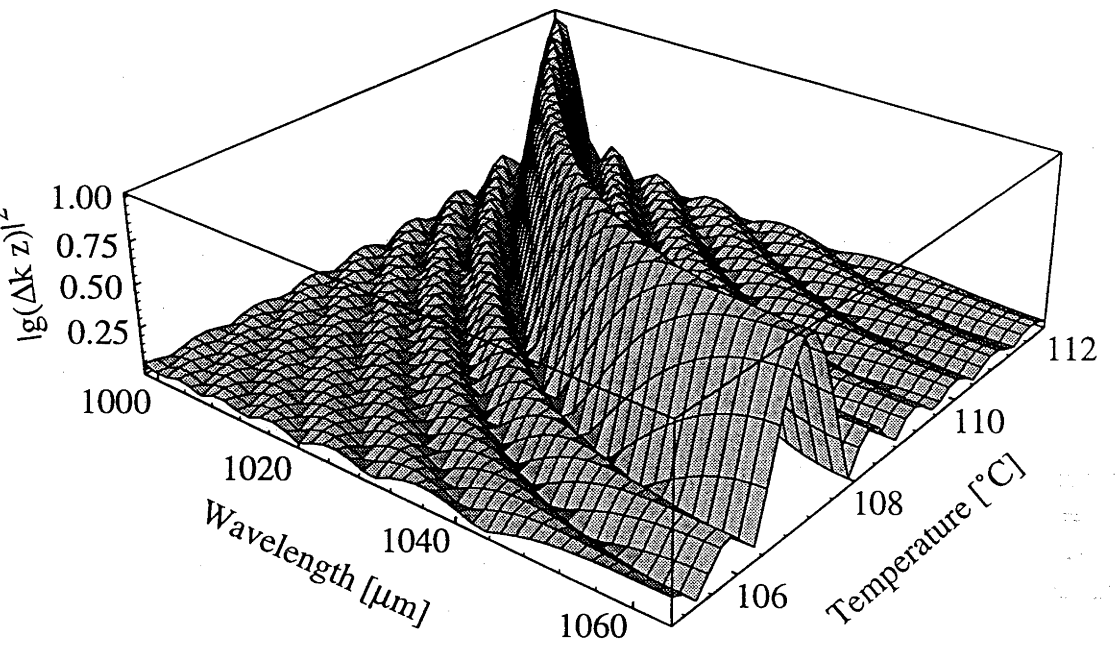

Figure 2.9: Plot of nonlinear coupling phase mismatch function, $|g(\Delta kZ)|^2$, versus wavelength and crystal temperature.

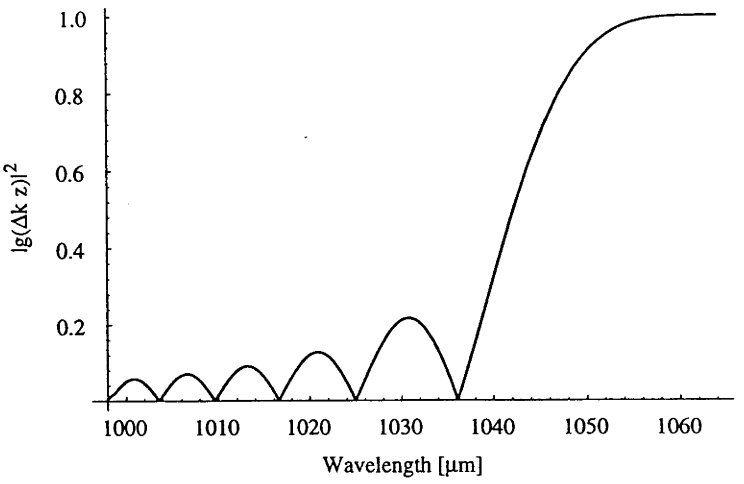

Figure 2.10: Plot of nonlinear coupling phase mismatch function, $|g(\Delta kZ)|^2$, versus wavelength at optimum temperature for SHG. Note the gain peak at 1031 nm.

occur in separate nonlinear media within the one cavity. This is easy to understand physically, as the phase matching can be optimised for say, SHG in one crystal, and NDOPO in the other. In refs [13, 14, 16, 17] and in this thesis competing SHG & NDOPO occur *simultaneously* within the one nonlinear medium. How is this possible given that in these systems the crystal is carefully phase matched to give the optimum SHG effect?

To understand this consider the nonlinear coupling. As was shown in section 2.2.3 the nonlinear coupling, μ, is a function of phase mismatch Δk and the crystal length, Z, via the nonlinear coupling phase mismatch function $|g(\Delta kZ)|^2$ (which is defined in eqn 2.9). As discussed in section 2.2.1, the phase mismatch is a function of refractive index. Thus, for example, using the refractive index expression for 5% MgO : $LiNbO_3$ [20] we obtain:

$$\Delta k \simeq -8666(1-\lambda_0/\lambda_s)^2 cm^{-1} + 7.49(T-T_0)cm^{-1}K^{-1} \tag{2.56}$$

where $\lambda_0 = 1064$ nm, $T_0 = 107.05°C$. Substituting this into $|g(\Delta kZ)|^2$ gives the dependence of the nonlinear coupling on wavelength and crystal temperature: Fig. 2.9 plots this explicitly. If we optimise the nonlinear coupling for SHG of a 1064 nm beam, then we are sitting on top of the ridge at $T = 107.05°C$ ($g(\Delta kZ) = 1$). At this temperature there is still gain for wavelengths other than 1064 nm, as shown in Fig. 2.10 which is a slice through Fig. 2.9 at $T = 107.05°C$. In the 10 nm around 1064 nm the gain is reduced only slightly from the optimum, $g(\Delta kZ) > 0.9$; even 33 nm away there is considerable gain ($g(\Delta kZ) = 0.22$ @ 1031 nm, c.f. with the measurements in section 7.1). If the signal and idler modes of the NDOPO are resonant at any of these wavelengths there will be sufficient nonlinear coupling for significant competition to occur.

2.5 Cooperating $\chi^{(2)}$ nonlinearities

The concept of cooperating nonlinearities bears closer examination. Afterall, in standard SHG the complementary OPO process certainly occurs - photons at 2ν can be converted to photons at ν. (The equations of motion for SHG and OPO differ only in the position of the the pump term, the interaction terms are exactly the same.) How then is the concept

of cooperating nonlinearities useful? As we saw in the last section, it's useful when the complementary $\chi^{(2)}$processes have non-symmetrical effects. Thus in (N)DOPO pump clamping [21], downconversion depletes the single, forward pass, pump wave. Yet up-conversion generates a backward travelling wave at the pump frequency, making it appear as if pump light is reflected - even though there is no mirror or cavity for the pump. The up- and down- conversion processes share the same modes, but an asymmetrical effect, power calming, results. We describe such a results as being due to cooperating, $\chi^{(2)}$processes.

Third order effects, such as a nonlinear phase shift (via the Kerr effect), are normally associated with the $\chi^{(3)}$nonlinearity of a medium. In standard nonlinear crystals, this is some 4 orders of magnitude weaker than the $\chi^{(2)}$nonlinearity. As the magnitude of nonlinear effects go as the square of the nonlinearity, this means third order effects are typically 8 orders of magnitude weaker than second order effects. However in recent years large "third order" effects, of the same order of magnitude as second order effects, have been produced via *cascaded* $\chi^{(2)}$nonlinearities. These systems have been the subject of extensive research [22, 23], including CW studies using cavities [24, 25]. At the heart of all of the effective third order effects is the production of a nonlinear phase shift: from that point one can obtain optical bistability, optical switching, and so on.

The origin of the the nonlinear phase shift in "cascaded" systems can be explained simply. Consider say, single pass SHG in a lossless crystal of length L. The fundamental field enters the crystal and begins to be strongly converted to second harmonic. However the crystal is phase matched so that it has a coherence length of L/2, i.e. beyond this distance the second harmonic converts back to fundamental. Only fundamental light exits the crystal. This would seem rather pointless, except that the light experiences a phase shift in both the SHG ($\nu \rightarrow 2\nu$) and OPO processes ($2\nu \rightarrow \nu$). As the $\chi^{(2)}$processes are nonlinear with intensity, so are the respective phase shifts: the total effect is an intensity dependent phase shift on the fundamental light. Obviously this effect will also occur in other $\chi^{(2)}$processes, such as OPO, and in cavity systems. The complementary $\chi^{(2)}$processes cooperate to give an overall effect: the nonlinear phase shifts from each individual $\chi^{(2)}$process are cumulative. This is non-symmetrical in that the nonlinear phase shifts add, as opposed to cancelling. Systems of cooperating $\chi^{(2)}$nonlinearities hold promise for applications including optical switching, nonlinear optical amplification [26], squeezing, and QND measurements [24].

In cavity systems there are *three* ways to produce a nonlinear phase shift: phase matching, detuning, and thermal absorption. We discuss each of these in turn in the following sections.

2.5.1 Higher order equations of motion

The preceding explanation of a nonlinear phase shift due to phase mismatch assumed that there is no net nonlinear conversion, i.e. there is no nonlinear loss. The alert reader is probably somewhat uncomfortable with this: afterall, the equations of motion from section 2.2.1 make it clear that at the point of zero nonlinear conversion there is also zero nonlinear phase shift. What's going on?

This discrepancy between intuitive model and equation is easily resolved: the standard equations of motion for SHG are incomplete. This is not a widely realised fact. We now present the derivation a more complete set of equations that highlight *which* third order effects are possible in a second order system.

Let us recap the argument that we used to derive the equations of motion in section

2.2.1. The interaction of the fields in the slowly varying envelope is described by eqns 2.5. Using the assumption that the fields interact weakly, we then integrated eqns 2.5 to give eqns 2.8. Eqns 2.8 describe, to first order in the nonlinearity, the fields after a single transit through the nonlinear medium. The cavity equations of motion were derived from this point.

To describe third order effects, it is necessary to have a description of the fields to second order in the nonlinearity. This is easily obtained by substituting eqns 2.8 into eqns 2.5 to give (writing $A_i(0) = A_i$):

$$\begin{aligned} A_1(Z) &= A_1 - i\kappa' A_3 A_1^* \mathcal{J}_1^* - \kappa'^2 (|A_1|^2 + |A_3|^2) A_1 \mathcal{J}_2 + i\kappa'^3 A_1^3 A_3^* \mathcal{J}_3 \\ A_3(Z) &= A_3 - i\kappa' A_1^2 \mathcal{J}_1 - 2\kappa'^2 |A_1|^2 A_3 \mathcal{J}_2^* + i\kappa'^3 A_3^2 A_1^2 \mathcal{J}_3 \end{aligned} \tag{2.57}$$

Where the functions $\mathcal{J}_1, \mathcal{J}_2, \mathcal{J}_3$ are:

$$\begin{aligned} \mathcal{J}_1 &= \int_0^Z e^{+i\Delta k z} dz = \frac{e^{+i\Delta k Z} - 1}{+i\Delta k} \\ &= Z \,\mathrm{sinc}(\tfrac{\Delta k Z}{2})\, e^{+i\frac{\Delta k Z}{2}} = Z\, g(\Delta k Z) \\ &= Z + \frac{i\Delta k}{2!} Z^2 + \frac{(+i\Delta k)^2}{3!} Z^3 + \ldots \\ \mathcal{J}_2 &= \int_0^Z \mathcal{J}_1 e^{-i\Delta k z} dz = \frac{Z - \mathcal{J}_1^*}{+i\Delta k} \\ &= \frac{Z^2}{2}\left[\mathrm{sinc}^2(\tfrac{\Delta k Z}{2}) + i\left(\mathrm{sinc}(\tfrac{\Delta k Z}{2})\mathrm{cosc}(\tfrac{\Delta k Z}{2}) - \frac{1}{\Delta k Z/2}\right)\right] \\ &= \frac{Z^2}{2} + \frac{i\Delta k}{6} Z^3 + \ldots \\ \mathcal{J}_3 &= \int_0^Z \mathcal{J}_1^2 e^{-i\Delta k z} dz = \frac{2\,Z - \mathcal{J}_1 - \mathcal{J}_1^*}{\Delta k^2} \\ &= \frac{Z^3}{6} + \ldots = \mathcal{J}_3^* \end{aligned} \tag{2.58}$$

The expansions of $\mathcal{J}_i$ are derived using the relation $e^x = \sum_0^\infty x^n/n!$. Notice that for $\Delta k = 0$, $\mathcal{J}_1 = Z$, $\mathcal{J}_2 = Z^2/2$, and $\mathcal{J}_3 = Z^3/6$: the higher order interactions exist even in the perfectly phase matched case. For use later, we introduce the scaled functions:

$$\mathcal{J}_1' = \frac{\mathcal{J}_1}{Z} = g(\Delta k z), \quad \mathcal{J}_2' = \frac{\mathcal{J}_2}{Z^2} \tag{2.59}$$

As can be seen directly from the definition of $\mathcal{J}_2$, the second order interactions are generated by first order interactions cooperatively interacting with other fields before leaving the cavity.

We can now derive the cavity equations of motion using exactly the same argument we presented previously [3]. Retaining only terms second order in κ and lower, and using defns 2.15 and eqn 2.13 we find:

$$\begin{aligned} \dot{\alpha}_1 &= -(\gamma_1 + i\Delta_1)\alpha_1 + \kappa\alpha_3\alpha_1^*\mathcal{J}_1^* - \frac{k^2}{2}(|\alpha_1|^2\frac{\tau_3}{r_3} - 2|\alpha_3|^2\frac{\tau_1}{r_1})\alpha_1\mathcal{J}_2 + \sqrt{2\gamma_1^c}A_1^{in} \\ \dot{\alpha}_3 &= -(\gamma_3 + i\Delta_3)\alpha_3 - \frac{\kappa}{2}\alpha_1^2\mathcal{J}_1 - \kappa^2\frac{\tau_1}{r_1}|\alpha_1|^2\alpha_3\mathcal{J}_2^* + \sqrt{2\gamma_3^c}A_3^{in} \end{aligned} \tag{2.60}$$

[3] The results presented in this section and section 2.2.1 were explicitly obtained for *plane* waves. R. Bruckmeier has derived the Gaussian wave form of these results: the singly resonant results are given in [27].

Similarly we can derive the nondegenerate equations of motion:

$$\begin{aligned}
\dot{\alpha}_1 &= -(\gamma_1 + i\Delta_1)\,\alpha_1 + \kappa\alpha_3\alpha_2^*\,\mathcal{J}_1^* - \frac{k^2}{2}(2|\alpha_2|^2\frac{\tau_3}{r_3} - 2|\alpha_3|^2\frac{\tau_2}{r_2})\alpha_1\,\mathcal{J}_2 \\
&\quad +\sqrt{2\gamma_1^c}A_1^{\text{in}} \\
\dot{\alpha}_2 &= -(\gamma_1 + i\Delta_1)\,\alpha_1 + \kappa\alpha_3\alpha_1^*\,\mathcal{J}_1^* - \frac{k^2}{2}(2|\alpha_1|^2\frac{\tau_3}{r_3} - 2|\alpha_3|^2\frac{\tau_1}{r_1})\alpha_2\,\mathcal{J}_2 \\
&\quad +\sqrt{2\gamma_1^c}A_2^{\text{in}} \\
\dot{\alpha}_3 &= -(\gamma_3 + i\Delta_3)\,\alpha_3 - \kappa\alpha_1\alpha_2\mathcal{J}_1 - 2\kappa^2(|\alpha_1|^2\frac{\tau_2}{r_2} - 2|\alpha_2|^2\frac{\tau_1}{r_1})\alpha_3\,\mathcal{J}_2^* \\
&\quad +\sqrt{2\gamma_3^c}A_3^{\text{in}}
\end{aligned} \tag{2.61}$$

Eqns 2.60 & 2.61 describe an incredibly rich array of behaviours.

• Terms that are zeroth order in κ are simply linear loss, $-\gamma_i\alpha_i$, linear gain, $+\sqrt{2\gamma_i^c}A_i^{\text{in}}$, and linear detuning, $\pm i\Delta_i\alpha_i$.

• First order terms in κ describe second order effects: parametric gain or loss, $+\text{Re}\,\mathcal{J}_1^*\kappa\alpha_i\alpha_j^*$, $-\text{Re}\,\mathcal{J}_1\kappa/2\;\alpha_i^2$; and parametric phase shifts, $\text{Im}\mathcal{J}_1^*\kappa\alpha_i\alpha_j^*$ $-\text{Im}\,\mathcal{J}_1\kappa/2\;\alpha_i^2$.

• Second order terms in κ describe third order effects: *intensity dependent absorptions*, two photon absorption (2PA), $-\text{Re}\,\mathcal{J}_2\,\kappa^2/2\,|\alpha_i|^2\alpha_i$, and Raman absorption, $+\text{Re}\,\mathcal{J}_2\,\kappa^2\,|\alpha_j|^2\alpha_i$; *intensity dependent phase shifts*, self phase modulation (SPM) or Kerr effect, $-\text{Im}\,\mathcal{J}_2\,\kappa^2/2\,|\alpha_i|^2\alpha_i$, and cross phase modulation (CPM) or cross-Kerr effect, $+\text{Im}\,\mathcal{J}_2\,\kappa^2\,|\alpha_j|^2\alpha_i$.

• The system is not a full third order system: for example, there are no terms describing four wave mixing (FWM), $i\kappa\alpha_j^2\alpha_i^*$, or third harmonic generation (THG).

A note on nomenclature. As can be seen from the above, intensity dependent phase shifts are third order effects. In $\chi^{(3)}$systems the intensity dependent phase shift is known as the *Kerr effect*: physically, it is an intensity dependent refractive index that leads to an intensity dependent phase shift. Strictly speaking, the SPM and CPM in the equations above cannot be described as Kerr effects, as they take place in a $\chi^{(2)}$system: they are only "effective Kerr effects". This is a cumbersome term. As the identification of intensity dependent phase shifts as Kerr effects is widespread, we will use the term "Kerr effect" in this thesis even though we are discussing $\chi^{(2)}$systems.

The system is similar in some respects to the purely third order system proposed by Jack et. al. [28], in which FWM, CPM, & SPM occur simultaneously. In the limit of small pumping of the Jack system, as far as quantum noise is concerned, the FWM term acts as an OPO/SHG term. Thus we expect the system described above to share certain characteristics with the Jack system, such as multiple bifurcation points, and squeezing that rotates in quadrature as the Kerr terms dominate. Investigating in detail the behaviour described by eqns 2.60 & 2.61 would in itself be another thesis. In the next section we concentrate solely on the effective Kerr effect that occurs in singly resonant SHG.

2.5.2 Phase mismatch induced Kerr effect

To derive the singly resonant case, it is not appropriate to apply adiabatic elimination to eqns 2.60, as they contain the reflectivity of the second harmonic cavity explicitly. (It can be done, but it requires considerable mathematical lendergermain.) Instead we start once again from the description of the field interaction in the SVEA (slowly varying envelope

approximation):

$$\begin{aligned}\frac{dA_1(z)}{dz} &= -i\kappa' A_3(z) A_1^*(z) f^*(\Delta kz) \\ \frac{dA_3(z)}{dz} &= -i\kappa' A_1^2(z) f(\Delta kz)\end{aligned} \tag{2.62}$$

We integrate the second harmonic to first order, remembering that $\int f(\Delta kz).dz = Zg(\Delta kz) = \mathcal{J}_1$:

$$A_3(Z) = A_3(0) - i\kappa' Z\, A_1^2(0)(\mathcal{J}_1/Z) = A_3(0) - i\kappa'\, A_1^2(0)\mathcal{J}_1 \tag{2.63}$$

As there is no initial second harmonic, $A_3(0) = 0$. Substituting this into eqn 2.62 gives:

$$\frac{dA_1(z)}{dz} = +\kappa'^2 |A_1(z)|^2 A_1(z) \mathcal{J}_1 f^*(\Delta kZ) \tag{2.64}$$

Integrating this gives:

$$A_1(Z) = A_1(0) - \kappa'^2 Z^2\, |A_1(z)|^2 A_1(z)(\mathcal{J}_2/Z^2) \tag{2.65}$$

Which, by our now standard technique, gives the equation of motion [24]:

$$\dot{\alpha}_1 = -(\gamma_1 + i\Delta_1)\, \alpha_1 - \mu \mathcal{J}_2' |\alpha_1|^2 \alpha_1 + \sqrt{2\gamma_1^c} A_1^{in} \tag{2.66}$$

where $\mu = h\nu_1(\kappa' Z r_1/\tau_1)^2$. Note that we are now using the scaled phase function, $\mathcal{J}_2'$. The real part of $\mathcal{J}_2'$ leads to SHG, i.e. an intensity dependent loss. The imaginary part of $\mathcal{J}_2'$ leads to an effective Kerr effect, i.e. an intensity dependent phase shift.

As pointed out earlier, intensity dependent losses (2PA, Raman) and phase shifts (SPM, CPM) are normally considered to be third order effects: they are seen in many applications involving $\chi^{(3)}$materials. Thus we see that a singly resonant frequency doubler is effectively a third order system, the third order effects occurring directly due to cooperating second order effects. For example, SHG in the singly resonant system is effectively two photon absorption, as when two fundamental photons form one second harmonic photon it is not stored but leaves the cavity immediately. The two fundamental photons have been removed from the system. If there is a second harmonic cavity, then there is a strong chance that the 2ν photon can downconvert back to fundamental photons - this is the normal parametric interaction.

Optical bistability can occur in any Kerr cavity where the linear and nonlinear detuning terms are of opposite sign. However both terms must be above a certain size, i.e there is a detuning threshold, for the linear detuning, and a power threshold, for the nonlinear detuning, that must be exceeded before bistability is observed.

The nonlinear detuning term, $-\mu \mathrm{Im}(\mathcal{J}_2')|\alpha_1|^2$, is obviously a function of input power. The threshold input power is found by solving eqn 2.66 in the steady-state case, $\dot{\alpha}_1 = 0$, under the condition of infinite slope in the cavity lineshape, $(\mathrm{d}|\alpha_1|^2/\mathrm{d}\Delta)^{-1} = 0$ [24]:

$$P_1^{bi\ thr} = h(2\nu)\frac{\gamma^2}{\mu}\left(\frac{\gamma_1}{\gamma_1^c}\right)^2 p(\Delta kz) = P_1^{min} p(\Delta kz) \tag{2.67}$$

where η is the cavity escape efficiency (eqn 2.53); and $p(\Delta kz)$ is the phase match function:

$$p(\Delta kz) = \frac{2}{3\sqrt{3}} \frac{|\mathcal{J}_2'|^2}{(|\mathrm{Im}\mathcal{J}_2'| - \sqrt{3}\ \mathrm{Re}\mathcal{J}_2')^3} \tag{2.68}$$

By definition $P_1^{bi\ thr}$ is the power required to reach bistability for the minimum necessary detuning, $\Delta_1^{bi\ thr}$. For detunings greater than this, power greater than $P_1^{bi\ thr}$ will be required to observe bistability.

We can rewrite eqn 2.67 as:

$$P_1^{bi\ thr} = \frac{\gamma_1^2 \tau^2}{\eta \Gamma_{SHG}} p(\Delta kz) \tag{2.69}$$

where Γ_{SHG} is the power conversion coefficient for SHG. This is defined as:

$$P_2 = \Gamma_{SHG}(P_1^{circ})^2 \tag{2.70}$$

The power conversion coefficient is a parameter that is widely used for comparison of different $\chi^{(2)}$systems. In travelling wave systems it can be measured directly (simply replace P_1^{circ} with the power of the travelling wave, P_1). In cavity systems it is somewhat inferential, as the circulating power is calculated from other measured parameters, but it nevertheless a useful measure of the effective nonlinearity.

The linear detuning threshold is the detuning at which the slope of the cavity lineshape becomes vertical. Thus the cavity detuning necessary to achieve bistability is given by:

$$\Delta_1^{bi\ thr} = -\text{sign}(\text{Im}\mathcal{J}_2{}')\frac{\sqrt{3}|\text{Im}\mathcal{J}_2{}'| + \text{Re}\mathcal{J}_2{}'}{|\text{Im}\mathcal{J}_2{}'| - \sqrt{3}\text{Re}\mathcal{J}_2{}'}\gamma_1 \tag{2.71}$$

Notice that for the case of zero nonlinear loss $\text{Re}\mathcal{J}_2{}' = 0$, the threshold for detuning reduces to the well-known value $\Delta_1^{bi\ thr} = \sqrt{3}\gamma_1$ [29].

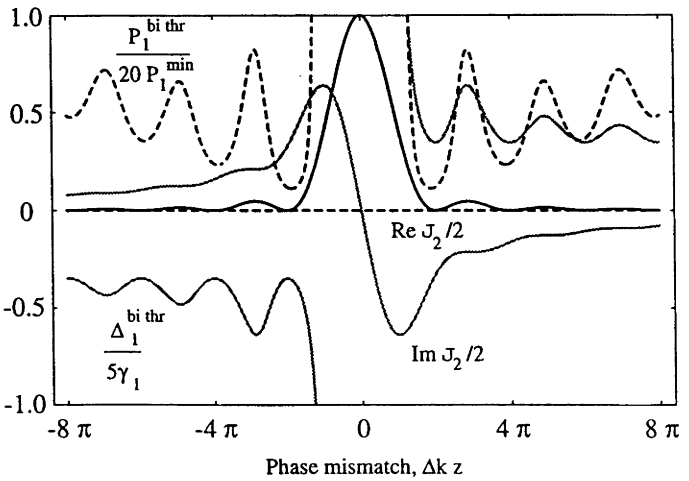

Figure 2.11: Phase mismatch dependence of the nonlinear conversion coefficient, $\text{Re}\mathcal{J}_2{}'$, the nonlinear phase shift coefficient , $\text{Im}\mathcal{J}_2{}'$, the normalised power threshold, $P_1^{bi\ thr}/P_1^{min}$, and the normalised cavity detuning at threshold, $\Delta_1^{bi\ thr}/\gamma_1$. The phase and detuning curves are in grey. Note that all curves have been scaled as indicated to fit into the one plot.

Fig. 2.11 plots the phase mismatch dependence of the real and imaginary parts of the nonlinear coefficient, $\mathcal{J}_2{}'$. Nonlinear conversion ceases at $\Delta kz = m\ 2\pi$ ($m = 1, 2, 3, \ldots$), i.e. when the real part of $\mathcal{J}_2$ becomes zero. At these points the system acts solely as a Kerr medium: the large body of literature on Kerr cavities applies exactly, without

change. The Kerr nonlinearity at $\Delta kz = m\,2\pi$ is $\pm\mu/(m\pi)$. This is very large compared to intrinsic third order nonlinearity of typical crystals ($\sim 10^8$ times larger). The strongest possible Kerr nonlinearity, which occurs at $\Delta kz = 2\pi$, is only π times smaller than the second order nonlinearity.

Fig. 2.11 also plots the normalised power threshold, $P_1^{bi\ thr}/P_1^{min}$, and the normalised cavity detuning at threshold, $\Delta_1^{bi\ thr}/\gamma_1$ versus the phase mismatch. Both functions show a striking 2π periodicity. The power minima lie on a line of slope $\pm 2/(3\sqrt{3})$ that intersects the origin. For large phase mismatch, the power maxima lie on a parallel lines that intersect the y axis at $P_1^{bi\ thr}/P_1^{min} \simeq 5$. Thus at large phase mismatch there is relatively little difference between the power maxima and minima. The detuning minima lie on a horizontal line that intercepts the y axis at $\Delta_1^{bi\ thr} = \sqrt{3}\gamma_1$. For large phase mismatch $\Delta_1^{bi\ thr}$ asymptotes to this line.

At $\Delta kz = 2\pi$ no net second harmonic is produced, as the nonlinearity is purely imaginary. However, considerable second harmonic is still produced *within* the cavity, and can act as a pump source for NDOPO: thus TROPO can still occur. In fact, the minimum optical bistability threshold power, $P_1^{bi\ thr}$, is more than twice the minimum TROPO threshold power, P_1^{min}. To avoid TROPO when investigating Kerr behaviour, it will be necessary to increase the TROPO threshold, P_1^{thr}, well above its minimum value P_1^{min} (which is discussed in section 2.4.1.

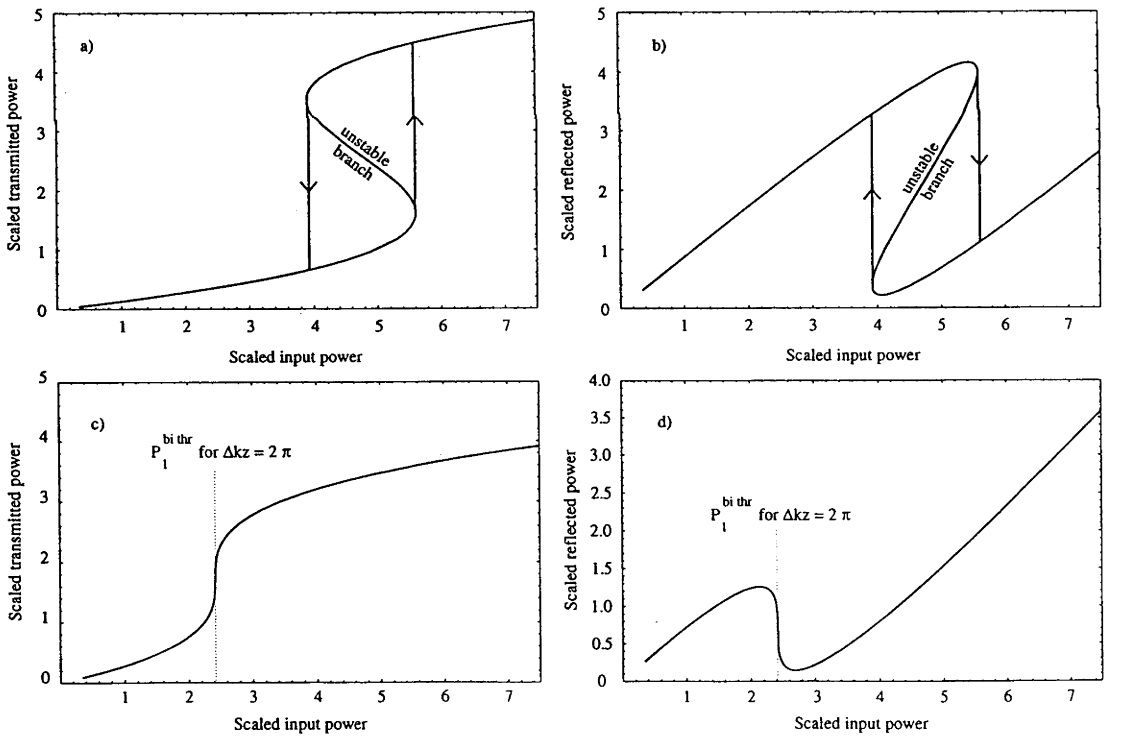

Figure 2.12: Transmitted and reflected power versus pump power. Powers scaled by P_1^{min}. Bistability occurs for detunings, $\Delta_1 \geq \Delta_1^{bi\ thr}$. a) & b) $\Delta_1 = 1.5\sqrt{3}\gamma_1 = 1.5\Delta_1^{bi\ thr}$. c) & d) $\Delta_1 = \Delta_1^{bi\ thr}(2\pi) = \sqrt{3}\gamma_1$.

Now consider the case $\Delta kz = 2\pi$, where the cavity acts purely as a Kerr cavity. The output power obviously varies as a function of linear detuning and pump power. In the literature this is normally investigated by fixing one of the phase terms in eqn 2.66 and

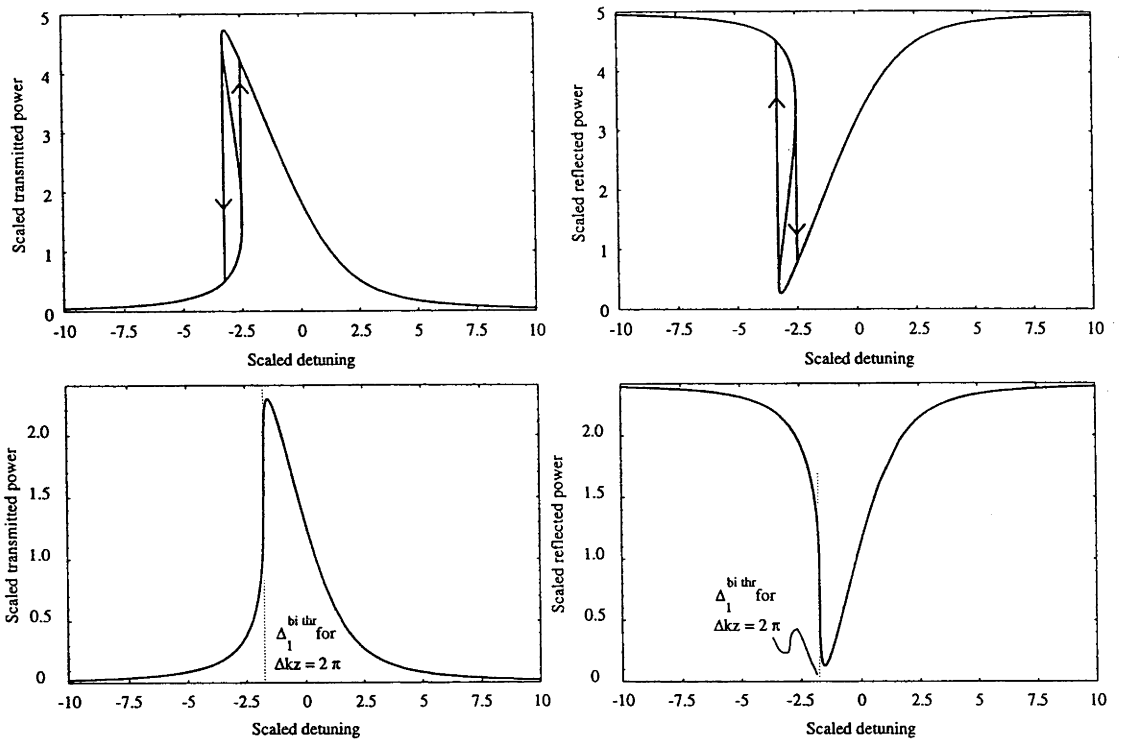

Figure 2.13: Transmitted and reflected lineshapes versus pump power. Power scaled by P_1^{min}, detuning scaled by γ_1. Bistability occurs for pump powers, $P_1 \geq P_1^{bi\ thr}$. a) & b) $P_1 = 5P_1^{min}$. c) & d) $P_1 = P_1^{bi\ thr}(2\pi) \simeq 2.4P_1^{min}$.

varying the other. Thus power bistability is observed when the cavity is locked to a linear detuning ($\Delta_1 \geq \Delta_1^{bi\ thr}$), and the power is varied. As shown in Fig. 2.12, there is a clear bistability. Detuning bistability (i.e. distortions of the line shapes), is observed when the power is held constant ($P_1 \geq P_1^{bi\ thr}$) and the cavity is scanned back and forth through resonance, as shown in Fig. 2.13. As the power approaches threshold, the line shapes begin to exhibit a marked asymmetry; at threshold the line shape has a vertical slope; above threshold the line shapes are bistable.

2.5.3 Detuning induced Kerr effect

While the physics in the previous two sections has only been developed in the last few years, it has been appreciated for a long time that it is possible to produce a nonlinear phase shift in cavity SHG simply by appropriate detuning. This was first pointed out in the seminal paper of Drummond et. al. [7, Section 8], and was alluded to in section 2.2.3. Restating equations 2.34& 2.35:

$$\dot{\alpha}_1 = -(\gamma_1 + i\Delta_1)\,\alpha_1 - \mu|\alpha_1|^2\alpha_1 + \sqrt{2\gamma_1^c}A_1^{\text{in}} \tag{2.72}$$

where the nonlinear interaction, μ, is:

$$\mu = \frac{\kappa^2}{2}\frac{(\gamma_3 - i\Delta_3)}{(\gamma_3^2 + \Delta_3^2)} \tag{2.73}$$

The real part of $\mu|\alpha_1|^2\alpha_1$ is the SHG term and the imaginary part is the Kerr term. Unlike the phase mismatch induced Kerr effect, the nonlinear loss *cannot* be suppressed in the detuning induced Kerr effect.

There is one caveat concerning this mechanism: for it to work, the system needs to be more doubly, than singly, resonant. That is, the second harmonic must act more like a resonance of the cavity, than as a freely propagating field. Consider the following argument. In the limit of low reflectivity the width of the second harmonic resonance becomes so large that its half points fall on adjoining cavity resonances (at ± 1 FSR). These build up resonances, which in turn overlap adjoining resonances, which in turn overlap adjacent resonances, and so on. The second harmonic output is no longer a resonance but a field. There is no longer a lineshape for the second harmonic cavity, the output is a wide flat line, and so there is no detuning dependence - there is no resonance to be detuned from! Thus there can be no detuning induced Kerr effect in singly resonant cavities.

Since its introduction, the detuning induced Kerr effect in SHG has rarely been considered. Given the notorious difficulty of working with doubly resonant SHG it is not surprising that no experiments on it have been performed.

Although it is not identified as such, the detuning induced Kerr effect *has* been considered in a series of papers concerning a (N)DOPO resonant at the pump and subharmonic frequencies simultaneously. Lugiato et. al predict that both bistability and self-pulsing will occur in a DOPO where the cavity is detuned with respect to the pump and subharmonic [30]. Richy et. al have demonstrated asymmetric lineshapes and pump hysteresis in a triply resonant (pump, signal, & idler) NDOPO detuned with respect to the pump & signal [31]. The detuning induced Kerr effect has even been used to generate transient squeezing (66 ms) of -1.2 dB (25%) [32]. Although the given explanation of these effects in the original references is somewhat complicated, the underlying mechanism is the detuning induced Kerr effect, as identified above.

2.5.4 Thermally induced Kerr effect

In experimental systems there is an additional mechanism that can cause an intensity dependent phase shift - absorption. Light that is absorbed in the crystal is converted to heat. Most optical crystals have a positive thermal coefficient, so that heat leads to expansion of the crystal.

Consider the situation of a monolithic cavity (the cavity is carved from the crystal) that is detuned onto resonance from high optical frequency. As resonance is approached, the circulating power increases, thus the absorbed power increases, heating the cavity and causing it to become longer. The increase in length pushes the resonance frequency to a lower frequency, so that it is necessary to decrease the optical frequency further to reach resonance. Eventually of course resonance is reached. As the frequency is decreased further, and the cavity comes off resonance, the cavity absorbs less heat and shortens slightly. At some detuning point, the cavity finds that the resonance condition is now at a markedly higher frequency than the detuning where it finds itself, and the output drops suddenly, switching to a low output. The resulting lineshape is markedly asymmetric: broadened to, and switching on, the low frequency side.

Now consider approaching resonance from the low frequency side. Light that enters the cavity heats it, lengthening the cavity and decreasing the cavity resonance frequency. At some detuning point the cavity suddenly finds itself near resonance, and the cavity switches to a high output. The resulting lineshape is also markedly asymmetric: narrowed to, and switching on, the high frequency side. The result is a thermally induced

Kerr effect.

Thermal absorption is time dependent. Thus thermal distortion of lineshapes can be avoided, or at least minimised, by scanning the cavity rapidly, i.e. many times faster than the inverse time constant of the absorption, so that the heat dumped into the cavity approaches a steady-state value and the cavity length effectively does not change during the scan.

The thermally induced Kerr effect is unavoidable when the cavity is locked. However it is slow to respond - typical thermal absorption time constants are on the order of seconds. Thus the thermally induced Kerr effect can be ignored if considering effects at frequencies much higher than it can respond, for example, examining the noise reduction at several MHz. (It does however complicate the locking the cavity to resonance.)

In this thesis we can always account for the thermal effect in of the two ways described above. However, if an experiment is such that the thermal effect cannot be ignored, then it can be modelled in one of two ways. In either case we add to the normal equation of motion the term "$i\,\mathrm{f(T)}\alpha_i$", where T is the temperature, and $\mathrm{f(T)} = \mathrm{FT(t)}$.

The Fourier thermal diffusion equation is:

$$\frac{\partial \mathrm{T}(\vec{\mathrm{r}},\mathrm{t})}{\partial \mathrm{t}} = -\kappa\nabla^2\mathrm{T}(\vec{\mathrm{r}},\mathrm{t}) + \mathrm{KI}_{\mathrm{light}} \tag{2.74}$$

where t is time, κ is the thermal conductivity, $\mathrm{T}(\vec{\mathrm{r}},\mathrm{t})$ is the time dependent spatial temperature distribution, K is the power to temperature conversion constant, and $\mathrm{I}_{\mathrm{light}}$ is the light intensity. We simplify this to:

$$\dot{\mathrm{T}} = -B\mathrm{T(t)} + A|\alpha_i|^2 \tag{2.75}$$

The thermal effect can be modelled by adding this equation to the other equations of motion (remember, they are coupled to it via the term $i\mathrm{FT(t)}\alpha_i$) and solving as normal. Alternatively an explicit solution to eqn 2.75 can be found. Solving the homogeneous part of eqn 2.75, $\dot{\mathrm{T}} = -B\mathrm{T(t)}$, gives:

$$\mathrm{T(t)} = \mathrm{T_0}e^{-B\mathrm{t}} \tag{2.76}$$

As an ansatz, we allow time variation of the constant, $\mathrm{T_0}$, and substitute into the inhomogeneous equation, 2.75, and solving, find:

$$\mathrm{T_0(t)} = \int_{\mathrm{t_0}}^{\mathrm{t}} e^{Bt'}\mathrm{A}|\alpha_i|^2\mathrm{d}t' \tag{2.77}$$

Substituting this into the eqn 2.76 gives:

$$\mathrm{T(t)} = \int_{\mathrm{t_0}}^{\mathrm{t}} e^{-B(\mathrm{t}-\mathrm{t}')}\mathrm{A}|\alpha_i|^2\mathrm{d}t' \tag{2.78}$$

This can be substituted directly into the term $i\mathrm{FT(t)}\alpha_i$ in the equations of motion.

A more detailed analysis has been made for the case of a triply resonant (pump, signal, idler) optical parametric oscillator [33]. The phase shift was modelled by considering the change in refractive index due to the change in temperature, via the Sellmeier equations. Good qualitative agreement was found between the model and experiment.

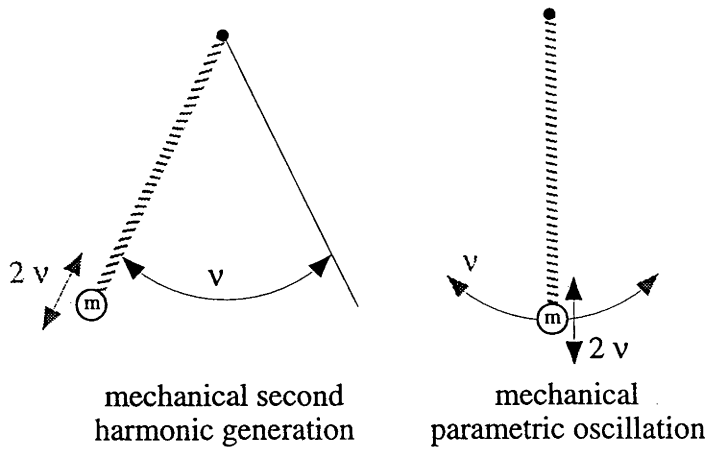

Figure 2.14: Spring pendulum. *left hand side*: mechanical second harmonic generation. The pendulum is driven at $\omega = 2\pi\nu$. For certain values of pendulum length, L, spring coupling, k, and mass m they system is phase matched and the mass oscillates along the pendulum with a frequency 2ω. *right hand side*: mechanical parametric oscillation. The mass is driven at 2ω as shown. Above a certain driving amplitude at phase match the pendulum begins to oscillate with a frequency ν.

2.6 A mechanical analogy

Some people (I am one) find that consideration of the mechanical analogs of optical systems deepens their physical intuition. Second order optical systems are simply two harmonic oscillators (the cavity modes) coupled by a nonlinear interaction (the $\chi^{(2)}$interaction). A simple mechanical analog exists for such systems. Consider the *spring pendulum*, as shown in Fig. 2.14, a coil spring of length, L, mass, μ, and spring constant, k, that is suspended by one end so that it acts as a pendulum supporting a end mass, m. The spring pendulum experiences mechanical losses, such as friction (analogous to optical losses.) Gravity acts vertically downward.

The spring pendulum is characterised by two frequencies, the frequency of the pendulum oscillation, $\nu_p = 1/(2\pi)\sqrt{(m+\mu/2)/(m+\mu/3)/g/L}$, and the frequency of the spring oscillation, $\nu_s = 1/(2\pi)\sqrt{k/(m+\mu/3)}$. The pendulum can be driven (analogous to the pump field) by moving the pivot point horizontally at the frequency ν_p; the spring can be driven by moving the pivot point vertically at the frequency ν_s, or by moving the end mass at the frequency ν_s. The interaction is nonlinear because when the pendulum oscillates the spring experiences a downward centrifugal force that at a frequency twice that of the pendulum frequency.

If the pivot point is driven horizontally at a frequency ν_p', such that $\nu_s' = 2\nu_p'$, then energy couples strongly from the pendulum to the spring [34], which starts oscillating at ν_s'. This is mechanical second harmonic generation. For $\nu_s' = 2\nu_p'$, there must be "phase matching", i.e. $kL = 4g(m+\mu/2)$. Even though the spring pendulum is lossy, there is no threshold: as long as the spring pendulum is phase matched, *any* driving amplitude at ν_p will lead to an oscillation at at ν_s. This is because at any position except the vertical, there is always a velocity component that is along the the spring: this will tend to drive the spring. (Grab a spring and a lump of metal and try this experiment, it works remarkably well! Mind you, you will have to spend a little time finding the phase matched length.)

Now consider driving the pivot point vertically at a frequency ν_s', again where $\nu_s' =$

$2\nu_p'$. At first the spring oscillates at the frequency, ν_s', in the vertical direction. If there is zero loss, then any infinitesimally small horizontal perturbation (analogous to quantum noise) will kick the pendulum sideways. Once away from the vertical the velocity has a component perpendicular to the spring that can drive the pendulum oscillation at the frequency ν_p'. This is mechanical subharmonic generation. Now consider the case with loss. Again an infinitesimally small horizontal perturbation kicks the spring sideways. However if the spring motion does not contain enough energy to overcome the damping, the spring remains vertical. The stronger the damping, the more energy is needed. The energy is provided by the amplitude of the driving motion. Thus a threshold exists for mechanical subharmonic generation, analogous to the optical case.

For optimum mechanical second and sub harmonic generation a phase matching condition has to be fulfilled. If it is very far from being fulfilled, then no coupling between oscillators occurs (they are independent harmonic oscillators). This allows us to visualise the Kerr effect as follows. Change the system parameters slightly so that there is a slight phase mismatch. Again drive the pivot horizontally with a frequency, ν_p'. Energy is now coupled from the pendulum to the spring, but it is returned back to the pendulum. Under these conditions the spring does not oscillate. Instead the pendulum motion lags/leads the driving field with a phase that depends on the amplitude of the driving motion. This is the mechanical analogy to the Kerr effect.

2.7 Summary of $\chi^{(2)}$effects

Basic $\chi^{(2)}$effects can be categorised as upconversion and downconversion effects. The former includes second and sum frequency generation (SHG & SFG), the latter includes (non)degenerate optical parametric oscillation (N)DOPO.

Multiple $\chi^{(2)}$nonlinearities interact in one of two ways. Competing nonlinearities are those that do not share the same frequencies, for example $\nu \rightleftharpoons 2\nu \rightleftharpoons \nu \pm \Delta_2$, or, $\nu \pm \Delta_1 \rightleftharpoons 2\nu \rightleftharpoons \nu \pm \Delta_2$. Cooperating nonlinearities are those that do share the same frequencies, $\nu \rightleftharpoons 2\nu$ or $\nu \pm \Delta_1 \rightleftharpoons 2\nu$, but interact to produce an asymmetrical result, such as an intensity dependent phase shift.

In a singly resonant SHG cavity competition occurs between SHG & NDOPO. This competition has a power threshold, produces nondegenerate modes in a frequency range around the fundamental, and causes clamping of the second harmonic power.

Cooperating nonlinearities can cause a strong intensity dependent phase shift, aka Kerr effect. It can be induced via phase matching, detuning, or by thermal effects. The Kerr effect in cavities leads to optical bistability, which has thresholds in both detuning and power.

Chapter 2 bibliography

[1] Walter Koechner, *Solid-State Laser Engineering*, Fourth Edition, Springer-Verlag, Berlin, 1996

[2] Amnon Yariv, *Quantum Electronics*, Third Edition, John Wiley & Sons, Singapore, 1989. N.B. The half should be removed from the equation immediately preceding (16.6-7).

[3] V. Pruneri, R. Koch, P. G. Kazansky, W. A. Clarkson, P. St. J. Russel and D. C. Hanna, Optics Letters, **20**, no. 23, p. 2375, 1995. *49 mW of cw blue light generated by first-order quasi-phase-matched frequency doubling of a diode-pumped 946-nm Nd:YAG laser*

[4] W. R. Bosenberg, A. Drobshoff, J. I. Alexander, L. E. Myers and R. L. Byer, Optics Letters, **21**, no. 10, p. 713, 1996. *Continuous-wave singly resonant optical parametric oscillator based on periodically poled $LiNbO_3$;*

W. R. Bosenberg, A. Drobshoff, J. I. Alexander, L. E. Myers and R. L. Byer, Optics Letters, **21**, no. 17, p. 1336, 1996. *93% pump depletion, 3.5-W continuous-wave, singly resonant optical parametric oscillator*

[5] G. D. Boyd and D. A. Kleinman, J. Appl. Phys. **39**, p. 3597, 1968. *Parametric Interaction of Focussed Gaussian Light Beams*

[6] T. C. Ralph, Physics Department, Australian National University, Australia, 1996. *private communication*

[7] P. D. Drummond, K. J. McNeil, and D. F. Walls, Optica Acta, **27**, no. 3, pp. 321 - 335, 1980. *Non-equilibrium transitions in sub/second harmonic generation I. Semiclassical theory*

[8] R. Paschotta, M. Collett, P. Kürz, K. Fiedler, H.-A. Bachor, and J. Mlynek, Physical Review Letters, **72**, no. 24, pp. 3807 - 3810, 1994. *Bright Squeezed Light from a Singly Resonant Frequency Doubler*

[9] M. A. M. Marte, Phys. Rev. A **49**, p. 3166, 1994. *Competing nonlinearities*

[10] G. T. Moore, and K. Koch, IEEE Journ. Quant. Elec. **29**, no. 3, p. 961, 1993. *Optical Parametric Oscillation with Intracavity Sum-Frequency Generation*

[11] E. C. Cheung, K. Koch, and G. T. Moore, Opt. Lett. **19**, no. 23, p. 1967, 1994. *Frequency upconversion by phase-matched sum-frequency generation in an optical parametric oscillator*

[12] K. Koch, G. T. Moore, and E. C. Cheung, J. Opt. Soc. Am. B **12**, no. 11, p. 2268, 1995. *Optical parametric oscillation with intracavity difference-frequency mixing*

[13] R. Byer, Gintzon Laboratory, Stanford University, U.S.A., *personal communication*, 1996.

[14] S. Schiller and R. L. Byer, J. Opt. Soc. Am. B **10**, no. 9, p. 1696, 1993. *Quadruply resonant optical parametric oscillation in a monolithic total-internal-reflection resonator*

[15] G. T. Moore, K. Koch, and E. C. Cheung, Opt. Comm. **113**, p. 463, 1995. *Optical parametric oscillation with intracavity second-harmonic generation*

[16] S. Schiller, G. Breitenbach, S. F. Pereira, R. Paschotta, A. G. White and J. Mlynek, Proc. SPIE **2378**, Y. Shevy ed., p. 91, 1995. *"Generation of continuous-wave bright squeezed light", in Laser Frequency Stabilization and Noise Reduction*

[17] S. Schiller, G. Breitenbach, R. Paschotta, and J. Mlynek, Appl. Phys. Lett. **68**, no. 24, p. 3374, 1996. *Subharmonic-pumped continuous-wave parametric oscillator*

[18] M. A. M. Marte, Phys. Rev. Lett. **74**, no. 24, p. 4815, 1995. *Sub-Poissonian Twin Beams via Competing Nonlinearities*

M. A. M. Marte, Acta Physica Slovaca **45**, no. 3 , p. 253, 1995. *Mutual influence of two $\chi^{(2)}$-nonlinearities and the generation of sub-Poissonian twin beams*

M. A. M. Marte, J. Opt. Soc. Am. B **12**, no. 11, p. 2296, 1995. *Nonlinear dynamics and quantum noise for competing $\chi^{(2)}$ nonlinearities*

[19] A. G. White, P. K. Lam, M. S. Taubman, M. A. M. Marte, S. Schiller, D. E. McClelland, & H.-A. Bachor, Physics Review A, accepted 1997. *Classical and quantum signatures of competing $\chi^{(2)}$ nonlinearities*

[20] R. C. Eckardt, C. D. Nabors, W. J. Kozlovsky, and R. L. Byer, J. Opt. Soc. Am. B, **8**, p. 646, 1991. *Optical parametric oscillator frequency tuning and control*

[21] A. E. Siegman, Appl. Opt. **1**, no. 6, p. 739, 1962. *Nonlinear Optical Effects: An Optical Power Limiter*

[22] for example, see references in: G. Assanto, G.I. Stegeman, M. Sheik-Bahae, and E. VanStryland, J. Quant. Elec. **31**, p. 673, 1995. *Coherent Interactions for All-Optical Signal Processing via Quadratic Nonlinearities*

[23] G. Stegeman, M. Shei-Bahae, E. W. Van Stryland and G. Assanto, Opt. Lett. **18**, no. 1, p. 13, 1993. *Large nonlinear phase shifts in second-order nonlinear-optical processes*

[24] A. G. White, J. Mlynek, and S. Schiller, Europhys. Lett., **35**, no. 6, p. 425, 1996. *Cascaded second-order nonlinearity in an optical cavity*

[25] Z. Y. Ou, Opt. Comm., **124**, p. 430, 1996. *Observation of nonlinear phase shift in CW harmonic generation*

[26] P. L. Chu, B. A. Malomed, and G. D. Peng, Opt. Comm. **128**, p. 76, 1996. *Nonlinear amplification in a second-harmonic-generating system*

[27] S. Schiller, R. Bruckmeier, and A. G. White, Optics Communications, to appear, 1997. *Classical and quantum properties of the subharmonic-pumped parametric oscillator*

[28] M. W. Jack, M. J. Collett, and D. F. Walls, Phys. Rev. A, **51**, no. 4, p. 3318, 1995. *Enhanced squeezing due to the influence of two instabilities*

[29] I. E. Protsenko, L. A. Lugiato, Opt. Comm., **109**, p. 304, 1994. *Noiseless amplification in the optical transistor*

[30] L. A. Lugiato, C. Oldano, C. Fabre, E. Giacobino, and R. J. Horowicz, Il Nuovo Cimento, **10**, no. 8, p. 959, 1988. *Bistability, Self-Pulsing and Chaos in Optical Parametric Oscillators*

[31] C. Richy, K. I. Petsas, E. Giacobino, C. Fabre and L. A. Lugiato, J. Opt. Soc. Am. B, **12**, no. 3, p. 456, 1995. *Observation of bistability and delayed bifurcation in a triply resonant optical parametric oscillator*

[32] K. Kasai and C. Fabre, preprint, 1996. *Squeezing of the pump beam in optical parametric interaction*

[33] K.-X. Sun, N. C. Wong, J. H. Shapiro, Massachusetts Institute of Technology, USA. Oral presentation at CLEO 1993: *Thermal Hysteretic Effects in a Triply Resonant Optical Parametric Oscillator*

[34] S. Schiller, PhD thesis, Edward L. Ginzton Laboratory, Stanford University, Stanford, California, USA, 1993. *Principles and applications of optical monolithic total-internal-reflection resonators*

Chapter 3

Quantum Models

One does not discover new lands without consenting to lose sight of the shore for a very long time

André Gide, *The Counterfeiters*

Physical theories have two equally important aspects: the *formalism* of the theory, and the *interpretation* of the theory. The formalism of quantum optics is often regarded as complex and mathematically demanding. In this chapter we show that it is in fact relatively straightforward. Further, we present intuitive and powerful interpretations of quantum noise that we use throughout this thesis: the sideband and ball-on-stick pictures. In detail, in the first section we derive some of the principal results of quantum optics directly from classical optics. In the second section we briefly discuss the two principal methods of modelling quantum optical systems, the Schrödinger and Heisenberg approaches. In the third section we illustrate the simplicity and ease of use of the Heisenberg approach by deriving the noise characteristics of an empty cavity. In the fourth section we discuss photodetection and the phase sensitive detection of light.

3.1 Quantum optics formalism without pain

The behaviour of light freely propagating in space is described by the source free Maxwell's equations. From these it is possible to derive the electromagnetic field as a function of position, $\mathbf{r}$, and time, t [1]

$$\mathbf{E}(\mathbf{r},t) = i\sum_j \left(\frac{\hbar\omega_j}{2\varepsilon_0}\right)^{1/2} [a_j \mathbf{u}_j(\mathbf{r})e^{-i\omega_j t} - a_j^* \mathbf{u}_j^*(\mathbf{r})e^{+i\omega_j t}] \tag{3.1}$$

where $\mathbf{u}_j(\mathbf{r})$ are mode functions containing polarisation and spatial phase information. The factor $(\hbar\omega_j/2\varepsilon_0)^{1/2}$ is chosen so that the Fourier amplitudes, a_j & a_j^*, are dimensionless, i.e. they are are solely complex numbers or *c-numbers*. In this representation the Fourier amplitudes are the orthogonal variables of the system.

The electromagnetic field is quantised by transforming the Fourier amplitudes to mutually adjoint operators, $\hat{a}_j$ & $\hat{a}^\dagger{}_j$ [2]. Transformation of orthogonal variables in this fashion is referred to as a *canonical transformation*.

Mathematically, the *commutator*, $\left[\hat{A},\hat{B}\right]$, is defined as the following operation [3]:

$$\left[\hat{A},\hat{B}\right] = \hat{A}\hat{B} - \hat{B}\hat{A} \tag{3.2}$$

If the commutator is zero, then $\hat{A}\hat{B} = \hat{B}\hat{A}$, and we say $\hat{A}$ and $\hat{B}$ *commute*. The operators

[1] The discussion presented in this section is basically that of reference [1].

[2] To remind the reader that operators are very different mathematical objects to complex numbers, throughout this thesis we will *always* mark operators with a circumflex, i.e. a " ˆ "

$\hat{a}_j$ & $\hat{a}^\dagger_j$ obey the boson commutation relations:

$$\begin{aligned} [\hat{a}_j, \hat{a}_k] &= 0 \\ \left[\hat{a}^\dagger_j, \hat{a}^\dagger_k\right] &= 0 \\ \left[\hat{a}_j, \hat{a}^\dagger_k\right] &= \delta_{jk} \end{aligned} \tag{3.3}$$

The electromagnetic field is now quantised. It is the introduction of the above relations that allow formal description of the nonclassical behaviour of the electromagnetic field in quantum optics.

Classically the total energy of the electromagnetic field is described by the Hamiltonian [1]:

$$\mathcal{H} = \frac{1}{2}\int \left(\varepsilon_0 \mathbf{E}^2 + \frac{\mathbf{B}^2}{\mu_0}\right) d\mathbf{r} \tag{3.4}$$

where ε_0 and μ_0 are respectively the permittivity and permeability of free space, and E and B are the amplitude of the electric and magnetic components of the electromagnetic field.

After canonical transformation (using the boundary conditions of the mode functions, **u**, and eqn 3.1 and the equivalent expression for B) this expression becomes:

$$\hat{\mathcal{H}} = \sum_j h\nu_j \left(\hat{a}^\dagger_j \hat{a}_j + \frac{1}{2}\right) \tag{3.5}$$

This is just the Hamiltonian of a collection of quantised simple harmonic oscillators (SHO). Accordingly, the electromagnetic field can be considered to be a frequency ensemble of *modes*, each mode represented by a simple harmonic oscillator.

Several quantum representations of the electromagnetic field enjoy wide circulation. These include the number or Fock state representation, the coherent state representation, and the squeezed state representation. We will discuss these in the following three subsections.

3.1.1 Number states, or, Annihilation can Fock a state

The eigenstates of the simple harmonic oscillator Hamiltonian (eqn 3.5) are known as *number* or *Fock states*, and are written $|n_j\rangle$. They are eigenstates of the *number operator*, $\hat{n}_j = \hat{a}^\dagger_j \hat{a}_j$, such that:

$$\hat{n}_j |n_j\rangle = n_j |n_j\rangle \tag{3.6}$$

The value of the number state represents the number of photons in that mode, e.g. there are three photons in the mode $|3_j\rangle$, where j is the frequency of the mode.

Mathematically, number states are both orthogonal and complete, i.e:

$$\begin{aligned} \langle n_j | m_j \rangle &= \delta_{mn} \text{ and} \\ \sum_{n_j=0}^{\infty} |n_j\rangle\langle n_j| &= 1 \end{aligned} \tag{3.7}$$

As the number states form a complete orthonormal set, any other state can be expanded uniquely in terms of number states.

The operators $\hat{a}_j$ & $\hat{a}^\dagger_j$ when applied to the number state add and subtract a single photon from the mode, and are thus known as the *annihilation* and *creation* operators,

respectively. That is:

$$\begin{aligned}\hat{a}_j|n_j\rangle &= \sqrt{n_j}\,|n_j-1\rangle \\ \hat{a}^\dagger{}_j|n_j\rangle &= \sqrt{n_j+1}\,|n_j+1\rangle\end{aligned} \tag{3.8}$$

Note that the annihilation operator applied to the ground or *vacuum* state, $|0\rangle$ gives zero.

$$\hat{a}_j|0_j\rangle = 0|0_j\rangle = 0 \tag{3.9}$$

The eigenvalues of the number operator are simply $n_j = 0, 1, 2, \ldots$. The *expectation value* of an operator corresponds to a physical measurement of the quantity represented by that operator. The expectation value of the number operator is simply the number of photons in the mode, i.e.:

$$\langle n_j|\hat{n}|n_j\rangle = \langle n_j|(n_j|n_j\rangle) = n_j\langle n_j|n_j\rangle = n_j \tag{3.10}$$

The SHO Hamiltonian can be rewritten in terms of the number operator:

$$\hat{\mathcal{H}} = \sum_k h\nu_k\left(\hat{n}_j + \frac{1}{2}\right) \tag{3.11}$$

As the Hamiltonian represents the total energy of the system it is not surprising that it is the energy operator. The eigenvalues of the energy operator are $h\nu_j(n_j + 1/2)$, i.e:

$$\hat{\mathcal{H}}|n_j\rangle = h\nu_j(n_j + 1/2)|n_j\rangle \tag{3.12}$$

So the SHO Hamiltonian represents the sum of (the number of photons in each mode multiplied by the energy of the photon for that mode) plus (half the energy of the photon for that mode, which represents the energy of the vacuum fluctuations for that mode).

The expectation value of the SHO Hamiltonian when applied to the ground state is:

$$\langle 0_j|\hat{\mathcal{H}}|0_j\rangle = \frac{1}{2}\sum_j h\nu_j \tag{3.13}$$

That is, the ground state or vacuum energy is *not* zero. As there is no upper limit to frequency for electromagnetic radiation the energy of the vacuum is in fact infinite. [3] This detail is normally side-stepped by the observation that measurements are made on *relative* changes in the total energy of the electromagnetic field.

Physical light sources that correspond to the number state representation, i.e. all photons in the field are of exactly the same energy, are rare and normally require exotic apparatus for their production. Thus the number state representation is rarely used for modelling practical experiments.

3.1.2 Coherent states

For a laser running well above threshold, at detection frequencies well outside the laser linewidth, the light is accurately described by the coherent state representation $|\alpha\rangle$, where

[3] If an upper limit to the frequency of electromagnetic radiation does exist then the energy of the vacuum state will be finite, but very, very large. Whilst intuitive arguments can be made for such a limiting mechanism, it is not widely accepted that such a limit exists, and no satisfactory physical model has yet been suggested.

α is a complex-number. Unlike the number state representation, which only contains information about photon number (the phase is undefined), the coherent sate contains both amplitude and phase information.

Mathematically, coherent states are generated from the vacuum state via the *displacement* operator, $D(\alpha)$, i.e.:

$$|\alpha_j\rangle = \hat{D}(\alpha_j)|0_j\rangle \tag{3.14}$$

where

$$\hat{D}(\alpha_j) = e^{\alpha_j \hat{a}^\dagger{}_j - \alpha_j^* \hat{a}_j} \tag{3.15}$$

and α is an arbitrary complex number. Coherent states are eigenstates of the annihilation and creation operators, $\hat{a}$ & $\hat{a}^\dagger$. This means these operators are poorly named with respect to coherent states as they neither annihilate or create. That is:

$$\begin{aligned} \hat{a}_j|\alpha_j\rangle &= \alpha_j|\alpha_j\rangle \\ \langle\alpha_j|\hat{a}^\dagger{}_j &= \langle\alpha_j|\alpha_j^* \end{aligned} \tag{3.16}$$

An operator, $\hat{A}$, is *Hermitean* or *self-adjoint* if $\hat{A} = \hat{A}^\dagger$. As the annihilation and creation operators are non-Hermitean, the eigenvalues, α_j & α_j^*, are complex.

Expressed in terms of the number state, the coherent state is:

$$|\alpha_j\rangle = e^{-|\alpha_j|^2/2} \sum_{n_j=0}^{\infty} \frac{\alpha_j^{n_j}}{(n_j!)^{1/2}} |n_j\rangle \tag{3.17}$$

Note that we have kept the explicit frequency dependence, j. For a classically noiseless, freely propagating electromagnetic field, every mode of the field is a coherent state.

The mean value of the photon number, $\bar{n_j}$, in the coherent state is $|\alpha_j|^2$:

$$\begin{aligned} \bar{n_j} &= \langle\alpha_j|\hat{n}_j|\alpha_j\rangle \equiv \langle n_j\rangle \\ &= \langle\alpha_j|\hat{a}^\dagger{}_j\hat{a}_j|\alpha_j\rangle \\ &= \langle\alpha_j|\alpha_j^*\alpha_j|\alpha_j\rangle \\ &= |\alpha_j|^2\langle\alpha_j|\alpha_j\rangle \\ &= |\alpha_j|^2 \end{aligned} \tag{3.18}$$

The probability distribution of photons in the coherent state is Poissonian:

$$P(n_j) = |\langle n_j|\alpha_j\rangle|^2 = e^{-\langle n_j\rangle} \frac{\langle n_j\rangle^{n_j}}{n_j!} \tag{3.19}$$

This Poissonian nature is perhaps clearest expressed in the variance.

Classically, the variance, $V(w)$, and standard error, $\pm\Delta w$, of a measurable parameter, w, are defined as:

$$\begin{aligned} V(w) &= \Delta w^2 \\ &= (w - \bar{w})^2 \end{aligned} \tag{3.20}$$

For a quantum observable, $\hat{A}$, of a state, $|\psi\rangle$ this becomes:

$$\begin{aligned} V(\hat{A})_\psi &= \langle\Delta\hat{A}\rangle_\psi^2 \\ &= \langle\psi|(\hat{A} - \langle\hat{A}\rangle_\psi)|\psi\rangle \end{aligned}$$

$$\begin{aligned} &= \langle\psi|(\hat{A}^2 - 2\langle\hat{A}\rangle_\psi\hat{A} + \langle\hat{A}\rangle_\psi^2)|\psi\rangle \\ &= \langle\psi|\hat{A}^2|\psi\rangle - 2\langle\psi|\langle\hat{A}\rangle_\psi\hat{A}|\psi\rangle + \langle\psi|\langle\hat{A}\rangle_\psi^2)|\psi\rangle \\ &= \langle\hat{A}^2\rangle_\psi - 2\langle\hat{A}\rangle_\psi\langle\hat{A}\rangle_\psi + \langle\hat{A}\rangle_\psi^2)\langle\psi|\psi\rangle \\ &= \langle\hat{A}^2\rangle_\psi - \langle\hat{A}\rangle_\psi^2 \end{aligned} \tag{3.21}$$

where $\langle\hat{A}\rangle_\psi = \langle\psi|\hat{A}|\psi\rangle$ and $\langle\hat{A}^2\rangle_\psi = \langle\psi|\hat{A}^2|\psi\rangle$. The positive root of the variance, $+(\Delta\hat{A})_\psi$, is known as the *uncertainty*.

The variance of the photon number is thus:

$$\begin{aligned} V(\hat{n}_j)_\alpha &= \langle\Delta\hat{n}_j^2\rangle_\alpha \\ &= \langle\alpha_j|\hat{n}_j^2|\alpha_j\rangle - \langle\alpha_j|\hat{n}_j|\alpha_j\rangle^2 \\ &= \langle\alpha_j|(\hat{a}^\dagger{}_j\hat{a}_j)^2|\alpha_j\rangle - \langle\alpha_j|\hat{a}^\dagger{}_j\hat{a}_j|\alpha_j\rangle^2 \\ &= \langle\alpha_j|\hat{a}^\dagger{}_j\hat{a}_j\hat{a}^\dagger{}_j\hat{a}_j|\alpha_j\rangle - (|\alpha_j|^2)^2 \\ &= \langle\alpha_j|\hat{a}^\dagger{}_j(1 + \hat{a}^\dagger{}_j\hat{a}_j)\hat{a}_j|\alpha_j\rangle - |\alpha_j|^4 \\ &= \langle\alpha_j|\hat{a}^\dagger{}_j\hat{a}_j|\alpha_j\rangle + \langle\alpha_j|\hat{a}^\dagger{}_j\hat{a}^\dagger{}_j\hat{a}_j\hat{a}_j|\alpha_j\rangle - |\alpha_j|^4 \\ &= |\alpha_j|^2 + |\alpha_j|^4 - |\alpha_j|^4 \\ &= \bar{n}_j \end{aligned} \tag{3.22}$$

i.e. for the photon number of a coherent state, the variance equals the mean. This is *the* defining characteristic of a Poissonian distribution. Note that the variance and uncertainty of the photon number for the vacuum state, $|0\rangle$, are zero. That is, we are absolutely sure that we will not measure any photons in the vacuum state.

3.1.3 Quadrature operators and minimum uncertainty states

Measurements of electronic signals are homologous with measurements of optical signals [4]. We now introduce a concept that enjoys wide use in electronics. Consider an arbitrary voltage signal, V, described by a sine wave:

$$V = A\sin(\omega t + \phi) \tag{3.23}$$

This can expanded to:

$$V = A\sin(\omega t)\cos(\phi) + A\cos(\omega t)\sin(\phi) \tag{3.24}$$

If phase information is to be extracted from V, the it needs to be compared to a reference signal, known as the *local oscillator*, $V_0 = \sin(\omega t)$. The first term of eqn 3.24 is called the *in-phase* component, as it is in phase with the local oscillator. The second term is known as the *in-quadrature* component, as it is phase shifted $\pi/2$ with respect to the local oscillator. Somewhat confusingly, these components are also referred to as *quadratures* or *quadrature phases* (leading to the delightful term "in-quadrature quadrature").

In practice the signal V is often observed at the rate ω - the information in this case is being carried only by the amplitude A and relative phase of the signal ϕ. Thus we can

[4] The only difference is that of greatly increased frequency. Anything that is possible with electronic signals is, in principle at least, possible with optical signals. This includes nonlinear processes such as frequency doubling, parametric oscillation and frequency mixing

write, using the *rotating wave approximation*:

$$V = A\cos(\phi) + A\sin(\phi) = X_1 + X_2 \tag{3.25}$$

Once the two quadratures, X_1 & X_2, are measured, the amplitude and phase of the signal can be directly inferred: $A = \sqrt{X_1^2 + X_2^2}$ and $\phi = X_2/X_1$.

We now introduce operators that correspond to the quadratures of the electromagnetic field. To keep our notation uncluttered, we consider only a single mode of the field, and so drop the frequency dependent subscript, j. We introduce the *quadrature operators*, $\hat{X}_1$ and $\hat{X}_2$

$$\begin{aligned} \hat{X}_1 &= \hat{a} + \hat{a}^\dagger \\ \hat{X}_2 &= -i(\hat{a} - \hat{a}^\dagger) = e^{-i\pi/2}\hat{a} + e^{+i\pi/2}\hat{a}^\dagger \end{aligned} \tag{3.26}$$

Note that these operators are Hermitean, i.e. $\hat{X}_j = \hat{X}_j^\dagger$ [5]. The quadrature operators give dimensionless amplitudes ($\langle\psi|\hat{X}_1|\psi\rangle$ and $\langle\psi|\hat{X}_2|\psi\rangle$) for the two quadrature phases of the field mode, respectively the in-phase and in-quadrature components of the field mode.

For coherent states the quadrature amplitudes represent the real and imaginary parts of the field mode, and are thus commonly known as the *amplitude* and *phase* quadratures.:

$$\begin{aligned} \langle|\hat{X}_1|\rangle &= \langle\alpha|\hat{X}_1|\alpha\rangle = \langle\alpha|(\hat{a} + \hat{a}^\dagger)|\alpha\rangle = \langle\alpha|\hat{a}|\alpha\rangle + \langle\alpha|\hat{a}^\dagger|\alpha\rangle \\ &= \alpha + \alpha^* = 2\mathrm{Re}(\alpha) \\ \langle|\hat{X}_2|\rangle &= \langle\alpha|\hat{X}_2|\alpha\rangle = -i\langle\alpha|(\hat{a} - \hat{a}^\dagger)|\alpha\rangle = -i\langle\alpha|\hat{a}|\alpha\rangle - i\langle\alpha|\hat{a}^\dagger|\alpha\rangle \\ &= -i(\alpha - \alpha^*) = 2\mathrm{Im}(\alpha) \end{aligned} \tag{3.27}$$

Thus

$$2\alpha = \langle|\hat{X}_1|\rangle + i\langle|\hat{X}_2|\rangle \tag{3.28}$$

Fig. 3.1a) shows a representation of the coherent state as a phasor in quadrature space.

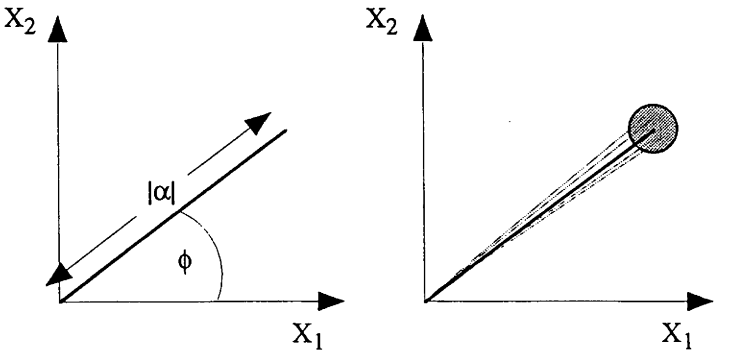

Figure 3.1: a) Coherent state as a phasor in quadrature space. b) as for (a), but including the uncertainty area. Grey lines represent other possible field values.

The amplitude of the coherent state, shown as $|\alpha|$ in the diagram, is given by $1/2\sqrt{\langle\hat{X}_1\rangle^2 + \langle\hat{X}_2\rangle^2}$,

[5] This follows automatically from the mathematical properties of operators. If $\hat{A}$ is non-Hermitean it can be decomposed into Hermitean components $(\hat{A}+\hat{A}^\dagger)$ and $-i(\hat{A}-\hat{A}^\dagger)$, where $\hat{A} = (\hat{A}+\hat{A}^\dagger)/2 - i(\hat{A}-\hat{A}^\dagger)/2i$.

and the phase of the coherent state, shown as ϕ in the diagram, is given by $\langle \hat{X}_2 \rangle / \langle \hat{X}_1 \rangle$. As we discuss below, this picture of a coherent state is still not complete. We have yet to consider the uncertainties in the state.

If $\hat{P}$ and $\hat{Q}$ are noncommuting Hermitean operators then the physical quantities P and Q cannot be simultaneously measured with zero uncertainty. This is known as *Heisenberg's Uncertainty Principle*. To see this[6], suppose $\hat{A}$ and $\hat{B}$ are two Hermitean operators and that all observables are taken for a fixed state $|\psi\rangle$. Now consider the expression :

$$\langle C \rangle = \langle \psi | (\hat{A} + iu\hat{B})(\hat{A} - iu\hat{B}) | \psi \rangle \tag{3.29}$$

This is the squared length of the vector $(\hat{A} - iu\hat{B})|\psi\rangle$ and is therefore always real and non-negative for positive u. Rearranging:

$$\begin{aligned} \langle C \rangle &= \langle \psi | (\hat{A}^2 + u^2 \hat{B} + iu\hat{B}\hat{A} - iu\hat{A}\hat{B}) | \psi \rangle \\ &= \langle A \rangle_\psi^2 + u^2 \langle B \rangle_\psi^2 - iu \langle [\hat{A}, \hat{B}] \rangle_\psi \end{aligned} \tag{3.30}$$

As $\langle C \rangle$ is positive for real u, then from the root of the quadratic solution ("$b^2 + 4ac$"):

$$\langle \hat{A}^2 \rangle_\psi \langle \hat{B}^2 \rangle_\psi \geq \frac{1}{4} |\langle [\hat{A}, \hat{B}] \rangle_\psi|^2 \tag{3.31}$$

Now let $\hat{A} = \hat{P} + \langle \hat{P} \rangle$ and $\hat{B} = \hat{Q} + \langle Q \rangle$. As $\langle \hat{P} \rangle$ and $\langle Q \rangle$ are numbers $[\hat{A}, \hat{B}] = [\hat{P}, \hat{Q}]$. Thus:

$$\begin{aligned} \langle \hat{A}^2 \rangle_\psi &= \langle \psi | (\hat{P}^2 + \langle \hat{P} \rangle^2 - 2\langle \hat{P} \rangle \hat{P}) | \psi \rangle \\ &= \langle \hat{P}^2 \rangle + \langle \hat{P} \rangle^2 - 2\langle \hat{P} \rangle^2 \\ &= \langle \hat{P}^2 \rangle - \langle \hat{P} \rangle^2 \\ &= \langle \Delta_P \rangle_\psi^2 \end{aligned} \tag{3.32}$$

And similarly, $\langle B^2 \rangle_\psi = \langle \Delta_Q \rangle_\psi^2$. Substituting into eqn 3.31 we obtain:

$$\begin{aligned} \langle \Delta_P \rangle_\psi^2 \langle \Delta_Q \rangle_\psi^2 &= 1/4 \, |\langle [\hat{P}, \hat{Q}] \rangle|^2 \\ \langle \Delta_P \rangle_\psi \langle \Delta_Q \rangle_\psi &= 1/2 \, |\langle [\hat{P}, \hat{Q}] \rangle| \end{aligned} \tag{3.33}$$

Thus the smaller the uncertainty in the measurement of the observable $\langle \hat{P} \rangle$, the greater the uncertainty in the observable $\langle \hat{Q} \rangle$.

The commutator for the quadrature operators is:

$$\left[\hat{X}_1, \hat{X}_2 \right] = 2i \tag{3.34}$$

Remembering that $|[\hat{X}_1, \hat{X}_2]| = 2$, the uncertainty relation for quadrature operators is thus:

$$\Delta_{X_1} \Delta_{X_2} = 1/2 |\langle [\hat{X}_1, \hat{X}_2] \rangle| = 1 \tag{3.35}$$

One quadrature cannot be measured to arbitrary accuracy without the other quadrature becoming arbitrarily uncertain.

Consider the variance of the amplitude and phase quadratures of the vacuum state. As the uncertainty of the photon number was zero, naïvely we might expect the quadrature variances to be zero. However from the uncertainty relation, eqn 3.35, we know this

[6] This proof is from reference [2].

cannot be. We find:

$$\begin{aligned} V(\hat{X}_1)_0 &= \langle \Delta X_1 \rangle_0^2 \\ &= \langle 0|\Delta \hat{X}_1{}^2|0\rangle \\ &= \langle 0|\hat{X}_1{}^2|0\rangle - \langle 0|\hat{X}_1|0\rangle^2 \\ &= \langle 0|(\hat{a}+\hat{a}^\dagger)^2|0\rangle - \langle 0|(\hat{a}+\hat{a}^\dagger)|0\rangle^2 \\ &= \langle 0|(\hat{a}^2+\hat{a}^\dagger\hat{a}+\hat{a}\hat{a}^\dagger+\hat{a}^{\dagger 2})|0\rangle - 0 \\ &= 0+0+\langle 0|(1+\hat{a}^\dagger\hat{a})|0\rangle + 0 = 1+0 \\ &= 1 \\ \langle \Delta \hat{X}_1 \rangle_0 &= \pm 1 \end{aligned} \tag{3.36}$$

Similarly for the phase quadrature:

$$\begin{aligned} V(\hat{X}_2)_0 &= \langle \Delta \hat{X}_2 \rangle_0^2 = 1 \\ \langle \Delta \hat{X}_2 \rangle_0 &= \pm 1 \end{aligned} \tag{3.37}$$

The vacuum state is noisy. This can be thought of as the standard background noise of the universe [7]. It is directly due to the $1/2h\nu$ energy present in each vacuum mode of the electromagnetic field. The noise level of the vacuum state is known by various names: the *standard quantum limit* or *SQL; shot noise;* or the *quantum noise limit* or *QNL*

How do the uncertainties of the coherent state compare with those of the vacuum state? The variance of the amplitude quadrature of the coherent state is

$$\begin{aligned} V(\hat{X}_1)_\alpha &= \langle \Delta \hat{X}_1 \rangle_\alpha^2 \\ &= \langle \alpha|\Delta \hat{X}_1{}^2|\alpha\rangle \\ &= \langle \alpha|\hat{X}_1{}^2|\alpha\rangle - \langle \alpha|\hat{X}_1|\alpha\rangle^2 \\ &= \langle \alpha|(\hat{a}+\hat{a}^\dagger)^2|\alpha\rangle - \langle \alpha|(\hat{a}+\hat{a}^\dagger)|\alpha\rangle^2 \\ &= \langle \alpha|(\hat{a}^2+\hat{a}^\dagger\hat{a}+\hat{a}\hat{a}^\dagger+\hat{a}^{\dagger 2})|\alpha\rangle \\ &\qquad - \left[\langle \alpha|\hat{a}|\alpha\rangle + \langle \alpha|\hat{a}^\dagger|\alpha\rangle\right]^2 \\ &= \langle \alpha|\hat{a}^2|\alpha\rangle + \langle \alpha|\hat{a}^\dagger\hat{a}|\alpha\rangle + \langle \alpha|(1+\hat{a}^\dagger\hat{a})|\alpha\rangle \\ &\quad + \langle \alpha|\hat{a}^{\dagger 2}|\alpha\rangle - [\alpha+\alpha^*]^2 \\ &= \alpha^2 + |\alpha|^2 + 1 + |\alpha|^2 + \alpha^{*\,2} - \left[\alpha^2 + \alpha^{*\,2} + 2|\alpha|^2\right] \\ &= 1 \\ \langle \Delta \hat{X}_1 \rangle_\alpha &= 1 \end{aligned} \tag{3.38}$$

Similarly for the phase quadrature:

$$\begin{aligned} V(\hat{X}_2)_\alpha &= \langle \Delta \hat{X}_2 \rangle_\alpha^2 = 1 \\ \langle \Delta \hat{X}_2 \rangle_\alpha &= \pm 1 \end{aligned} \tag{3.39}$$

The coherent state has exactly the same uncertainty as the vacuum state. This is what makes the coherent state worthy of attention. For both the coherent and vacuum states,

[7] This electromagnetic noise is present everywhere, at every frequency, in every direction. Your hand is a wonderful source of vacuum noise. This noise is *not* the remnant radiation from the Big Bang. That is at a microwave frequency only, and can only been seen by looking carefully at the sky.

the standard errors of the quadrature operators fulfill a special case of the Heisenberg uncertainty relation:

$$\langle \Delta \hat{X}_1 \rangle_\alpha \langle \Delta \hat{X}_2 \rangle_\alpha = 1 \tag{3.40}$$

Any state with uncertainties that fulfill this relation is known as a *minimum uncertainty state* or *MUS*. As we shall see, both coherent and vacuum states are special cases of the infinite set of *minimum uncertainty squeezed states*.

The phasor diagram must be modified to include an uncertainty outline, as shown in Fig. 3.1(b). This is often, and imaginatively, titled the *ball-on-stick diagram*. The phasor diagram can be interpreted in either the frequency or time domain. In the frequency domain, each frequency mode of the electromagnetic field has a separate ball-on-stick diagram. As we shall see, the uncertainty outline (a circle for a minimum uncertainty state) can differ from mode to mode: a new picture must be drawn for each frequency of the field.

3.1.4 Squeezed states

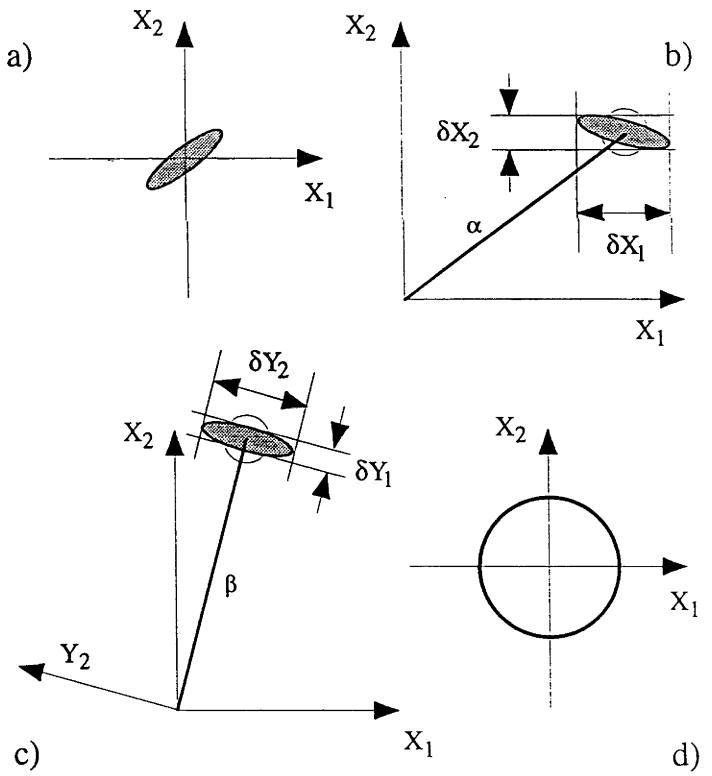

Figure 3.2: a) Vacuum squeezing. b) Bright squeezing. c) Bright squeezing in rotated quadrature space. Y_1, Y_2 shown on diagram. d) Number state.

Squeezed states are states where the uncertainty in one quadrature is less than the standard quantum limit, that is to say, quieter than the normal background noise of the universe. The production, measurement and modelling of these somewhat unusual states will take up much of the discussion in this thesis.

Any quadrature of the field mode may be smaller than the SQL, not only the in-phase and in-quadrature quadratures. That quadrature is said to be *squeezed*, it's complemen-

tary quadrature is sometimes said to be *anti-squeezed*. Minimum uncertainty squeezed states are states where the squeezed and anti-squeezed quadratures fulfill the minimum uncertainty relation, eqn 3.40.

This is best illustrated with phasor plots. *Vacuum* squeezed states are electromagnetic states without any coherent excitation, as shown in Fig. 3.2(a). *Bright* squeezed states are electromagnetic states with a coherent excitation, as shown in Fig. 3.2(b). For bright squeezed states, fluctuations in the amplitude quadrature lie along the vector, α, as shown. Fluctuations in the phase quadrature are at right angles to this.

Mathematically, both forms of squeezing are generated from the vacuum state. Vacuum squeezed states are defined as:

$$|0,\varepsilon\rangle = \hat{S}(\varepsilon)|0\rangle \tag{3.41}$$

and bright squeezed states are defined as:

$$|\alpha,\varepsilon\rangle = D(\alpha)S(\varepsilon)|0\rangle \tag{3.42}$$

where the unitary squeeze operator, $S(\varepsilon)$ is:

$$\hat{S}(\varepsilon) = exp(1/2\varepsilon^*\hat{a}^2 - 1/2\varepsilon\hat{a}^{\dagger 2}) \tag{3.43}$$

and $\varepsilon = re^{2i\phi}$. ϕ represents the quadrature angle of the squeezing: $\phi = 0$ is amplitude squeezing, $\phi = \pi/2$ is phase squeezing. As shown in Fig. 3.2(c) we define rotated quadrature operators, $\hat{Y}_1$ and $\hat{Y}_2$, that define a rotated complex amplitude, β:

$$\begin{aligned} \beta &= \alpha e^{-i\phi} \\ &= 1/2(\langle\hat{X}_1\rangle + i\langle\hat{X}_2\rangle)e^{-i\phi} \\ &= 1/2(\langle\hat{Y}_1\rangle + i\langle\hat{Y}_2\rangle) \end{aligned} \tag{3.44}$$

The squeeze operator attenuates one quadrature component of β whilst amplifying the complementary quadrature. The degree of amplification and attenuation is set by the *squeeze factor*, $r = |\varepsilon|$. For a squeezed state, the rotated quadrature uncertainties are:

$$\begin{aligned} \langle\Delta\hat{Y}_1\rangle_{\alpha,r} &= e^{-r} \\ \langle\Delta\hat{Y}_2\rangle_{\alpha,r} &= e^{+r} \end{aligned} \tag{3.45}$$

which fulfill the minimum uncertainty relation (eqn 3.40). The photon number of a squeezed state is:

$$\langle\hat{N}\rangle_{\alpha,r} = |\alpha|^2 + \sinh^2 r \tag{3.46}$$

Note that a squeezed vacuum ($\alpha = 0$) contains photons. That is, a squeezed vacuum state is not really a vacuum state, as it contains more than zero energy. It requires energy to alter the uncertainty circle of quantum noise limited states, be they vacuum or coherent.

How does a squeezed state compare to a number state? The quadrature variances for a number state are:

$$\langle\Delta\hat{X}_1\rangle_n = \langle\Delta\hat{X}_2\rangle_n = 2n + 1 \tag{3.47}$$

As shown in Fig. 3.2(d), in quadrature space the number state is an annulus with radius $\sqrt{n}$ and width = 1. The number state is certainly not a minimum uncertainty state in

quadrature space. However it *is* a minimum uncertainty state in number/phase space[8], whilst in that parameter space, vacuum, coherent and squeezed states are not. Although a detailed treatment is beyond the scope of this thesis, we point out that in a parameter space where a state is a minimum uncertainty state (squeezed state in quadrature space; number state in number/phase space) the Wigner function is always positive. Further, in quadrature space minimum uncertainty states are always Gaussian, and the uncertainty outline, which is a contour of the Wigner function, is always an ellipse. The number state in quadrature space has a Wigner function with negative values, corresponding to *negative* classical probabilities.

3.1.5 Linearisation

Linearisation is an approximation that makes most empirical quantum optics possible. It is only valid for detection of bright, steady-state, electromagnetic fields, i.e. fields with amplitudes much larger than their fluctuations. (From the phasor diagram point of view, the last requirement is that the "stick" is much longer than the width of the "ball".)

In linearisation, operators are decomposed into two components, one a c-number, the other an operator. The c-number component is the steady-state (and thus independent of time) expectation value of the operator. The operator component describes the time-varying fluctuations of the field. For example, linearising the annihilation operator of the coherent state:

$$\hat{a} \cong \alpha + \delta\hat{a}(t) \tag{3.48}$$

where ϕ is the phase of the coherent state. For the rest of this thesis we shall not explicitly write the time dependence of the fluctuation operator. These fluctuation operators are homologous with the fluctuations discussed in previous section (i.e. $\delta\hat{A} \equiv \Delta\hat{A}$). Previously established operator relations apply to the fluctuation operators. Thus, the quadrature fluctuation operators are:

$$\begin{aligned} \delta\hat{X}_1 &= (\delta\hat{a} + \delta\hat{a}^\dagger) \\ \delta\hat{X}_2 &= -i(\delta\hat{a} - \delta\hat{a}^\dagger) \end{aligned} \tag{3.49}$$

Linearisation offers insight into the physics of various measurements. Consider, for a real coherent field, the number operator:

$$\hat{n} = \hat{a}^\dagger\hat{a} \cong \alpha^2 + \alpha(\delta\hat{a} + \delta\hat{a}^\dagger) \tag{3.50}$$

where we have omitted the higher order (and thus negligible) terms in the fluctuations. We see that the number operator for a coherent field fluctuates around a mean value, and that the fluctuations are only observable because they're scaled by the field. Fluctuations in photon number correspond to fluctuations in the amplitude quadrature (compare eqns 3.49 and 3.50). We can thus write the expectation value for the photon number of a coherent field as:

$$\langle\hat{n}\rangle_\alpha = \langle\hat{a}^\dagger\hat{a}\rangle_\alpha \cong \alpha^2 + \alpha\langle\delta\hat{X}_1\rangle_\alpha \tag{3.51}$$

As the average value of the amplitude quadrature fluctuations is zero, the average photon number is α^2.

[8]This argument is valid, if somewhat hypothetical. The number operator is well defined. The phase operator is not, and still remains the subject of active research.

3.1.6 The sideband picture

In previous sections we've introduced several seemingly disparate concepts: coherent and squeezed states; quadrature operators; linearisation; and phasor diagrams. In this section we present a physically intuitive picture that unifies these concepts, and allows intuitive interpretation of the existing squeezing literature.

Consider a classical optical field of frequency Ω. It can be represented by a complex phasor on a frequency line, see Fig. 3.3(a). We refer to this phasor as the carrier. Amplitude modulation at a frequency ω is represented by two smaller phasors, referred to as *sidebands*, that are displaced from the carrier by $\pm\omega$. The relative height of the sidebands with respect to the carrier defines the modulation depth. The phasors are parallel to, and in the same direction as, the carrier, as shown in Fig. 3.3(b). Both sidebands beat with the carrier. It is the power of this beat signal that is measured experimentally. Phase modulation is represented by an infinite set of sidebands, spaced at ω. The sidebands are in the plane perpendicular to the carrier, and their relationship with one another is shown in Fig. 3.3(c). The modulation depth, and therefore the relative heights of the sidebands is given by a Bessel function. For small modulation depths the higher order sidebands are very small and can be ignored. In this limit phase modulation can be represented by just the first two sidebands at $\pm\omega$. As discussed later (see section 3.4.4), phase modulation is normally detected by converting it to amplitude modulation. (A simple way to do this is to rotate the carrier 90 degrees whilst leaving the sidebands unaffected.)

Any signal or modulation can be decomposed into amplitude and phase components. For a classical field no signal is detected at a frequency ω unless there is explicit modulation at that frequency. However real optical fields are not classical: there is noise at every detection frequency. For a coherent field this noise is at the standard quantum limit. We now explain this noise using the sideband picture.

In section 3.1.5 the operators $\hat{a}$ & $\hat{a}^\dagger$ were decomposed into a steady state component, α, and frequency dependent fluctuation operators $\delta\hat{a}$ & $\delta\hat{a}^\dagger$ respectively. In the sideband picture the fluctuation operators $\delta\hat{a}$ & $\delta\hat{a}^\dagger$ are considered to be tiny sidebands of fixed length located at $\pm\omega$ with respect to the carrier. The carrier has amplitude 2α: without loss of generality we define it to be real. Now consider the fluctuation operators $\delta\hat{a}$ & $\delta\hat{a}^\dagger$ at a specific sideband frequency, ω for a coherent state. The operators fluctuate randomly around the frequency axis at all frequencies (i.e. for all observation bandwidths of the frequency ω.) As they are uncorrelated they fluctuate at random with respect to each other. At any given instant $\delta\hat{a}$ & $\delta\hat{a}^\dagger$ may be parallel to one another and the carrier, giving amplitude modulation; at another, they may be out of phase with one another but both perpendicular to the carrier, giving phase modulation; and at yet another, any combination between these. Thus on average there is modulation, i.e. noise, at every quadrature: the magnitude of the modulation is constant, and the same for all quadratures and sideband frequencies. It is this noise that is represented by a circle on the phasor, or ball-on-stick, diagram.

Although the power of the sideband fluctuations is minute, it is the beating between the fluctuation sidebands and the carrier that provides the measurable quantum noise. (As can be seen from eqns 3.50 & 3.51.)

Naturally, in the sideband picture the formalism derived in section 3.1.3 applies without change. The amplitude modulation fluctuations are simply fluctuations in the amplitude quadrature, $\delta\hat{X}_1 = \delta\hat{a} + \delta\hat{a}^\dagger$ ($\delta\hat{a}$ & $\delta\hat{a}^\dagger$ have the same phase as each other and the carrier). Likewise, the phase modulation fluctuations are simply the fluctuations in the phase quadrature, $\delta\hat{X}_2 = \pm i(\delta\hat{a} - \delta\hat{a}^\dagger)$ ($\delta\hat{a}$ & $\delta\hat{a}^\dagger$ are 180° out of phase with each other

and both 90° out of phase with the carrier). The sideband picture also makes clear why the operators $\delta\hat{a}$ & $\delta\hat{a}^\dagger$ cannot be measured explicitly: this would correspond to a measurement of the power of one sideband solely. In contrast, photodetection measures the power of the beat between the sidebands.

Linear processes, such as absorption or mixing at a beam splitter, affect the carrier and sidebands differently but do not change the statistics of a coherent field. The magnitude of the output carrier is attenuated or amplified. However the magnitude of the output field sidebands is the same as the input field sidebands. This is because the linear process mixes uncorrelated input vacuum and coherent fields that have the same magnitude sidebands. (For a 50/50 beamsplitter, half of the coherent sideband and half of the vacuum sideband gives the same magnitude sideband as the initial coherent sideband.)

Nonlinear processes differ in that they can *correlate* the sidebands in some fashion. For example, consider degenerate four-wave-mixing: it correlates the sidebands at $\pm\omega$ so that they are parallel to each other and the carrier [4]. Consider the effect of say, 10% correlation of this type on a coherent field. Previously there was equal likelihood that that sidebands would combine to give modulation of the amplitude, phase, or any quadrature in between. However the sidebands are now correlated so that they now add more often to form amplitude modulation, and thus less often to form phase modulation [9]. Accordingly the amplitude quadrature becomes noisier, the phase quadrature quieter. Previously both quadratures were shot noise limited: the amplitude quadrature is now anti-squeezed; the phase quadrature is squeezed (by 10%). In the ball-on-stick picture the noise outline is now an ellipse, elongated along the carrier. The ellipse is narrower than the original quantum noise circle.

Using this picture it is clear why a linear process degrades squeezing. It mixes in uncorrelated, quantum noise level, sidebands, and thus reduces the correlation between the sidebands of the squeezed field. (For a 50/50 beamsplitter with an incident 10% squeezed field, the output fields are 5% squeezed.)

The sideband picture complements the ball-on-stick picture. Using both it is possible to develop an intuitive understanding of squeezing in any nonlinear system.

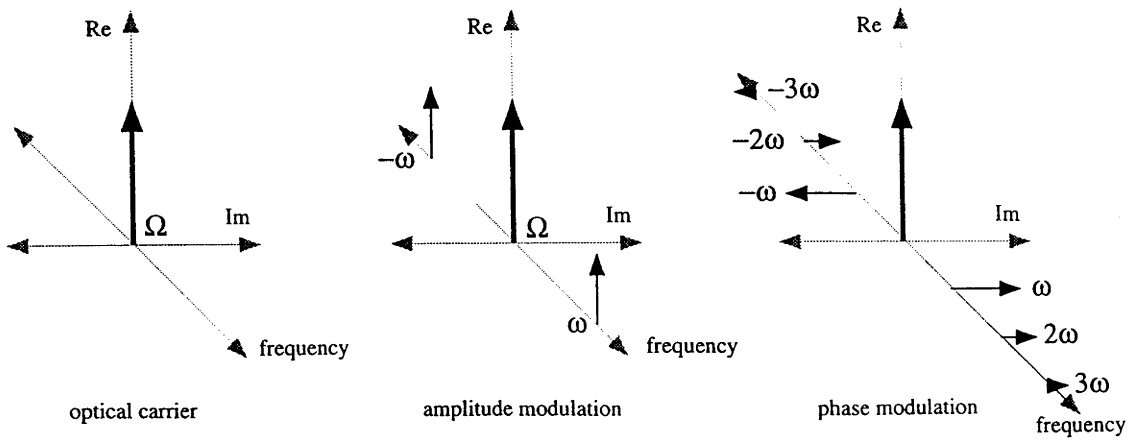

Figure 3.3: Sideband diagrams. a) optical carrier b) amplitude modulation c) phase modulation

[9]This is a physically intuitive way of stating Heisenberg's uncertainty principle. As we have seen, the behaviour of the sidebands is described mathematically by the commutator.

3.1.7 Limits of the sideband picture

How far can the sideband picture be taken? In the last section we stated that it can be used for any linearised system. This may strike some readers as surprising, afterall, operators are mathematically very different objects to electromagnetic field vectors. The following argument puts the correspondence between the two on a formal footing.

Consider an electromagnetic field with small positive and negative sidebands:

$$E = E_0 + \delta E_+ + \delta E_- \tag{3.52}$$

where δE_+ & δE_- are located at $\pm\omega$ with respect to the carrier, E_0. The variance of the intensity of this electromagnetic field is:

$$\begin{aligned} \mathrm{Var}(I) &= \mathrm{Var}\langle EE^* \rangle \\ &= \langle (EE^*)^2 \rangle - \langle EE^* \rangle^2 \\ &= E_0^2 \langle \delta E_+^2 + \delta E_-^2 + 2\delta E_+ \delta E_- \rangle \end{aligned} \tag{3.53}$$

where the final value of the variance will depend on the exact definition of δE_+ & δE_-.

In linearised quantum mechanics, the photon number variance is given by:

$$\begin{aligned} V_n &= \alpha^2 V_{X_1} \\ &= \alpha^2 \left\{ \langle \delta \hat{X}_1{}^2 \rangle - \langle \delta \hat{X}_1 \rangle^2 \right\} \\ &= \alpha^2 \left\{ \langle (\delta \hat{a} + \delta \hat{a})^2 \rangle - \langle \delta \hat{a} + \delta \hat{a} \rangle^2 \right\} \\ &= \alpha^2 \langle \delta \hat{a}^2 + \delta \hat{a}^{\dagger 2} + \delta \hat{a}^\dagger \delta \hat{a} + \delta \hat{a} \delta \hat{a}^\dagger \rangle \end{aligned} \tag{3.54}$$

Comparing eqns 3.53 and 3.54, it does appear that the sidebands δE_+ & δE_- are analogous to the operators $\delta \hat{a}$ & $\delta \hat{a}^\dagger$. However this is not quite the complete story.

The operators $\delta \hat{a}$ & $\delta \hat{a}^\dagger$ fulfill the commutation rule $\left[\delta \hat{a}, \delta \hat{a}^\dagger\right] = 1$. Applying this (in the case of a coherent field) we find that the self correlation of a given quadrature is $V_{X_i} = \langle \delta \tilde{X}_i, \delta \tilde{X}_i \rangle = 1$ (i.e any given quadrature is quantum noise limited); and the cross-correlation between orthogonal quadratures is $V_{X_1, X_1} = \langle \delta \tilde{X}_1, \delta \tilde{X}_2 \rangle = 0$ (i.e. orthogonal quadratures are totally uncorrelated).

For a coherent electromagnetic field, E, these criteria stipulate that the sideband amplitude modulation ($\delta E_+ + \delta E_-$) or phase modulation ($-i\left[\delta E_+ - \delta E_-\right]$) must be at the quantum noise limit; and that there is zero correlation between sideband amplitude and phase modulation. These criteria are fulfilled when the positive and negative sidebands are totally uncorrelated ($\langle \delta E_+ \delta E_- \rangle = 0$) and of identical size ($\langle \delta E_+^2 \rangle = \langle \delta E_-^2 \rangle$ where $\langle \delta E_+^2 + \delta E_-^2 \rangle = 1$). With these definitions, the sideband and fluctuation operator behaviours are identical.

Thus for linearised systems the behaviour of the operators $\delta \hat{a}$ & $\delta \hat{a}^\dagger$ can be correctly described by considering the operators to represent small sidebands of the optical field - this is an interpretation only, the formalism is unchanged. Both linear and nonlinear process can be understood in terms of manipulation, and in particular correlation, of these sidebands.

3.1.8 Equations of motion

In section 3.1.5 we stressed that linearisation is possible only when the field is in the steady-state. The most convenient way to ascertain this is to derive an equation of motion

for the optical system, and then solve it to see if steady-state solutions exist [10].

Classically a perfect (i.e lossless) simple harmonic oscillator is described by the equation of motion:

$$\dot{x} = i\Omega x \tag{3.55}$$

On integration the variable x oscillates indefinitely with angular frequency Ω. As the system is lossless, it does not interact with the rest of the universe. To model the effect of an irreversible (in the thermodynamic sense) interaction with the rest of the universe (for example, friction in a mechanical system) we introduce the damping term, γ, so that:

$$\dot{x} = (i\Omega - \gamma)x \tag{3.56}$$

The system is now described as *open*. On integration, the variable x now undergoes an oscillatory exponential decay.

For a quantised system, the equation of motion of operator, $\hat{x}$[11], can be found directly from the Hamiltonian of the system using the following relation [3]:

$$i\hbar\,\dot{\hat{a}} = [\hat{a}, \hat{\mathcal{H}}] \tag{3.57}$$

The Hamiltonian for a quantised simple harmonic oscillator of frequency ν, is:

$$\mathcal{H} = h\nu_j \left(\hat{a}^\dagger \hat{a} + \frac{1}{2}\right) \tag{3.58}$$

Thus the equation of motion of the quantised Fourier amplitude, $\hat{a}$, for a quantised simple harmonic oscillator is:

$$\dot{\hat{a}} = i\Omega\hat{a} \tag{3.59}$$

which is clearly analogous to the equation of motion for a classical simple harmonic oscillator, eqn 3.55. Once again the classical variables have been transformed to operators. By inspection then it would seem straightforward to write the equation of motion for a quantised, damped, simple harmonic oscillator as:

$$\dot{\hat{a}} = (i\Omega - \gamma)\hat{a} \tag{3.60}$$

However *this is incorrect*. It does not include the vital influence of vacuum noise that is introduced by the coupling to the rest of the universe. To account for this, we model the universe as a reservoir of an infinite number of electromagnetic modes, with Hamiltonian [5]:

$$\mathcal{H}_{uni} = i\hbar \int_{\infty}^{\infty} \Omega \hat{B}^\dagger(\Omega)\hat{B}(\Omega)d\Omega \tag{3.61}$$

where $\hat{B}$ and $\hat{B}^\dagger$ are the boson annihilation and creation operators respectively. The thermodynamically irreversible interaction of this reservoir with an arbitrary system operator, $\hat{c}$, is described by the Hamiltonian:

$$\mathcal{H}_{uni} = ih \int_{\infty}^{\infty} \sqrt{2\gamma}(\hat{B}^\dagger(\Omega)\hat{c} - \hat{B}(\Omega)\hat{c}^\dagger)d\Omega \tag{3.62}$$

[10] The discussion in this section is adapted from reference [6].

[11] In the *Heisenberg* picture of quantum mechanics, the operators are time dependent and the state vectors are not. In the *Schrödinger* picture the opposite is true. In the *interaction* picture both operators and state vectors are time dependent. The discussion here applies to the Heisenberg picture.

where we use the *Markovian approximation*, that the coupling constant $\sqrt{2\gamma}$ is independent of frequency. We can now write the equation of motion for $\hat{c}$ as [5]:

$$\dot{\hat{c}} = \frac{1}{i\hbar}\left[[\hat{c}, \mathcal{H}_{rev}] - \left\{\left[\hat{a}, \hat{c}^\dagger\right](\gamma\hat{c} + \sqrt{2\gamma}\delta\hat{B}(t)) - (\gamma\hat{c}^\dagger + \sqrt{2\gamma}\delta\hat{B}^\dagger(t))\,[\hat{a}, \hat{c}]\right\}\right] \tag{3.63}$$

where $\delta\hat{B}(t)$ is defined with respect to some arbitrary time t_0:

$$\delta\hat{B}(t) = \int e^{-i\Omega(t-t_0)}\hat{B}_0(\omega)d\Omega \tag{3.64}$$

The first term of equation 3.63 is the normal equation of motion for a closed system, i.e. eqn 3.57. Substituting the quantised simple harmonic oscillator, eqn 3.5, into eqn 3.63 we obtain the eqn of motion for $\hat{a}$:

$$\dot{\hat{a}} = (i\Omega - \gamma)\hat{a} - \sqrt{2\gamma}\delta\hat{B} \tag{3.65}$$

It is not necessary to repeat this calculation for each new system under consideration. In practice it is possible to write equations of motion for optical systems by inspection. However it is vital to remember, for each coupling port γ_x, to add a term like "$\sqrt{2\gamma_x}\delta\hat{B}$". Further, in optical systems the equations of motion are normally written in the *rotating wave frame*, i.e. the system is observed at the optical frequency, $\nu = \Omega/(2\pi)$. Thus the optical frequency term, $i\Omega$ is omitted from the equations of motion.

3.2 Thickets of solutions

Theoretical quantum optics in large part consists of deriving a suitable Hamiltonian for a system and then extracting from it the system dynamics (i.e. the equations of motion) and the noise spectra, which can then be compared to experiment.

The broad outline of this approach was apparent early in the piece, for example, Fig. 3.4 shows a conceptual map of possible approaches to modelling a laser, as drawn by Haken in 1970 [7]. However the fine details were unclear, and so for example the theoretical laser output spectra in [7] lack a quantum noise floor entirely. It took another 20 years of research before a simple and robust approach to modelling quantum optical systems was available.

Until 1984 the most serious problem was that no sensible procedure existed to model the input and output of a quantised cavity. Thus for the optical parametric oscillator the optimum output squeezing at zero frequency was simultaneously predicted to be perfect [8] and limited to 50% [9]. With the development of the *input-output formalism* [10, 11, 12] this serious limitation was removed. The input/output formalism allowed, in an elegant fashion, systems to be modelled with squeezed, coherent, or thermal input fields. (Using the formalism the OPO problem was quickly resolved: in principle, perfect squeezing can occur at zero frequency in the output field, reducing to the quantum noise limit at a high frequencies with a Lorentzian bandwidth set by the cavity.)

Until the late 1980's the Schrödinger approach (emphasised in grey on the right hand side of Fig. 3.4) was favoured by the majority of the quantum optics community. In the Schrödinger approach the operators are constant and the states vary with time. Fig. 3.5 shows the approach in more detail: it is quite involved. The penultimate product of this approach are drift and diffusion matrices, A & D, that respectively describe the system dynamics and noise properties. Deriving spectra from these is computationally intensive,

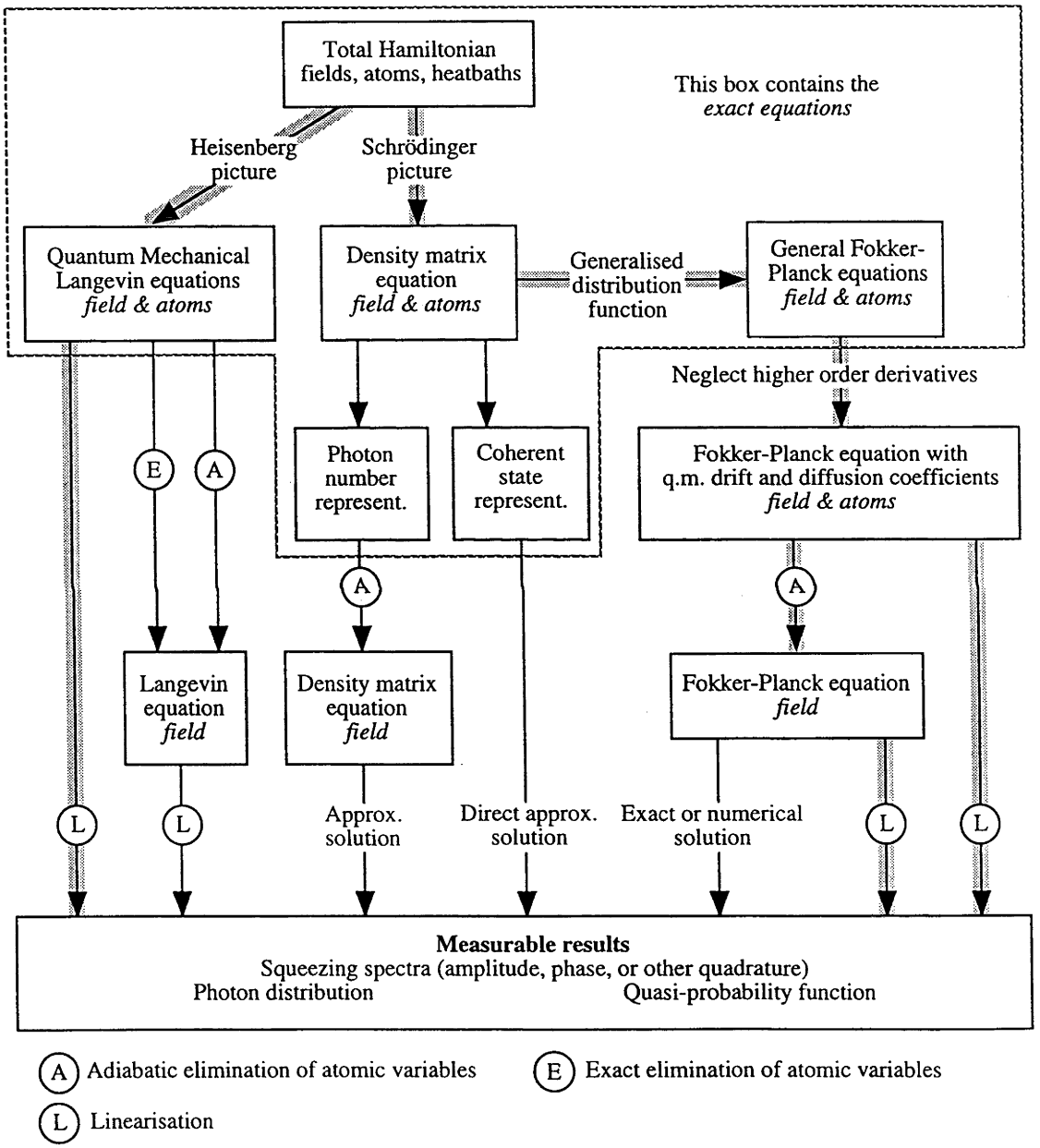

Figure 3.4: Conceptual map of possible approaches to modelling a quantum optical system. Adapted from Haken, 1970 [7].

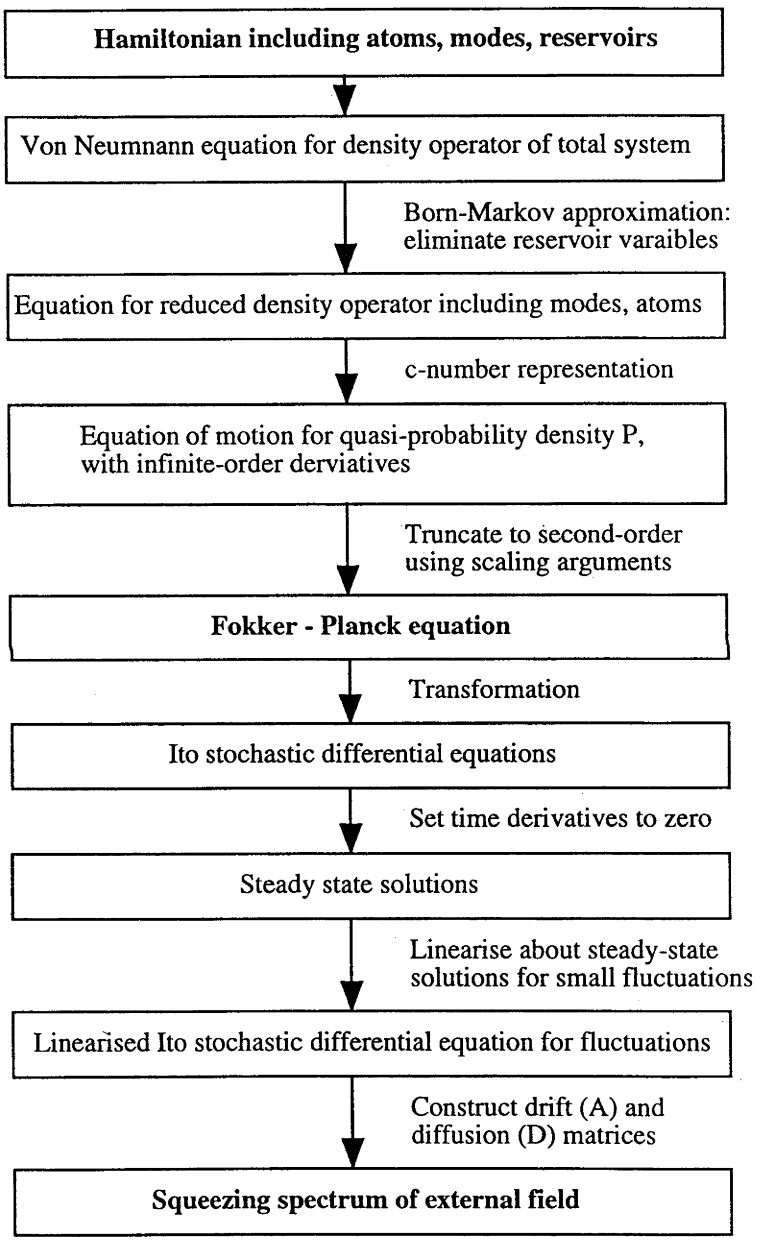

Figure 3.5: Detailed flow chart of the Schrödinger approach to modelling quantum optical systems. This approach is highlighted in grey on the right hand side of Fig. 3.4.

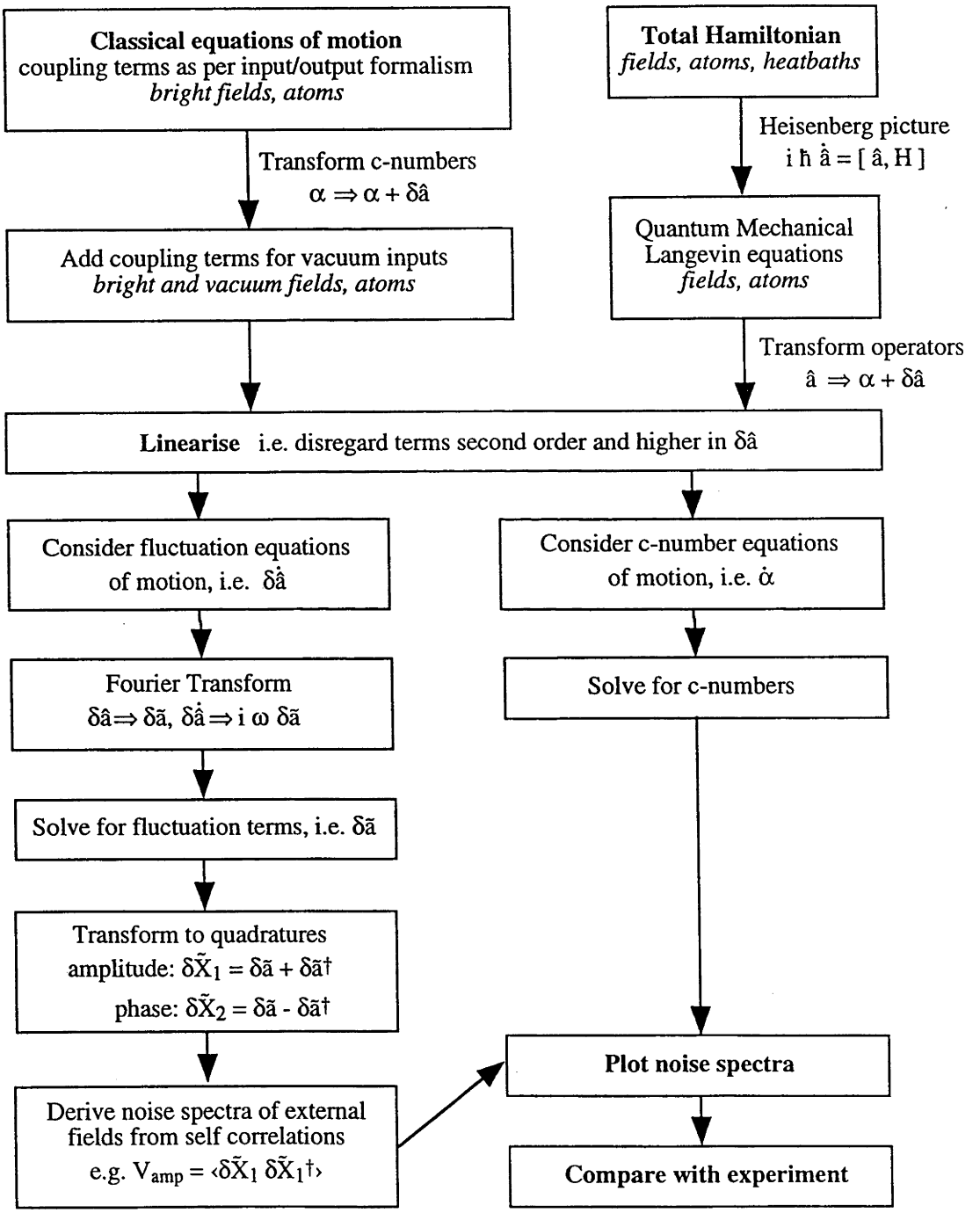

Figure 3.6: Detailed flow chart of the Heisenberg approach to modelling quantum optical systems. This approach is highlighted in grey on the left hand side of Fig. 3.4.

as it involves matrix inversion, and modelling practical systems nearly always involves a final numerical, rather than algebraic, solution. Despite these shortcomings, the approach was popular as it was obviously rigorous and thus reliable.

An alternative approach is the Heisenberg approach, shown in grey on the left hand side of Fig. 3.4. The operators vary in time and the states are constant. Fig. 3.6 shows the approach in more detail. The strength of this approach is both it's computational simplicity and it's analytical descriptions of the system dynamics and spectra. This allows an intuitive understanding of noise sources in practical systems that is not possible with the Schrödinger approach due to its requisite numerical solutions. The quantum optics community had always been aware of the Heisenberg approach and it was used to model very simple systems such as empty cavities. Despite this the Heisenberg approach has only recently begun to gain in popularity. In 1989 it was highlighted in a paper as the *semi-classical method* [13]. Considerable scepticism initially greeted this paper, as many felt that the method lacked necessary rigour. However it was quickly shown that the results were exactly equivalent to those of traditional methods [14]. In essence, it does not matter whether the linearisation occurs at the end of the calculation (the traditional, or Schrödinger, approach) or at the beginning (the semiclassical, or Heisenberg, approach). A further cause of reluctance was that it was not at all obvious how to model active systems in the Heisenberg approach - this problem has only been recently solved [15].

Due to its simplicity and intuitive nature we prefer the Heisenberg approach in this thesis, using it in Chapters 3 & 6-9. Comparison with the Schrödinger approach may be made in Chapter 4, where it is used to model and compare active and passive SHG. In the next section we walk the reader through the Heisenberg approach by modelling the empty, passive, cavity. This is not solely a pedagogical exercise: it allows us brevity later on when modeling the more complicated nonlinear systems; and the empty cavity results are of considerable importance in themselves.

3.3 A walk through the Heisenberg approach

3.3.1 The empty cavity: equations of motion

Consider the ring cavity shown in Fig. 3.7. The cavity irreversibly couples through a pump coupling port at mirror m_1, a transmission port at mirror m_2, and an absorption port represented by a mirror m_ℓ. Mirrors m_3 & m_4 are ideal reflectors and so are not coupling ports. The equations of motion for a passive lossless cavity are:

$$\begin{aligned} \dot{\hat{a}} &= -(\gamma + i\Delta)\hat{a} \\ \dot{\hat{a}}^\dagger &= -(\gamma + i\Delta)\hat{a}^\dagger \end{aligned} \tag{3.66}$$

By inspection we add coupling terms to write the quantised equations of motion for the open cavity:

$$\begin{aligned} \dot{\hat{a}} &= -(\gamma + i\Delta)\hat{a} + \sqrt{2\gamma_{m1}}\hat{A}_{pump} + \sqrt{2\gamma_{m2}}\hat{A}_{aux1} + \sqrt{2\gamma_{m\ell}}\hat{A}_{aux2} \\ \dot{\hat{a}}^\dagger &= -(\gamma + i\Delta)\hat{a}^\dagger + \sqrt{2\gamma_{m1}}\hat{A}^\dagger{}_{pump} + \sqrt{2\gamma_{m2}}\hat{A}^\dagger{}_{aux1} + \sqrt{2\gamma_{m\ell}}\hat{A}^\dagger{}_{aux2} \end{aligned} \tag{3.67}$$

where the total cavity decay rate is $\gamma = \gamma_{m1} + \gamma_{m2} + \gamma_{m\ell}$.

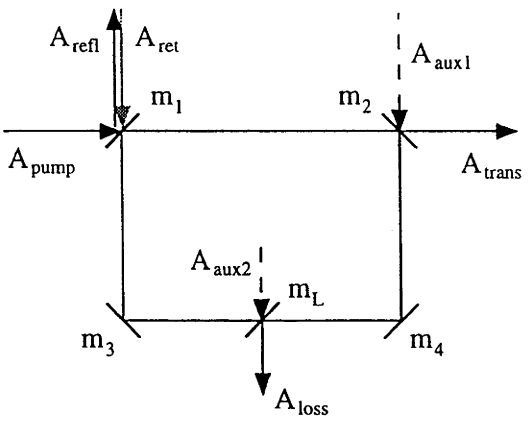

Figure 3.7: Schematic of empty cavity. Mirror m_1 couples the pump; mirrors m_2 & m_ℓ respectively couple vacuum fields from the transmitted and loss ports; mirrors m_3 & m_4 are perfect reflectors and so do not couple vacuum in.

3.3.2 The empty cavity: linearisation

Linearising we can write for the fluctuation operators:

$$\begin{aligned}\delta\dot{\hat{a}} &= -(\gamma + i\Delta)\delta\hat{a} + \sqrt{2\gamma_{m1}}\delta\hat{A}_{pump} + \sqrt{2\gamma_{m2}}\delta\hat{A}_{aux1} + \sqrt{2\gamma_{m\ell}}\delta\hat{A}_{aux2} \\ \delta\dot{\hat{a}}^\dagger &= -(\gamma + i\Delta)\delta\hat{a}^\dagger + \sqrt{2\gamma_{m1}}\delta\hat{A}^\dagger{}_{pump} + \sqrt{2\gamma_{m2}}\delta\hat{A}^\dagger{}_{aux1} + \sqrt{2\gamma_{m\ell}}\delta\hat{A}^\dagger{}_{aux2}\end{aligned} \tag{3.68}$$

Combining these equations we obtain the equations of motion for the quadrature operators:

$$\begin{aligned}\delta\dot{\hat{X}}_1 &= -\gamma\delta\hat{X}_1 + \Delta\delta\hat{X}_2 + \sqrt{2\gamma_{m1}}\delta\hat{X}_1^{pump} + \sqrt{2\gamma_{m2}}\delta\hat{X}_1^{aux1} + \sqrt{2\gamma_{m\ell}}\delta\hat{X}_1^{aux2} \\ \delta\dot{\hat{X}}_2 &= -\gamma\delta\hat{X}_2 - \Delta\delta\hat{X}_1 + \sqrt{2\gamma_{m1}}\delta\hat{X}_2^{pump} + \sqrt{2\gamma_{m2}}\delta\hat{X}_2^{aux1} + \sqrt{2\gamma_{m\ell}}\delta\hat{X}_2^{aux2}\end{aligned} \tag{3.69}$$

3.3.3 The empty cavity: Fourier transform

The fluctuation operators are intrinsically time dependent, i.e. $\delta\hat{c} = \delta\hat{c}(t)$. We define the *Fourier transform* of the fluctuation operators as:

$$\begin{aligned}\delta\tilde{c} &= \delta\tilde{c}(\omega) \\ &= FT[\delta\hat{c}(t)] \\ &= \int_{-\infty}^{\infty} \delta\hat{c}(t)e^{i\omega t}dt\end{aligned} \tag{3.70}$$

In this thesis the tilde will always signify a Fourier transformed operator. The Fourier transform obeys the normal mathematical rules for derivation and conjugation:

$$\begin{aligned}FT[\frac{d}{dt}\hat{c}(t)] &= -i\omega\tilde{c}(\omega) \\ FT[\hat{c}(t) \otimes \hat{d}(t)] &= \tilde{c}(\omega)\tilde{d}(\omega)\end{aligned} \tag{3.71}$$

The Fourier transform of the quadrature operator eqns of motion (eqn 3.69) is thus:

$$\begin{aligned}\delta\tilde{X}_1 &= \frac{+\Delta\delta\tilde{X}_2\sqrt{2\gamma_{m1}}\delta\tilde{X}_1^{pump}+\sqrt{2\gamma_{m2}}\delta\tilde{X}_1^{aux1}+\sqrt{2\gamma_{m\ell}}\delta\tilde{X}_1^{aux2}}{\gamma-i\omega}\\ \delta\tilde{X}_2 &= \frac{-\Delta\delta\tilde{X}_1\sqrt{2\gamma_{m1}}\delta\tilde{X}_1^{pump}+\sqrt{2\gamma_{m2}}\delta\tilde{X}_1^{aux1}+\sqrt{2\gamma_{m\ell}}\delta\tilde{X}_1^{aux2}}{\gamma-i\omega}\end{aligned} \tag{3.72}$$

Solving these to eliminate the intracavity fluctuation operator, $\delta\tilde{X}_{1,2}$, we obtain:

$$\begin{aligned}\delta\tilde{X}_1 = \frac{\sqrt{2\gamma_{m1}}(\delta\tilde{X}_1^{pump}+q\delta\tilde{X}_2^{pump})+\sqrt{2\gamma_{m2}}(\delta\tilde{X}_1^{aux1}+q\delta\tilde{X}_2^{aux1})}{+\sqrt{2\gamma_{m\ell}}(\delta\tilde{X}_1^{aux2}+q\delta\tilde{X}_2^{aux2})}\\ \hline (1+q^2)(\gamma-i\omega)\end{aligned} \tag{3.73}$$

where:

$$q=\frac{\Delta}{\gamma-i\omega} \tag{3.74}$$

The subscript $i=1(2)$ indicates the amplitude (phase) quadrature, whilst the subscript $j=2(1)$ indicates the complementary quadrature, i.e. phase (amplitude).

3.3.4 The empty cavity: boundary conditions

The boundary conditions for the reflected, transmitted and absorbed light of the empty cavity are:

$$\begin{aligned}\tilde{A}_{refl} &= \sqrt{2\gamma_{m1}}\tilde{a}-\tilde{A}_{pump}\\ \tilde{A}_{trans} &= \sqrt{2\gamma_{m2}}\tilde{a}-\tilde{A}_{aux1}\\ \tilde{A}_{loss} &= \sqrt{2\gamma_{m\ell}}\tilde{a}-\tilde{A}_{aux2}\end{aligned} \tag{3.75}$$

And thus for the quadrature fluctuation operators are:

$$\begin{aligned}\delta\tilde{X}_i^{refl} &= \sqrt{2\gamma_{m1}}\tilde{X}_i-\tilde{X}_i^{pump}\\ \delta\tilde{X}_i^{trans} &= \sqrt{2\gamma_{m2}}\tilde{X}_i-\tilde{X}_i^{aux1}\\ \delta\tilde{X}_i^{trans} &= \sqrt{2\gamma_{m\ell}}\tilde{X}_i-\tilde{X}_i^{aux2}\end{aligned} \tag{3.76}$$

On Fig. 3.7 we have indicated in grey a return field, $\tilde{A}_{ret}$. For a ring-cavity (in the absence of nonlinear effects) this return field does not affect the mode $\tilde{a}$. It sets up a mode with identical spatial properties to $\tilde{a}$ that circulates in the opposite direction. However for a standing wave cavity, the return field becomes the auxiliary field, $\tilde{A}_{ret}=\tilde{A}_{aux1}$ and thus has considerable influence.

Experimentally only the reflected and transmitted beams can be measured. Substituting eqns 3.73 into eqns 3.76 we see that the fluctuations in the reflected and transmitted beams are:

$$\begin{aligned}\delta\tilde{X}_i^{refl} = &\left[2\gamma_{m1}-(1+q^2)(\gamma+i\omega)\right]\delta\tilde{X}_i^{pump}+2q\gamma_{m1}\delta\tilde{X}_j^{pump}\\ &+2\sqrt{\gamma_{m1}\gamma_{m2}}(\delta\tilde{X}_i^{aux1}+q\delta\tilde{X}_j^{aux1})\\ &+2\sqrt{\gamma_{m1}\gamma_{m\ell}}(\delta\tilde{X}_i^{aux2}+q\delta\tilde{X}_j^{aux2})\end{aligned}$$

$$\gamma - i\omega$$

$$\delta\tilde{X}_i^{trans} = 2\sqrt{\gamma_{m1}\gamma_{m2}}(\delta\tilde{X}_i^{pump} + q\delta\tilde{X}_j^{pump}) + 2q\gamma_{m2}\delta\tilde{X}_j^{aux1} + \left[2\gamma_{m2} - (1+q^2)(\gamma+i\omega)\right]\delta\tilde{X}_i^{aux1} + 2\sqrt{\gamma_{m2}\gamma_{m\ell}}(\delta\tilde{X}_i^{aux2} + q\delta\tilde{X}_j^{aux2})$$

$$\gamma - i\omega \tag{3.77}$$

3.3.5 The empty cavity: deriving spectra

The noise spectra, V_i, for the quadratures $\tilde{X}_i$ observed on a state ψ are found from the self correlations of the fluctuation operators, i.e.:

$$\begin{aligned} V_{X_i}(\omega) &= \langle \delta\tilde{X}_i, \delta\tilde{X}_i^\dagger \rangle_\psi \\ &= \langle \delta\tilde{X}_i \delta\tilde{X}_i^\dagger \rangle_\psi - \langle \delta\tilde{X}_i \rangle_\psi \langle \delta\tilde{X}_i^\dagger \rangle_\psi \end{aligned} \tag{3.78}$$

Independent fields have zero correlation:

$$\langle \tilde{X}_i^{(j)}, \tilde{X}_i^{(k)} \rangle = 0, \quad (j) \neq (k) \tag{3.79}$$

So from equations 3.77 the spectra for the reflected and transmitted beams are:

$$V_{X_i}^{refl}(\omega) = |2\gamma_{m1} - (1+q^2)(\gamma+i\omega)|^2 V_{X_i}^{pump} + 4q^2\gamma_{m1}V_{X_j}^{pump} + 4\gamma_{m1}\gamma_{m2}(V_{X_i}^{aux1} + q^2 V_{X_j}^{aux1}) + 4\gamma_{m1}\gamma_{m\ell}(V_{X_i}^{aux2} + q^2 V_{X_j}^{aux2})$$

$$(\gamma^2+\omega^2)(1+q^2)^2$$

$$V_{X_i}^{trans}(\omega) = 4\gamma_{m1}\gamma_{m2}(V_{X_i}^{pump} + q^2 V_{X_j}^{pump}) + 4q^2\gamma_{m1}V_{X_j}^{aux1} + |2\gamma_{m2} - (1+q^2)(\gamma+i\omega)|^2 V_{X_i}^{aux1} + 4\gamma_{m2}\gamma_{m\ell}(V_{X_i}^{aux2} + q^2 V_{X_j}^{aux2})$$

$$(\gamma^2+\omega^2)(1+q^2)^2 \tag{3.80}$$

3.4 Cavity configurations and photodetection

In this thesis two configurations of the empty cavity are of considerable importance: the *symmetric cavity* and the *single-ended* cavity. We now examine these in turn.

3.4.1 The symmetric cavity

A symmetric lossless cavity has two coupling ports of equal strength, i.e. $\gamma_{m1} = \gamma_{m2} = \gamma/2$, $\gamma_{m\ell} = 0$. Consider the perfectly resonant case, $\Delta = 0 \Rightarrow q = 0$. The reflected and

transmitted spectra for either quadrature become:

$$\begin{aligned} V_{X_i}^{refl}(\omega) &= \frac{\omega^2 V_{X_i}^{pump} + \gamma^2 V_{X_i}^{aux1}}{\gamma^2 + \omega^2} \\ V_{X_i}^{trans}(\omega) &= \frac{\gamma^2 V_{X_i}^{pump} + \omega^2 V_{X_i}^{aux1}}{\gamma^2 + \omega^2} \end{aligned} \tag{3.81}$$

where $i = 1, 2$ represents the amplitude and phase quadrature, respectively. At zero frequency, $\omega = 0$, the cavity is transparent to the input fields, i.e.:

$$\begin{aligned} V_{X_i}^{refl}(0) &= V_{X_i}^{aux1}(0) \\ V_{X_i}^{trans}(0) &= V_{X_i}^{pump}(0) \end{aligned} \tag{3.82}$$

This is known as the *impedance-matched* case: the reflected field contains no information from the pump at all. At high frequencies $\omega \to \infty$, the cavity acts as a perfect reflector of the input fields, i.e.:

$$\begin{aligned} V_{X_i}^{refl}(\infty) &= V_{X_i}^{pump}(\infty) \\ V_{X_i}^{trans}(\infty) &= V_{X_i}^{aux1}(\infty) \end{aligned} \tag{3.83}$$

A resonant symmetric lossless cavity acts as a *low-pass filter* of the input fields. We will refer to such a cavity as a *mode cleaner*, as the high frequency noise of the pump field is cleaned off the transmitted field [12].

What is the effect of detuning? Consider the case $\Delta = \gamma$. At zero frequency $\omega = 0, \Rightarrow q = 1$. The cavity is no longer simply transparent to the input fields: it mixes the input fields *and* the quadratures of the input fields. The reflected and transmitted fields are identical:

$$V_{X_i}^{refl}(0) = V_{X_i}^{trans}(0) = \frac{[V_{X_i}^{pump}(0) + V_{X_j}^{pump}(0)] + [V_{X_i}^{aux1}(0) + V_{X_j}^{pump}(0)]}{4} \tag{3.84}$$

At high frequencies, $\omega \to \infty, \Rightarrow q = 0$, the cavity again acts as a perfect reflector of the input fields, i.e.:

$$\begin{aligned} V_{X_i}^{refl}(\infty) &= V_{X_i}^{pump}(\infty) \\ V_{X_i}^{trans}(\infty) &= V_{X_i}^{aux1}(\infty) \end{aligned} \tag{3.85}$$

A non-resonant symmetric lossless cavity acts as a low-pass filter *and* mixer of the input fields and quadratures. This is clearly undesirable in mode cleaners: to function efficiently they must be locked onto resonance.

3.4.2 The single-ended cavity

A lossless single-ended cavity is a cavity with a sole coupling port, i.e. $\gamma_{m1} = \gamma, \gamma_{m2} = \gamma_{m\ell} = 0$. Consider the perfectly resonant case, $\Delta = 0 \Rightarrow q = 0$. The reflected spectrum for either quadrature is independent of frequency:

$$V_{X_i}^{refl}(\omega) = V_{X_i}^{pump}(\omega) \tag{3.86}$$

[12] Actually the name was originally coined to describe the spatial cleaning properties of such a cavity. The input field can be spatially very messy (read "non-Gaussian") but the transmitted field is always Gaussian.

The resonant single-ended cavity simply acts as a perfect mirror.

Now consider a detuned cavity where $\Delta = \gamma$. At zero frequency $\omega = 0, \Rightarrow q = 1$. The cavity *rotates* the quadratures of the input field, i.e.:

$$\begin{aligned} V_{X_1}^{refl}(0) &= V_{X_2}^{pump}(0) \\ V_{X_2}^{refl}(0) &= V_{X_1}^{pump}(0) \end{aligned} \tag{3.87}$$

At high frequencies, $\omega \to \infty, \Rightarrow q = 0$, the cavity does not rotate the quadratures of the field but once again acts as a perfect reflector of the input field, i.e.:

$$V_{X_i}^{refl}(\infty) = V_{X_i}^{pump}(\infty) \tag{3.88}$$

The detuned single-ended cavity rotates the zero-frequency component with respect to the high frequency sidebands. As discussed shortly, this behaviour is most useful as it allows us to examine any quadrature of the pump field.

3.4.3 Photodetection

Photodetectors detect the power of the field. The mean optical power of a state $|\psi\rangle$ is:

$$P_{opt} = h\nu\langle\hat{n}\rangle_\psi = h\nu\langle\hat{a}^\dagger\hat{a}\rangle_\psi \tag{3.89}$$

In section 3.1.5 we introduced the concept of linearisation. We now rewrite eqn 3.48 as:

$$\begin{aligned} \tilde{a}(\omega) &\cong \alpha + \delta\tilde{a}(\omega) \\ &= e^{-i\phi(0)}|\alpha| + e^{-i\phi(w)}\delta\tilde{a}(\omega) \end{aligned} \tag{3.90}$$

where $\phi(0)$ is the phase of the zero-frequency component of the field, and $\phi(\omega)$ are the phases of the fluctuation components of the field.

For a coherent state, the mean optical power is:

$$P_{opt}(\omega) = h\nu|\alpha|^2 + h\nu e^{-2i\varphi}|\alpha|[\delta\tilde{a}(\omega) + e^{+2i\varphi}\delta\tilde{a}^\dagger(\omega)] \tag{3.91}$$

where:

$$\varphi = \phi(\omega) - \phi(0) \tag{3.92}$$

The zero-frequency (steady-state) component of the field, $|\alpha|$ is known as the *carrier* of the field, as it carries most of the energy. Note that the power measured due to the fluctuations depends on the frequency dependent phase relationship between the carrier and the sideband, φ. Rewriting 3.91 in terms of the quadrature fluctuation operators we obtain:

$$P_{opt}(\omega) = h\nu|\alpha|^2 + \frac{h\nu e^{-2i\varphi}}{2}|\alpha|[\delta\tilde{X}_1(\omega)(1 + e^{+2i\varphi}) + i\delta\tilde{X}_2(\omega)(1 - e^{+2i\varphi})] \tag{3.93}$$

Using eqns 3.78 and 3.93, we find that the photon number, or power, spectrum is related to the amplitude and quadrature fluctuation spectra by:

$$V_n(\omega) = |\alpha|^2\left[\frac{V_{X_1}(\omega)}{2} + \frac{V_{X_2}(\omega)}{2} + \frac{1}{4}e^{-2i\varphi}(1 + e^{+4i\varphi})\{V_{X_1}(\omega) + V_{X_2}(\omega)\}\right] \tag{3.94}$$

3.4.4 Phase sensitive detection

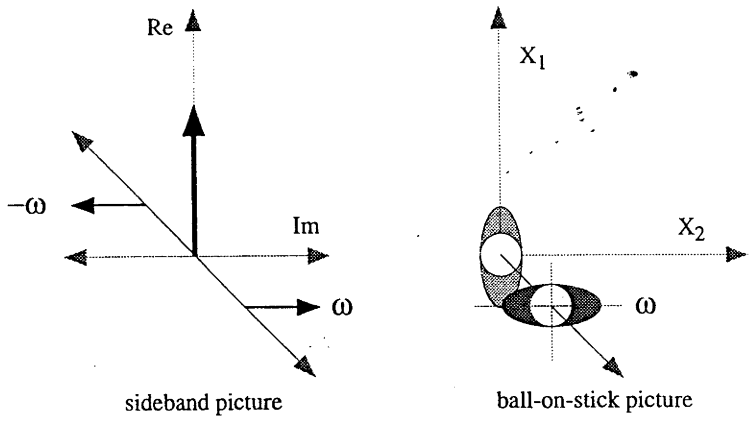

Figure 3.8: Quadrature rotation from single ended cavity. *left hand side*: sideband picture. *right hand side*: ball-on-stick picture.

Consider the single-ended cavity discussed in the last section. In the resonant case, there is a flat frequency response, with $V_{X_i}^{refl}(\omega) = V_{X_i}^{pump}(\omega)$. There is no differential rotation between the carrier and sideband components of the pump field, $\phi(0) = \phi(\omega), \Rightarrow \varphi = 0$. The measured power spectrum is thus:

$$V_n^{refl}(\omega) = |\alpha|^2 V_{X_1}^{pump}(\omega) \tag{3.95}$$

For direct detection of fields [13] (including fields relayed by perfect mirrors), the power fluctuation spectrum is related to the amplitude quadrature fluctuation spectrum.

Now consider the detuned single-ended cavity, $\Delta = \gamma$. The zero-frequency component of the pump field is rotated by $\pi/2$, e.g. $V_{X_1}^{refl}(0) = V_{X_2}^{pump}(0)$, whilst the high frequency components are unaffected, $V_{X_1}^{refl}(\infty) = V_{X_1}^{pump}(\infty)$. Thus the relative phase between carrier and sideband is $\varphi = \phi(\infty) - \phi(0) = \pi/2$. The measured power spectrum at high frequencies is thus:

$$V_n^{refl}(\infty) = |\alpha|^2 V_{X_2}^{pump}(\infty) \tag{3.96}$$

At high frequencies the power fluctuation spectrum of the reflected field is related to the phase quadrature fluctuation spectrum of the pump field. In general, the fluctuation spectrum of *any* pump quadrature can be measured by varying the cavity detuning, Δ.

A detector placed after a non-resonant single-ended cavity acts as a *phase sensitive detector*, i.e. it can detect any quadrature of the field. It enjoys several advantages, and one disadvantage, compared to the standard phase sensitive detector, the *homodyne* detector. The homodyne detector is a balanced detector (see next section) with a local oscillator field input at the vacuum port. The local oscillator must have the same properties as the signal field (frequency, spatial mode, etc.) and so in practice is normally derived from the same source. As the local oscillator must be much stronger than the signal (at least an order of magnitude) this constrains considerably the power available to the signal beam. A further experimental constraint is that the spatial mode-match between the

[13] As no steady-state phase information is measured in direct detection, it is possible, without loss of generality, to define the detected field as real and the carrier phase angle, $\phi(0)$, as zero. This is often done to simplify theoretical arguments. However as the theory presented here is in terms of the relative phase between sideband and carrier, φ, we don't need this definition.

local oscillator and signal beam is critical, and needs careful attention. The cavity based phase sensitive detector avoids these limitations. The carrier acts as the local oscillator, the sideband as the signal beam. The only disadvantage is that the cavity linewidth must be an order of magnitude smaller than the signal frequency, so that the approximation $\omega \to \infty$ is valid.

3.4.5 Balanced detection

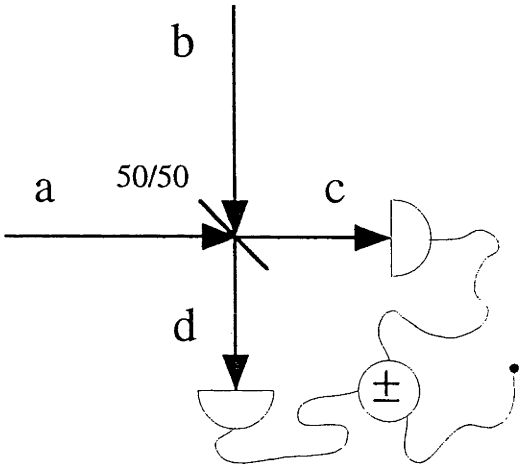

Figure 3.9: Schematic of a balanced detector.

Fig. 3.9 shows the balanced detector. Operators $\tilde{a}, \tilde{b}$ and $\tilde{c}, \tilde{d}$ represent the annihilation operators of the two input and output fields of a beam splitter, respectively. They are related by:

$$\begin{aligned} \tilde{c} &= \sqrt{1-\xi}\,\tilde{a} - \sqrt{\xi}\,\tilde{b} \\ \tilde{d} &= \sqrt{\xi}\,\tilde{a} + \sqrt{1-\xi}\,\tilde{b} \end{aligned} \tag{3.97}$$

where ξ is the beamsplitter reflectivity. The system is balanced when $\xi = 0.5$ as each input field contributes equally to each output field, i.e.:

$$\begin{aligned} \tilde{c} &= \sqrt{0.5}\,\tilde{a} - \sqrt{0.5}\,\tilde{b} \\ \tilde{d} &= \sqrt{0.5}\,\tilde{a} + \sqrt{0.5}\,\tilde{b} \end{aligned} \tag{3.98}$$

We assume the input fields are linearisable and, without loss of generality, real:

$$\begin{aligned} \tilde{a} &= \alpha + \delta\tilde{a}(\omega) \\ \tilde{b} &= \beta + \delta\tilde{b}(\omega) \end{aligned} \tag{3.99}$$

As the following argument is true for all frequencies, we drop the explicit frequency dependence of the fluctuation operator, writing $\delta\tilde{a}(\omega) \to \delta\tilde{a}$. The number operators for the added and subtracted signals are:

$$\begin{aligned} \tilde{n}^+ &= \tilde{c}^\dagger\tilde{c} + \tilde{d}^\dagger\tilde{d} \\ &= \alpha^2 + \beta^2 + \alpha(\delta\tilde{a} + \delta\tilde{a}^\dagger) + \beta(\delta\tilde{b} + \delta\tilde{b}^\dagger) \end{aligned}$$

$$= \alpha^2 + \beta^2 + \alpha\delta\tilde{X}_1{}^a + \beta\delta\tilde{X}_1{}^b \tag{3.100}$$

and

$$\begin{aligned} \tilde{n}^- &= \tilde{c}^\dagger\tilde{c} - \tilde{d}^\dagger\tilde{d} \\ &= 2\alpha\beta + \alpha(\delta\tilde{b} + \delta\tilde{b}^\dagger) + \beta(\delta\tilde{a} + \delta\tilde{a}^\dagger) \\ &= 2\alpha\beta + \alpha\delta\tilde{X}_1{}^b + \beta\delta\tilde{X}_1{}^a \end{aligned} \tag{3.101}$$

Now consider the case where one input field is bright, $\alpha \neq 0$, and the other is vacuum, $\beta = 0$. The number operators for the added and subtracted signals become:

$$\tilde{n}^+ = \alpha^2 + \alpha\delta\tilde{X}_1{}^a \tag{3.102}$$

and:

$$\tilde{n}^- = 0 + \alpha\,\delta\tilde{X}_1{}^b \tag{3.103}$$

For a linearised operator, the absolute value of the steady state component gives the mean value. Thus for the added and subtracted signals:

$$\begin{aligned} \langle\tilde{n}^+\rangle_\psi &= \alpha^2 \\ \langle\tilde{n}^-\rangle_\psi &= 0 \end{aligned} \tag{3.104}$$

On average, there is no energy in the subtracted signal. However there are still fluctuations. For a linearised operator, the spectrum is found by taking the self correlations of the fluctuation component. The power spectra of the added and subtracted signals are thus:

$$\begin{aligned} V_{n+}(\omega) &= \alpha^2\, V_{X_1^a}(\omega) \\ V_{n-}(\omega) &= \alpha^2\, V_{X_1^b}(\omega) = \alpha^2 \end{aligned} \tag{3.105}$$

The power spectrum of the added signal is proportional to the amplitude spectrum of the bright field, a; the power spectrum of the subtracted signal is proportional to the amplitude spectrum of the vacuum field, b, which is the quantum noise limit. A balanced detector thus allows comparison of the power (and thus amplitude) fluctuation spectrum of any input field, a, with the quantum noise limit. If the balanced detector is used in conjunction with a detuned single-ended cavity, the fluctuation of *any* quadrature can be compared to the quantum noise limit.

Chapter 3 bibliography

[1] D. F. Walls & G. J. Milburn, *Quantum Optics*, First Edition, Springer-Verlag, Berlin, 1994

[2] J. L. Martin, *Basic quantum mechanics*, First Edition, Oxford University Press, Oxford, 1982

[3] E. Merzbacher, *Quantum Mechanics*, Second Edition, John Wiley & Sons, Inc., New York, 1970

[4] H.-A. Bachor, *A guide to experiments in quantum optics*, First Edition, VCH Publishers, New York, 1997; H.-A. Bachor and D. E. McClelland, Physica Scripta, **T40**, p. 40, 1992. *Quantum optics experiments with atoms*

[5] C. Gardiner, *Quantum Noise*, First Edition, Springer-Verlag, Berlin, 1991

[6] B. C. Buchler, *Feedback Control of Laser Intensity Noise*, Honours Thesis, Australian National University, Canberra, 1996

[7] H. Haken, *"Laser Theory", in Encyclopedia of Physics, Volume XXV/2c, Light and Matter Ic, Chief Editor S. Flügge*, First Edition, Springer-Verlag, Berlin, 1970

[8] B. Yurke, Physics Review A, **20**, no. 1, p. 408, 1984. *Use of cavities in squeezed state generation*

[9] G. Milburn and D. F. Walls, Optics Communications, **39**, p. 410, 1981.

[10] M. J. Collett and C. W. Gardiner, Physics Review A, **30**, no. 3, p. 1386, 1984. *Squeezing of intracavity and travelling-wave light fields produced in parametric amplification*

[11] C. W. Gardiner and M. J. Collett, Physics Review A, **31**, no. 6, p. 3761, 1985. *Input and output in damped quantum systems: Quantum stochastic differential equations and the master equation*

[12] M. J. Collett and D. F. Walls, Physics Review A, **32**, no. 5, p. 2887, 1985. *Squeezing spectra for nonlinear optical systems*

[13] S. Reynaud and A. Heidmann, Optics Communications, **71**, p. 209, 1989.

[14] C. Fabre, E. Giacobino, A. Heidmann, L. Lugiato, S. Reynaud, M. Vadacchino and W. Kaige, Quantum Optics, **2**, p. 159, 1990. *Squeezing in detuned degenerate optical parametric oscillators*

[15] T. C. Ralph, C. C. Harb and H.-A. Bachor, Phys. Rev. A, **54**, no. 5, p. 4359, 1996. *Intensity noise of injection-locked lasers: Quantum theory using a linearised input-output method*

Chapter 4

Limits to squeezing in SHG

A vacuum is a hell of a lot better than some of the stuff that nature replaces it with.

Tennessee Williams, *Cat On A Hot Tin Roof*

As one of the simplest nonlinear optical processes, second harmonic generation (SHG) has been extensively investigated as a source of nonclassical light. Both active (occurs within a laser cavity) and passive (occurs in a cavity external to a laser) SHG have been modelled and found to be potential sources of squeezed light. There have been many and varied predictions and the relationship between them all has not been particularly clear (for example, some are apparently mutually inconsistent).

In 1981 Drummond et.al considered doubly resonant SHG and predicted anti-bunching of the fundamental if a second harmonic field was also injected [1]. The next year Mandel considered single pass SHG and found that the second harmonic field was not necessary: predicting both squeezing and anti-bunching in the fundamental field [2]. For a doubly resonant sub/second harmonic generation system, Milburn and Walls predicted in 1983 that the quadrature of the fundamental squeezing could be altered by altering the phase of an injected second harmonic [3]. Widespread attention began to be focussed on SHG as a source of squeezing after the paper of Lugiato et. al in 1983. They predicted, for doubly resonant SHG pumped solely at the fundamental, that both the fundamental and second harmonic would be squeezed (the predicted second harmonic squeezing was smaller than that of the fundamental). They also emphasised the critical role of the value of the ratio of the damping constants of the two modes [4]. In 1985 Collett and Walls showed that, in principle at least, *perfect* squeezing was possible in either the fundamental or the second harmonic at the critical point of doubly resonant SHG (the self-pulsing instability) [5]. Prompted by experimental difficulties, Collett and Paschotta realised that double resonance was not necessary to produce squeezing, and predicted second harmonic squeezing from a singly resonant cavity [6]. The strong correlation between the fundamental and second harmonic has also been proposed as the basis of a QND like measurement scheme [7].

Perfect squeezing can only be achieved when there is a strong interaction between the fundamental and second harmonic. Experimentally this dictates a doubly resonant system. Passive doubly resonant SHG systems are technically complicated, as practical passive cavities require locking systems to remain resonant. To date, singly resonant systems have proved to be much stabler than doubly resonant: the maximum length of time squeezing has been observed in doubly resonant SHG has been 10 s; singly resonant systems squeeze continuously for hours. As active modes are automatically resonant there is a strong experimental attraction to active SHG as it requires locking of, at most, only the second harmonic cavity. It promises strong squeezing in technically elegant systems.

Various techniques have been used to model active SHG. In the *good cavity* limit where the atomic decay rates are much higher than the relevant field decay rates, as is the case for a gas laser, the system is modelled by adiabatically eliminating the atomic variables

[8]. This introduces broadband atomic noise which degrades the correlation between the amplitudes of the second harmonic and the fundamental. Nevertheless, a maximum of 50% squeezing of the amplitude of the second harmonic has been predicted, with an optimum value at zero frequency and decreasing with frequency. This has been elegantly explained as the Poissonian photons of the fundamental being converted with high efficiency to second-harmonic photons which consequently have half-Poissonian statistics [9]. In the *bad cavity* limit, where the field decay rate of the mode of interest is much greater then the atomic decay rate and the decay rate of the other mode [10, 11], the bandwidth of the atomic noise is small and there is a high correlation between the amplitude of the second harmonic and the fundamental. Appropriate interaction between the two cavity modes allows perfect squeezing at non-zero frequencies. Until the treatment in this chapter was developed [12], no treatment to date had reconciled these two regimes within the one model.

In this chapter we present an overall picture that unifies previous descriptions. We consider both active and passive SHG, and include the critical role of laser noise. In particular we evaluate the squeezing available using Nd:YAG as an active gain medium and investigate which approaches are the most experimentally promising.

In the first two sections we model both active and passive SHG via the Schrödinger approach. These sections can be skimmed, or even skipped, by all but the connoisseurs as the Schrödinger approach is mathematically heavy-going and the final results aren't particularly informative in themselves. However the third section is crucial. In it we investigate the regimes of squeezing numerically, endeavouring to provide a physically intuitive picture for each result. These intuitive pictures will be used in latter chapters. In the last section we summarise the results, and conclude that active SHG is not, and will not be in the foreseeable future, a practical source of squeezed light.

4.1 Theory: Schrödinger approach

There have been successful squeezing experiments via passive SHG; there have been none via active SHG. Accordingly we approach modelling the two systems a little differently. As we know squeezing via passive SHG is possible, we consider the optimum squeezing available in a practical situation, i.e. for a multi-port, lossy system with achievable or near-achievable nonlinearities. To date most treatments of squeezing in passive SHG have concentrated on the ideal regime, i.e. single ended, lossless systems that can attain extreme nonlinearities, with a coherent pump or with idealized laser phase noise [13]. We explicitly model the pump as the intrinsically noisy output of a laser: for the case of singly resonant passive SHG, we have compared our model with experimental results and found excellent agreement (see, [14] and next chapter). In this chapter we also model the doubly resonant case [1].

In contrast, we do not know if squeezing via active SHG is possible, so we allow ourselves a little more freedom, and consider situations with extreme nonlinearities. Previously active SHG has been studied using either the Haken-Lamb or Lax-Louisell laser models. The Haken-Lamb model retains all the laser dynamics of a 2-level system. However for many lasers it is not possible to correctly describe the threshold behaviour using a 2-level model. The Lax-Louisell model is a 3-level system in which the lasing coherence has been adiabatically eliminated. Unfortunately crucial dynamical behaviour is lost in

[1] All the theory in this section was originally derived by Dr T. Ralph and published in [12].

this limit. In this chapter we use a 3-level model [15] similar to Lax-Louisell except that it retains all laser dynamics explicitly.

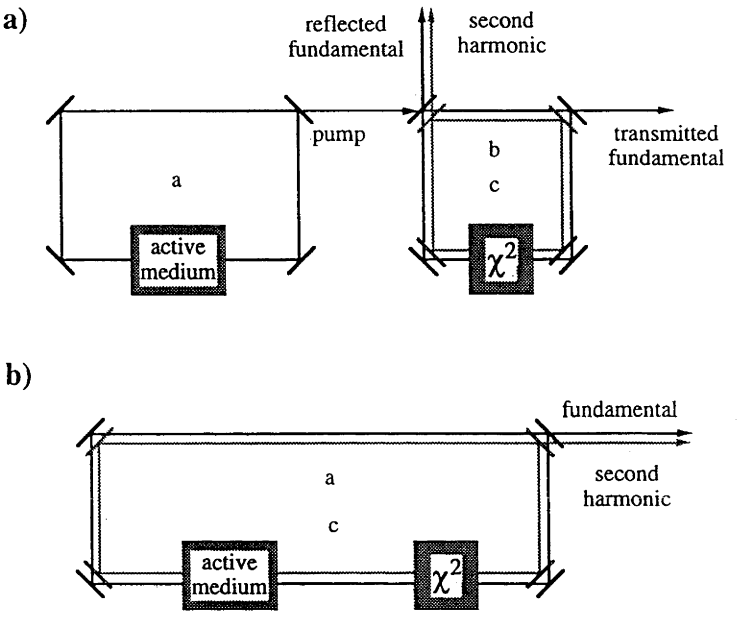

Figure 4.1: Schemata of active and passive second harmonic generation respectively. a is the lasing mode, b is the fundamental mode of the SHG cavity, and c is the second harmonic mode.

4.1.1 Hamiltonians and master equations

Figs 4.1a & b are schematics of active and passive second harmonic generation respectively. The same laser model is used for both, and consists of N 3-level atoms interacting with an optical ring cavity mode via the resonant Jaynes-Cummings Hamiltonian. In the interaction picture this is:

$$\hat{\mathcal{H}}_{las} = i\hbar g_{23} \sum_{\mu=1}^{N} (\hat{a}^\dagger \hat{J}_{23}^- - \hat{a}\hat{J}_{23}^+) \tag{4.1}$$

where carets indicate operators; g_{23} is the dipole coupling strength between the atoms and the cavity; $\hat{a}$ & $\hat{a}^\dagger$ are the lasing mode annihilation and creation operators; $\hat{J}_{23}^-$ & $\hat{J}_{23}^+$ are the collective Hermitean conjugate lowering and raising operators between the $|i\rangle$th and $|j\rangle$th levels of the lasing atoms. Level 1 is the ground level. The field phase factors have been absorbed into the definition of the atomic operators.

For the passive case the standard Hamiltonian for SHG is used [1]:

$$\hat{\mathcal{H}}_{pshg} = i\hbar\frac{\kappa}{2}(\hat{b}^{\dagger 2}\hat{c} - \hat{b}\hat{c}^{\dagger 2}) \tag{4.2}$$

where $\hat{b}$ & $\hat{b}^\dagger$ are the fundamental annihilation and creation operators, $\hat{c}$ & $\hat{c}^\dagger$ are the second harmonic annihilation and creation operators, and κ is the coupling parameter for the interaction between the two modes. For the active case the Hamiltonian is essentially

the same, except now the fundamental and the lasing mode are one and the same, so that:

$$\hat{\mathcal{H}}_{ashg} = i\hbar\frac{\kappa}{2}(\hat{a}^{\dagger 2}\hat{c} - \hat{a}\hat{c}^{\dagger 2}) \tag{4.3}$$

where the other terms are as above.

For both cases standard techniques [16] are used to couple the lasing atoms and cavities to reservoirs and to derive a master equation for the reduced density operator ρ of the system. Included in the laser model are spontaneous atomic emission from level $|3\rangle$ to level $|2\rangle$, and from level $|2\rangle$ to level $|1\rangle$, at rates γ_{23} and γ_{12} respectively. Incoherent pumping of the laser occurs at a rate Γ; the rate of collisional or lattice induced phase decay of the lasing coherence is γ_p.

In general optimum squeezing in these systems occurs at zero detuning, accordingly will not examine the effect of non-zero detunings. However in passing we mention the varied effects due to detuning: the quadrature of the squeezing can be rotated [17, 18]; the squeezing can be degraded as the intracavity intensity is lowered and less power is available to drive the nonlinearity; the form of the nonlinearity can change [1]; and the stability point of the system can move [8].

In the passive case the driving of the SHG cavity by the laser is modelled using the cascaded quantum system formalism of Carmichael [19] and Gardiner [20]. The laser cavity damping rate due to the output port which pumps the passive cavity is $2\gamma_a$; the cavity decay rate for the fundamental mode of the passive cavity is $2\gamma_b$; and the cavity decay rate for the second harmonic mode is $2\gamma_c$. The resulting interaction picture master equation is:

$$\begin{aligned}
\frac{\partial}{\partial t}\hat{\rho} &= \frac{1}{i\hbar}[\hat{\mathcal{H}}_{las}, \hat{\rho}] + \frac{1}{i\hbar}[\hat{\mathcal{H}}_{pshg}, \hat{\rho}] + \frac{1}{2}\left(\gamma_{12}L_{12} + \gamma_{23}L_{23}\right)\hat{\rho} + \frac{\Gamma}{2}\left(L_{13}\hat{\rho}\right)^{\dagger} \\
&\quad + \frac{1}{4}\gamma_p\left[2(\hat{J}_3 - \hat{J}_3)\,\hat{\rho}\,(\hat{J}_3 - \hat{J}_3) - (\hat{J}_3 - \hat{J}_3)^2\,\hat{\rho} - \hat{\rho}(\hat{J}_3 - \hat{J}_3)^2\right] \\
&\quad + \gamma_a(2\hat{a}\hat{\rho}\hat{a}^{\dagger} - \hat{a}^{\dagger}\hat{a}\hat{\rho} - \hat{\rho}\hat{a}^{\dagger}\hat{a}) \\
&\quad + \gamma_b(2\hat{b}\hat{\rho}\hat{b}^{\dagger} - \hat{b}^{\dagger}\hat{b}\hat{\rho} - \hat{\rho}\hat{b}^{\dagger}\hat{b}) \\
&\quad + \gamma_c(2\hat{c}\hat{\rho}\hat{c}^{\dagger} - \hat{c}^{\dagger}\hat{c}\hat{\rho} - \hat{\rho}\hat{c}^{\dagger}\hat{c}) \\
&\quad + 2\sqrt{\gamma_a\gamma_b}(\hat{a}\hat{\rho}\hat{b}^{\dagger} + \hat{b}\hat{\rho}\hat{a}^{\dagger} - \hat{\rho}\hat{a}^{\dagger}\hat{b} - \hat{\rho}\hat{a}\hat{b}^{\dagger}), \\
L_{ij}\hat{\rho} &= 2\hat{J}_{ij}^{-}\hat{\rho}\hat{J}_{ij}^{+} - \hat{J}_{ij}^{+}\hat{J}_{ij}^{-}\hat{\rho} - \hat{\rho}\hat{J}_{ij}^{+}\hat{J}_{ij}^{-}
\end{aligned} \tag{4.4}$$

Similarly in the active case the fundamental cavity damping rate is $2\gamma_a$ and the cavity decay rate for the second harmonic mode is $2\gamma_c$. The interaction picture master equation is:

$$\begin{aligned}
\frac{\partial}{\partial t}\hat{\rho} &= \frac{1}{i\hbar}[\hat{\mathcal{H}}_{las}, \hat{\rho}] + \frac{1}{i\hbar}[\hat{\mathcal{H}}_{ashg}, \hat{\rho}] + \frac{1}{2}\left(\gamma_{12}L_{12} + \gamma_{23}L_{23}\right)\hat{\rho} + \frac{\Gamma}{2}\left(L_{13}\hat{\rho}\right)^{\dagger} \\
&\quad + \frac{1}{4}\gamma_p\left[2(\hat{J}_3 - \hat{J}_3)\,\hat{\rho}\,(\hat{J}_3 - \hat{J}_3) - (\hat{J}_3 - \hat{J}_3)^2\,\hat{\rho} - \hat{\rho}(\hat{J}_3 - \hat{J}_3)^2\right] \\
&\quad + \gamma_a(2\hat{a}\hat{\rho}\hat{a}^{\dagger} - \hat{a}^{\dagger}\hat{a}\hat{\rho} - \hat{\rho}\hat{a}^{\dagger}\hat{a}) \\
&\quad + \gamma_c(2\hat{c}\hat{\rho}\hat{c}^{\dagger} - \hat{c}^{\dagger}\hat{c}\hat{\rho} - \hat{\rho}\hat{c}^{\dagger}\hat{c}), \\
L_{ij}\hat{\rho} &= 2\hat{J}_{ij}^{-}\hat{\rho}\hat{J}_{ij}^{+} - \hat{J}_{ij}^{+}\hat{J}_{ij}^{-}\hat{\rho} - \hat{\rho}\hat{J}_{ij}^{+}\hat{J}_{ij}^{-}
\end{aligned} \tag{4.5}$$

4.1.2 Semiclassical equations

The semiclassical equations of motion are obtained directly from the master equation by making the approximation of factorising expectation values.

The semiclassical equations of motion for the passive case are:

$$\begin{aligned}
\dot{\mathrm{J}_{23}} &= g_{23}(\mathrm{J}_3 - \mathrm{J}_2)a - \frac{1}{2}(\gamma_{23} + \gamma_{12} + 2\gamma_p)J_{23} \\
\dot{\mathrm{J}_2} &= +g_{23}(\mathrm{J}_{23}a^* - \mathrm{J}_{23}^* a) + \gamma_{23}J_3 - \gamma_{12}J_2 \\
\dot{\mathrm{J}_3} &= -g_{23}(\mathrm{J}_{23}a^* - J_{23}^* a) + \Gamma J_1 - \gamma_{23}J_3 \\
\dot{\mathrm{a}} &= g_{23}J_{23} - \gamma_a a \\
\dot{\mathrm{b}} &= \kappa b^* \mathrm{c} - \gamma_b b - 2\sqrt{\gamma_a \gamma_b}a \\
\dot{\mathrm{c}} &= -\gamma_a a - \frac{\kappa}{2}b^2
\end{aligned} \tag{4.6}$$

and their conjugate equations. The absence of circumflexes indicate semi-classical expectation values. Here γ_a is the total loss rate of the laser cavity; γ_b is the total loss rate of the fundamental cavity; γ_c is the total loss rate of the second harmonic cavity; and κ is the coupling constant between fundamental and second harmonic.

We use the following standard scaling with the number of atoms N:

$$\begin{aligned}
a' &= \frac{a}{\sqrt{\mathrm{N}}} \quad b' = \frac{b}{\sqrt{\mathrm{N}}} \\
J_i' &= \frac{J_i}{\mathrm{N}} \quad J_{ij}' = \frac{J_{ij}}{\mathrm{N}} \\
\kappa' &= \kappa\sqrt{\mathrm{N}} \quad g_{23}' = g_{23}\sqrt{\mathrm{N}}
\end{aligned} \tag{4.7}$$

In the active case the equations of motion for the active medium are unchanged, however the equations for the fundamental and second harmonic modes become:

$$\begin{aligned}
\dot{\mathrm{a}} &= g_{23}\mathrm{J}_{23} - \gamma_a a + \kappa a^* c \\
\dot{\mathrm{c}} &= -\gamma_c c - \frac{\kappa}{2}a^2
\end{aligned} \tag{4.8}$$

and their conjugate equations. The conditions for semiclassical steady state are obtained by setting derivatives to zero.

4.1.3 Noise spectra

The drift and diffusion matrices are listed at the end of the chapter. Their calculation, by obtaining c-number (complex number) Fokker-Planck equations from the master equation using positive-p representation, is tedious but standard [21]. We linearise the optical modes:

$$z'(t) = z_0 + \delta \mathrm{z} \tag{4.9}$$

where z represents modes a, b, or c; and z_0 is the semiclassical steady state. For brevity we will from this point on use a, b, ... to mean the scaled steady state solutions, e.g. $a \equiv a_0$. The spectral matrix $S(\omega)$ is defined as the Fourier transformed matrix of the two time correlation functions of these small quantum perturbations ($\delta\alpha_j$) about the semiclassical steady state, i.e.

$$S_{ij} = \int_{-\infty}^{+\infty} e^{-i\omega t}\langle \delta\alpha_i(t+\tau), \delta\alpha_i(t)\rangle \mathrm{d}\tau_i \tag{4.10}$$

where we have used the notation $\langle X, Y\rangle = \langle XY\rangle - \langle X\rangle\langle Y\rangle$ and the ordering of the perturbations for the passive and active cases respectively is:

$$\begin{aligned}\delta\alpha &= (\delta\mathrm{a}, \delta\mathrm{a}^\dagger, \delta\mathrm{b}, \delta\mathrm{b}^\dagger, \delta\mathrm{c}, \delta\mathrm{c}^\dagger, \delta\mathrm{J}_{23}^-, \delta\mathrm{J}_3, \delta\mathrm{J}_2, \delta\mathrm{J}_{23}^+)\\ \delta\alpha &= (\delta\mathrm{a}, \delta\mathrm{a}^\dagger, \delta\mathrm{c}, \delta\mathrm{c}^\dagger, \delta\mathrm{J}_{23}^-, \delta\mathrm{J}_3, \delta\mathrm{J}_2, \delta\mathrm{J}_{23}^+)\end{aligned} \tag{4.11}$$

The spectral matrix may be calculated from the Fokker Planck equations in both cases. The solution for the spectral matrix is:

$$S(\omega) = (A - i\omega I)^{-1} D (A^{\mathrm{T}} + i\omega I)^{-1} \tag{4.12}$$

where A & D are the drift and diffusion matrices, respectively and I is the identity matrix. The squeezing spectrum is then defined by:

$$V_{X_\theta}(\omega) = \int_{-\infty}^{+\infty} e^{-i\omega t} \langle X_\theta(t+\tau), X_\theta(t)\rangle \mathrm{d}\tau \tag{4.13}$$

We obtain noise spectra for modes a, b, or c by defining the quadrature phase amplitude of the transmitted field z as

$$X_\theta(t) = \mathrm{z}_{out} e^{-i\theta} + \mathrm{z}_{out}^\dagger e^{+i\theta} \tag{4.14}$$

where again z represents modes a, b, or c. Setting $\theta = 0$ gives the amplitude noise spectra. Using the input/output formalism of Collett and Gardiner [22] we are able to obtain the spectra in terms of the spectral matrix S(ω). In the passive case, using the ordering of eqn 4.11, we obtain for the laser, transmitted fundamental, and second harmonic respectively:

$$\begin{aligned}V_{\mathrm{X}_1}^{las} &= 1 + 2\gamma_a \left[S_{12}(\omega) + S_{21}(\omega) + e^{-2i\theta} S_{11}(\omega) + e^{+2i\theta} S_{22}(\omega)\right]\\ V_{\mathrm{X}_1}^{\nu trans} &= 1 + 2\gamma_b^{trans} \left[S_{78}(\omega) + S_{87}(\omega) + e^{-2i\theta} S_{77}(\omega) + e^{+2i\theta} S_{88}(\omega)\right]\\ V_{\mathrm{X}_1}^{2\nu} &= 1 + 2\gamma_c \left[S_{9\,10}(\omega) + S_{10\,9}(\omega) + e^{-2i\theta} S_{99}(\omega) + e^{+2i\theta} S_{10\,10}(\omega)\right]\end{aligned} \tag{4.15}$$

where γ_b^{trans} is the loss rate of the fundamental transmission (not the pump mirror). The spectra of the reflected fundamental depends on both the noise of the laser mode and the noise of the fundamental. The amplitude spectra is thus given by:

$$\begin{aligned}V_{\mathrm{X}_1}^{\nu refl} &= 1 + 2\gamma_b^{refl}[S_{78}(\omega) + S_{87}(\omega) + S_{77}(\omega) + S_{88}(\omega)] + 2\gamma_a\\ &\quad [S_{12}(\omega) + S_{21}(\omega) + S_{11}(\omega) + S_{22}(\omega)]\\ &\quad +2\sqrt{\gamma_b^{refl}\gamma_a}[S_{71}(\omega) + S_{72}(\omega) + S_{82}(\omega) + S_{81}(\omega)\\ &\qquad + S_{17}(\omega) + S_{18}(\omega) + S_{27}(\omega) + S_{28}(\omega)]\end{aligned} \tag{4.16}$$

In the active case, again using the ordering of eqn 4.11, we obtain spectra for the fundamental and second harmonic respectively as:

$$\begin{aligned}V_{\mathrm{X}_1}^{\nu} &= 1 + 2\gamma_a \left[S_{12}(\omega) + S_{21}(\omega) + e^{-2i\theta} S_{11}(\omega) + e^{+2i\theta} S_{22}(\omega)\right]\\ V_{\mathrm{X}_1}^{2\nu} &= 1 + 2\gamma_c \left[S_{78}(\omega) + S_{87}(\omega) + e^{-2i\theta} S_{77}(\omega) + e^{+2i\theta} S_{88}(\omega)\right]\end{aligned} \tag{4.17}$$

These spectra can be generated numerically using eqn 4.12 and the drift and diffusion matrices.

4.2 Experimental modelling and numerical parameters

We are particularly interested in experimental systems pumped by Nd:YAG lasers. Although Nd:YAG lasers are four level systems, we can accurately model them with a three level model as the decay rate of from the fourth to the third level is very much faster (approximately tenfold) than the other decay rates of the system, and so has negligible effects on the dynamics of the system. Accordingly we use the following values:

$$\begin{aligned} \gamma_{23} &= 5 \times 10^{-5}\gamma_{12} \quad \gamma_{13} = 2\gamma_{23}\gamma_{12} \\ \gamma_{tot} &= (\gamma_p + \gamma_{13} + \gamma_{23} + 1)\gamma_{12} \\ \sigma &= 6.5 \times 10^{-23}\mathrm{m}^2 \quad \gamma_p = 9000\gamma_{12} \\ g_{23} &= \sqrt{\frac{c_{yag}\sigma\rho_{yag}\gamma_{tot}}{4}} \end{aligned} \tag{4.18}$$

where the speed of light in Nd:YAG is $c_{yag} = 1.64 \times 10^8 \mathrm{m.s}^{-1}$; the density of Nd atoms in Nd:YAG is $\rho_{yag} = 1.38 \times 10^{26}$ atoms.m^{-3} and σ is the stimulated emission cross-section. The decay rate from level 2 to 1 is $\gamma_{12} = 1/(30 \times 10^{-9})\mathrm{s}^{-1}$.

Please note that although the expressions for squeezing spectra are given in terms of angular frequency ([w] = rad.s^{-1}), the decay rates are in expressed in Hertz ([f] = s^{-1}), as is customary. All spectra in this paper are plotted in Hz (s^{-1}).

We also wish to model the lossy, multi-port nature of experimental cavities. The total loss rate for a standing wave cavity is given by:

$$\gamma_z = \gamma_z^{refl} + \gamma_z^{trans} + \gamma_z^{abs} \tag{4.19}$$

where z is the mode; the first two terms are the loss rates through the front and end mirrors of a standing wave cavity and the last term is the loss rate due to absorption. The mirror decay rates are related to the mirror transmissions by eqn 2.23. The loss due to absorption is given by $\gamma_z^{abs} = c_{yag}/(2p) \log e^{-\alpha_{YAG}\ell}$ where α_{YAG} is the absorption loss per unit distance and ℓ is the physical crystal length.

The interaction is scaled by the number of lasing atoms as shown in eqn 4.7. The number of lasing atoms, N, can be estimated one of two ways. The first is to calculate the effective mode volume and then to use the known density of Nd atoms in YAG ($\rho_{yag} = 1.38 \times 10^{20}$atoms.cm^{-3}). An alternative is to use an expression for the output power:

$$\mathrm{P}_{las} = 2h\nu N\gamma_{12}\gamma_a^{out}a^2 \tag{4.20}$$

where h is Planck's constant; ν is the laser frequency; and γ_a^{out} is the loss rate of the laser output mirror. Using the measured laser power the number of atoms is to be N= 10^{17}.

The models presented here are for doubly resonant systems. This allows exploration of various squeezing regimes by smoothly varying the interaction between the modes. In order to model singly resonant systems we simply take the appropriate bad cavity limit. In this way the results of an explicitly singly resonant theory can be exactly duplicated without loss of generality.

Table 4.1: Squeezing limits

	PASSIVE				ACTIVE			
	Ideal Limit		Lossy with pump noise		Ideal Limit		Lossy with pump noise	
mode	2ν	ν	2ν	ν	2ν	ν	2ν	ν
singly resonant case	$V_{opt} = 1/9$, $\Omega_{opt} = 0$	$V_{opt} = 2/3$, $\Omega_{opt} = 0$	$V_{opt} \cong 0.5$, $\Omega_{opt} \cong 1.1\gamma_{12}$	$V_{opt} \cong 0.95$, $\Omega_{opt} \cong 1.2\gamma_{12}$	$V_{opt} = 1/2$, $\Omega_{opt} = 0$	$V_{opt} = 1/2$, $\Omega_{opt} = 0$	No sqz'ing owing to high γ_p	No sqz'ing owing to high γ_p
	Fig. 4.2a		Fig. 4.2b		Fig. 4.5			
doubly resonant case	$V_{opt} = 0$, $\Omega_{opt} \neq 0$	$V_{opt} = 0$, $\Omega_{opt} \neq 0$	$V_{opt} \cong 0.1$, $\Omega_{opt} \cong 1.5\gamma_{12}$	$V_{opt} \cong 0.3$, $\Omega_{opt} \cong 0.5\gamma_{12}$	$V_{opt} = 0$, $\Omega_{opt} \neq 0$	$V_{opt} = 0$, $\Omega_{opt} \neq 0$	$V_{opt} \cong 1/2$, $\Omega_{opt} \cong 0$	No sqz'ing owing to high γ_p
	Fig. 4.3a	Fig. 4.4a	Fig. 4.3b	Fig. 4.4b	Fig. 4.6	not shown	Fig. 4.9	

4.3 Regimes of squeezing

Table 4.1 summarises the results of this section. The optimum predicted squeezing for both active and passive SHG is considered for the two principal configurations: singly resonant at the fundamental frequency ν; and doubly resonant. Two limits of the squeezing are tabled: *ideal* and *lossy with pump noise*. The ideal limit comes from consideration of a coherently pumped, single-ended, lossless device, and is only included for easy comparison with previous theoretical literature. However all the plots in this chapter come from consideration of a lossy device. Thus, even when coherently pumped, the maximum plotted squeezing is not the ideal, as a fraction of the squeezing goes unobserved (i.e. it is absorbed or transmitted through the other port.) Thus the maximum value of squeezing in Fig. 4.3 is 0.28, and not the ideal value of 1/9 as listed in the table.

The lossy with pump noise "limit" comes from consideration of the experimental case of a multi-port, lossy device pumped by a Nd:YAG laser. It is not a limit in the sense that these figures cannot be bettered - it simply summarises the effect of laser noise as shown in the plots and provides a realistic guide to the noise suppression that can be expected. In addition, the typical detection frequencies at which the best noise suppression occurs are listed in table 1. They indicate the optimum point of operation for a squeezing experiment and are given as multiples of the linewidth of the SHG cavity at the fundamental.

4.3.1 Passive SHG

Why does SHG squeeze? Consider the following argument. It is clear from equation 2.34 that singly resonant SHG acts as a nonlinear loss term. That is, the stronger the field, the proportionately larger the reduction in intensity. Now consider the ball-on-stick picture for the fundamental field inside the cavity, Fig. 4.2. The stick length is reduced as power is lost to the second harmonic field. The ball at the end of the stick is also affected. The "top" of the ball (the point furtherest from the origin) is reduced more than the "bottom" of the ball (the point closest to the origin) as it is of greater power. Thus the ball is squeezed along the amplitude axis of the stick, and the light is amplitude squeezed. (Of course, the ball is extended along the phase quadrature axis as the light obeys Heisen-

berg's uncertainty principle.) As explained later, the apportioning of squeezing from the intracavity fundamental field to the extracavity fundamental and second harmonic fields depends on the relative cavity decay rates and the strength of the nonlinear interaction.

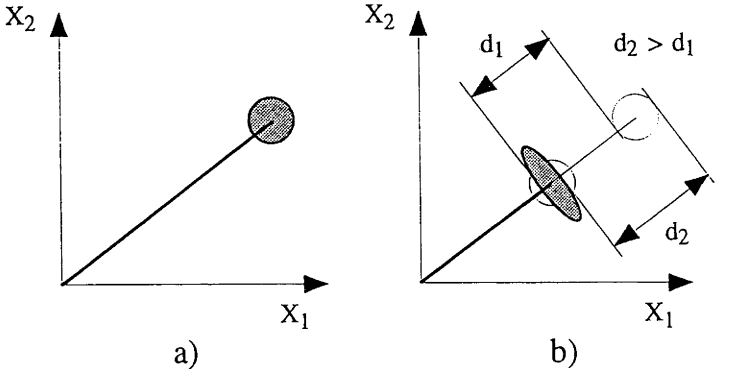

Figure 4.2: Intuitive explanation of SHG squeezing. Phasor diagrams for an intracavity fundamental field a) without and b) with SHG: the top of the uncertainty area is more intense than the bottom, and so is reduced more by the SHG, i.e. $d_2 > d_1$.

Good squeezing of the second harmonic requires the second harmonic loss rate to be higher than that of the fundamental cavity, i.e., $\gamma_c > \gamma_b$. However to obtain perfect squeezing, it is not desirable that γ_c be arbitrarily larger than γ_b. To see this, consider the singly resonant case (the bad cavity limit for 2ν), $\gamma_c \gg \gamma_b$. Fig. 4.3a [2] shows the noise spectrum with a coherent pump: the maximum squeezing occurs at zero frequency, in the vicinity of the optimum value of 1/9 (see earlier comment), and then degrades with frequency. Perfect squeezing cannot be achieved.

If a laser pump is used, as shown in Fig. 4.3b, the situation degrades further due to the large amounts of low frequency noise added by the laser. This effectively moves the maximum squeezing out in frequency whilst reducing it's value. These results suggest a partial explanation for the results of Paschotta et. al [6]: the observed deviation between theory and experiment increased as a function of power. This can be simply explained via our model as the noise tail of the laser masking the squeezing. As the laser power is increased, the laser noise increases with respect to the shot noise [3], decreasing the observed squeezing.

How then can perfect squeezing be obtained? Consider the doubly resonant case. A critical pump power exists for doubly resonant SHG: at this power the system begins self-pulsing [1, 23]. Before the critical point there exists a large damped oscillation in the phase quadratures of both fields: at the critical point this becomes undamped and becomes the self-pulsing frequency, ω_{osc}. This large oscillation in the phase quadrature depresses the amplitude quadrature, via Heisenberg's uncertainty principle. At the critical point, where the phase quadrature at ω_{osc} is infinitely noisy, the amplitude quadrature is infinitely quiet, i.e perfectly squeezed. Thus to obtain perfect squeezing we need to force the system close to the critical point. This can be done by increasing the power or nonlinearity, or it can be done by adjusting the cavity decay rates so that the two modes interact

[2] The reader is advised to note the *shape* of the plots, and not worry too much about the exact numbers used to get them. For completeness, the parameter values are given in the figure captions.

[3] Quantum noise scale as the square root of the optical power; classical noise scales as the optical power.

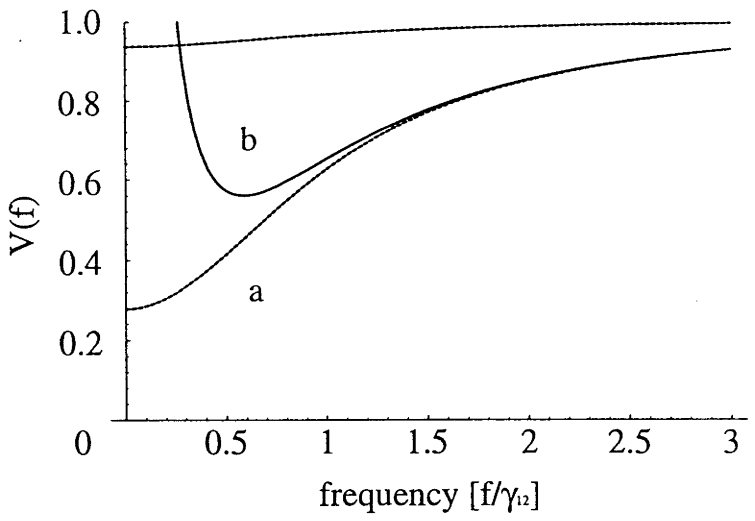

Figure 4.3: Spectra for passive SHG in the singly resonant case. The parameters have been optimised to squeeze the second harmonic, i.e. $\gamma_c \gg \gamma_b$, where $\gamma_b = .604\gamma_{12}$, $\gamma_c = 77.6\gamma_{12}$, scaled nonlinearity $\kappa = 120000$ (approximately 12600 s-1 unscaled), for a pump power of 120 mW. Please note that the frequency axis is scaled by $\gamma_{12} = 33.3$ MHz. a) dotted lines - spectra obtained using a coherent pump. The lower trace is the second harmonic, the upper trace the fundamental. b) unbroken line - second harmonic spectrum obtained using a laser pump. The squeezing is masked at low frequencies.

more strongly. In Fig. 4.4 we adjust only the second harmonic decay rate from the system of Fig. 4.3. The large squeezing dip at ω_{osc} is clearly evident. Note that the maximum squeezing for the laser pump case is nearly equal to the ideal case: the squeezing at high frequencies is much less affected by the pump noise.

While much of the behaviour discussed for the second harmonic will apply to the fundamental, the two modes are by no means identical. Experimentally it would be possible to build a doubler resonant only at the second harmonic, but in CW operation, unrealistically high fundamental pump powers are then required to drive the doubling process. A high finesse cavity for the fundamental light is employed to build up sufficient power. However as good squeezing of the fundamental requires that the fundamental cavity be lossier than that of the second harmonic $\gamma_b > \gamma_c$), a doubly resonant system is necessary. This is confirmed by the rather poor noise suppression of the fundamental light shown in Figs 4.3 & 4.4.

Spectra of the fundamental light from a doubly resonant passive doubler, for both coherent and laser pump, are shown in Figs 4.5a & b respectively. For the coherent pump the squeezing at zero frequency is modest (the maximum possible value is 2/3), however due to the strong interaction between the modes (despite the relative difference in loss rates, c.f. Fig. 4.3) there is a large oscillation that dips to nearly zero. Note that the fundamental spectra in this figure are for a cavity where the fundamental is strongly transmitted. The distinction is important when there is a noisy pump beam. In general the reflected beam consists of two components, the part that interacts with the cavity (the mode and impedance matched component) and the part that just reflects off of the cavity without interacting. This latter component contributes additional noise to the reflected beam that can mask the squeezing.

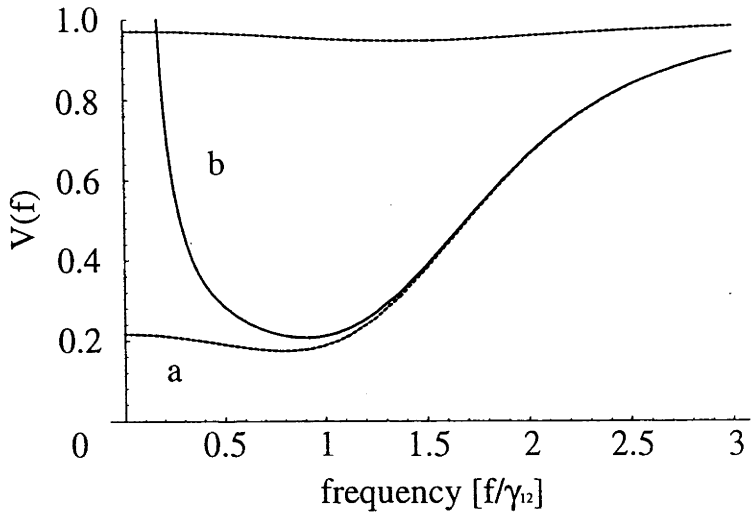

Figure 4.4: Spectra for passive SHG in the doubly resonant case. The parameters are optimised to squeeze the second harmonic, and are as for Fig. 4.3, except now $\gamma_c = 9.06\gamma_{12}$. a) dotted lines - spectra obtained using a coherent pump. The lower trace is the second harmonic, the upper trace the fundamental. Note the squeezing on the second harmonic is much improved with no increase in interaction strength or pump power. b) unbroken line - second harmonic spectrum obtained using a laser pump. Again the squeezing is masked at low frequencies.

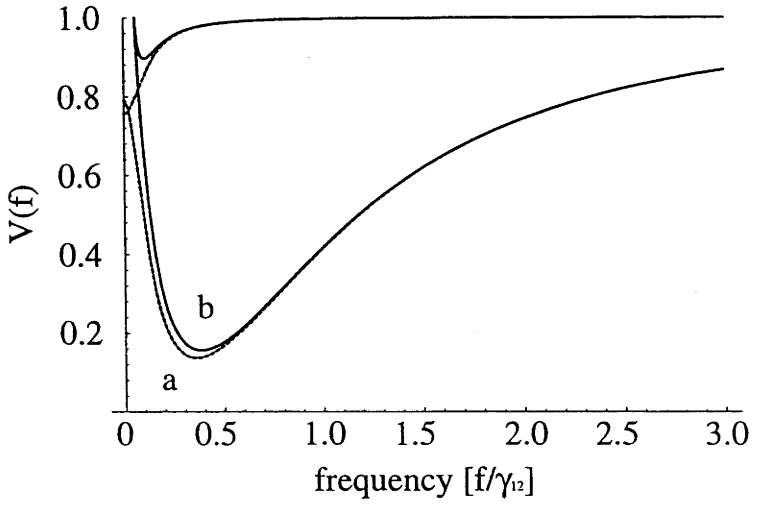

Figure 4.5: Spectra for passive SHG in the doubly resonant case. The parameters have been optimised to squeeze the fundamental, i.e. $\gamma_b > \gamma_c$, where $\gamma_b = 3.46\gamma_{12}$, $\gamma_c = .362\gamma_{12}$. The interaction and pump power are the same as for Figs 4.3 & 4.4. a) dotted lines - spectra obtained using a coherent pump. The lower trace is the fundamental, the upper trace the second harmonic. Note that the fundamental is squeezed well beyond the 2/3 limit of the singly resonant case. In the appropriate ideal case perfect squeezing is possible. b) unbroken lines - spectra obtained using a laser pump. Note the squeezing is destroyed at low frequencies. The lower trace is the fundamental, the second harmonic trace is above shot noise, and thus not visible on this plot.

The squeezing of the two modes behaves differently as the interaction is increased. In the second harmonic case the squeezing is optimised as the interaction is strengthened (i.e. κ is increased). This is not the case for the fundamental. At a given pump power the squeezing degrades for $\kappa \to \infty$. There is an optimum nonlinear interaction value: for sufficiently large interactions the squeezing is degraded at all detection frequencies. This can be understood via the following analogy. Consider the frequency doubler as a nonlinear beam splitter, with an incident fundamental beam split into, say, a transmitted fundamental beam and a reflected second harmonic beam. The incident beam is the fundamental field inside the doubler, and is strongly squeezed in direct proportion to κ. As κ is increased the squeezing on the incident fundamental increases and importantly, the "reflectivity" of the beamsplitter increases. Thus in the limit of infinite κ all the incident fundamental becomes second harmonic which is strongly squeezed. Conversely as κ is increased the fraction of incident fundamental that is transmitted (i.e. light remaining at the fundamental wavelength) becomes less and less, with a concomitant decrease in the squeezing.

4.3.2 Active SHG

For clarity we will first consider active SHG under the assumption that the atomic dephasing rate, γ_p, is zero (the next section explains why this is desirable). Consider the singly resonant limit, $\gamma_c \gg \gamma_a$. With a sufficiently high pump rate we obtain the spectra shown in Fig. 4.6. For both the fundamental and second harmonic modes the squeezing is maximum at zero frequency and then degrades with increasing detection frequency in a Lorentzian like manner excepting the region of excess noise due to the laser's resonant relaxation oscillation (RRO) [5]. Noise features present in the fundamental trace, both relaxation oscillation and squeezing are present on the second harmonic trace but amplified away from the quantum limit.

As we are using a laser model that can produce rate-matched squeezing [15] it is necessary to confirm that the SHG process is indeed the source of the noise suppression. This was checked by turning off the doubling process, i.e setting κ to zero, and by adjusting the pump rate such that the output power stays the same. We see a larger relaxation oscillation and no squeezing. The doubling process can significantly damp the relaxation oscillation: a thousandfold reduction is not unusual. By increasing the pump rate a small amount of squeezing at low detection frequencies can be created, which is due to rate matching. We conclude that the preeminent cause of the squeezing predicted in Fig. 4.6 is second harmonic generation and not rate matching.

Fig. 4.7 considers the doubly resonant case in the limit of very high pump rate. As was discussed in the previous section improved amplitude squeezing is expected due to the phase oscillation between the fundamental and second harmonic modes. However the changes to the noise spectra are dramatic compared to the passive case. The relaxation oscillation noise of both modes is suppressed, particularly that of the fundamental, and downshifted in frequency. Two regimes of squeezing become evident, that before and that after the relation oscillation; hereafter they are called the low and high frequency regimes, respectively. The second harmonic low frequency squeezing increases significantly and attains the maximum possible value of 1/2 at zero frequency. Likewise the high frequency squeezing is pushed very close to zero in a broad region that is much

[5] The RRO can be considered as an oscillation between photons stored in the lasing medium and photons stored in the laser mode.

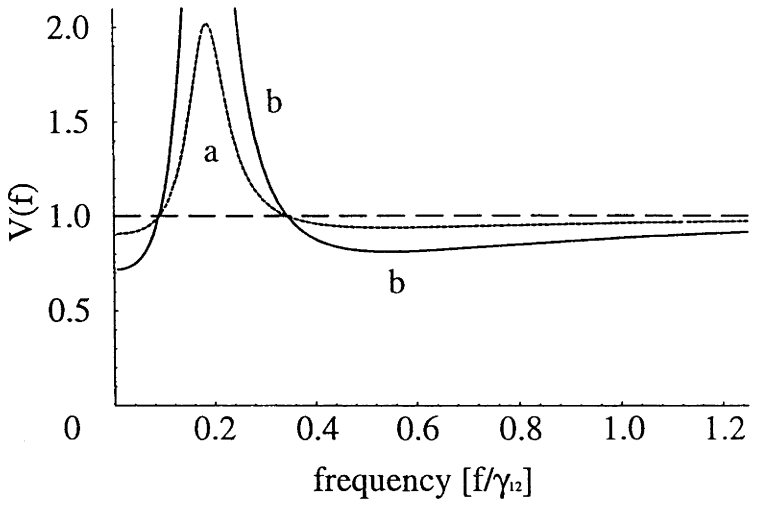

Figure 4.6: Spectra for active SHG in the singly resonant case. The parameters have been optimised to squeeze the second harmonic, i.e. $\gamma_c \gg \gamma_a$, where $\gamma_a = .6\gamma_{12}$, $\gamma_c = 36000\gamma_{12}$, scaled nonlinearity $\kappa = 50000$ (approximately 5220 s-1 unscaled), pump rate of $\Gamma = 8 \times 10^{-5}\gamma_{12}$ ($\Gamma_{thresh} = 4.08 \times 10^{-9}\gamma_{12}$) and dephasing rate, $\gamma_p = 0$. a) dotted line - fundamental spectrum. b) unbroken line - second harmonic spectrum. Note that noise features present on the fundamental, relaxation oscillation and squeezing both, are amplified away from the quantum limit.

larger than even the bandwidth of the second harmonic cavity. Both the high and the low frequency squeezing regimes have been separately described in previous works. We now understand the relationship between these regimes, and see that both are possible in the one model for the one set of parameters.

Consider, as in Fig. 4.8, an active doubler resonant at the second harmonic (the bad cavity limit for ν), $\gamma_a \gg \gamma_c$. A high pump rate is required simply to induce lasing. As the interaction is strong both the low and high squeezing regimes are evident (c.f. Fig. 4.6), however unlike the second harmonic case the noise features of the second harmonic are no longer amplified versions of those of the fundamental. The low frequency squeezing of the fundamental is less than that of the second harmonic; the high frequency squeezing is greater.

In the doubly resonant case, $\gamma_a > \gamma_c$, the low frequency squeezing tends to be buried under the relaxation oscillation - it is not robust compared to the second harmonic case. Although the high frequency squeezing survives, further consideration of this case is omitted for reasons explained in the next section.

4.3.3 Ugly reality: the effect of dephasing

Up to this point the atomic dephasing γ_p (the decay rate of the lasing coherence) was considered to be zero. In solid state systems, such as Nd:YAG, this is not even approximately true as there is a large dephasing value due to coupling between phonons of the crystal and the energy levels of the laser (or for gas lasers due to atomic and molecular collisions). What then is the effect of large γ_p?

In the passive case the output spectrum of the laser becomes noisier for large γ_p: the relaxation oscillation is down shifted in frequency, and it is amplified, even at the high frequencies in the very tail of the oscillation. The extra pump noise leads to a further

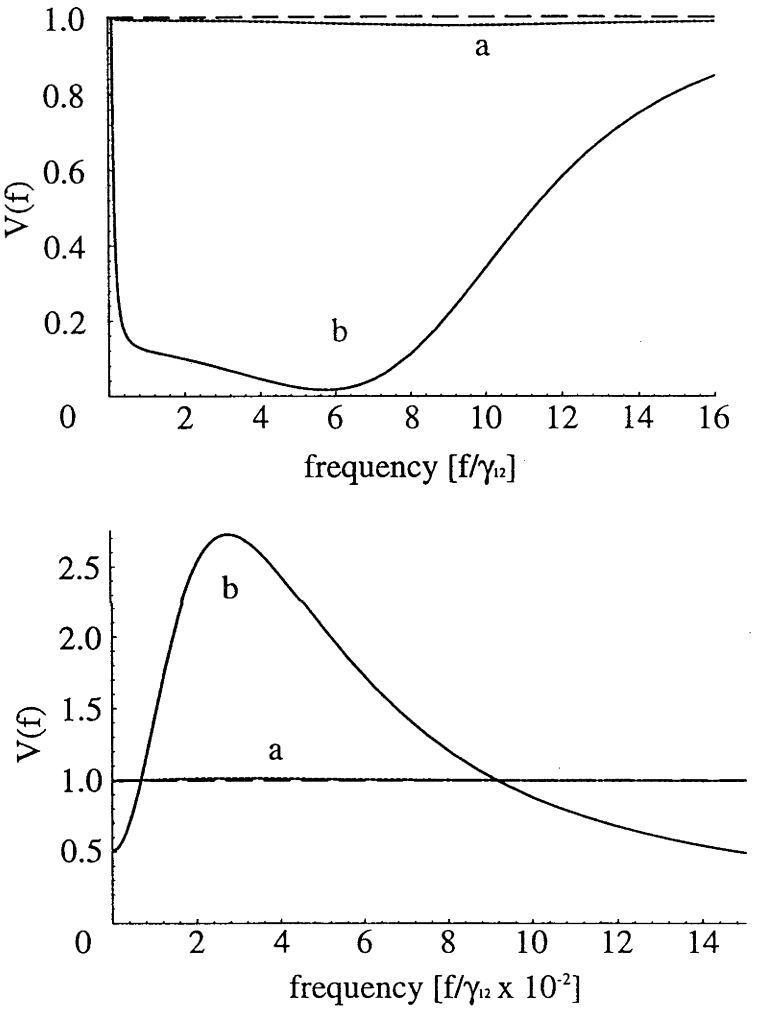

Figure 4.7: Spectra for active SHG in the doubly resonant case. There are two plots, covering different frequency ranges. The parameters have been optimised to squeeze the second harmonic and are as for Fig. 4.7 except now $\gamma_c = 36\gamma_{12}$. a) dotted line - fundamental spectrum b) unbroken line - second harmonic spectrum. Note the two regions of squeezing: low frequency, before the relaxation oscillation, with maximum squeezing of 0.5; high frequency, above the relaxation oscillation frequency with almost perfect squeezing.

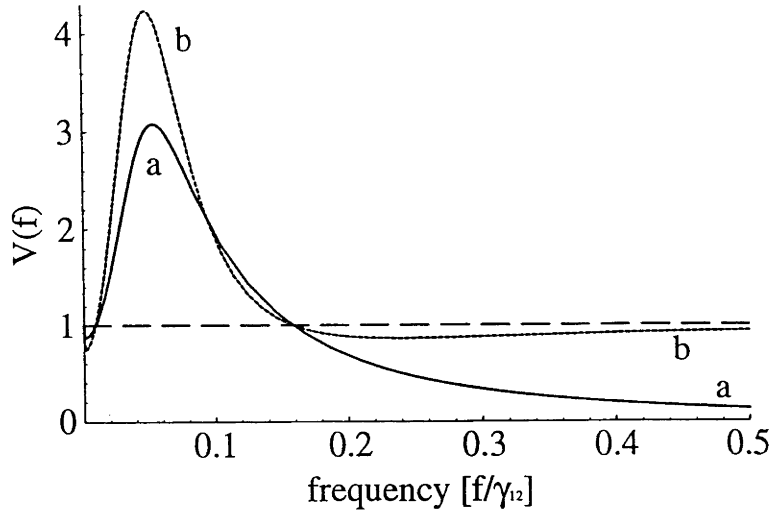

Figure 4.8: Spectra for active SHG in the doubly resonant case. The parameters have been optimised to squeeze the fundamental, i.e. $\gamma_a \gg \gamma_c$, where $\gamma_a = 3600\gamma_{12}$, $\gamma_c = .6\gamma_{12}$, $\kappa = 50000$, pump rate of $\Gamma = 3.99 \times 10^{-2}\gamma_{12}$ ($\Gamma_{thresh} = 2.92 \times 10^{-5}\gamma_{12}$) and dephasing rate, $\gamma_p = 0$. a) dotted line - fundamental spectrum. Note that both the relaxation oscillation and the squeezing at low frequencies of the fundamental is less than the second harmonic. b) unbroken line - second harmonic spectrum.

degradation of squeezing as the minimum point of the spectrum is reduced and moved up in frequency by a small amount. Overall the effect of large γ_p is minimal.

In the active case increasing γ_p is of notable effect. The laser threshold increases; the critical point threshold decreases, in some parameter regimes it is lower than the laser threshold and the system is consequently unstable; and considerable noise is introduced at frequencies below the dephasing value. The squeezing on the fundamental is particularly sensitive, with even low dephasing values, such as $\gamma_p = 0.5\gamma_a$, completely masking the squeezing. The squeezing of the second harmonic survives, albeit in a somewhat unlikely regime. This is illustrated in Fig. 4.9 where the singly resonant system of Fig. 4.7 is evaluated for dephasing values of $\gamma_p = 0$, $18\gamma_{12}$, and $35\gamma_{12}$; corresponding to $\gamma_p = 0$, $0.5\gamma_c$ and $0.97\gamma_c$. Note that the degradation of the low frequency squeezing is much less pronounced and that it does not visibly degrade between the latter two values of γ_p.

This behaviour is perhaps best considered as follows. Dephasing adds considerable phase noise inside the laser cavity, which is added directly to the fundamental and consequently transmitted to the second harmonic. The survival of the low frequency second harmonic amplitude squeezing reflects the fact that when using direct detection one only sees amplitude noise at zero frequency. However, at higher frequencies the cavities mixes in the internal phase noise. Thus the higher the dephasing rate, the narrower the region of squeezing, as the phase noise at a given frequency is stronger. Remembering that the parametric process also takes place in second harmonic generation, the phase noise on the second harmonic generates additional amplitude noise on the fundamental. As a consequence, none of the low frequency fundamental squeezing survives.

Contrast this with the passive case. Here the internal phase noise of the laser is not directly involved in the doubling process. The narrow output linewidth of the laser filters the phase noise considerably, consequently only a relatively small amount of excess noise is added to the pump.

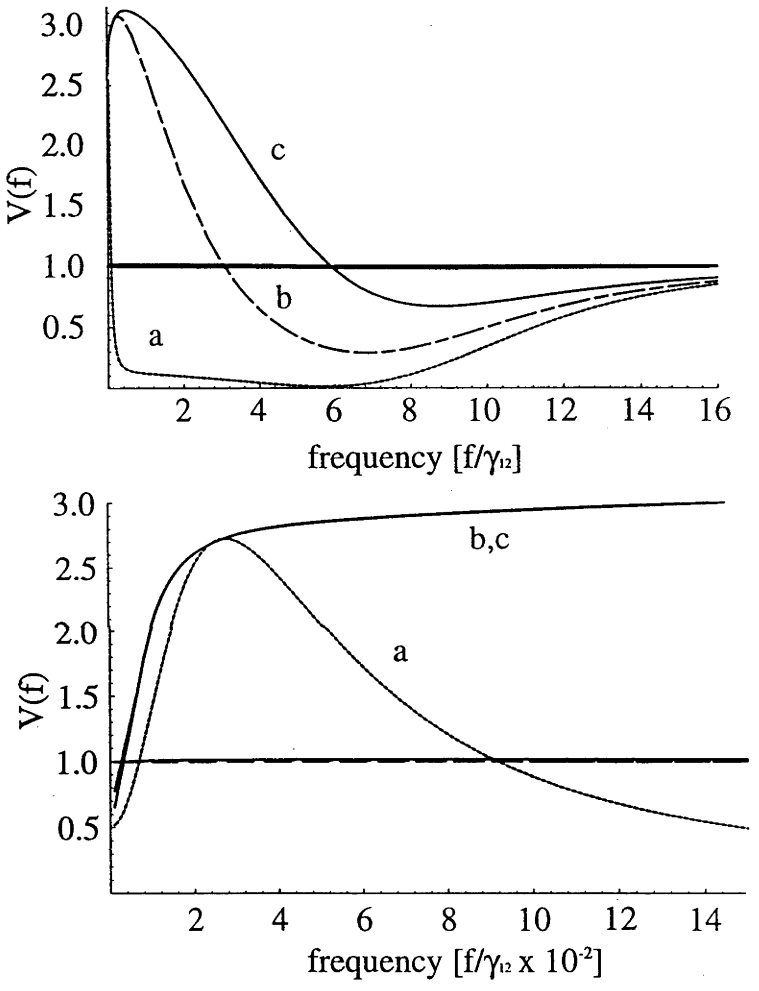

Figure 4.9: Spectra showing effect of non-zero dephasing on active SHG, squeezing optimised for second harmonic. Excepting the dephasing rates, other parameters are as for Fig. fig:SFDfig6. There are two plots, covering different frequency ranges. For a) - c) the significantly squeezed trace is the second harmonic. a) dotted lines - fundamental and second harmonic spectra for $\gamma_p = 0$. b) long-short lines - fundamental and second harmonic spectra for $\gamma_p = 18\gamma_{12}$. Note that both the low and high frequency squeezing is degraded. c) unbroken lines - fundamental and second harmonic spectra for $\gamma_p = 35\gamma_{12}$. Compared to b) the high frequency squeezing is further degraded while the low frequency squeezing is much less affected.

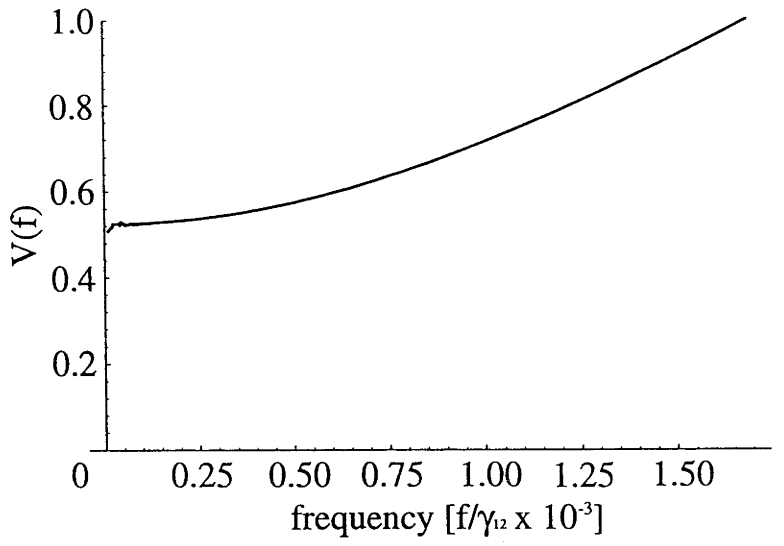

Figure 4.10: Demonstration that in the active case low frequency squeezing of the second harmonic is possible even with very high dephasing. The parameters are as for Fig. 4.7, except now $\gamma_p = 9000\gamma_{12}$ and pump rate $\Gamma = 1.8 \times 10^{-5}\gamma_{12}$. Note that our model does not include pump noise of the laser, which in real systems will totally mask this effect

It should be noted that the dephasing rate of Nd:YAG at room temperature is much higher than the values considered in Fig. 4.9: we approximate it for the moment by $\gamma_p = 9000\gamma_{12}$. At this value the high frequency squeezing in both the fundamental and second harmonic cases is destroyed, as classical noise is introduced below frequencies of $9000\gamma_{12}$ (300 GHz). To access this squeezing in the laboratory a way of reducing γ_p must be found, either through judicious choice of medium or cooling.

Theoretically the low frequency squeezing of the second harmonic persists even for this value of the dephasing. To illustrate this, consider the system discussed for Fig. 4.7 except with dephasing rate $\gamma_p = 9000\gamma_{12}$ and pump rate $\Gamma = 1.8 \times 10^{-5}\gamma_{12}$. This is illustrated in Fig. 4.10. Squeezing near the 50% limit occurs at zero frequency, but it degrades quickly with increasing detection frequency to the quantum limit (by 56kHz). It should be stressed that our laser model ignores both pump noise for the laser and thermal noise, which in real lasers raises the noise floor at low frequencies (10^5 times above quantum noise for a Lightwave Nd:YAG laser), completely masking this effect. In addition unrealistically high pump powers are required, or alternatively a system with an extremely low threshold.

4.4 SHGing and squeezing: it's better to be passive

Passive SHG is already used as a source of bright squeezed light. As modelled here, pump noise is a significant effect in passive SHG, and as reported in the next chapter, reducing the pump noise significantly improves the squeezing. Although active SHG is experimentally attractive, and other analyses have found the theoretical potential to be high, we find that active SHG is not a suitable source of squeezed light and is unlikely to be so in the foreseeable future. This is primarily due to the high dephasing values that are inherent in most laser systems: only if an active system with small dephasing could be found would active SHG be suitable for squeezing. Even then the issue of high pump

rates would need to be addressed. Unfortunately any of these options offers experimental complications at least as large as that of doubly resonant passive SHG, and with no extra benefit as regards the squeezing.

Chapter 4 bibliography

[1] P. D. Drummond, K. J. McNeil and D. F. Walls, Optica Acta, **28**, no. 2, p. 211, 1981. *Non-equilibrium transitions in sub/second harmonic generation*

[2] L. Mandel, Optics Communications, **42**, no. 6, p. 437, 1982. *Squeezing and photon antibunching in harmonic generation*

[3] G. J. Milburn and D. F. Walls, **27**, no. 1, p. 392, 1983. *Squeezed states and intensity fluctuations in degenerate parametric oscillation*

[4] L. A. Lugiato, G. Strini, and F. De Martini, Optics Letters, **8**, no. 5, p. 256, 1982. *Squeezed states in second harmonic generation*

[5] M. J. Collett and D. F. Walls, Physical Review A, **32**, no. 5, p. 2887, 1985. *Squeezing spectra for nonlinear optical systems*

[6] R. Paschotta, M. Collett, P. Kürz, K. Fiedler, H.-A. Bachor and J. Mlynek, Phys. Rev. Lett., **72**, p. 3807, 1994. *Bright squeezed light from a singly resonant frequency doubler*

[7] M. Dance, M. J. Collett and D. F. Walls, Physical Review Letters, **66**, no. 9, p. 1115, 1991. *Quantum-Nondemolition Measurements via Second-Harmonic Generation;*

M. Dance, M. J. Collett and D. F. Walls, Physical Review A, **48**, no. 2, p. 1532, 1993. *Quantum-nondemolition schemes to measure quadrature phases using intracavity harmonic generation.*

[8] A. Sizmann, R. Schack and A. Schenzle, Europhysics Letters, **13**, no. 2, p. 109, 1990. *Squeezed Light from a Self-Frequency-Doubling Laser;*

R. Schack, A. Sizmann, and A. Schenzle, Physical Review A, **43**, no. 11, p. 6303, 1991. *Squeezed light from a laser with an internal $\chi^{(2)}$-nonlinear element*

[9] D. F. Walls, M. J. Collett and A. S. Lane, Physical Review A, **42**, no. 7, p. 4366, 1990. *Amplitude-noise reduction in lasers with intracavity nonlinear elements*

[10] P. García-Fernández, L. A. Lugiato, F. J. Bermejo, and P. Galatola, Quantum Optics, **2**, p. 49, 1990. *Amplitude squeezing from second-harmonic generation in a laser cavity*

[11] R. B. Levien, M. J. Collett and D. F. Walls, Quantum Optics, **2**, p. 365, 1990. *Quantum noise reduction in lasers with intracavity second-harmonic generation and injected signal;*

M. J. Collett and R. B. Levien, Physical Review A, **43**, no. 9, p. 5068, 1991. *Two-photon-loss model of intracavity second-harmonic generation;*

R. B. Levien, M. J. Collett and D. F. Walls, Physical Review A, **47**, no. 3, p. 2324, 1993. *Second-harmonic generation inside a laser cavity with slowly decaying atoms*

[12] A. G. White, T. C. Ralph, and H.-A. Bachor, Journ. Opt. Soc. Am. B, **31**, no. 7, p. 1337, 1996. *Active versus passive squeezing by second-harmonic generation*

[13] T. A. B. Kennedy, T. B. Anderson, and D. F. Walls, Physical Review A, **40**, no. 3, p. 1385, 1989. *Effects of laser phase fluctuations on squeezing in intracavity second-harmonic generation*

[14] T. C. Ralph, M. S. Taubman, A. G. White, D. E. McClelland, and H.-A. Bachor, Opt. Lett., **20**, no. 11, p. 1316, 1995. *Squeezed light from second-harmonic generation: experiment versus theory*

[15] T. C. Ralph and C. M. Savage, Physical Review A, **44**, no. 11, p. 7809, 1991. *Squeezed light from a coherently pumped laser*

[16] W. H. Louisell, *Quantum Statistical Properties of Radiation*, Wiley-Interscience, New York, 1973;

H. Haken, *"Laser Theory", in Encyclopedia of Physics, Volume XXV/2c, Light and Matter Ic, Chief Editor S. Flügge*, First Edition, Springer-Verlag, Berlin, 1970

[17] G. J. Milburn, M. D. Levenson, R. M. Shelby, S. H. Perlmutter, R. G. DeVoe, and D. F. Walls, Journ. Opt. Soc. Am. B, **4**, no. 10, p. 1476, 1987. *Optical-fiber media for squeezed-state generation*

[18] P. Galatola, L. A. Lugiato, M. G. Porecca, P. Tombesi, and G. Leuchs, Optics Communications, **85**, p. 95, 1991. *??*

[19] H. J. Carmichael, Phys. Rev. Lett., **70**, p. 2273, 1993. *Quantum Trajectory Theory for Cascaded Open Systems*

[20] C. W. Gardiner, Phys. Rev. Lett., **70**, p. 2269, 1993.

[21] P. D. Drummond and D. F. Walls, Physical Review A, **23**, no. 5, p. 2563, 1981. *Quantum theory of optical bistability. II. Atomic fluorescence in high Q cavity*

[22] C. W. Gardiner and M. J. Collett, Physical Review A, **31**, p. 3761, 1985. *Input and output in damped quantum systems: Quantum stochastic differential equations and the master equation*

[23] As the system is driven harder, this becomes a period doubling route to chaos. That is as the power is increased the self-pulsing is period-2, then period-4, then period-8, and so, until it is totally chaotic [24].

[24] C. M. Savage and D. F. Walls, Optica Acta, **30**, no. 5, p. 557, 1983. *Optical chaos in second-harmonic generation*

Chapter 4 appendix: drift and diffusion matrices

For the passive case the drift, A, and diffusion, D, matrices are respectively:

$$A =$$

$$\begin{bmatrix}
\gamma_a & 0 & 0 & 0 & 0 & 0 & -g_{23} & 0 & 0 & 0 \\
0 & \gamma_a & 0 & 0 & 0 & 0 & 0 & 0 & 0 & -g_{23} \\
2\sqrt{\gamma_a\gamma_{b1}} & 0 & \gamma_b & -\kappa c & -\kappa b^* & 0 & 0 & 0 & 0 & 0 \\
0 & 2\sqrt{\gamma_a\gamma_{b1}} & -\kappa c^* & \gamma_b & -\kappa b & 0 & 0 & 0 & 0 & \\
0 & 0 & \kappa b & 0 & \gamma_c & 0 & 0 & 0 & 0 & 0 \\
0 & 0 & 0 & \kappa b^* & 0 & \gamma_c & 0 & 0 & 0 & 0 \\
J^* & 0 & 0 & 0 & 0 & 0 & \gamma^p_{tot} & 0 & g_{23}a & 0 \\
g_{23}J_{23} & g_{23}J_{23} & 0 & 0 & 0 & 0 & g_{23}a & \Gamma+\gamma_{23}+\gamma_{13} & \Gamma & g_{23}a \\
g_{23}J_{23} & g_{23}J_{23} & 0 & 0 & 0 & 0 & g_{23}a & -\gamma_{23}-\gamma_{13} & \gamma_{12} & g_{23}a \\
0 & J^* & 0 & 0 & 0 & 0 & 0 & 0 & g_{23}a & \gamma^p_{tot}
\end{bmatrix}$$

where $\gamma^p_{tot} = (\gamma_{13}+\gamma_{23}+\gamma_{12}+2\gamma_p)/2$ and $J^* = -g_{23}(J_3 - J_2)$. And:

$$D =$$

$$\begin{bmatrix}
0 & 0 & 0 & 0 & 0 & 0 & 0 & 0 & 0 & 0 \\
0 & 0 & 0 & 0 & 0 & 0 & 0 & 0 & 0 & 0 \\
0 & 0 & \kappa c & 0 & 0 & 0 & 0 & 0 & 0 & 0 \\
0 & 0 & 0 & \kappa c^* & 0 & 0 & 0 & 0 & 0 & 0 \\
0 & 0 & 0 & 0 & 0 & 0 & 0 & 0 & 0 & 0 \\
0 & 0 & 0 & 0 & 0 & 0 & 0 & 0 & 0 & 0 \\
0 & 0 & 0 & 0 & 0 & 0 & g_{23}2J_{23}a & 0 & -\gamma_{12}J_{23} & \Gamma J_1 + (1+2\gamma_p)J_3 \\
0 & 0 & 0 & 0 & 0 & 0 & 0 & \gamma_{coh1} & -g_{23}2J_{23}a - \gamma_{23}J_3 & 0 \\
0 & 0 & 0 & 0 & 0 & 0 & 0 & 0 & \gamma_{coh2} & 0 \\
0 & 0 & 0 & 0 & 0 & 0 & 0 & 0 & -\gamma_{12}J_{23} & g_{23}2J_{23}a
\end{bmatrix}$$

where $\gamma_{coh1} = -g_{23}2J_{23}a + \gamma_{23}J_3 + \Gamma J_1 + \gamma_{13}J_3$ and $\gamma_{coh2} = -g_{23}2J_{23}a + \gamma_{12}J_2 + \gamma_{23}J_3$. For the active case the drift, A, and diffusion, D, matrices are respectively:

$$A =$$

$$\begin{bmatrix}
\gamma_b & -\kappa c^* & -\kappa a & 0 & -g_{23} & 0 & 0 & 0 \\
-\kappa c & \gamma_b & 0 & -\kappa a & 0 & 0 & 0 & -g_{23} \\
\kappa a & 0 & \gamma_c & 0 & 0 & 0 & 0 & 0 \\
0 & \kappa a & 0 & \gamma_c & 0 & 0 & 0 & 0 \\
-g_{23}(J_3 - J_2) & 0 & 0 & 0 & \gamma^p_{tot} & 0 & g_{23}a & 0 \\
g_{23}J_{23} & g_{23}J_{23} & 0 & 0 & g_{23}a & \Gamma + \gamma_{12} & -\Gamma & g_{23}a \\
g_{23}J_{23} & g_{23}J_{23} & 0 & 0 & g_{23}a & -\gamma_{23} - \gamma_{13} & \gamma_{12} & g_{23}a \\
0 & -g_{23}(J_3 - J_2) & 0 & 0 & 0 & -g_{23}a & 0 & \gamma^p_{tot}
\end{bmatrix}$$

and:

$$D =$$

$$\begin{bmatrix}
\kappa c & 0 & 0 & 0 & 0 & 0 & 0 & 0 \\
0 & \kappa c & 0 & 0 & 0 & 0 & 0 & 0 \\
0 & 0 & 0 & 0 & 0 & 0 & 0 & 0 \\
0 & 0 & 0 & 0 & 0 & 0 & 0 & 0 \\
0 & 0 & 0 & 0 & g_{23}2J_{23}a & 0 & 0 & \Gamma J_1 + \gamma_{12}J_3 + 2\gamma_p J_3 \\
0 & 0 & 0 & 0 & 0 & 0 & -g_{23}2J_{23}a - \gamma_{23}J_3 & 0 \\
0 & 0 & 0 & 0 & -\gamma_{12}J_{23} & 0 & \gamma_{coh1} & -\gamma_{12}J_{23} \\
0 & 0 & 0 & 0 & 0 & 0 & 0 & g_{23}2J_{23}a
\end{bmatrix}$$

Chapter 5

Experimental design

Nothing is impossible to the man who hasn't got to do it himself.

Anon

Figure 5.1 shows the core experimental layout that was used to obtain the results in this thesis. In this chapter we discuss in detail the design, implementation and characteristics of each stage of the experiment, proceeding componentwise from the laser to the balanced detectors.

5.1 The laser

In the past 5 years the nonplanar ring oscillator (NPRO) Nd:YAG laser has become the pump laser of choice for frequency conversion experiments. Its chief advantages over competing technologies are its high stability, easy frequency tunability, narrow linewidth operation, and well collimated output.

The Nd:YAG NPRO lasers used in the experiments in this thesis were all members of the Lightwave Laser 122 series: at the Australian National University the 200 mW (122-1064-300-F, serial no: 207); at the Universität Konstanz the 300 mW (122-1064-200-F, serial no: 127) and the 500 mW (122-1064-500). The laser frequency in the 122 series can be tuned via two ports: the *slow* port, where the laser crystal temperature is changed; and the *fast* port, where a piezo placed on top of the laser crystal is tuned so that it compresses the crystal.

When the crystal temperature is increased both the physical cavity length and the refractive index increase: and so the laser frequency decreases. As the slow port is thermal it responds best to driving frequencies under the order of a Hertz. The slow port range and gain is considerable, over the temperature range 20–50 °C the average tuning coefficient is $\simeq -1$GHz/°C [1]. The laser itself is not stable over this entire range, at some temperatures it undergoes a mode hop and two modes coexist, often with some instability caused by their competition for gain. Table 5.1 shows the stable single mode regimes for the ANU laser: within the stable temperature range the tuning coefficient of the laser is $\simeq -3.1$GHz/°C [1] or $\simeq +1.20$GHz/V. The slow port can be linearly driven over a range of ± 50V, beyond this the response is nonlinear.

The fast port of the laser allows considerably quicker frequency scanning, but at the expense of range: Lightwave cites a range of $>$ 30MHz for frequencies below 100kHz with a tuning coefficient of $>$ 1MHz/V. In 1994 Cantatore et. al [2] showed that it was possible to phase and amplitude modulate the laser light using the fast port. Cantatore et. al found that at frequencies between 0.5MHz and 1MHz the laser output was both phase and amplitude modulated: at certain frequencies, believed to correspond to mechanical resonances of the piezo/crystal assembly, the residual amplitude modulation was reduced by an order of magnitude and the modulation became chiefly phase. This is an incredibly useful phenomenon, as it allows phase modulation of the laser for locking purposes without the addition of a phase modulator (which is to be avoided from both

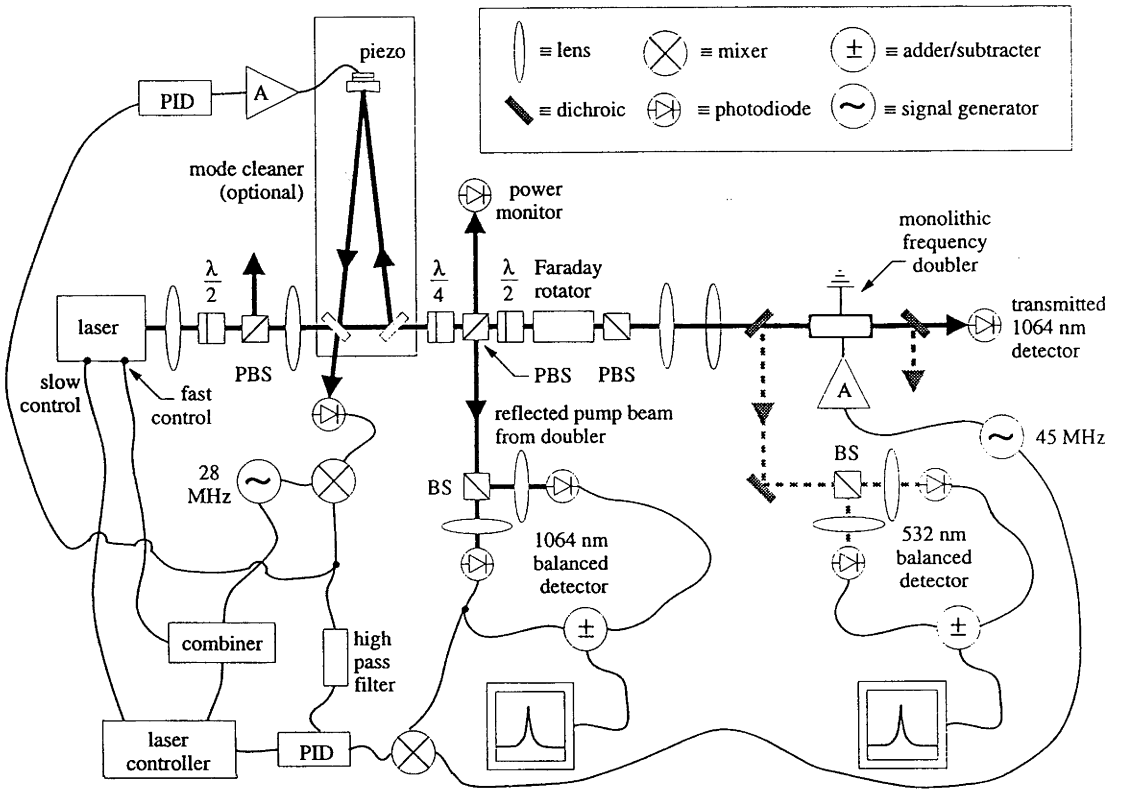

Figure 5.1: Core experimental layout. The light source is a p-polarised Nd:YAG monolithic ring laser (Lightwave 122) producing 200–500 mW of linearly polarised light at 1064 nm. The output of the laser is passed through a variable attenuator (a half-wave plate ($\frac{\lambda}{2}$) and polarising beamsplitter assembly) and is then incident on a three mirror, mode cleaning, ring cavity of linewidth 800 kHz. Locking of the mode cleaner is effected using a 27.650 MHz frequency modulation applied directly to the laser, and an error signal derived from the reflected light from the input mirror of the mode cleaner. At low frequencies, < 500 Hz, the mode cleaner cavity length is made to track the laser frequency via a piezo on the end mirror, while at high frequencies, > 500 Hz, the laser frequency is made to track the mode cleaner. The output of the mode cleaner is slightly elliptically polarised, this is corrected back to linear polarisation using a zero order quarter wave plate ($\frac{\lambda}{2}$). The light then passes through a a Faraday isolator: this prevents light from returning to the laser, and allows easy access to the retroreflected beam. The light is then incident on the frequency doubling cavity. Locking of the monolithic cavity is effected by placing a 45.167 MHz frequency modulation directly across the xy faces of the MgO:$LiNbO_3$ doubling cavity. The error signal is derived from the reflected beam and is used to lock the laser at both low (< 500 Hz) and high frequencies to the mode of the monolith. The output second harmonic at 532 nm is s-polarised and separated from the 1064 nm pump via two dichroic beam splitters. It is incident on two angled FND-100 photodetectors with retroreflectors, giving quantum efficiency $65\% \pm 5\%$. The outputs are added and subtracted and sent to the spectrum analyser. BS = beamsplitter; PBS = polarising beamsplitter; PID = proportional/integrator/differentiator; A = amplifier; $\lambda/2$ = zero order half wave plate; $\lambda/4$ = zero order quarter wave plate.

Table 5.1: Single mode temperature regimes for ANU Lightwave 122.

NPRO temperature [°C]	Stable interval [°C]
20.0 - 21.6	1.6
22.2 - 26.9	4.7
27.7 - 32.3	4.6
33.1 - 37.5	4.4
38.2 - 42.4	4.2
43.1 - 47.0	3.9
47.6 - 50.0	2.4

loss and mode match considerations). In the course of our experiments we found that this behaviour extends to well above 80 MHz, with the modulation intensity reducing with driving frequency. For the majority of the ANU experiments the laser was phase modulated at 27.650MHz (this accuracy was necessary, a change in the last decimal place leading to considerable amplitude modulation). The one caveat concerning modulation at such high frequencies is that care must be taken not to feed too much power into the piezo: Lightwave advises that powers above 1 W couple too much heat into the laser crystal and can cause permanent laser damage.

The fast port can be a source of considerable noise at low frequencies (i.e. below the resonant relaxation oscillation). If the fast port is unterminated, or terminated by a 50Ω cable, then a series of large (10's of dB above the noise floor) spikes are observed on both the amplitude and phase of the laser light. The spikes appear to be pickup-driven resonances of the piezo: if the port is terminated by a ground or a 50Ω load, the spikes are severely reduced. Lightwave recommends terminating the fast port when not in use. Even when in use, we have found it good practice to pass all signals to the fast port through a 10dB attenuator, which provides sufficient loading to damp the spikes.

As the laser temperature is increased the laser power decreases by a few percent. As power limitations were initially a concern in most of our experiments, the lasers were run as a matter of preference at low temperatures. As Table 5.1 shows, this also gives the broadest temperature range of single mode operation. The decrease in power is basically linear, however occasionally there appeared to be a slight sinusoidal modulation around the line of best fit. This may be due to the laser polarisation being slightly temperature dependent, the sinusoidal variation being due to the analysing effect of the internal quarter- and half-wave plate and linear polariser assembly of the Lightwave.

A rare, but known, failure mode was observed with the Konstanz 300 mW laser. For just over half the temperature tuning range the laser ran dual, instead of single, mode. Closer inspection showed that the secondary, lesser power, mode was at a frequency 2.7nm lower than the main mode. As Fig. 5.2 shows, the secondary mode could be up to 16% of the power of the primary mode, as its power was reduced by increasing the temperature the primary mode increased in power by a few percent, contrary to the normal trend. The secondary mode was observed to go through its own mode hops independently of the primary mode. According to Tom Kane of Lightwave [3], the secondary mode is the 1061 nm line of Nd:YAG. The line can only be avoided by running the laser above 35°C, or if the full tuning range of the laser is required, replacing the laser crystal.

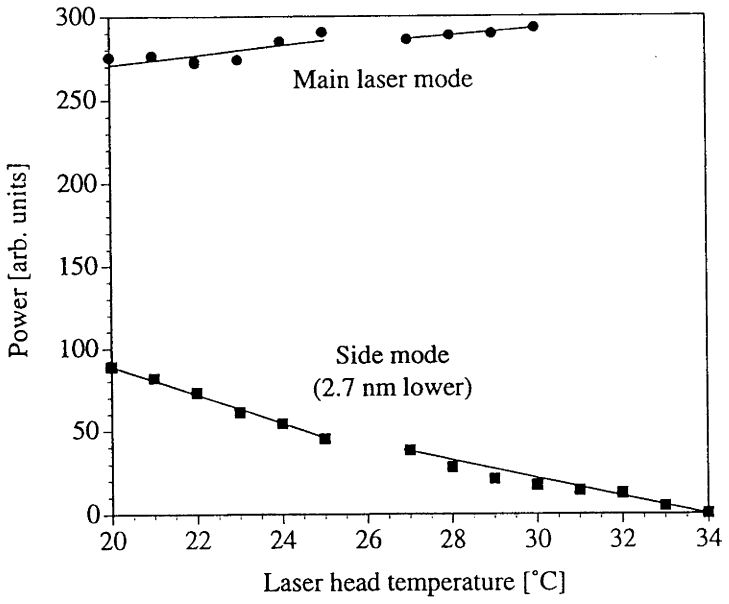

Figure 5.2: Power of primary and secondary lasing modes versus temperature for the Lightwave 122 300mW laser. Note that by 35°C the secondary mode has disappeared. The presence of this mode effectively halves the tuning range of the laser.

5.2 The modecleaner

The normal application of mode cleaning cavities in quantum optics is to provide a spatially and noise cleaned beam for the local oscillator beam in a homodyne detector. This requires very narrow linewidths, and, as the signal field is a squeezed vacuum or very weak squeezed bright field [5], output powers of only a few mW. This is achieved by designing for as high a finesse as possible, using high reflectance coupling mirrors and/or lengthy perimeters. Our application is further constrained by requiring transmission of high powers, in excess of 100 mW. This limits the modecleaner finesse, as the intracavity powers rapidly approach the damage threshold of many commercially available mirrors.

We settled on a three mirror, triangular ring cavity design. The mirrors were custom built by A. G. Thompson & Co., Adelaide, South Australia to the following specifications: input and output couplers reflectivity 98% (loss > .02%), third mirror high reflector, i.e reflectivity of >99.9%. The cavity perimeter was 2.450m ±5mm, the free spectral range (FSR) of the cavity was thus FSR= $c_0/(np) = 1/\tau = 122$ MHz. From Siegman [7] the finesse of an optical cavity is:

$$\mathcal{F} = \frac{\pi\sqrt{g_{rt}}}{1 - g_{rt}} \tag{5.1}$$

where:

$$g_{rt} = 1 - \sqrt{R_1 R_2 (R_3 \ldots) R_{loss}} = R_{tot} \tag{5.2}$$

where R_i & T_i are the reflectivity and transmittivity of mirror i, respectively; R_{loss} is the fraction of absorbed power; and R_{tot} is the total reflectivity of the cavity. It is related to the total decay rate, γ_{tot} by (recalling eqn 2.22):

$$\gamma_{tot} = \frac{1 - \sqrt{R_{tot}}}{\tau} = \frac{1 - g_{rt}}{\tau} \tag{5.3}$$

The bandwidth of the cavity is related to the finesse by:

$$\mathcal{F} \simeq \frac{\mathrm{FSR}}{\mathrm{FWHM}} \tag{5.4}$$

where FWHM is the cavity bandwidth or linewidth (the terms are often, and confusingly, used interchangeably). Alternatively, the bandwidth is related to the cavity decay rate by:

$$\mathrm{FWHM} = \frac{\gamma_{tot}}{\pi\sqrt{g_{rt}}} \simeq \frac{\gamma_{tot}}{\pi} \tag{5.5}$$

The circulating power is [8]:

$$\frac{P^{refl}}{P^{in}} = \frac{T_1\mathcal{F}^2}{\pi^2 g_{rt}} \tag{5.6}$$

For the specified reflectivities the figures for predicted finesse and circulating power gain are 138 and 36, respectively. As discussed in the next chapter, the high circulating power traps dust in the cavity beams, and eventually deposits this dust onto the cavity mirrors, increasing the cavity loss. The predicted cavity bandwidth is $\approx$ 800 kHz; i.e the output is reduced by 3 dB (factor of 2) at $\approx$ 400 kHz. As the RRO of the laser (resonant relaxation oscillation, also see next chapter) is at 542 kHZ, this should provide significant noise filtering. As discussed in Chapter 6, linewidths narrower than this do not significantly increase the final observed squeezing, but would make the cavity much harder to lock. The transmitted and reflected powers are given by [7]:

$$\begin{aligned} \frac{P^{refl}}{P^{in}} &= \frac{1}{R_1}\frac{(R_1 - g_{rt})^2}{(1 - g_{rt})^2} \\ \frac{P^{trans}}{P^{in}} &= \frac{T_1 T_2}{(1 - g_{rt})^2} \end{aligned} \tag{5.7}$$

For the specified reflectivities and absorption we predict that 1.2% of the power will be reflected and 64% will be transmitted, the rest is absorbed (c.f. Chapter 6). Thus in the best case the modecleaner will attenuate the 200 mW laser beam to 128 mW. This is still adequate power for our experiment. Note that the cavity can be fully characterised by direct measurement of just five experimental parameters: the cavity perimeter, cavity linewidth, and incident, reflected and transmitted powers.

5.3 Up the optical path

Optical loss is a particularly critical concern in squeezing experiments. Loss in the pumping path degrades the optical power necessary to drive the nonlinear effect, which reduces the maximum generated squeezing; loss in the detection arm introduces uncorrelated noise (from the vacuum) which quickly reduces the maximum observed squeezing. Accordingly all components in the experiment were chosen on the basis of low loss. The focussing lenses were either V-line coated at the appropriate wavelength or broadband AR coated in the suitable wavelength range, with loss typically $< 0.1\%$. For the infrared, the original steering mirrors were quartered 2" aluminium coated Newport mirrors. However these were relatively lossy (R$<$ 95 – 96%); and were eventually replaced by a combination of New Focus 1064nm dielectric coated mirrors (5104, R$>$ 99%) and Rimkevicius 1064nm dielectric coated mirrors (R$>$ 98%). All optics used in the ANU experiments are listed in Table 5.2

Table 5.2: Optics used in experiment.

Description	Wavelength [nm]	Manufacturer	Model No.	Comments
$\lambda/2$ plate zero order	1064	Newport	10RP02-34	loss $< 0.2\%$ 1" round
$\lambda/4$ plate zero order	1064	Newport	10RP04-34	loss $< 0.2\%$ 1" round
$\lambda/4$ plate zero order	532	Newport	10RP04-16	loss $< 0.2\%$ 1" round
non-polarising beam splitter (NPBS)	1064	Newport	05BC16NP.9	$50/50\pm5\%$ 1/2" round
polarising beam splitter (PBS)	1064	Newport	05BC16PC.9	loss $< 2\%$ 1/2" round
non-polarising beam splitter (NPBS)	532	Newport	05BC16NP.3	$50/50\pm5\%$ 1/2" round
polarising beam splitter (PBS)	532	Newport	05BC16PC.3	loss $< 2\%$ 1/2" round
dichroic (long wave pass filter)	1064 /532	Newport	03BDL001	losses $< 0.1, < 0.2\%$ 1" round
Aluminium steering mirror	BBIR	Newport	20D10ER.2	loss $\simeq 4-5\%$ 2" round
dielectric steering mirror	1064	New Focus	5104	loss $< 1\%$ 1" round
dielectric steering mirror	1064	Rimkevicius	custom	loss $< 2\%$ 1" square
dielectric steering mirror	532	Rimkevicius	custom	loss $< 2\%$ 1" square
assorted lenses plano-convex	1064 /532	Newport	KPXxxxAR.yy	loss $< 0.2\%$ 1",2" round

Fig. 5.1 is conceptually correct, but does not show the actual physical layout of the experiment. To fit the experiment into the available table space, the optical path was folded through 90° just before the Faraday isolator. The large angle reflection from the folding mirror caused the beam to become elliptically polarised (as did, to a different degree, transmission through the modecleaner); the $\lambda/4$ plate was used to rotate the beam back to linear polarisation so that the beam propagated through the Faraday isolator without additional loss.

Initially a commercial Faraday isolator (OFR IO-2-YAG, serial #:8043) was utilised. However due to its small aperture (2mm) and the relatively large beam diameter it was found to attenuate the beam by up to 30%. At ANU we constructed our own isolator, using Newport polarising beam splitters (see Table 5.2) and a Faraday rotator (aperture 10mm) constructed for ANU by Dr Anatoly Masalov of the Lebedev Physical Institute, Moscow, Russia. The Faraday isolator assembly functions as shown in Fig. 5.3: the polarisation of the light is shown above the incident beam and below the reflected beam. The incident, horizontally polarised beam, passes unchanged through the first polarising beam splitter (PBS); is rotated 45° by the $\lambda/2$ plate; is rotated back to horizontal by

the Faraday rotator; passes unchanged through the second PBS and is then incident on the reflecting surface, be it monolith or mirror. The horizontally polarised component of the reflected beam again passes unchanged through the second PBS (the rest is reflected out); is rotated $-45°$ by the Faraday rotator; and hence rotated to the vertical by the $\lambda/2$ plate and then reflected perpendicular to the incident beam path by the first PBS. If the reflecting mirror or cavity does not alter the polarisation then all of the reflected light exits through the port marked "out" (the second PBS is to increase the overall isolation of the Faraday isolator). At Konstanz, we borrowed a Gsänger Faraday Isolator (FR 1065/8, aperture 8mm) from Gsänger Optoelectronik Gmbh: this had similar performance to the ANU isolator. Note that as only the power and noise from the "in" port is incident on the reflecting surface, this is a suitable technique for coupling squeezed vacuum into the dark port of interferometers, which is of particular interest in gravity wave interferometry.

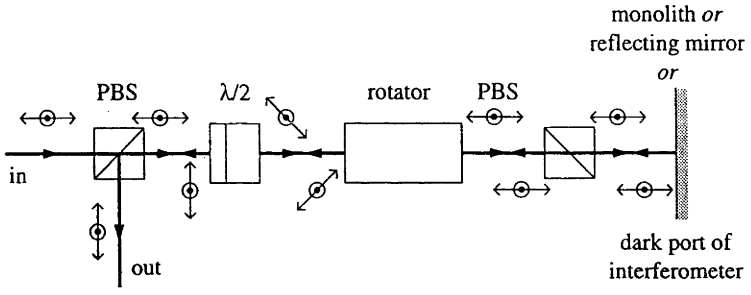

Figure 5.3: Operation of a Faraday isolator. The polarisation of the beam is shown above the incident beam, and below the reflected beam. If the mirror at the right does not affect polarisation, then all the light that enters the "in" port exits via the "out" port. Note that only the noise of the "in" port is coupled into the reflecting mirror.

The power coupled to the monolithic cavity is also reduced by nonperfect modematch and alignment. Modematching was optimised using two lenses mounted on Newport xyz mounts; alignment was optimised using a custom built beamsteerer. A beamsteerer consists of two mirrors fixed to the one substrate. If the substrate is rotated horizontally or vertically then the output beam is displaced horizontally or vertically; if one mirror is tilted horizontally or vertically with respect to the other then the output beam angle is altered horizontally or vertically. The beamsteerer thus allows separate control of the 4 degrees of freedom necessary to align the cavity. We found that using the beamsteerer it was possible to align a cavity very quickly (less than 10 minutes) compared with traditional alignment procedures.

5.4 Designing the SHG cavity

5.4.1 Types of cavity

Fig. 5.4 shows the three basic styles of nonlinear optical cavity: external mirror, hemilithic, and monolithic (these styles can be either standing wave or ring). In the external mirror design the majority of cavity reflections are external to the nonlinear medium. The intracavity loss is high due to the two air/crystal interfaces. However it is advantageous in doubly resonant SHG as it allows both mirrors to be scanned, so that the fundamental and second harmonic modes can be independently locked. The increased dispersion also

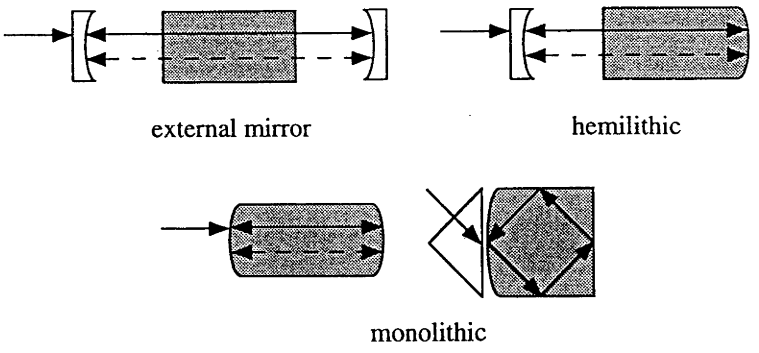

Figure 5.4: The three basic styles of nonlinear optical cavity. *external mirror* most cavity reflections external to nonlinear crystal. *hemilithic* one cavity reflection external to nonlinear crystal. *monolithic* all cavity reflections internal to nonlinear crystal.

acts to suppress TROPO, which allows greater SH squeezing ([6], see Chapter 7.) The hemilithic design (*hemilith*, lit. "half-a-piece") is a good compromise: it halves the number of intracavity surfaces and thus the intracavity loss but it still leaves free an external mirror that can be scanned for locking purposes. The monolithic design (*monolith*, lit. "one piece") avoids loss due to intracavity surfaces (the mode is confined totally within the crystal) but at the expense of losing a locking degree of freedom. The laser frequency can be locked to the cavity resonance but, due to practical effects that are explained later, the cavity length cannot be adjusted so that the cavity resonance matches the laser frequency. Combinations of the three basic styles are possible, for example a hemi-monolith, where the fundamental is resonated solely in a monolith and the second harmonic is resonated between the external mirror and end reflector of the monolith.

Loss is critical in SHG, as the maximum conversion efficiency, η_{nl} is equal to the outcoupling ratio, $\eta_{nl} = \gamma_1^c/\gamma_1 \approx T_1/T_{tot}$. Loss directly increases the total decay rate, γ_1, and thus reduces the maximum conversion efficiency. The outcoupling decay rate, γ_1^c, can be increased accordingly, but this in turn shifts the pump power required to reach the maximum conversion efficiency (see eqn 2.42). If designing a doubler purely as a source of SH (for example to pump an OPO), the best design approach is to have as large an outcoupler as possible, with the point of maximum conversion efficiency, $P_1^{max\ conv}$, just under the maximum available power at the fundamental. It is not wise to have $P_1^{max\ conv}$ higher than the maximum available pump power as the slope of the conversion efficiency is quite steep up to this point. Conversely, there is no particular advantage to pumping at powers much greater than $P_1^{max\ conv}$ as above it the conversion efficiency slowly degrades, and the system becomes susceptible to TROPO (see Chapter 7). For the complementary process, OPO, the point of maximum conversion efficiency $P_1^{max\ conv}$ is the threshold power, P_3^{thr}. A cavity designed to the above criteria is very suitable for the production of vacuum squeezing by OPO: near threshold the squeezing is near perfect and the high escape efficiency ensures that the majority of the squeezing is detected.

The design criteria are different for the generation of good SH squeezing. At the point of maximum conversion efficiency, regardless of what power this actually is, the second harmonic is squeezed by 3 dB (see next chapter). It is plainly advantageous to have this at low, easily detected, optical powers. The cavity should be designed so that $P_1^{max\ conv}$ is relatively low with respect to the maximum pump power. This enables the cavity to be driven far above $P_1^{max\ conv}$, which is the strong squeezing regime. The cavity should also be designed with dispersive elements to suppress TROPO, which degrades the SH

squeezing (see Chapter 7). At the start of this thesis, the neither QROPO or TROPO had been observed, and the latter point was not appreciated. Further the state of the art material technology at the time could not reliably produce high nonlinearity/low loss materials, so low loss was the overwhelming design criterion – the monolithic cavity style was chosen.

5.4.2 Monolith design

There are several forms of monolithic, or internal mirror, cavities. The oldest is the whispering gallery resonator [9], where typically the light is confined by a infinite series of total internal reflections (TIR's) in a sphere. WGM's have been investigated for a number of applications in the past 30 years, including lasing (in dye microdroplets [10], and Nd:YAG spheres [11]) and as high Q optical cavities (Q's in excess of 10^8 have been reported [12, 13]). Their chief disadvantages are small size (and hence high sensitivity to mechanical vibration) and highly elliptical output modes (Bessel as opposed to Gaussian modes). As the technology for polishing small perovskite (the structure of MgO:LN) spheres had not been perfected at the time (and still has not) this design option was not pursued.

There are three methods to form a mirror in a monolithic resonator: total internal reflection, frustrated total internal reflection (FTIR), and dielectric coating of a surface. These three methods can be combined as required and over the past decade most of these have been explored at Stanford University. In the late 80's Kozlovsky et. al. demonstrated singly resonant SHG in a dielectric mirror, standing wave monolith [14] and in a combined TIR/dielectric mirror, travelling wave monolith [15]. S. Schiller et. al. demonstrated doubly resonant SHG and QROPO (see Chapter 7) in a monolith that used solely FTIR and TIR, which they called a MOTIRR (monolithic TIR resonator) [16]; Serkland et. al. used a MOTIRR to demonstrate 1064nm pumped OPO [17]. At Konstanz Universität Bruckmeier et. al. constructed a cavity that used all three methods for use in a QND experiment [18].

Once we decided to focus on squeezing via singly resonant SHG (see Chapter 6) we settled on a standing wave cavity with dielectric mirrors as this had the lowest achievable loss. (Such cavities are not suitable for doubly resonant SHG, as they lack a locking degree of freedom, see section 5.5). We selected the well-tested crystal MgO:$LiNbO_3$[1] as the nonlinear medium since it exhibits a large $\chi^{(2)}$ for SHG of 1064 nm light as well as low bulk absorption and scatter loss. $LiNbO_3$ is doped with MgO to avoid the photorefractive effect, which in pure LN is known to cause crystal damage at high intensities - pure LN cannot be used in our experiments. The chief disadvantage of doping is that it increases the crystal inhomogeneities and scattering and so decreases the nonlinearity to loss ratio (see Chapter 8).

Our chief concern when designing the resonator was to maximise the nonlinearity. For $LiNbO_3$ the phase matching length, i.e the length of maximum nonlinear interaction (see Chapter 2), is 12.5mm. We cut the monolith to this length. The loss figure for LN is normally quoted as 0.1%/cm, for 12.5mm the round trip loss is thus 0.25% ($R_{\text{loss}} = 99.75\%$). At the point of maximum conversion efficiency ($P_1^{\text{max conv}}$) the second harmonic is squeezed by 3dB. Experimentally, we desire $P_1^{\text{max conv}}$ to be a low power so that we can drive the crystal far above it and produce strong squeezing. If the outcoupling decay rate is much higher than the loss decay rate ($\gamma_1^c \gg \gamma_1^{\text{loss}}$), then $P_1^{\text{max conv}}$ is high. To keep it

[1] Magnesium oxide doped lithium niobate; aka MgO:LN; aka "maglen". n = 2.233

low, we chose an outcoupling reflectivity of $R_1 = 99.60\%$, and an end mirror reflectivity of $R_1 > 99.9\%$. The predicted finesse is thus 840, and the predicted power build up in the absence of SHG (the "cold cavity") is 280: the high circulating power ensures a large nonlinear interaction. However this is at the expense of a narrow cold cavity linewidth (FWHM = 6.4 Mhz, noise reduced by 3dB at 3.2 MHz). This something of a trade-off as the squeezing bandwidth is proportional to the cold cavity bandwidth[2], and a large squeezing bandwidth is preferred as the laser adds considerable noise at low frequencies which destroys the squeezing (see chapters 4 & 6).

As the monolith is so short it has a high FSR – 5.4 GHz. It is not possible to scan quickly over the full FSR of the monolith: the fast port of the laser only has *in extremis* a range of 100MHz; scanning via the piezoelectric effect (200V/mm, i.e. 1000V over 5 mm) does not give a significantly greater range. Users of MgO:$LiNbO_3$ are typically advised against applying high voltages across the crystal when high optical powers are present. However we have observed no ill effects after more than 3 years of applying 1000V (ramped over 20mS) whilst several Watts of light were present in the crystal.

The nonlinearity, μ, scales as the square of intensity: as intensity is the ratio of power to area a small beam diameter is obviously desirable. However with Gaussian (as opposed to waveguided) beams it is not desirable to focus the beam as tightly as possible. If this is done the beam expands very rapidly away from the focus, so that at the ends of the crystal the intensity is quite low and the contribution to the total nonlinearity is small. Nor is a large, parallel beam desirable, as the interaction is quite weak along the entire length of the crystal. The optimum interaction occurs somewhere between these limits. The following rule of thumb is useful: for a symmetric resonator, set the waist size so that the crystal length is twice the Rayleigh length. The Rayleigh length is defined as:

$$z_R = \frac{\pi w_0^2 n}{\lambda} \tag{5.8}$$

where w_0 is the spot size at the waist, n is the refractive index and λ is the wavelength of the light (note that higher frequencies have longer Rayleigh lengths). Thus for a 12.5mm LN crystal the desired Rayleigh length is 6.25 mm, which translates to a 30.8 μm waist for 1064 nm. (For the Konstanz crystal these figures are 5mm and 27.5 μm, respectively). From Siegman [7], the waist of a resonator is given by:

$$w_0^2 = \frac{L\lambda}{n\pi}\sqrt{\frac{g_1 g_2(1-g_1 g_2)}{(g_1+g_2-g_1 g_2)^2}} \tag{5.9}$$

where L is the length of a standing wave cavity, λ is the wavelength, n is the refractive index and g_i is:

$$g_i = 1 - \frac{L}{ROC_i} \tag{5.10}$$

where ROC_i is the radius of curvature for mirror i. The monolith is symmetric, so $g_1 = g_2$.

The ANU crystal was cut and polished by CSIRO, Sydney, Australia, the final dimensions being $5(x) \times 12.5(y) \times 5(z)$ mm, where (z) is the optic axis. A set of standard curvatures was available from CSIRO: the 14.24 mm radius was closest to optimum, giving a waist of 32.7μm, and the cavity ends were cut accordingly. The dual wavelength dielectric mirror coatings were produced by LZH, Hannover, Germany. The specified

[2] As SHG is loss from the fundamental, it broadens the cavity linewidth, this is the "hot cavity" linewidth: squeezing has this bandwidth.

reflectivities were 99.60% ± 0.03% @ 1064 nm & ~ 4% @ 532 nm for the front coating; 99.90% ± 0.03% @ 1064 nm & 99.9% @ 532 nm for the back coating. The xy faces of the crystal were gold coated by LZH to allow electro-optic modulation of the cavity. The nonlinearity, μ, could not be estimated *a priori*. As the effective nonlinearity, μ, depends on the cavity geometry and the crystal quality (inhomogeneities etc.) it is not surprising that estimates of μ inferred from the literature varied by up to a factor of two. Experimentally we inferred a maximum value of $\mu = 0.012$ (see chapters 6 & 7).

5.4.3 Future design considerations

The criteria used to design the ANU crystal are now effectively obsolete. Materials are now commercially available with very high nonlinearity to loss ratios (e.g. $KNbO_3$, PPLN). This suggests a completely different approach to designing cavities for SH squeezing: as the nonlinearity to loss ratio is so large the high finesse constraint can be relaxed and attention focussed wholly on minimising $P_1^{\text{max conv}}$.

Aside from finesse, the other method to increase the stored power in a cavity is to increase the cavity length (there is more room to store photons). As this narrows the cavity linewidth the outcoupler reflectivity can be accordingly lowered, which has the side benefit of increasing the conversion efficiency. However the feasibility of this is critically linked to the strength of the nonlinearity. In our experiments the nonlinearity was inferred to be $\mu \approx 0.01$. Say that the nonlinearity for a 50mm piece of PPLN is 9 times higher than this, i.e. $\mu = 0.09$ (a not unreasonable estimate). The intracavity loss is relatively high, 5 cm @ 0.1%/cm + 2 surfaces @ 0.1%/surface = 0.7% intracavity loss. We consider an external mirror, bowtie cavity with an optical perimeter of 4cm and reflectivities of $R_1 = 0.90\%$, and $R_2 = R_3 = R_4 = 99.9\%$. With these values, $P_1^{\text{max conv}} \simeq 10mW$ (!), the conversion efficiency at this point (assuming perfect mode match) is $\eta_{nl} = 0.90$ and the cold cavity linewidth is $\simeq$ 15MHz. These figures are better than those obtained from the ANU and Konstanz monoliths, and for a far simpler experimental design: it is certainly worth pursuing. Note that $P_1^{\text{max conv}}$ scales inversely with μ (eqn 2.42): if the nonlinearity is simply that of normal LN then $P_1^{\text{max conv}} \approx$ 90mW which is not at all favourable.

Doubly resonant SHG has a much lower $P_1^{\text{max conv}}$ than the singly resonant case [19]. However doubly resonant systems are considered technically difficult as the second harmonic mode needs to be locked to resonance. In a tight corner it is worth considering the intermediate situation, where the power of the second harmonic is built up by a low reflectivity mirror (say 10% as opposed to AR). The second harmonic is still such a broad resonance that it does not need locking (unless the experimenter is very, very, unlucky). (The equations in section 5.2 break down for low R, as $\arcsin(\theta) \neq \theta$ for large θ. Keeping this in mind, for our example of R=10%, we very roughly calculate a finesse for the second harmonic of 2 and a half, a circulating power twice the incident power and a FWHM for the resonance of two fifths of the FSR, as FWHM/FSR= $1/\mathcal{F}$).

5.4.4 The Wrong Polarisation

The inhomogeneities of the crystal lead to another subtle effect that can totally upset the experiment – which however is fortunately rare, and easily avoided. In MgO:LN, the refractive indices of the s- and p- polarisations of 1064nm are quite different. Consequently the TEM_{00} modes of the the s- and p- polarisations are, in general, resonant at different frequencies. The cavity is driven at p-polarisation, however due to inhomogeneities in

the crystal, a small amount of light is scattered from the p- polarisation into the s-.

In a typical experiment this appears as the following. When scanning over several cavity linewidths (say, via the fast port of the laser) the p-polarised TEM_{00} mode is clearly evident as a large peak. The s-polarised mode appears as a very small peak some distance from the large peak: typically it cannot be eliminated via improving the alignment and mode match - if desired, unambiguous identification can be made by rotating the input polarisation. As the thermal port of the laser is slowly scanned, all the peaks slowly move across the range set by the fast scan of the laser. However, and this is a key point, the s- and p-polarisation peaks move at different rates: the s-polarised peak moving more rapidly than the p-. At some laser temperature, the s- and p-polarisations become frequency degenerate: when this happens, considerable power exchange occurs between the two, with the s-polarised mode able to rob almost all of the power from the desired p-polarised mode[3]. Obviously if this occurred when the cavity was locked and generating second harmonic (as did happen occasionally) the results were disastrous. However it is a simple effect to avoid, simply changing the laser temperature destroys the degeneracy of the two modes and the problem ceases to exist.

5.5 The locking system

Up to three locking loops were required in this experiment: two optical and one thermal. Nominally these loops are independent, although of course they are coupled through the optical interactions. For example, as the monolith comes into resonance extra heat is dumped into the cavity and the thermal loop must adjust accordingly; in turn the cavity expands and the frequency drops and both the monolith and modecleaning loops must then adjust; and so on.

The thermal locking loop was used to maintain the crystal temperature to mK stability. The loop consisted of a heater, oven, detector and temperature controller. At the time of construction, no peltier heaters existed that could run reliably in excess of 100 °C (this is no longer true), so a resistive heater was constructed. It consisted of three 20Ω resistors (RS-WH20), wired in parallel; one resistor was attached to each free side of the oven. The oven itself was a $32 \times 35 \times 44$mm copper block, with an internal space to accommodate the crystal coffin. The oven block was large so as to give a large thermal mass: this was desired as only limited heating power was available ($\approx$ 4.5 W), and the large thermal mass insulated the crystal from ambient temperature fluctuations. The combination of large thermal mass and resistive-only heating led to a large time constant, with the system taking 10-20 minutes to stabilise to a new temperature setting. (Alternatively, if excess power and/or peltier heating/cooling is available it is better to design for a small thermal mass so that the time constant is much smaller.) The crystal coffin was variously a Macor©(ceramic) or Teflon©coffin that electrically insulated the crystal from the oven. Although much harder to machine (it is very brittle) Macor is to be preferred to Teflon as at high temperatures Teflon outgases. The crystal resided inside the coffin between two thin copper strips, which were used to apply up to 1000V across the crystal. The temperature sensor was a 220 kΩ bead thermistor (RS 256-051) that was set deep into the oven, it was not placed on or near the crystal. The design philosophy was to stabilise the core temperature of the oven and let this stable environment provide the heat for the crystal.

[3]R. Bruckmeier has modelled this and found it to be equivalent to an avoided crossing between the two polarisations [21].

The temperature controller design was adapted from that of Bradely et. al. [22] by Alex Eades, Matthew Taubman, and this author. The controller is a parallel PID design, that has as its input the thermistor as one arm of a resistance bridge. Small changes in temperature lead to small resistance, and thus voltage, changes - this is the locking signal. The accuracy of the circuit comes from the accurately known resistor values (ppm) in the resistance bridge. The option of placing ppm resistors on a internal peltier board, to stabilise their values and reduce long term drift, was designed into the system but never implemented as the long term drift was found to be within tolerance. The output was converted from a current push/pull stage of Bradley's original design (necessary for driving peltiers) to a simple current stage ("push vs pull" current is not meaningful w.r.t. a resistor). Two 3.5 digit displays were used: one displayed the set point of the controller (a.bc V), the other the error signal (cd.e mV). At the stable operating point for the thermal locking loop the error signal read 00.0 mV, from this we inferred a stability of $\pm.05$ mV, or, reading from the thermistor chart, ± 1mK.

Table 5.3: Amplifiers and signal generators.

Description	Frequency [MHz]	Manufacturer	Model No.	Comments
HV amplifier	DC – 0.002	David Cooper ANU	–	1 kV
power amplifier (thumper)	0.25 – 150	Electronic Navigation Industries	325LA	25 W
power amplifier (bronze)		ISOMET	RFA-1108	5 W
power amplifier (black)		Minicircuits	ZHL-1A	1 W
power amplifier (black)		Q-BIT	QB538	
signal amplifier (bronze)	0.01 – 500	MITEQ	AU-1261	"low-noise"
signal amplifier (silver)	5 – 500	TRONTECH	W500EF-AGC	> 60dB gain
signal generator	0.1 Hz - 2 MHz	Goodwill Instruments	GFG-8050	5 V
signal generator	0.35 – 50	Tektronix	190B	10 V
signal generator	30 – 100	National	VP-8177A	> 0.09 V
signal generator	1 – 520	Wavetek	3000-200	1 V

The optical locking loops were all Pound-Drever (reflected beam) or modified Pound-Drever (transmitted beam) schemes. As discussed earlier, the laser was phase modulated directly at 27.650 MHz to provide the phase modulation for the modecleaner; the MgO:LN crystal was modulated at 45.167 MHz to provide the phase modulation for the monolithic cavity. In both cases the reflected (or occasionally transmitted beam) was detected by a photodetector; the RF signal from this detector was mixed with the local oscillator used to drive the original phase modulation; the output of the mixer was then

the locking signal. Both locking loops are shown in Fig. 5.1. We now consider the optical locking loops separately.

The modecleaner locking signal was sent to a custom PID (MCPID, constructed by Matthew Taubman [23]): this unit had very high gain at frequencies below 1 kHz, above this the gain was steeply rolled off to avoid exciting the piezo resonances. The PID output was split into low and high frequency components: the low frequency component drove a 1000V amplifier that in turn drove the piezo that held the third modecleaner mirror; the high frequency component was fed into the laser locking loop (of which, more later). The modecleaner was a problematic beast to lock: due to its long perimeter and separated mirrors it was very sensitive to vibration. The following mechanical adjustments reduced, but by no means eliminated, this sensitivity. The mirrors were mounted in commercial mirror holders that were in turn mounted on solid metal blocks. It was found that stainless steel, as opposed to aluminium, blocks decreased the sensitivity of the modecleaner to air-carried acoustic vibrations but increased the sensitivity to table-carried vibrations. As the table was mechanically well insulated, this was an acceptable trade-off. The spurious motion of the third mirror was damped by wedging the metal mount between two rubber machine mounts that were themselves firmly attached to the table. The piezo was mounted on a brass counter-weight, which improved the mechanical resonances of the piezo/mirror assembly. Two separate series of these were observed: 4,8,12.. and 6,12,.. kHz. In future we advise experimenters to avoid this design: it is worth exploring the Lutz Pickelmann design of sandwiching the mirror between two oppositely wired piezos and preloading the mirror/piezo assembly.

By itself, the modecleaner could be locked solely with the low frequency PID output. However once the monolithic cavity was also locked, the modecleaner was no longer able to respond sufficiently and it was necessary to modulate the laser frequency so that at high frequencies it tracked the narrow resonance of the modecleaner as well as the considerably broader resonance of the monolith. This situation was plainly prone to conflict, and various noise signals due to this competition were clearly evident on the noise spectra (see next chapter). If the MCPID and 1000V amplifier were replaced with a higher slew rate combination that could cope with the frequency changes introduced by the monolith locking loop then it would no longer be necessary to tie the two optical locking loops together.

The monolith locking signal was fed into a PID controller (UNIPID, constructed by Matthew Taubman [23]). The output of this was fed into another UNIPID which was used to add the high frequency signal from the mode cleaner locking loop. The combined output was fed into a laser controller (another Matt Taubman product [23]). The laser controller supplied ± 100V and ± 50V to the fast and slow ports of the laser, respectively. As the fast port was also used to phase modulate the laser, the fast locking and 27 MHZ signals were added via a junction box, to prevent the locking signal from destroying the signal generator.

The monolith and laser were locked together by changing the laser frequency. It is in principle possible to instead alter the monolith resonance frequency via the piezoelectric effect - this would then remove the competition between monolith and modecleaner locking signals. However this is inadvisable as at high voltages and optical powers the MgO:LN crystal becomes susceptible to photorefractive damage. It is also impossible in practice as the high DC voltage and optical fields cause "charge screening", i.e. positive and negative charges within the crystal lattice migrate so that they cancel out the applied DC field. In bulk MgO:LN this cannot be avoided, nor can it be sidestepped by increasing the applied DC voltage, as this quickly reaches the dielectric breakdown value for LN.

Table 5.4: General RF components.

Description	Frequency [MHz]	Manufacturer	Model No.	Comments
mixer	0.2–500	Minicircuits	ZP-10514	
splitter/combiner	5–500	Minicircuits	ZFSC-2-1	0°
splitter/combiner	1–500	Minicircuits	ZFSCJ-2-1	180°
adder/subtractor	5–1000	ANZAC (MA-COM)	H-1-4	
RF switch	1–500	Minicircuits	ZFSW-2-46	*off*:0V *on*:−7V
attenuator, x dB	DC–1500	Minicircuits	CAT-x	
variable attenuator		RS Components: Hatfield	610-506	
switchable delay line		EG&G ORTEC	DB463	

5.6 The detection systems

There were three quite separate components of the detection systems: the optical spectrum analysers, the photodetectors themselves, and the optical and electronic arrangement of the balanced detectors.

The generated second harmonic was s-polarised and picked off the pump path with a dichroic (technically a long wave pass optical filter). Some residual infrared remained on the SH beam, so it was reflected into the visible detection system via another dichroic, which attenuated the IR to a negligible amount. The reflected infrared was extracted from the pump beam path via the Faraday isolator, and input directly into the IR detection system.

5.6.1 Optical spectrum analysers

An optical spectrum analyser (OSA) is a scanning confocal optical cavity. In the ideal limit an OSA is insensitive to alignment and mode mismatch: all the even higher order spatial modes of the cavity are frequency degenerate with the TEM_{00}, and all the odd higher order spatial modes are frequency degenerate and located 1/2 FSR away from the TEM_{00}. If the cavity is reasonably well aligned the odd peak becomes very small and only one large peak per FSR is observed as the cavity is scanned. Extra optical frequencies clearly show up as additional peaks.

In our experiments the OSA's were used to detect the presence of TROPO (see Chapters 2 & 7). The OSA's are not shown in Fig. 5.1: they were set-up so that they could intercept some or all of the light from the balanced detection arms of the experiment. Both OSA's were standing wave cavities, and relatively narrow linewidth. The infrared OSA was constructed in-house from two HR@1064nm, 15cm mirrors (FWHM< 500kHz); the visible OSA was a commercial Tropel model (FWHM< 200kHz).

5.6.2 Photodetectors

In this thesis we sought to detect squeezing of both infrared and visible light on beams ranging in power from 30 to 100 mW. In addition to handling relatively high optical power, our detectors required high quantum efficiency (QE) and relatively high frequency response (MHz to 10's of MHZ). Singly each of these features is readily available with commercial photodiodes, as are some combinations of two of these features (e.g. high QE and power handling but poor frequency response; high frequency response and QE but poor power handling; etc). However it is very difficult to find a commercial photodiode that combines all three.

Quantum efficiency is critical in squeezing as loss quickly degrades the squeezing. The QE of a single photodiode can be raised by a combination of the following: removing the glass of the diode case; angling the diode to near Brewster's angle for the diode material; directing the light reflected from the diode back onto the diode with a curved mirror (retroreflecting); AR coating the diode surface. All but the last were used in these experiments [4]. Until recently the workhorse photodiode for visible photodetection in quantum optics has been the EG&G FND-100: we constructed a photodetector with this photodiode and using the above techniques measured a maximum QE of $65 \pm 2\%$ at 532 nm. (In the late 1980's QE's of 80% were reported [25]. However it appears that EG&G changed their manufacturing process, and with FND-100's purchased from 1992 onwards the best measured figure has been 65%.) Care must be taken when retroreflecting: it was found that optical feedback from the detectors could both initiate and alter the properties of TROPO (see Chapters 2 & 7).

The quantum efficiency was calculated by measuring the DC optical power before the detector (taking care not to over or under focus the beam, and to ensure that it was consistently the same size) with a NIST traceable power detector; and measuring the DC photocurrent drawn by the photodiode (by placing an ammeter in line with the photodiode power supply). The quantum efficiency is calculated from:

$$QE = \frac{n_{electron}}{n_{photon}} = \frac{h\nu}{q}\frac{I}{P} \tag{5.11}$$

where I and P are the measured DC photocurrent and optical power, respectively.

Better QE's are possible with Hamamatsu silicon photodiodes. We also constructed photodetectors based around the Hamamatsu S1721, S1722, and S3590 photodiodes. Table 5.5 summarises the results. These are the DC quantum efficiencies (of which more later).

The photodetectors in this thesis were built around the dual DC/AC circuit designed by Mal Gray [24]. The basic design is as shown in Fig. 5.5. The DC output has a low-pass filter frequency corner of $\approx$ 160kHz. The AC output was amplified by low noise monolithic RF amplifier (variously a Minicircuits MAR-6 or Hewlett Packard MIMIC,INA-01170). The coupling capacitor and amplifier effectively act as a high pass filter, this combined with the inductor, resistor, and capacitor combination between the photodiode and ground (which causes a zero in the frequency response) allowed rolling off and significant suppression of the resonant relaxation oscillation (RRO). This was necessary to avoid saturation of the RF amplifier.

[4] Owens et.al showed that the QE can also be increased by using a *bounce detector* arrangement, where a second photodetector is used to detect light reflected from the first, and the photocurrents of the two detectors are added. They report a maximum QE of 1.00 ± 0.01 at 830nm using Hamamatsu S1721 photodiodes.

Table 5.5: Photodiodes. For the visible photodiodes the quantum efficiency (QE) was measured when the photodiode was driven at 30V. * = with glass.

Photodiode	Material	QE w/o glass	optimised QE	Max. power	Comments
EG&G FND-100	silicon	46%	65%	$< 50mW$	@ 532 nm $\Phi = 2.54$mm
Hamamatsu S1721	silicon	74%	91%	$< 50mW$	@ 532 nm $\Phi = 2.54$mm
Hamamatsu S1722	silicon	63%	–	$< 50mW$	@ 532 nm $\Phi = 4.1$mm
Hamamatsu S3590	silicon	85%	88%	$< 100mW$	@ 532 nm 10×10mm
EG&G C30641G	InGaAs	75%*	80%	$< 50mW$	@ 1064 nm area= 1mm^2
EG&G C30642G	InGaAs	64%*	–	$< 50mW$	@ 1064 nm area= 2mm^2

Squeezing has been detected in experiments for over a decade. Yet it is only recently that the problem of measuring the noise of high power optical beams near the quantum limit at RF frequencies has begun to be addressed. Currently, there is no widely accepted model for the behaviour of *pin* photodiodes in this limit (high power, high frequency, near QNL): this would not matter if the DC and AC responses were similarly behaved, but as the following observations show, they are not. The observations are not due to quirks in the design of the AC section of the photodetector circuit, excepting the photodiode this is easily modelled and understood - they are due to the photodiode itself.

The RF noise power varies as a function of the beam diameter. Obviously if the beam is underfocussed (diameter larger than photosensitive area) then not all the light is captured by the detector: both the AC (RF power) and DC (quantum efficiency) responses decrease. However if the beam is overfocussed (diameter somewhat smaller than photosensitive area), the AC and DC responses are longer the same: the RF power can drop significantly, no change observed in the DC current. The effect is power dependent: no AC saturation is observed at low powers with a given diameter; yet at higher optical powers significant AC saturation is observed. It is necessary to increase the beam diameter to recover the AC response. Clearly the AC response is clearly dependent on the optical power density, and a a consequence there exists an optimum beam size for photodetection (between the under- and over- focussing diameters). The FND-100 was reasonably tolerant with respect to this behaviour; the S-1721 was not, it had a very narrow range of waists where the RF power was maximised.

At high optical powers, increasing the reverse bias voltage can vastly improve the AC response of the photodiode, whilst again changing the DC response only minimally. It is as if a certain amount of electrical power is required to respond at RF frequencies, and if this power is not supplied then the RF response is severely attenuated. All the visible photodiodes in this thesis were run with a reverse bias voltage of at least 50V, below this the RF response was notably attenuated for high ($> 20 - 30$ mW) optical powers. Once again, the S1721 showed greater sensitivity to this effect than the FND100.

Thermal effects also affect the AC response. When the photodiode can was not well heatsunk (it was free standing in air), increasing the incident optical power consistently

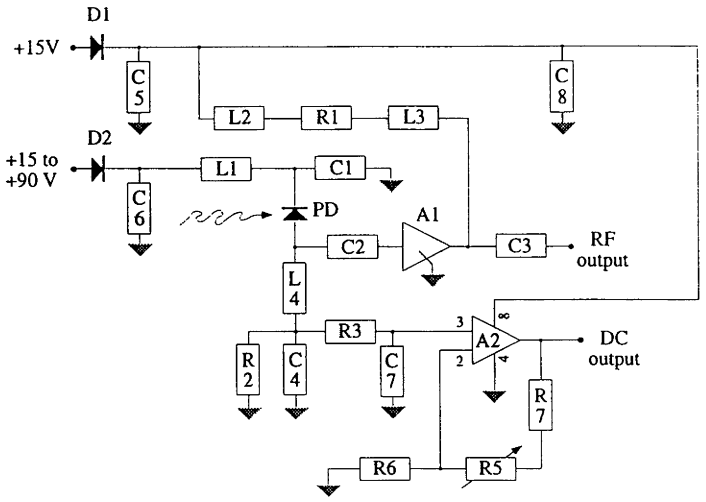

Figure 5.5: Photodetector circuit. PD = photodiode (EG&G FND100 or Hamamatsu S1721, S1722, or S3590). A1 = Minicircuits MAR6 or Hewlett Packard MIMIC INA-01170. D1 = D2 = 1n4007 diode. R1 = 680Ω (for MAR6) or 250Ω (for INA-01170); R2 = 100Ω; R3 = 1.1kΩ; R5 = 20kΩ potentiometer; R6 = 1.1kΩ; R7 = 100kΩ. C1 = 1nF; C2 = 1 or 10 nF; C3 = 0.1μF; C4 = 10nF; C5 = 22μF; C6 = C7 = 1nF. L1 = L2 = 10μH; L3 = L4 = 1μH.

caused the AC response to increase for FND100 photodiodes and decrease for S1721 photodiodes. To avoid these thermal effects, the photodetectors were constructed so that the photodiode cans were snugly and firmly in contact with either brass or copper heat sinks. A slight thermal effect could still be observed with the brass heatsinks, none at all with the copper.

Despite awareness of, and care taken to avoid, the above phenomena, the AC response of the high power and quantum efficiency photodiodes is still not fully understood. For example, for a 30mW 532 nm beam 1.7 dB of squeezing was measured using the FND100 photodetectors (see next chapter); using the measured DC quantum efficiency of 65% we inferred 3 dB of actual squeezing (which was very consistent with the theoretical predictions, see Chapter 6). Using the S1721 photodetectors to measure the same beam, 2.1 dB of squeezing is observed; however from the measured DC quantum efficiency of 91% we inferred only 2.4 dB of squeezing. Given that the S1721 was observed to be more susceptible to affects that change the AC response, we suggest the following. There exists an effective AC quantum efficiency for photodetection. Ideally this is the same as the DC value, but it may be degraded from it by a variety of phenomena (power density saturation, insufficient reverse bias, thermal effects). In this specific instance the S1721 AC quantum efficiency would appear to be 77%, as opposed to 91%. (We do not consider the alternative, adjusting the AC response of the FND100, for two reasons: the FND100 was observed to be much less sensitive to AC effects than the S1721; the observed output from the FND100 agrees with theoretical predictions for the measured and inferred cavity parameters, the S1721 output does not.)

It is not clear why the S1721 response is so degraded in this instance. One possible explanation is immediately obvious (there may be others). The over- and under- focussing regions may begin to overlap as the incident optical power is increased. Thus, it is not possible to make the beam any larger as not all of it will be captured, yet even for the

maximum beam size there will be some saturation due to the overfocussing effect. If this is true then the observed AC response should appear to decrease with increasing optical power. Considering the physical mechanism of photodetection, it may not be the actual optical power that causes the overfocussing effect, but the amount of photocurrent. The problem is no doubt exacerbated by turning the photodiodes to increase the DC quantum efficiency, for circular beams this transforms the incident light to an ellipse. To avoid this experiments are planned using a D-lens which will ensure the beam is circular (minimum power density) for the turned photodiodes [26]: further work is also required to understand the relationship between these phenomena. Given these results, the visible squeezing results presented in this thesis are those taken using the FND100 based photodetectors.

5.6.3 Balanced detectors

As discussed in section 3.4.5, balanced detection requires a 50/50 beamsplitter. In practice commercial nonpolarising beamsplitters are rarely 50/50, varying by up to 5%. Accordingly we did not use a nonpolarising beam splitter, instead using various $\lambda/2$ plate and polarising beam splitter combinations. For the infrared detector the two output beams were at right angles to one another and orthogonally polarised: as the individual detectors were not turned to Brewster's angle the different polarisations were not troublesome. For the visible balanced detector the lowest loss solution was found to be a beamsplitter, nominally coated for 543nm, turned so that the two output beams were separated by $\approx 110°$, the polarisations were somewhat different, so care was needed when optimising the quantum efficiency via turning the photodetectors to Brewster's angle.

For both the infrared and visible cases the AC outputs of the two individual photodetectors were sent to an an adder/subtractor (see Table 5.4). The two outputs of the adder/subtractor were connected to an electronic switch, the output of which was sent to a HP-8568B signal analyser. This enabled quick switching between the added and subtracted signals without physically disconnecting cables. All cables were carefully matched for length. In practice the observed spectra from the individual photodetectors had slightly different frequency dependencies (i.e. shapes). By varying the retroreflection, angle tuning, and optical balance, it was possible to accurately balance the two photodetectors over limited frequency ranges, as the situation demanded. For example, better than 40 dB cancellation between 8–12 MHz with lesser cancellation, $<$ 20dB, at 45 MHz. In the high cancellation frequency regimes, the detectors were balanced to within 0.1 dB.

It was occasionally necessary to split the photodetector signal, normally between the photodetector and adder/subtractor, to obtain a locking signal or to obtain a signal for feedback measurements [23]. If this is done, *it is vitally important that the splitters are correctly balanced and isolated.* For example, the output of the adder/subtractor changes if one of the splitter outputs, *before* the adder/subtractor, is not terminated, or drives a poorly impedance matched load. (This is fairly normal behaviour for RF components.) To avoid any such problems, we systematically placed amplifiers, which incidentally act as RF amplifiers, on all splitter outputs.

Chapter 5 bibliography

[1] *Diode-pumped solid-state non-planar ring laser: users manual*, Lightwave Electronics Corporation, Mountain View, California, USA, October 1992

[2] G. Cantatore, F. Della Valle, E. Milotti, P. Pace, E. Zavattini, E. Polacco, F. Perrone, C. Rizzo, G. Zavattini and G. Ruoso, Rev. Sci. Instrum., **66**, no. 4, p. 2785, 1995. *Frequency locking of a Nd:YAG laser using the laser itself as the optical phase modulator*

[3] Tom Kane, *private communication*, Lightwave Electronics Corporation, Mountain View, California, USA, July 1995

[4] E. S. Polzik, J. Carri and H. J. Kimble, Applied Physics B, **55**, p. 279, 1992. *Atomic spectroscopy with squeezed light for sensitivity beyond the vacuum-state limit*

[5] G. Breitenbach, T. Müller, S. F. Pereira, J.-Ph. Poizat, S. Schiller and J. Mlynek, J. Opt. Am. Soc. B, **12**, no. 11, p. 2304, 1995. *Squeezed vacuum from a monolithic optical parametric oscillator*

[6] H. Tsuchida, Opt. Lett., **20**, no. 21, p. 2240, 1995. *Generation of amplitude-squeezed light at 431 nm from a singly resonant frequency doubler*

[7] A. E. Siegman, *Lasers*, First Edition, University Science Books, California, 1986

[8] This is from [7, p.418]. Please note that there is a misprint on p. 418, the numerator should be t_1^2 NOT $t_1 t_2$.

[9] see references in: S. C. Hill and R. E. Benner, *"Morphology-dependent resonances", in Optical Effects Associated With Small Particles, Chief Editor S. Ramaseshan*, Advanced Series in Applied Physics, 1987

[10] H.-B. Lin, A. L. Huston, B. L. Justus and A. J. Campillo, Optics Letters, **11**, no. 10, p. 614, 1986. *Some characteristics of a droplet whispering-gallery-mode laser*

[11] T. Baer, Optics Letters, **12**, no. 6, p. 392, 1987. *Continuous-wave laser oscillation in a Nd:YAG sphere*

[12] V. B. Braginsky, M. L. Gorodetsky and V. S. Ilchenko, Physics Letters A, **137**, no. 7,8, p. 393, 1989. *Quality-factor and nonlinear properties of optical whispering-gallery modes*

[13] L. Collot, V. Lefèvre-Seguin, M. Brune, J. M. Raimond and S. Haroche, preprint, 1993. *Very high Q Whispering-gallery Mode Resonances Observed on fused Silica Microspheres*

[14] W. J. Kozlovsky, C. D. Nabors and R. L. Byer, Optics Letters, **12**, no. 12, p. 1014, 1987. *Second-harmonic generation of a continuous-wave diode-pumped Nd:YAG laser using an externally resonant cavity*

[15] W. J. Kozlovsky, C. D. Nabors and R. L. Byer, IEEE Journ. Quant. Elec., **24**, no. 6, p. 913, 1988. *Efficient Second Harmonic Generation of a Diode-Laser-Pumped Nd:YAG Laser Using Monolithic $MgO:LiNbO_3$ External Resonant Cavities*

[16] S. Schiller and R. L. Byer, Journ. Opt. Soc. Am. B, **10**, no. 9, p. 1696, 1993. *Quadruply resonant optical parametric oscillation in a monolithic total-internal-reflection resonator*

[17] D. K. Serkland, R. C. Eckardt and R. L. Byer, Optics Letters, **19**, no. 14, p. 1046, 1994. *Continuous-wave total-internal-reflection optical parametric oscillator pumped at 1064 nm*

[18] R. Bruckmeier, K. Schneider, S. Schiller and J. Mlynek, Physical Review Letters, **78**, no. 7, p. 1243, 1997. *Quantum Nondemolition Measurement Improved by a Squeezed Meter Input*

[19] Z. Y. Ou and H. J. Kimble, Optics Letters, **18**, no. 13, p. 1055, 1993. *Enhanced conversion efficiency for harmonic generation with double resonance*

[20] Z. Y. Ou, Optics Communications, **124**, p. 430, 1996. *Observation of nonlinear phase shift in CW harmonic generation*

[21] R. Bruckmeier, Fakultät für Physik, Universität Konstanz, Germany, (private communication), 1995.

[22] C. C. Bradley, J. Chen and R. G. Hulet, Rev. Sci. Instrum., **61**, no. 8, p. 2097, 1990. *Instrumentation for the stable operation of laser diodes*

[23] M. S. Taubman, PhD thesis, Physics Department, Australian National University, Canberra, October 1995. *The quantum mechanics of electro-optic feedback, second harmonic generation, and their interaction*

[24] M. Gray, PhD thesis, Physics Department, Australian National University, Canberra, January 1995. *Quantum Noise Limited Interferometry*

[25] A. Sizmann, Physikalisches Institut, Universität Erlangen-Nürnberg, Germany, (private communication), 1993.

[26] P. K. Lam, Physics Department, Australian National University, Canberra, 1997. *private communication*

Chapter 6

Squeezing in SHG

This is not the end. It is not even the beginning of the end. But it is, perhaps, the end of the beginning.

Winston Churchill

As discussed in Chapter 4, in the early to mid 80's there was a considerable body of theoretical literature that indicated SHG was a suitable source of squeezed light. With this in mind, the first demonstration of SHG squeezing was made by Pereira et. al in 1988 [1]. They used a $LiNBO_3$ crystal in a doubly resonant, external mirror, standing wave cavity, and observed transient (10 ms) squeezing of 13%/-0.6 dB on a $<$ 10mW reflected fundamental beam. Their experiment was chiefly limited by dispersion, i.e. the tendency for the fundamental and second harmonic waves to get out of phase with one another due to air/crystal interfaces and the mirror coatings. The interface problem was elegantly overcome in the experiment of Sizmann et. al [2]. By using a doubly resonant *monolithic* cavity they were able to observe transient (ms) squeezing of 19%/-0.9 dB on a 100 μW second harmonic beam. The clever use of monolithic technology attracted widespread attention. Using this technology Kürz et. al were eventually able to observe, for up to 10 s at a time, 52%/-3.2 dB squeezing on a 3.2 mW reflected fundamental beam [3]. In all of these experiments the observed squeezing was much less than that expected from theory, even after correction for nonperfect quantum efficiency and electronic noise. This degradation was attributed to the problem of maintaining double resonance, i.e actively stabilising both the fundamental and second harmonic cavities. Technical difficulties with this limited both the achievable nonlinearity and the length of time which squeezing could be produced.

Prompted by these difficulties, the theory was reexamined by Collett and Paschotta. They found that double resonance was not necessary to produce squeezing, and predicted second harmonic squeezing from a singly resonant cavity. In 1994 Paschotta et. al used a singly resonant monolith that only needed to be locked at the fundamental. Stable squeezing of 20%/-0.94 dB was observed on a $\simeq$ 30mW second harmonic beam [4]. After correction for detection efficiency and electronic noise the observed squeezing was significantly less than the predicted value of -2.2 dB. This was attributed to either laser noise or a thermal effect, as a strong power bistability, thought to be due to thermal problems, was observed for high pump powers.

In 1995 Ralph et. al [5] observed 13%/-0.6 dB second harmonic squeezing and identified laser noise as one source of squeezing degradation. By accurately modelling the driving laser they obtained excellent agreement between theory and experiment for their system. However their model was developed using the Schrödinger approach (see Chapter 4) and was thus computationally laborious and not very intuitive. In the same year Tsuchida [6] observed -2.4 dB second harmonic squeezing but again agreement between theory (-3.0 dB) and experiment was poor.

The other SHG system that holds great promise as a source of bright strongly squeezed light is travelling wave SHG. In 1993 Li & Kumar predicted that amplitude squeezing of both the fundamental (100%) and the second harmonic (50%) was possible for single pass

Table 6.1: Experiments in squeezing via SHG

[!ht]

Paper	Observed squeezing	Power (mW)	λ (nm)	Obs. time	Agrees with theory
Cavity systems: doubly resonant					
1988 Pereira et. al	13%/-0.6 dB	< 10	1064	10 ms	No
1990 Sizmann et. al	19%/-0.9 dB	0.100	532	1 ms	No
1993 Kürz et. al	52%/-3.2 dB	3.2	1064	10 s	No
singly resonant					
1994 Paschotta et. al	20%/-0.94 dB	$\simeq 30$	532	stable	No
1995 Ralph et. al	13%/-0.6 dB	30	532	stable	Yes
1995 Tsuchida et. al	42%/-2.4 dB	64	431	stable	No
1996 White et. al	30%/-1.7 dB	34	532	stable	Yes
Travelling wave:					
1996 Youn et. al.	6%/-0.3 dB	0.10av	532	n.a.	No

SHG. The phase matched case is particularly simple, with the prediction of fundamental amplitude squeezing of $V_{X_1}(0) = 1 - \eta$ where η is the nonlinear conversion parameter. In 1996 Youn et. al [7] observed a modest 7%/-0.3 dB for pulsed travelling wave SHG: again, agreement between theory and experiment was poor.

In this chapter we examine the squeezing produced by singly resonant SHG. The results in this chapter were published in 1996 [8]. In the first section we derive the nonlinear interaction terms and the quantum noise characteristics via the Heisenberg approach. In the second section we introduce the concept of a "modular" approach to noise propagation in quantum optics systems, with particular reference to the experimental system presented in the last chapter. In the third section we present and compare the experimental and theoretical results. We find excellent agreement between theory and experiment. In the last section we briefly discuss the future of squeezing via SHG.

6.1 Quantum theory of the frequency doubler

The classical models of frequency doubling presented in Chapter 2 did not consider the noise properties of the light. In this section we use the Heisenberg approach to derive the noise properties of frequency doubled systems.

6.1.1 Deriving the interaction terms

The beauty of starting from the Hamiltonian is that derivation of the equations of motion is straightforward. In Chapter 3 we derived from the Hamiltonian the decay and coupling terms for the equations of motion. We now derive the nonlinear interaction terms. (Compare this with derivation with that of Chapter 2 where deriving the nonlinear interaction terms was an involved process that required particular care with scaling so as to fulfill energy conservation.)

Consider the interaction Hamiltonian for SHG/DOPO:

$$\mathcal{H} = i\hbar\frac{\kappa}{2}(a^{\dagger 2}_1 a_3 - a_1^2 a^\dagger{}_3) \tag{6.1}$$

Using eqn 3.57 we can obtain the interaction terms for the degenerate equations of motion for a second order system. For the low frequency mode (known as the fundamental or subharmonic for SHG/DOPO respectively):

$$i\hbar\dot{a}_1 = i\hbar\frac{\kappa}{2}(a_1 a^{\dagger 2}_1 a_3 - a_1 a_1^2 a^\dagger{}_3 - a^{\dagger 2}_1 a_3 a_1 + a_1^3 a^\dagger{}_3) \tag{6.2}$$

The second and fourth terms cancel. Repeatedly applying the commutator relation gives:

$$\begin{aligned}
\dot{a}_1 &= \frac{\kappa}{2}(a_1 a^{\dagger 2}_1 - a^{\dagger 2}_1 a_1)a_3 \\
&= \frac{\kappa}{2}(a_1 a^{\dagger 2}_1 - a^\dagger{}_1(1 + a_1 a^\dagger{}_1))a_3 \\
&= \frac{\kappa}{2}(a_1 a^{\dagger 2}_1 - a^\dagger{}_1 - (1 + a_1 a^\dagger{}_1)a^\dagger{}_1)a_3 \\
&= \frac{\kappa}{2}(-a^\dagger{}_1 - a^\dagger{}_1)a_3 \\
&= -\kappa a^\dagger{}_1 a_3
\end{aligned} \tag{6.3}$$

Similarly for the high frequency mode (known as the second harmonic or pump for SHG/DOPO respectively):

$$\begin{aligned}
\dot{a}_3 &= \frac{\kappa}{2}(a_3 a^{\dagger 2}_1 a_3 - a_3 a_1^2 a^\dagger{}_3 - a^{\dagger 2}_1 a_3 a_3 + a_1^2 a^\dagger{}_3 a_3) \\
&= \frac{\kappa}{2}(a_1^2 a^\dagger{}_3 a_3 - a_3 a_1^2 a^\dagger{}_3) \\
&= +\frac{\kappa}{2}a_1^2
\end{aligned} \tag{6.4}$$

Note the factor of half in the high frequency mode. This was not at all obvious in the classical derivation.

Similarly derivation of the interaction terms for the nondegenerate equations of motion is straightforward. The interaction Hamiltonian for SFG/NDOPO is:

$$H = i\hbar\frac{\kappa}{2}(a^\dagger{}_1 a^\dagger{}_2 a_3 - a_1 a_2 a^\dagger{}_3) \tag{6.5}$$

The interaction term for the signal equation of motion is thus:

$$\begin{aligned}
\dot{a}_1 &= -\frac{\kappa}{2}(a^\dagger{}_1 a^\dagger{}_2 a_3 a_1 - a_1 a_2 a^\dagger{}_3 a_1 - a_1 a^\dagger{}_1 a^\dagger{}_2 a_3 + a_1 a_1 a_2 a^\dagger{}_3) \\
&= -\frac{\kappa}{2}(a^\dagger{}_1 a_1 - a_1 a^\dagger{}_1)a^\dagger{}_2 a_3 \\
&= -\frac{\kappa}{2}a^\dagger{}_2 a_3
\end{aligned} \tag{6.6}$$

And similarly for the idler equation of motion:

$$\dot{a}_2 = -\frac{\kappa}{2}a^\dagger{}_1 a_3 \tag{6.7}$$

Whilst for the pump equation of motion:

$$\begin{aligned}\dot{a}_3 &= +\frac{\kappa}{2}(a_3 a^\dagger{}_1 a^\dagger{}_2 a_3 - a_3 a_1 a_2 a^\dagger{}_3 - a^\dagger{}_1 a^\dagger{}_2 a_3^2 + a_1 a_2 a^\dagger{}_3 a_3) \\ &= +\frac{\kappa}{2} a_1 a_2 (a^\dagger{}_3 a_3 - a_3 a^\dagger{}_3) \\ &= +\frac{\kappa}{2} a_1 a_2 \end{aligned} \tag{6.8}$$

For the remainder of this section we consider only the degenerate equations of motion. However our calculational methods can be easily extended to the nondegenerate case.

6.1.2 Quantum noise of the singly resonant doubler

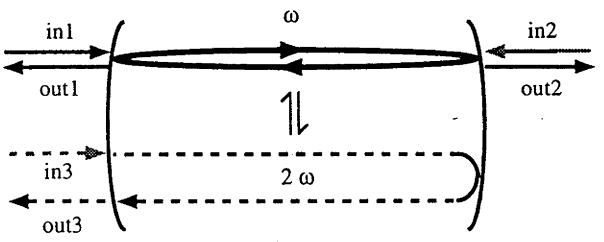

Figure 6.1: Schematic of singly resonant doubler. in1 = fundamental power coupling input, in2 = fundamental transmission and loss input, in3 = second harmonic vacuum input.

Using the interaction terms derived in the last section, we can write the equations of motion for SHG/OPO as:

$$\begin{aligned}\dot{\hat{a}}_1 &= -(\gamma_1 + i\Delta_1)\hat{a}_1 + \kappa \hat{a}^\dagger{}_1 \hat{a}_2 + \sqrt{2\gamma_1^c}\hat{A}_1^{in1} + \sqrt{2\gamma_1^\ell}\hat{A}_1^{in2} \\ \dot{\hat{a}}_3 &= -(\gamma_3 + i\Delta_3)\hat{a}_3 - \kappa/2\hat{a}_1^2 + \sqrt{2\gamma_3}\hat{A}_2^{in3} \end{aligned} \tag{6.9}$$

where we have explicitly set the low frequency mode to have non-perfect escape efficiency, $\eta = \gamma_1^c/\gamma_1$. As Fig. 6.1 shows, we consider a standing wave cavity where the two inputs (coupling and combined transmission and loss) for the low frequency mode are labelled in1 & in2, and the input for the high frequency mode is labelled in3. For singly resonant SHG, we can set $\Delta_3 = 0$ (see section 2.5.3). Adiabatically eliminating the second harmonic (see section 2.2.3) we obtain:

$$\hat{a}_3 = -\frac{\kappa}{2\gamma_3}\hat{a}_1^2 + \sqrt{\frac{2}{\gamma_3}}\hat{A}_2^{in3} \tag{6.10}$$

Substituting this into eqn 6.9:

$$\dot{\hat{a}}_1 = -(\gamma_1 + i\Delta_1)\hat{a}_1 - \mu \hat{a}^\dagger{}_1 \hat{a}_1 \hat{a}_1 + 2\sqrt{\mu}\hat{a}^\dagger{}_1 \hat{A}_3^{in3} + \sqrt{2\gamma_1^c}\hat{A}_1^{in1} + \sqrt{2\gamma_1^\ell}\hat{A}_1^{in2} \tag{6.11}$$

where $\mu = \kappa^2/(2\gamma_2)$. Linearising (see sections 3.1.5 & 3.3.2) we obtain the fluctuation equation of motion:

$$\begin{aligned}\delta\dot{\hat{a}}_1 &= -(\gamma_1 + i\Delta_1)\delta\hat{a}_1 - \mu(2|\alpha_1|^2\delta\hat{a}_1 + \alpha_1^2\delta\hat{a}^\dagger{}_1) + 2\sqrt{\mu}(A_3^{in3}\delta\hat{a}^\dagger{}_1 + \alpha_1^*\delta\hat{A}_3^{in3}) \\ &\quad + \sqrt{2\gamma_1^c}\hat{A}_1^{in1} + \sqrt{2\gamma_1^\ell}\hat{A}_1^{in2} \end{aligned} \tag{6.12}$$

Recalling that for SHG, $A_3 = 0$, the quadrature fluctuation equations of motion for the fundamental are (see section 3.1.3):

$$\begin{aligned}
\delta\dot{\hat{X}}_1 &= -(\gamma_1 + 2\mu|\alpha_1|^2 + \frac{\mu}{2}\left[\alpha_1^2 + \alpha_1^{*2}\right])\delta\hat{X}_1 + (\Delta_1 + i\frac{\mu}{2})\left[\alpha_1^2 - \alpha_1^{*2}\right])\delta\hat{X}_2 \\
&\quad +\sqrt{\mu}(\alpha_1 + \alpha_1^*)\delta\hat{X}_1{}^{\text{in3}} - i\sqrt{\mu}(\alpha_1 - \alpha_1^*)\delta\hat{X}_2{}^{\text{in3}} \\
&\quad +\sqrt{2\gamma_1^c}\delta\hat{X}_1{}^{\text{in1}} + \sqrt{2\gamma_1^\ell}\delta\hat{X}_1{}^{\text{in2}} \\
\delta\dot{\hat{X}}_2 &= -(\gamma_1 + 2\mu|\alpha_1|^2 - \frac{\mu}{2}\left[\alpha_1^2 + \alpha_1^{*2}\right])\delta\hat{X}_2 - (\Delta_1 - i\frac{\mu}{2})\left[\alpha_1^2 - \alpha_1^{*2}\right])\delta\hat{X}_1 \\
&\quad +\sqrt{\mu}(\alpha_1 + \alpha_1^*)\delta\hat{X}_2{}^{\text{in3}} - i\sqrt{\mu}(\alpha_1 - \alpha_1^*)\delta\hat{X}_1{}^{\text{in3}} \\
&\quad +\sqrt{2\gamma_1^c}\delta\hat{X}_2{}^{\text{in1}} + \sqrt{2\gamma_1^\ell}\delta\hat{X}_2{}^{\text{in2}}
\end{aligned} \tag{6.13}$$

Fourier transforming (see section 3.3.3) this becomes:

$$\begin{aligned}
\delta\tilde{X}_1 &= \frac{\sqrt{2\gamma_1^c}\delta\tilde{X}_1{}^{\text{in1}} + \sqrt{2\gamma_1^\ell}\delta\tilde{X}_1{}^{\text{in2}} + \sqrt{\mu}(\alpha_1 + \alpha_1^*)\delta\tilde{X}_1{}^{\text{in3}}}{} \\
&\quad \frac{-i\sqrt{\mu}(\alpha_1 - \alpha_1^*)\delta\tilde{X}_2{}^{\text{in3}} + (\Delta_1 + i\frac{\mu}{2})\left[\alpha_1^2 - \alpha_1^{*2}\right]\delta\tilde{X}_2}{\gamma_1 + 2\mu|\alpha_1|^2 + \mu/2(\alpha_1^2 + \alpha_1^{*2}) - i\omega} \\
\delta\tilde{X}_2 &= \frac{\sqrt{2\gamma_1^c}\delta\tilde{X}_2{}^{\text{in1}} + \sqrt{2\gamma_1^\ell}\delta\tilde{X}_2{}^{\text{in2}} + \sqrt{\mu}(\alpha_1 + \alpha_1^*)\delta\tilde{X}_2{}^{\text{in3}}}{} \\
&\quad \frac{-i\sqrt{\mu}(\alpha_1 - \alpha_1^*)\delta\tilde{X}_1{}^{\text{in3}} - (\Delta_1 - i\frac{\mu}{2})\left[\alpha_1^2 - \alpha_1^{*2}\right]\delta\tilde{X}_1}{\gamma_1 + 2\mu|\alpha_1|^2 - \mu/2(\alpha_1^2 + \alpha_1^{*2}) - i\omega}
\end{aligned} \tag{6.14}$$

Eliminating the cross terms we obtain the expression:

$$\delta\tilde{X}_i = \frac{C_i(D_j + E_j) + F_j(D_i + E_i)}{F_iF_j - C_iC_j} \tag{6.15}$$

where the subscripts $i = 1, 2$ and $j = 2, 1$ denote the quadrature and its complement; C_i is the coupling term,

$$C_i = \pm(\Delta \pm i\frac{\mu}{2}\left[\alpha_1^2 - \alpha_1^{*2}\right]); \tag{6.16}$$

The "+" sign is used for C_i; the "−" sign for C_j. D_i is the fundamental noise input term,

$$D_i = \sqrt{2\gamma_1^c}\delta\tilde{X}_i^{\text{in1}} + \sqrt{\gamma_1^\ell}\delta\tilde{X}_i^{\text{in2}}; \tag{6.17}$$

E_i is the second harmonic noise input term,

$$E_i = +\sqrt{\mu}(\alpha_1 + \alpha_1^*)\delta\tilde{X}_i^{\text{in3}} \pm i\sqrt{\mu}(\alpha_1^* - \alpha_1)\delta\tilde{X}_i^{\text{in3}}; \tag{6.18}$$

and F_i is the nonlinear loss term,

$$F_i = \gamma_1 + 2\mu|\alpha_1|^2 \pm \frac{\mu}{2}(\alpha_1^2 + \alpha_1^{*2}) - i\omega \tag{6.19}$$

Consider the quadrature fluctuations $\delta\tilde{X}_i$. Detuning couples to $\delta\tilde{X}_i$ the complementary quadrature fluctuations from both the fundamental and second harmonic noise inputs,

$C_i(D_j + E_j)$. As a general rule, extra sources of vacuum noise are to be avoided, as they introduce, extra uncorrelated noise and this tends to decrease the squeezing. Further, increasing the detuning increases the effective decay rate (see section 2.2.3) which decreases the field α_1 and thus the nonlinear interaction term, $\mu|\alpha_1|^2$. Thus the overall effect of detuning is to introduce additional noise and a weaker nonlinearity: the squeezing degrades. For zero detuning, $\Delta = 0$, $\alpha = \alpha^*$ & $C_i = 0$, and $|\alpha_1^2|$ is a maximum: the squeezing is optimal.

Now consider the boundary conditions for SHG in the singly resonant case. For the reflected fundamental and the generated second harmonic these are (see eqns 2.32 & 2.36):

$$\begin{aligned} \hat{\mathrm{A}}_1^{\mathrm{out1}} &= \sqrt{2\gamma_1^c}\hat{\mathrm{a}}_1 - \hat{\mathrm{A}}_1^{\mathrm{in1}} \\ \hat{\mathrm{A}}_3^{\mathrm{out3}} &= \sqrt{\mu}\hat{\mathrm{a}}_1^2 - \hat{\mathrm{A}}_1^{\mathrm{in3}} \end{aligned} \tag{6.20}$$

Linearising and Fourier transforming, we obtain:

$$\begin{aligned} \delta\tilde{\mathrm{X}}_i^{\mathrm{out1}} &= \sqrt{2\gamma_1^c}\tilde{\mathrm{X}}_i - \tilde{\mathrm{X}}_i^{\mathrm{in1}} \\ \delta\tilde{\mathrm{X}}_i^{\mathrm{out3}} &= \sqrt{\mu}\left[\delta\tilde{\mathrm{X}}_i(\alpha_1 + \alpha_1^*) \pm i\delta\tilde{\mathrm{X}}_i(\alpha_1 - \alpha_1^*)\right] - \delta\tilde{\mathrm{X}}_i^{\mathrm{in3}} \end{aligned} \tag{6.21}$$

For zero detuning the fluctuations in the reflected fundamental and generated second harmonic fields are:

$$\begin{aligned} \delta\tilde{\mathrm{X}}_i^{\mathrm{out1}} &= \sqrt{2\gamma_1^c}\left[\frac{D_i + E_i}{F_i}\right] - \delta\tilde{\mathrm{X}}_i^{\mathrm{in1}} \\ \delta\tilde{\mathrm{X}}_i^{\mathrm{out3}} &= 2\alpha_1\sqrt{\mu}\left[\frac{D_i + E_i}{F_i}\right] - \delta\tilde{\mathrm{X}}_i^{\mathrm{in3}} \end{aligned} \tag{6.22}$$

Using eqns 6.16-6.19, we take the self correlations (see section 3.3.5) to obtain the noise spectrum for the reflected fundamental:

$$\begin{aligned} V_{\mathrm{X}_i}^{\mathrm{out1}}(\omega) &= \frac{\left[\left(2\gamma_1^c - \gamma_1 - \left[\begin{smallmatrix}3\\1\end{smallmatrix}\right]\mu\alpha_1^2\right)^2 + \omega^2\right] V_{\mathrm{X}_i}^{\mathrm{in1}}(\omega) + 4\gamma_1^c\left[\gamma_1^\ell V_{\mathrm{X}_i}^{\mathrm{in2}}(\omega) + 2\mu\alpha_1^2 V_{\mathrm{X}_i}^{\mathrm{in3}}(\omega)\right]}{\left(\gamma_1 + \left[\begin{smallmatrix}3\\1\end{smallmatrix}\right]\mu\alpha_1^2\right)^2 + \omega^2} \\ &= V_{\mathrm{X}_i}^{\mathrm{in1}}(\omega) + \\ &\quad 4\gamma_1^c \frac{\left[\gamma_1^\ell V_{\mathrm{X}_i}^{\mathrm{in2}}(\omega) + 2\mu\alpha_1^2 V_{\mathrm{X}_i}^{\mathrm{in3}}(\omega)\right] - \left(\gamma_1^\ell + \left[\begin{smallmatrix}3\\1\end{smallmatrix}\right]\mu\alpha_1^2\right) V_{\mathrm{X}_i}^{\mathrm{in1}}(\omega)}{\left(\gamma_1 + \left[\begin{smallmatrix}3\\1\end{smallmatrix}\right]\mu\alpha_1^2\right)^2 + \omega^2} \end{aligned} \tag{6.23}$$

and the noise spectrum for the generated second harmonic:

$$\begin{aligned} V_{\mathrm{X}_i}^{\mathrm{out3}}(\omega) &= \frac{8\mu\alpha_1^2\left[\gamma_1^c V_{\mathrm{X}_i}^{\mathrm{in1}}(\omega)\gamma_1^\ell V_{\mathrm{X}_i}^{\mathrm{in2}}(\omega)\right] + \left[\left(\left[\begin{smallmatrix}1\\3\end{smallmatrix}\right]\mu\alpha_1^2 - \gamma_1\right)^2 + \omega^2\right] V_{\mathrm{X}_i}^{\mathrm{in3}}(\omega)}{\left(\gamma_1 + \left[\begin{smallmatrix}3\\1\end{smallmatrix}\right]\mu\alpha_1^2\right)^2 + \omega^2} \\ &= V_{\mathrm{X}_i}^{\mathrm{in3}}(\omega) + \end{aligned}$$

$$8\mu\alpha_1^2 \frac{\left[\gamma_1^c V_{X_i}^{in1}(\omega)\gamma_1^\ell V_{X_i}^{in2}(\omega)\right] - (\gamma_1 \pm \mu\alpha_1^2) V_{X_i}^{in3}(\omega)}{\left(\gamma_1 + \left[{}^3_1\right]\mu\alpha_1^2\right)^2 + \omega^2} \tag{6.24}$$

The ports *in2* & *in3* are vacuum inputs, so $V_{X_i}^{in2}(\omega) = V_{X_i}^{in3}(\omega) = 1$. Eqns 6.23 & 6.24 simplify to:

$$\begin{aligned} V_{X_i}^{out1}(\omega) &= 1 - 4\gamma_1^c \frac{(V_{X_i}^{in1}(\omega) - 1)\left(\gamma_1^\ell + \left[{}^3_1\right]\mu\alpha_1^2\right) \pm \mu\alpha_1^2}{\left(\gamma_1 + \left[{}^3_1\right]\mu\alpha_1^2\right)^2 + \omega^2} \\ V_{X_i}^{out3}(\omega) &= 1 + 8\mu\alpha_1^2 \frac{\gamma_1^c (V_{X_i}^{in1}(\omega) - 1) \mp \mu\alpha_1^2}{\left(\gamma_1 + \left[{}^3_1\right]\mu\alpha_1^2\right)^2 + \omega^2} \end{aligned} \tag{6.25}$$

The intuitive explanation for this squeezing is given in 4.3.1.

6.1.3 Squeezing limits

It can be seen from eqns 6.25 that both the reflected fundamental and the generated second harmonic can be squeezed. To find the optimum possible squeezing, consider the case of perfect coupling efficiency, $\gamma_1^c = \gamma_1$, and quantum noise limited input $V_{X_i}^{in1} = 1$. At high frequencies, $\omega \to \infty$, both the reflected fundamental and generated second harmonic are quantum noise limited in all quadratures and thus minimum uncertainty states:

$$\begin{aligned} V_{X_1}^{out1}(\infty) &= V_{X_2}^{out1}(\infty) = 1 \\ V_{X_1}^{out3}(\infty) &= V_{X_2}^{out3}(\infty) = 1 \end{aligned} \tag{6.26}$$

The maximum possible second harmonic squeezing occurs at zero frequency, $\omega = 0$, and infinite nonlinear interaction, $\mu\alpha_1^2 \to \infty$. The reflected fundamental is quantum noise limited. Both fields are minimum uncertainty states:

$$\begin{aligned} V_{X_1}^{out1}(0) &= 1 \qquad V_{X_2}^{out1}(0) = 1 \\ V_{X_1}^{out3}(0) &= \frac{1}{9} \qquad V_{X_2}^{out3}(0) = 9 \end{aligned} \tag{6.27}$$

The maximum possible fundamental squeezing occurs at zero frequency, $\omega = 0$, and finite nonlinear interaction, $\mu\alpha_1^2 = \gamma_1$. As this is the impedance matching point for the cavity (as $\gamma_1^c = \gamma_1$) the reflected field is a mildly squeezed vacuum[1], the second harmonic is somewhat squeezed. Neither field is a minimum uncertainty state, as $V_{X_1} V_{X_2} = 7/6$:

$$\begin{aligned} V_{X_1}^{out1}(0) &= \frac{2}{3} \qquad V_{X_2}^{out1}(0) = \frac{7}{4} \\ V_{X_1}^{out3}(0) &= \frac{7}{9} \qquad V_{X_2}^{out3}(0) = \frac{3}{2} \end{aligned} \tag{6.28}$$

All these limits are for the ideal case. In practical systems the squeezing will be less as $\gamma_1^c = \gamma$ is unobtainable and most seriously, $V_{X_1} = 1$ only at high frequencies. In practical lasers $V_{X_1} \gg 1$ as the detection frequency nears zero. As we shall see, this driving noise

[1] In 1991 Sizmann et. al. [10] proposed producing a strongly squeezed vacuum from the impedance matched reflection of a doubly resonant SHG cavity. In practice, the observed vacuum squeezing in both cases will be degraded by the non-modematched portion of the pump beam.

can totally obscure the squeezing.

6.2 Transfer of noise: a modular approach

A critical but often overlooked characteristic of quantum optics experiments is their sensitivity to source noise and its effect throughout the experiment. This has implications both for practical applications, where source noise is endemic, and for modelling, which most often assumes a coherent, and thus quantum noise limited at all frequencies, source.

The best known example of a system insensitive to source noise is the squeezed vacuum produced by optical parametric oscillation. By assuming the source is a coherent state, excellent agreement has been obtained between theory and experiment [11]. This is not the case for bright squeezing produced by processes such as Kerr interactions, rate matched lasers, or second harmonic generation. In such processes the statistics of the source beam carry over to the output beam. If the source beam is modelled as a coherent state for experiments where the source has intrinsic excess noise, the agreement between theory and experiment is quite poor [4] [6].

The development of the cascaded quantum formalism [12] allowed the noise characteristics of the source to be fully modelled and propagated via a master equation approach. The formalism was first tested for the case of squeezed light produced by second harmonic generation [5]. As Fig. 6.2 (a) shows, the system was modelled as a second harmonic generator driven by a solid state laser, which in turn was pumped by a coherent state. As is clear from Chapter 4, the cascaded formalism does not lend itself to analytical solutions, making physical interpretation of the theory difficult [13].

The noise spectra derived in this Chapter and Chapter 3 are effectively *transfer functions*: they alter an input function, $V^{in}(\omega)$, to an output function, $V^{out}(\omega)$. Such a transfer function can be derived for any quadrature of any linearisable optical element, be it active or passive, linear or nonlinear. This allows any optical element to be treated as a standalone module. Complex optical systems are modelled by simply combining these modules, and looking at the final output.

In Fig. 6.2 (b) we show the conceptual layout of the SHG squeezing experiment. The second harmonic generator is driven by a laser of frequency ν_1 and produces amplitude quadrature squeezed light of frequency $2\nu_1$. The driving laser, which is in turn pumped by a diode laser array, has intrinsic amplitude noise, which masks the squeezing at low frequencies. To improve the squeezing, the driving laser is passed through a narrow linewidth mode cleaning cavity, which reduces the linewidth of the amplitude noise. The system is particularly simple in that the transfer of noise is one way only, and it is not necessary to model the effects of optical feedback for any of the modules. The transfer function for the second harmonic generator is given by the second equation in eqns 6.25; that of the mode cleaning cavity is given by the second equation in eqns 3.81; and that of the laser is given in the next section, in eqn 6.32. Combining these three equations to give the output spectrum of the system is straightforward. Furthermore, modelling removal of the mode cleaner is trivial: the term V_{las}^{out} is used instead of V_{cav}^{out} as the input term $V_{X_1}^{in1}$ in eqn 6.25; and the parameter representing the power driving the second harmonic generator is adjusted. All other parameters remain fixed. Compare this to Schrödinger approach as given in [5, 9], which requires laborious numerical calculations.

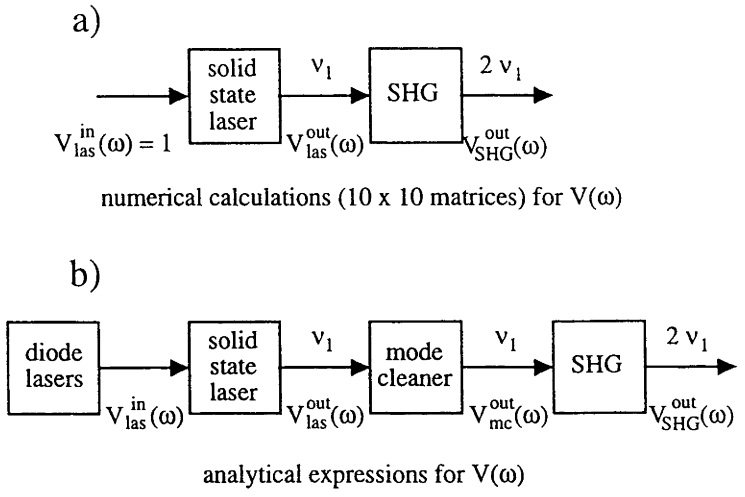

Figure 6.2: Conceptual layout. a) is the system of [5]. A second harmonic generator is driven by a coherently pumped laser of frequency ν_1 and produces amplitude quadrature squeezed light of frequency $2\nu_1$. Predictions are obtained via numerical calculation of large matrices. b) is the system presented in this chapter. To accurately reflect the experimental situation the solid state laser is modelled with a noisy diode laser pump. The solid state laser has intrinsic amplitude noise which masks the squeezing at low frequencies: to improve the squeezing, the laser can be passed through a narrow linewidth mode cleaning cavity which reduces the linewidth of the amplitude noise. Analytical spectra are presented for each stage of the experiment.

6.2.1 The laser model

A comprehensive quantum model of a Nd:YAG laser, including its transfer function, is given in [14]. In this section we briefly review the results applicable to our experiment. As shown in Fig. 6.3 the Nd:YAG laser is a four level system. As level 4 decays very rapidly with respect to the other three levels it can be adiabatically eliminated, allowing the laser to be modelled as a three level system. The equations of motion for the system are then:

$$\begin{aligned}
\dot{\alpha}'_{las} &= \frac{G}{2}(J'_3 - J'_2)\alpha'^2_{las} - \gamma_{las}\alpha'^2_{las} \\
\dot{J}'_2 &= G(J'_3 - J'_2)\alpha'^2_{las} + \gamma_{32}J'_3 - \gamma_{21}J'_2 \\
\dot{J}'_3 &= -G(J'_3 - J'_2)\alpha'^2_{las} - \gamma_{32}J'_3 + \Gamma J'_1 \\
N &= J_1 + J_2 + J_3
\end{aligned} \tag{6.29}$$

where G is the stimulated emission rate, $G = \sigma_s \rho c'$; σ_s is the stimulated cross section for the Nd:YAG laser; ρ is the density of the Nd atoms in the YAG crystal; c' is the speed of light in the laser medium; γ_{32} and γ_{21} are the spontaneous emission rates from levels $|3\rangle$ to $|2\rangle$, and $|2\rangle$ to $|1\rangle$, respectively; Γ is the rate of incoherent pumping of the lasing transition; γ_{las1} and γ_{las2} are the cavity decay rates for the output mirror and all other losses, respectively; $\gamma_{las} = \gamma_{las1} + \gamma_{las2}$ is the total cavity decay rate; α'_{las} and J'_i are the semiclassical solutions for the laser mode and atomic populations, respectively; and N is the number of active atoms. To aid calculation, the equations of motion are scaled by N,

i.e.:

$$\alpha_{las} = \frac{\alpha'_{las}}{\sqrt{N}}, \quad J_i = \frac{J'_i}{N} \tag{6.30}$$

The steady state solutions are:

$$\begin{aligned} \alpha &= \sqrt{\frac{J_2(\gamma_{21}-\gamma_{32})}{2\gamma_{las}}} \qquad J_1 = \frac{\gamma_{21}J_2}{\Gamma} \\ J_2 &= \frac{1-2\gamma_{las}/G}{\gamma_{21}/\Gamma+2} \qquad J_3 = J_2 + \frac{2\gamma_{las}}{G} \end{aligned} \tag{6.31}$$

The amplitude quadrature output spectrum, V_{las}^{out} is:

$$\begin{aligned} V_{las}^{out} = \; & 1 + \\ & (2\gamma_{las1})^2[\omega^2 + (G\alpha_{las}^2 + \gamma_{32} + \Gamma)^2] - 8\gamma_{las1}\gamma_{las}G\alpha_{las}^2(G\alpha_{las}^2 + \gamma_{32} + \Gamma) \\ & +2\gamma_{las1}G^2\alpha_{las}^2(\Gamma J_1 V_{las}^{in} + \gamma_{32}J_3) + 2\gamma_{las1}G[(\gamma_{32}+\Gamma)^2 + \omega^2](J_3 + J_2) \\ & +4\gamma_{las1}\gamma_{las2}[(G\alpha_{las}^2 + \gamma_{32} + \Gamma)^2 + \omega^2] \\ & \hline \\ & (2G\alpha_{las}^2\gamma_{las} - \omega^2)^2 + \omega^2(G\alpha_{las}^2 + \gamma_{32} + \Gamma)^2 \end{aligned} \tag{6.32}$$

where ω is the detection frequency and V_{las}^{in} is the amplitude quadrature spectrum of the diode laser array field that pumps the Nd:YAG laser. As can be seen from the denominator of eqn 6.32 there is a resonance in the spectrum at the frequency $\omega_{RRO}^2 = 2G\alpha_{las}^2\gamma_{las}$. If this resonance is underdamped, $2G\alpha_{las}^2\gamma_{las} > (G\alpha_{las}^2 + \gamma_{32} + \Gamma)^2$, then a strong resonance appears at ω_{RRO}, known as the resonant relaxation oscillation (RRO). The RRO can be considered as an oscillation between photons stored in the lasing medium and photons stored in the laser mode. Below ω_{RRO} the spectrum is dominated by pump noise (the noise of the diode laser array) and quantum noise from the spontaneous emission and phase decay of the coherence. Above ω_{RRO} these noises roll off due to the filtering effect of the lasing cavity, so that at high frequencies the laser approaches the quantum noise limit. It is the tail of the large noise feature due to the RRO that we wish to attenuate with the mode cleaning cavity.

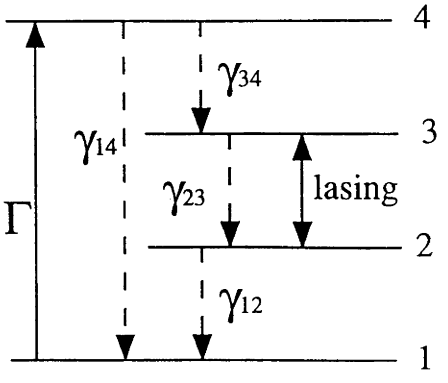

Figure 6.3: Laser level scheme. The fourth level decays very rapidly, and so can be adiabatically eliminated. Lasing occurs between levels three and two.

6.3 The experiment

6.3.1 The laser

The values for the material parameters of Nd:YAG can be found in the existing literature: $\sigma_s = 6.5 \times 10^{-23}\text{m}^2$; $\rho = 1.38 \times 10^{26}\text{atoms.m}^{-3}$; $c' = 1.640 \times 10^{8}\text{m.s}^{-1}$; $\gamma_{32} = 4.3 \times 10^{3}\text{s}^{-1}$; $\gamma_{21} = 3.3 \times 10^{7}\text{s}^{-1}$ [15, p. 49]; thus $G = 1.47 \times 10^{12}\text{s}^{-1}$. The Lightwave laser is most similar to that produced by Lazer Zentrum Hannover: the latter has a perimeter of $p = 28.5$ mm; an input coupler reflectivity of $R = 96.8\%$; and internal round trip losses of 1.6% [16]. We use these parameters to model the Lightwave. Using equation 2.22 we find $\gamma_{las1} = 9.28 \times 10^{7}\text{s}^{-1}$ & $\gamma_{las} = 1.39 \times 10^{8}\text{s}^{-1}$. Γ is the only fit parameter required; its value is determined by fitting the frequency of the predicted RRO to that of the experimentally observed RRO. The latter for our laser is 542 kHz, and so $\Gamma = 8.703\text{s}^{-1}$. The diode laser arrays used to pump the Nd:YAG laser suffer large, very broadband, amplitude noise. We model the diode laser spectrum as white noise 52 dB above shot noise, i.e. $V_{las}^{in}(\omega) \simeq 160000$. This is consistent with the directly measured noise power for diode arrays [19].

The Lightwave 122 has an internal *noise-eater*, i.e. an optoelectronic feedback circuit that reduces the peak power of the RRO. Unfortunately the noise-eater significantly increases the noise in frequency regime that we desire to be quantum noise limited. Accordingly all data in this thesis have been taken with the noise-eater turned off.

The experimental noise spectra were obtained by examining the photocurrent with a Hewlett Packard spectrum analyser (HP-8568B). Despite its name, this instrument is actually a *signal* analyser: incoming photocurrent is digitally processed on the assumption that the input is made up of sinusoidal signals. Thus whilst the absolute power for large signals is correctly displayed, stochastic noise (such as the quantum noise floor) is displayed at powers 2 dB lower than the true power [18, p. 33] [17, p. 26]. For large signals, the signal to noise measurements must be corrected by 2 dB; for signals of the same power as the noise (nominal SNR = 1) the correction is 0.4 dB.

Although discussed in Hewlett-Packard's technical literature, this discrepancy is not at all widely appreciated in the quantum optics community. For experiments that look at the relationship between two similar noise spectra, such as squeezing experiments, the analyser behaviour can be ignored as it equally affects both spectra. However the analyser behaviour *cannot* be ignored when comparing deterministic signals to noise, as in QND and noiseless amplification experiments.

In this section we are interested in modelling the observed output of the laser. Due to the analyser effect, the observed spectra is nonlinearly distorted with respect to the actual spectra (almost no correction necessary at the peak of the RRO; ≈ 2 dB correction necessary at the quantum noise floor; varies in between). Fortunately this nonlinear behaviour can be mimicked reasonably well by a brute force adjustment to our model. Consider curve (a) in Fig. 6.4: the experimentally observed spectrum for 14 ± 0.5 mW of Nd:YAG light, attenuated from an output power of ≈ 210 mW. This observed spectra is distorted by the analyser effect: the theoretical spectra for this case (210mW attenuated to 14 mW) is not shown, as it does not match the observed spectra at all. However if we arbitrarily adjust our model (300mW attenuated to 14 mW) we obtain curve (b): the fit is very good, albeit a little high in the region 5-15 MHz. This is the only such adjustment necessary in this thesis.

6.3.2 The modecleaner

The mirror reflectivities were directly measured to be $R_1 = 97.5 \pm 0.1\%$, and $R_2 = 97.9 \pm 0.1\%$, at an incident angle of 45 degrees; and $R_3 = 99.89 \pm 0.1\%$ at an incident angle of 0 degrees. The losses of the mirrors 1 & 2 were inferred to be 0.35%. The cavity perimeter was measured to be 2.450 m $\pm$ 5 mm. From this we calculate the free spectral range (FSR) to be 122.4 MHz ($\mathcal{FSR} = c_0/(np)$). It is now possible to calculate the decay rates using eqn 2.22: the total decay rate is $\gamma_{mc} = 3.33 \times 10^6 s^{-1}$, the incoupling rate is $\gamma_{mc'1} = 1.29 \times 10^6 s^{-1}$ and the outcoupling rate is $\gamma_{mc2} = 1.54 \times 10^6 s^{-1}$.

The optimum modematch measured for the cavity was $96.0 \pm 0.5\%$, and the optimum measured impedance match was $88 \pm 1\%$. The total power matching factor, $\mathcal{M}$, is thus:

$$\mathcal{M} = 0.96 \times 0.88 = 0.8448 \tag{6.33}$$

The transmitted power was measured to be $60.1 \pm 0.5\%$, and was a maximum immediately following cleaning of all the mirrors. In the hour following a mirror clean the transmitted power asymptoted to $\approx$ 50% as the high circulating power in the cavity trapped and carried dust onto the mirrors (the cavity is free-standing in unfiltered air). The observed transmitted power is in excellent agreement with the predicted transmitted power, which is given by:

$$\frac{P^{trans}}{P^{in}} = \mathcal{M}\frac{4\gamma_{mc1}\gamma_{mc2}}{\gamma_{mc}^2} = 0.607 \tag{6.34}$$

Curves (c) & (d) in Fig. 6.4 show the predicted and measured spectra for a beam of 14 mW transmitted through the modecleaner. The agreement between theory and experiment is excellent. The effect of the modecleaner is clear: there is substantial noise reduction as seen by the quantum noise limited frequency moving from 45 MHZ to 7MHz.

6.3.3 The frequency doubler

The doubler cavity perimeter is measured to be 25.0 m $\pm$ 0.5 mm. From this we calculate the free spectral range (FSR) to be 5.370 GHz ($\mathcal{FSR} = c_0/(np)$).

When the monolith is at room temperature there is very little nonlinear coupling (if the room is darkened some second harmonic can be observed but it is microwatts or smaller.) The linewidth of the cavity is only set by the mirror reflectivities and material loss: this is the natural, or "cold", cavity linewidth. When the monolith is heated to $\simeq 110°C$ the nonlinear coupling becomes significant, and the additional loss from the fundamental to the second harmonic significantly broadens the cavity mode. This is the power broadened, or "hot", cavity linewidth.

Hot or cold, the linewidth can be measured directly. The monolithic cavity is scanned through the TEM_{00} mode and the FWHM of the transmitted beam is measured with an oscilloscope. A frequency scale is provided by modulating the laser at 20 MHz which produces obvious side peaks. The ratio of the FWHM (in s) to the distance between the sidepeaks (in s) times twice the modulation frequency gives the FWHM in MHz. for the cold cavity, the measured FWHM is 5.67 ± 0.10 MHz. From this we can infer a total decay rate of $\gamma_1 = 1.78 \times 10^7 s^{-1}$.

The maximum observed second harmonic conversion efficiency is $\eta_{nl} = 56\%$. From, $\eta_{nl} = \gamma_1^c/\gamma_1$ we can infer the outcoupling decay rate, $\gamma_1^c = 9.95 \times 10^6 s^{-1}$. The strength of the nonlinear coupling does not alter the maximum second harmonic conversion efficiency, only the power at which it occurs.

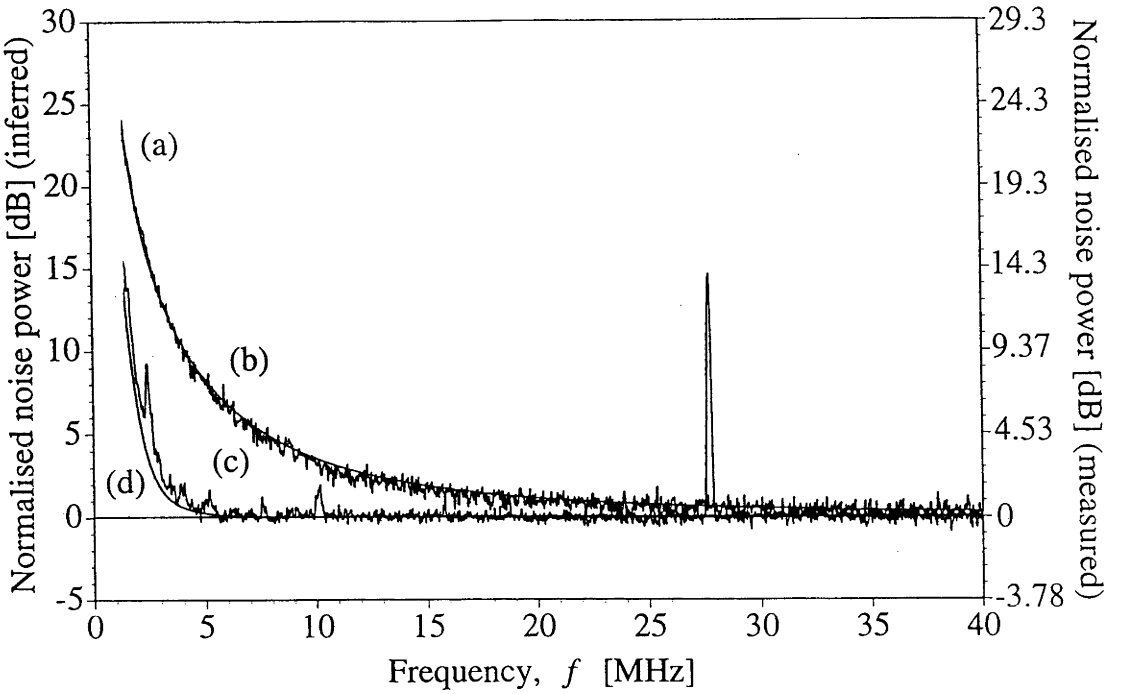

Figure 6.4: A comparison of the mode cleaner and laser output spectra for power incident on the infrared balanced detector of 14 mW. The experimental traces have been corrected for electronic noise. The upper traces, (a) & (b) are, respectively, the experimental and theoretical traces for the output spectrum of the laser (with the noise eater turned off). The lower traces (c) & (d) are the equivalent for the mode cleaner output spectrum. The noise filtering action of the mode cleaner is very clear. While the laser is not quantum noise limited until beyond 50 MHz, the output of the mode cleaner is quantum noise limited beyond 7 MHz. The large peak at 27.6 MHz is the modulation signal for the locking of the mode cleaner.

In theory the temperature (phase match) for maximum second harmonic generation is the temperature where greatest squeezing will occur. In principle the phasematching curve is a sinc function: best squeezing results should be obtained at the peak. However in practice the phase matching curve is not a sinc function, and due to the presence of a parasitic OPO and a Kerr effect (see next two chapters), the optimum squeezing was not observed for the maximum nonlinearity. At the point of optimum squeezing, we infer $\mu = 0.10$.

The second harmonic generator produces squeezed light at 532 nm that is picked off with a dichroic and detected via a self-homodyne detector. In general the quantum efficiency of available photodetectors is lower in the green than in the infrared. To maximise quantum efficiency, the photodetectors (EG&G FND-100) have the external glass removed, are turned to Brewsters angle, and the reflected light is directed back onto the detector via a curved retroreflector. These measures push the quantum efficiency of each detector to $65\% \pm 5\%$.

The second harmonic generator was pumped with a mode matched power of 81 mW, producing 34 mW of second harmonic light. Higher pump powers than this cause the onset of parasitic parametric oscillation (see next chapter) which degrades the squeezing. Fig. 6.5 clearly shows the effect of driving noise on the squeezing of the second harmonic.

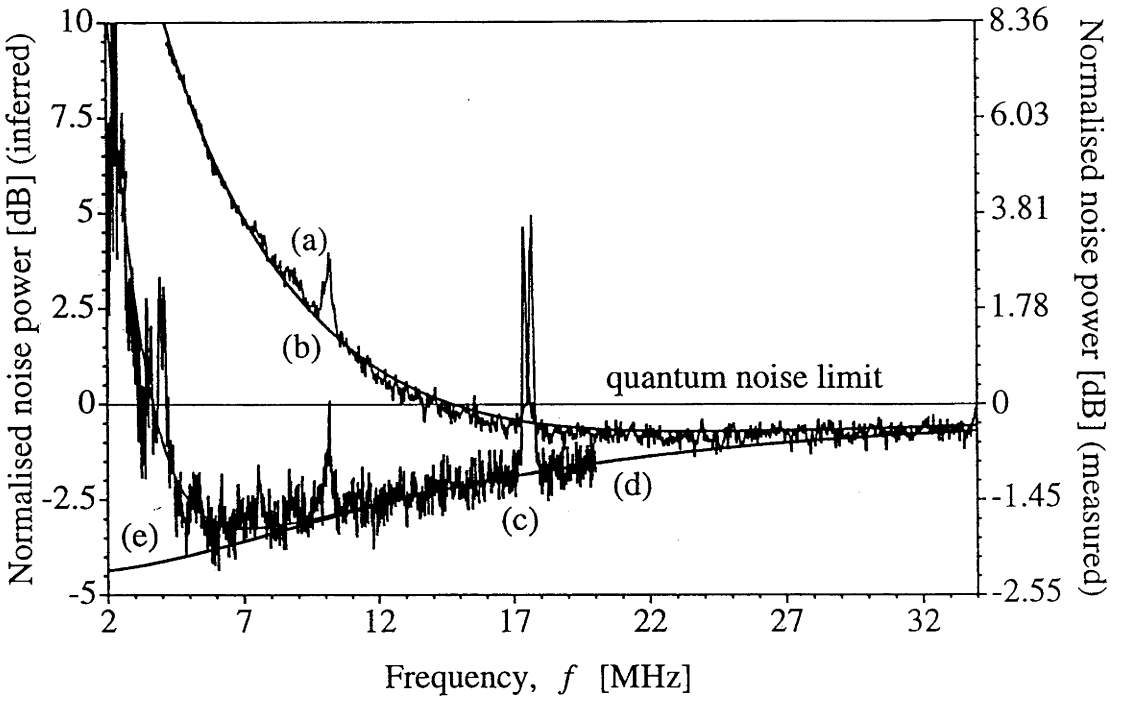

Figure 6.5: Squeezing spectra of the second harmonic. The mode matched power of the fundamental was 81 mW, the second harmonic power was 34 mW. The experimental traces have been corrected for electronic noise. Trace (a) and trace (c) are the spectra obtained for the experiment run without and with the mode cleaner respectively. The maximum squeezing and detection frequency of occurrence in each case are: trace (a), 0.47 dB (0.75 dB inferred) at 23 MHz; trace (c), 1.7 dB (3.0 dB inferred) at 7.5 MHz. The sub shot noise noise feature at 10 MHz on trace (c) is residual noise from the locking systems of the mode cleaner and the second harmonic generator. Traces (b) and (d) are the theoretical plots corresponding to the experimental traces. Trace (e) is the theoretical prediction for the squeezing if there were no extra noise present at all, i.e the driving field were coherent.

First consider the system without the modecleaner. Trace (a) is the second harmonic spectrum: it is far from the ideal result (quantum noise limited pump) as shown by trace (e). Trace (b) is the theoretical spectrum taking into account the laser noise. The agreement between theory and experiment is excellent: very clearly, the laser noise causes significant degradation of the squeezing. To produce trace (e), eqn 6.25 was used with $V_{X_1}^{in1} = 1$; to produce trace (b) the term $V_{X_1}^{in1}$ in eqn 6.25 was replaced with V_{las}^{out}, i.e. eqn 6.32.

Now consider the effect of the modecleaner. As trace (c) shows, the squeezing is considerably improved: the maximum squeezing is moved from 0.47 dB (0.75 dB inferred) at 23 MHz to 1.6 dB (3.0 dB inferred) at 7.5 MHz, and the spectrum above 11 MHz is that predicted for the ideal case with no excess pump noise. The sub shot noise feature at $\simeq$10 MHz is residual noise from the locking system (c.f. Fig. 6.4). The agreement with theory, trace (d), is again excellent. To reiterate our earlier point: the only changes to the model between producing traces (b) and (d) was the inclusion of the mode cleaner (equation 3.81) at the appropriate place in equation 6.25, and an adjustment of the parameter representing the optical power reaching the monolith. All other parameters remain fixed.

The squeezing measurement is a sensitive test of the modular model. For example, the diode lasers that pump the solid state laser have considerable excess noise (more than 50 dB above the quantum noise limit). In [5] this was not considered - the diode laser was modelled as quantum noise limited, and yet excellent agreement was obtained between theory and experiment. This is not true for the modecleaner case, where there is a greater degree of squeezing. The approximation that the diode laser pump is quantum noise limited gives poor agreement between theory and experiment: it is necessary to include the correct amount of excess classical noise.

The excellent agreement between theory and experiment, and the inclusion of the modecleaner which led to the large observed improvement in squeezing (from 0.75 dB to 3.0 dB, inferred), suggests a significant improvement is possible in the system of reference [6]. The modular approach can be applied to any experiment where transfer of source noise is significant, notably injection locked laser systems [19] and holds great potential for modelling complicated multi element experiments, such as gravity wave interferometers.

6.4 Squeezing via SHG: the next generation?

As an optical source, SHG offers power, stability, and simplicity. Squeezing via second harmonic generation was first demonstrated in 1988: however it has been criticised as a squeezing source as it has not been well characterised. This is no longer a valid criticism: in this chapter we have identified, modelled, and tested against experiment the effect of pump noise on the squeezing. Further, in the next two chapters we do the same for the effects of competing and cooperating nonlinearities, respectively. Squeezing via SHG in practical systems is now well characterised and understood. There are likely to be two directions of research for the next generation of experiments: cavity systems and travelling wave systems.

Consider the cavity system is this thesis. There are several obvious improvements and extensions that would allow miniaturisation of the experimental setup, improved stability, and greater squeezing. Most immediate is replacement of the current modecleaner. The relatively low reflectivity of the mirrors necessitate a long perimeter to achieve the desired narrow linewidth. However the lengthy perimeter allows for differential vibration of its component mirrors, making it hard to lock, and the large footprint clutters the experimental layout. The 2 m ring cavity could be replaced with a much shorter standing wave cavity with higher reflectivity mirrors. For example, REO supplies mirrors for 1064 nm with absorption and scatter loss of 5 ppm and transmission of $\simeq$ 30 ppm. An 8 cm cavity with these mirrors would have an equivalent linewidth to the 2 m cavity. The reflected beam could be extracted by inputting the beam through a polarising beam splitter and quarter wave ($\lambda/4$) plate; the transmitted beam would need to be passed through a quarter wave plate to return it to linear polarisation. If the cavity is built around an Invar©spacer, it will be intrinsically stable, and, as it is almost totally enclosed, much less susceptible to dust problems.

The current experimental setup could also be extended by adding an external mirror for 532 nm. For high reflectivities this would require another locking loop to maintain the second harmonic cavity on resonance. As discussed in Chapter 4, the addition of a cavity at the second harmonic will tend to improve the squeezing at a frequency well away from zero frequency. This further evades the problems of low frequency laser noise.

A longer term, and perhaps more desirable, improvement is to redesign the SHG

cavity. A larger linewidth is desirable, as it allows large squeezing at higher frequencies away from the pump noise of the laser. This can be achieved by a combination of a shorter cavity perimeter and/or using one of the new high nonlinearity materials, such as PPLN (periodically poled $LiNbO_3$) or BLIRA-free $KNbO_3$ [2]. The higher nonlinearity also allows the cavity to be driven harder for a fixed pump power, improving the magnitude of the squeezing. The higher nonlinearity lowers the TROPO threshold: it is desirable to design a cavity with dispersive elements to avoid this (see next chapter). The combination of these features may allow the modecleaner to be dispensed with entirely.

As mentioned in the introduction it has been predicted that strong squeezing will be available via travelling wave SHG. The recently developed periodically poled materials appear to be the materials of choice for the next generation of these experiments. Previously high peak power pulses were necessary to attain strong interactions in travelling wave SHG systems: now it is possible to use CW light. The Stanford group recently achieved 40% nonlinear conversion *single-pass* with a 50 mm long waveguide pumped with a 5.6 W 1064 nm beam, generating 2.25 W at 532nm [20]. It is very likely that the residual 3.35 W 1064 nm beam was squeezed by -2.2 dB/40% (S= $1 - \eta = 1 - .4 = .6$) over a very wide detection bandwidth (no cavity linewidth means the limit is set by the material response).

Observations of such very bright beams will be non-trivial: as discussed in section 3.4.4 one possible technique is to lock the beam to a cavity that transmits most of the beam power and then detect the squeezing on the low power reflected beam at a frequency much higher than the cavity linewidth. Alternatively, if the squeezing bandwidth is optical, then it may be possible to observe the squeezing by shining the beam onto a low-loss high-power diffraction grating and examining the vacuum squeezing at the line immediately adjacent to 1064nm. A small amount of the carrier can be used as the local oscillator. This will either require extremely high bandwidth photodetection, or, as is more likely, frequency shifting of the local oscillator. A final possibility is to chop the light beam to reduce the DC power and observe the squeezing at frequencies well above, and away from the harmonics of, the chopping frequency.

Chapter 6 bibliography

[1] S. F. Pereira, Min Xiao, H. J. Kimble, and J. L. Hall, Phys. Rev. A, **38**, no. 9, p. 4931, 1988.*Generation of squeezed light by intracavity frequency doubling*

[2] A. Sizmann, R. J. Horowicz, G. Wagner, and G. Leuchs, Opt. Commun., **80**, no. 2, p. 138, 1990. *Observation of amplitude squeezing of the up-converted mode in second harmonic generation*

[3] P. Kürz, R. Paschotta, K. Fiedler, A. Sizmann, G. Leuchs, and J. Mlynek, **24**, no. 6, p. 449, 1993. *Squeezing by Second-Harmonic Generation in a Monolithic Resonator;*

P. Kürz, R. Paschotta, K. Fiedler, and J. Mlynek, Europhys. Lett., Appl. Phys. B, **55**, p. 216, 1992. *Bright Squeezed Light by Second-Harmonic Generation in a Monolithic Resonator*

[4] R. Paschotta, M. Collett, P. Kürz, K. Fiedler, H.-A. Bachor and J. Mlynek, Phys. Rev. Lett., **72**, p. 3807, 1994. *Bright squeezed light from a singly resonant frequency doubler*

[5] T. C. Ralph, M. S. Taubman, A. G. White, D. E. McClelland, and H.-A. Bachor, Opt. Lett., **20**, no. 11, p. 1316, 1995. *Squeezed light from second-harmonic generation: experiment versus theory*

[2] BLIRA ≡ Blue Light Induced Red Absorption. The short wavelength light in $KnBO_3$ can induce additional absorption at long wavelengths in addition to the intrinsic loss of $KnBO_3$. This degrades the nonlinearity to loss ratio, and has been the bane of previous squeezing experiments with $KnBO_3$. Tsuchida [6] avoided BLIRA by carefully selecting pump wavelengths and crystal orientation

[6] H. Tsuchida, Opt. Lett., **20**, no. 21, p. 2240, 1995. *Generation of amplitude-squeezed light at 431 nm from a singly resonant frequency doubler*

[7] S. H. Youn, S.-K. Choi, P. Kumar, and R.-D. Li, Opt. Lett., **21**, no. 19, p. 1597, 1996. *Observation of sub-Poissonian light in a travelling-wave second-harmonic generation*

[8] A. G. White, M. S. Taubman, T. C. Ralph, P. K. Lam, D. E. McClelland, H.-A. Bachor, Physics Review A, **54**, p. 3400, 1996. *Experimental test of modular noise propagation theory for quantum optics*

[9] D. F. Walls & G. J. Milburn, *Quantum Optics*, First Edition, Springer-Verlag, Berlin, 1994

[10] A. Sizmann, K. fielder, P. Kürz, R. Paschotta and J. Mlynek, Technical Digest of the EQEC, p. 145, 1991. *Squeezed vacuum from second harmonic generation*

[11] E. S. Polzik, J. C. Carri, and H. J. Kimble, Phys. Rev. Lett., **68**, p. 3020, 1992. *??*

[12] C. W. Gardiner, Phys. Rev. Lett., **70**, p. 2269, 1993.

H. J. Carmichael, Phys. Rev. Lett., **70**, p. 2273, 1993. *Quantum Trajectory Theory for Cascaded Open Systems*

[13] A. G. White, T. C. Ralph, and H.-A. Bachor, Journ. Opt. Soc. Am. B, **31**, no. 7, p. 1337, 1996. *Active versus passive squeezing by second-harmonic generation*

[14] T. C. Ralph, C. C. Harb and H.-A. Bachor, Phys. Rev. A, **54**, no. 5, p. 4359, 1996. *Intensity noise of injection-locked lasers: Quantum theory using a linearised input-output method*

[15] W. Koechner, *Solid State Laser Engineering*, Fourth Edition, Springer-Verlag, Berlin, 1996

[16] I. Freitag, Lazer Zentrum Hannover, Hannover, Germany, *private communication*, 1994

[17] M. B. Gray, PhD thesis: *Quantum Noise Limited Interferometry*, Australian National University, Canberra, ACT 0200 Australia, 1995.

[18] Hewlett-Packard Technical Note, Application Note 150: *Spectrum Analyser Basics*, Hewlett-Packard Company, Blackburn, VIC 3130, Australia, 1992

[19] C. C. Harb, T. C. Ralph, E. H. Huntington, I. Freitag, D. E. McClelland and H.-A. Bachor, Physics Review A, **54**, no. 5, p. 4370, 1996. *Intensity-noise properties of injection-locked lasers*

[20] E. Gustafson, Stanford University, *private communication*, 1996.

Chapter 7

Competing nonlinearities: going TROPO

troppo *adj.* mentally ill, allegedly from exposure to a tropical climate

The Australian Concise Oxford Dictionary

Parametric oscillation in a frequency doubler was first observed in 1993 [1]. Such competing nonlinearities are currently the object of much work, both theoretical and experimental, as they offer the ability to generate widely tunable cw light. In this chapter we examine the experimental classical and quantum signatures of Triply Resonant Optical Parametric Oscillation (TROPO), i.e. parametric oscillation in a frequency doubler where the second harmonic is not resonant. In the first section we examine the frequency generation characteristics: cascaded sum and difference frequency generation cause production of new frequencies centred around both the fundamental *and* the second harmonic frequencies. In the second section we observe and discuss power clamping of the second harmonic field. In the third section we derive the second harmonic squeezing spectrum for TROPO from the quadruply resonant case (QROPO) and compare the experimental and theoretical results.

The classical behaviour of TROPO was presented in section 2.4. To recap, the second harmonic in singly resonant generation is able to act as the pump for a nondegenerate optical parametric oscillation. The NDOPO occurs simultaneously and competes with, the SHG. The conceptual layout is shown in Fig. 7.1. The core experimental setup is as discussed in the preceding two chapters. The reflected infrared and generated second harmonic beams were sent either to balanced-homodyne pairs (to examine the noise spectra), or to optical spectrum analysers (to examine the spectral content).

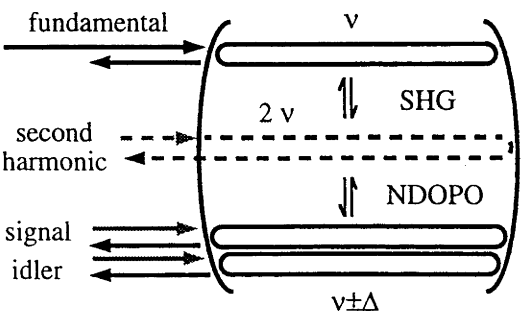

Figure 7.1: Conceptual layout of TROPO. Gray lines represent vacuum inputs, i.e. zero average power.

7.1 Frequency generation

The obvious signature of competition in TROPO is production of nondegenerate frequency modes once the system is driven above the competition threshold, i.e. N>1.

In section 2.4.2 it was calculated that the phase matching for nondegenerate frequency production was quite broad: 90% of the optimum nonlinear gain in the region 1064 ± 10 nm; 22% of the optimum nonlinear gain at 1031, 1097 nm. The nondegeneracy will be further limited by the cavity dispersion and the fixed bandwidth of the cavity mirrors ($\sim$ 40 nm centred at 1064 nm). How large a frequency nondegeneracy can be achieved in practice?

To test this experimentally the reflected infrared field was examined with a scanning diffraction grating whilst the cavity was scanned repeatedly through the TEM_{00} mode [1]. Scanning the monolith ensures that the cavity experiences a wide range of dispersions, and thus does not limit the possible resonances of the signal and idler. The output of the scanning grating is monitored with a silicon photodiode (EG & G FND-100). Fig. 7.2 shows the scanning grating output for the most nondegenerate case, $\Delta = 31$nm. This is the broadest nondegeneracy reported to date for this system. The large peak in the centre of the plot is the fundamental, at 1064 nm. The peak at the far left of the plot is the signal, that at the far right is the idler. The signal intensity is 4.3% of the 1064nm peak; the idler is much weaker. This may be intrinsic, i.e. idler production is weaker than signal, however it is more probable that this is due to the very steep roll-off in quantum efficiency in silicon photodetectors between 1000 & 1100 nm. The signal wavelength of 1033 nm agrees well with the calculated maximum of nonlinear gain centred at 1031 nm. The idler appears displaced slightly (2.5 nm) from its expected position of 1096 nm. This is an unavoidable artifact caused by hysteresis in the scanning motor of the scanning diffraction grating.

In practice, the phase matching curve is not simply the sinc function introduced in Chapter 2. (This is discussed in considerably more detail in the next chapter.) What is the effect of a non-ideal phase matching curve on the competition threshold?

To measure this, the monolith (#19) was again scanned repeatedly through the resonance. The reflected fundamental and generated second harmonic lineshapes were observed for signs of TROPO (see next section). Curve (a) in Fig. 7.3 is the observed threshold power versus the crystal temperature (and thus phase-matching). Curves (b) & (c) are the phase matching curves for SHG when driven by 33 mW of modematched fundamental. Curve (b) is single-pass SH, i.e. residual SH power generated on the first half of the round trip through the cavity that is transmitted through the high reflectivity mirror, and curve (c) is double-pass SH, i.e. the majority of the SH power that exits the AR coated side. Note that the threshold curve has two minima: roughly corresponding to maxima in the double pass and single pass power, respectively. In the latter case, even though minimal second harmonic is produced, the intracavity second harmonic field is large enough to pump the NDOPO.

The scanning diffraction grating is a slow method to analyse the spectral content of a field (it normally takes a minute or so to complete a scan). An optical spectrum analyser (OSA) allows quick spectral analysis of a field (in our case the scan time was 20 mS) but at the expense of absolute information. Optical spectrum analysers indicate the presence,

[1] The locked cavity results in this section were obtained with the ANU monolith ("the log"); the scanned cavity results in this section were obtained when the author was at Universität Konstanz, using "Kristall #19".

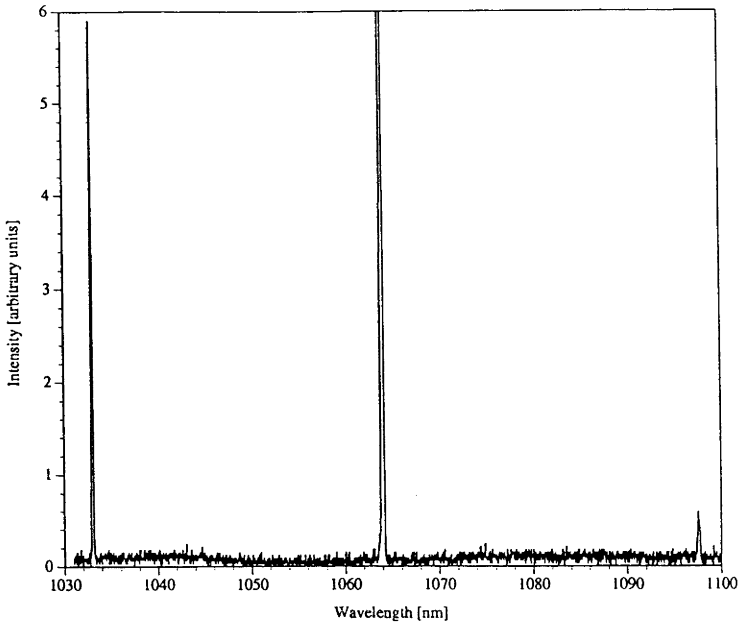

Figure 7.2: Broadband nondegenerate frequency production in the infrared. Light more than 30nm from 1064 is clearly visible.

but not the absolute optical frequency, of nondegenerate modes.

Fig. 7.4a is the output of the infrared optical spectrum analyser for the laser only. The laser frequency is clearly visible as the large spike on each side of the plot. (The small spike in the centre has no significance. It is due to misalignment of the analysed beam.) Fig. 7.4b is the output for the locked monolith (the log) just above threshold: note the strong conversion to signal and idler. The observed minimum threshold was 14 mW, the observed conversion efficiency at the minimum threshold was 60%. These values agree remarkably well with the calculated values. Using eqn 2.52 and the monolith parameters from Chapter 6, $\gamma_1^c = 9.94 \times 10^6$ & $\gamma_1 = 1.66 \times 10^7$, a nonlinear strength of $\mu = .012$ gives a calculated minimum threshold of $P_1^{min} = 14.3$ mW and a calculated conversion efficiency of $\eta = \gamma_1^c/\gamma_1 = 0.60$. The nonlinear value, μ, is different to that used in Chapter 6 as the crystal temperature was different. (As pointed in Chapter 6, the temperature for strongest nonlinear conversion was not the temperature for the strongest observed squeezing. For the parameters of Chapter 6, $P_1^{min} = 21$ mW.)

In locked operation, the signal and idler mode-hopped irregularly, stable operation occurred for up to ten minutes at a time. Gross control of the frequency and existence of the signal and idler was achieved by detuning the fundamental mode. As the monolith was detuned around resonance, the effective decay rate (see section 2.2.3) of the fundamental did not change greatly, but, due to dispersion mismatch, the effective decay rates of the signal and idler became very large (see section 2.3). This shifted the threshold power above the operating power and suppressed the NDOPO (c.f. eqn 2.48). In the system of [5], finer control was achieved by using a *hemilithic* cavity, i.e. a semi-monolithic design where a translatable cavity mirror is external to the MgO:$LiNbO_3$ crystal. Such a cavity has tunable dispersion, and allows for stable operation with long intervals between mode hops.

As the driving power was increased further two extra modes were observed in the

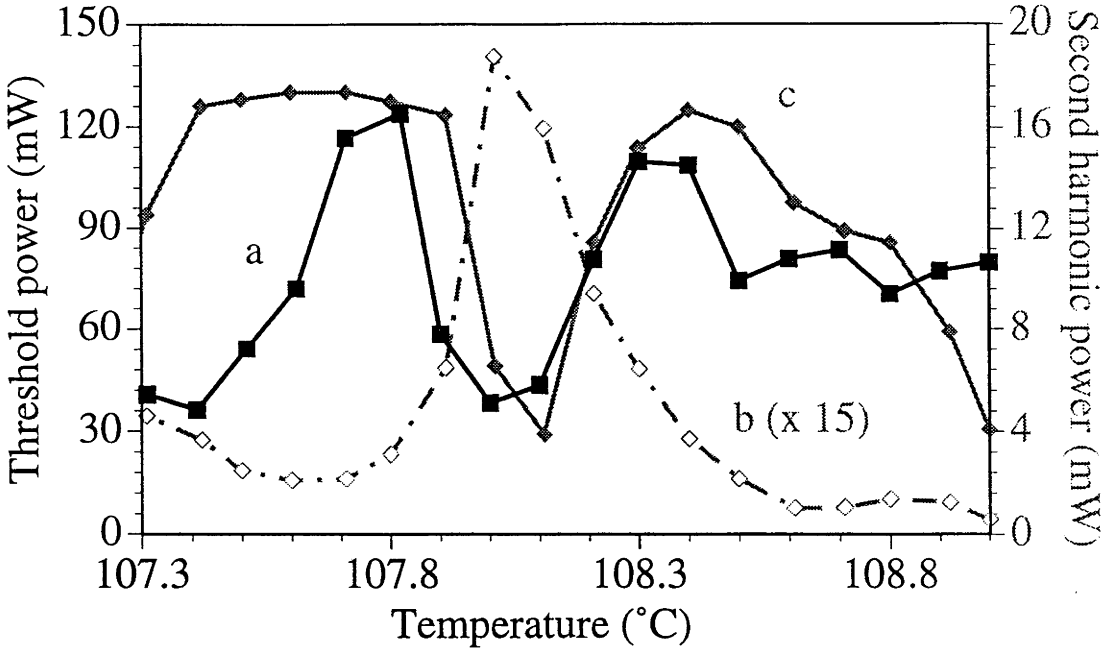

Figure 7.3: TROPO threshold and second harmonic power versus crystal temperature for Konstanz crystal. (a) observed threshold power; (b) single-pass SH power, (residual SH transmitted through high reflectivity mirror) & (c) double-pass SH power; as a function of crystal temperature (i.e. phase mismatch). Lines are guides for the eye.

infrared, and four extra modes were observed in the visible, Figs 7.4c,d - this is the first observation of extra modes around the second harmonic. Extra modes in the infrared were first observed in [2] where they were labelled as an extra signal idler pair. However it is impossible for parametric oscillation to drive two signal/idler mode pairs simultaneously, and such an explanation does not account for the extra modes in the visible. It was then proposed in [3] that the extra modes were due to cascaded second harmonic, sum and difference frequency generation between the signal, idler and pump fields. Figs 7.4c,d strongly support this mechanism. The extra modes in the visible are likely generated by SFG ($\nu + \nu_{s,i} = 2\nu \pm \Delta$) or SHG ($2\nu_{s,i} = 2\nu \pm 2\Delta$), whilst the extra pair in the infrared are from DFG with the visible modes ($\nu + \nu_{s,i} - \nu_{i,s} = 2\nu_{s,i} - \nu = \nu \pm 2\Delta$). Irrefutable proof of the mechanism will require a measurement of the absolute frequency of all the extra modes.

When the driving power was increased further, yet more modes were observed in the infrared field. This suggests that the cascading mechanism may be extended over quite a frequency range (observation of up to 8 extra mode pairs in the infrared has been reported [6]). Such systems of multiply competing nonlinearities hold great promise both as sources of frequency tunable light and for frequency measurement, e.g as a precise frequency chain.

Frequency chains can be made in many ways. One particularly elegant idea is the *FM laser*: a laser is modulated to produce sidebands at $\pm$ the FSR of the laser cavity. These build up and steal gain from the gain medium, and are in turn modulated at ± 1 FSR; the new sidebands at ± 2 FSR build up and steal gain and are in turn modulated, and so on. A broad frequency comb is generated, (with comb tooth spacing of 1 FSR) that is

chiefly limited by the gain bandwidth of the lasing medium. Now consider modulating a singly resonant doubler at 1 FSR and driving it well above the competition threshold. All other things being equal, the modulation will seed the signal and idler pair and a similar process to that in the FM laser will occur - with the advantage that frequency combs will be generated both in the infrared *and* the visible. Such a device should find immediate application in frequency chain measurements and applications.

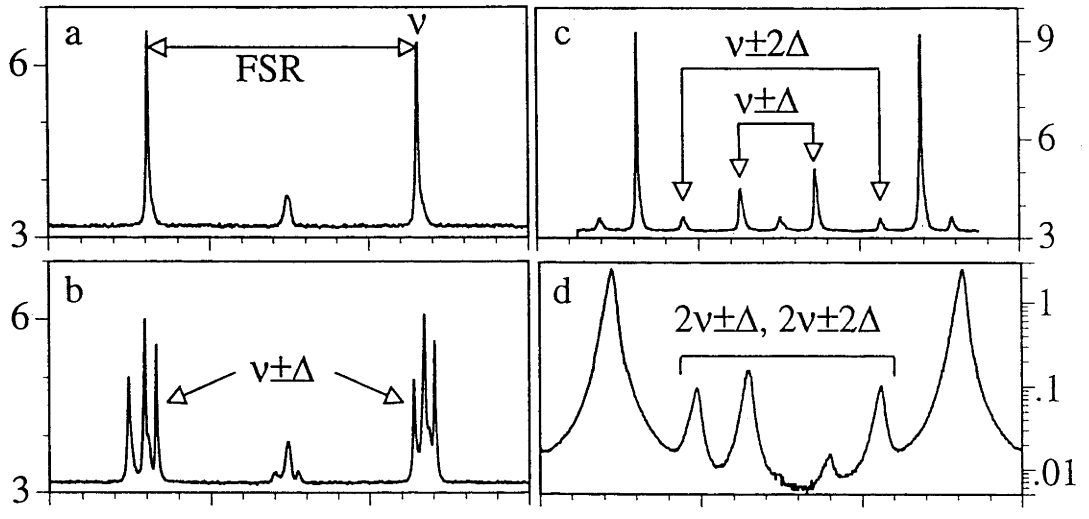

Figure 7.4: Optical spectrum analyser outputs of the locked monolith. All traces are intensity versus frequency (arbitrary units). The small peak in the middle of the infrared traces is due to imperfect alignment. *infrared traces* (a) from laser for P_1 =32 mW, FSR = free spectral range of the analyser; (b) from monolith for P_1 =14 mW, note signal and idler modes; (c) from monolith for P_1 =49 mW, note extra pair of modes; *visible trace* (d) from monolith for P_1 =155 mW , the ordinate is logarithmic to highlight the four extra frequencies.

7.2 Power signatures

For an empty cavity scanned through resonance the reflected and transmitted lineshapes have Lorentzian profiles. This is true of the monolith below the competition threshold, however above threshold the cavity lineshapes become quite notably distorted. At detunings where the signal and idler become resonant (i.e. at detunings where the driving power is above the competition threshold) the second harmonic lineshapes are depleted and the fundamental lineshapes are enlarged. The resulting lineshapes are not even approximately Lorentzian, with very obvious "hat" and "valley" shaped features on the infrared and visible lineshapes, respectively.

The signature of competition for a locked cavity is equally as dramatic. Fig. 7.5 shows experimental curves of second harmonic versus fundamental power for two different detunings. In curve (a) the second harmonic power is clamped at 23 mW at a threshold power of 41 mW. This threshold is much higher than the observed minimum threshold, P_1^{min} = 14.3 mW, as the signal and idler modes see high cavity losses due to dispersive mismatch. In curve (b) the monolith is tuned towards resonance so that the effective fundamental decay rate is lower than in curve (a), however the detuning increases the

dispersive mismatch, and thus $\gamma_{s,i}$, suppressing the NDOPO and moving the threshold to 54 mW. Fig. 7.5 was the first observation of power clamping, some 34 years after it was first predicted [7].

This phenomena has important consequences when designing nonlinear optical systems. Clamping is undesirable in many applications, such as frequency doubling to form a high power light source. With the development of low dispersion, efficient nonlinear cavities, clamping is expected to become a widely observed phenomenon. In the past year alone it has been observed in systems with competing SHG and NDOPO [4, 5, 8] and in an optical limiter formed by an OPO intracavity with a laser [9]. It can be suppressed via tunable dispersion, or avoided entirely by designing the system so that the minimum threshold point occurs at a power higher than maximum pump power. Ideally clamping shouldn't occur in many frequency doublers as they are optimised for maximum conversion efficiency, i.e. pumped at P_1^{min}. However in practice, many doublers are optimised by pumping them at powers above P_1^{min}. This is done because for powers less than P_1^{min} the conversion efficiency falls off very steeply: small variations in fundamental power lead to large variations in harmonic power. However above P_1^{min} the conversion efficiency falls off very slowly: the harmonic power is much more robust to small variations in the fundamental power. It is exactly this regime which is prone to competition.

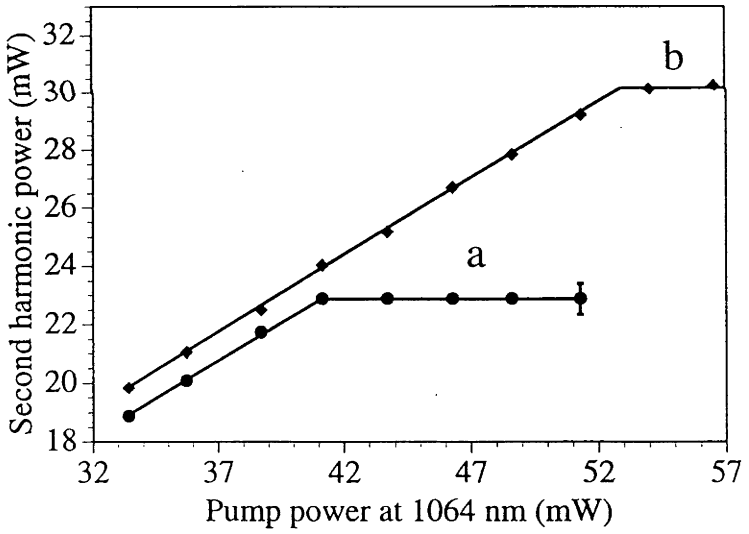

Figure 7.5: Second harmonic power versus fundamental power curves for two different detunings, (a) & (b). The systematic error bar is shown. All power measurements are NIST traceable with an absolute error of 7%.

7.3 Squeezing: 4 modes good, 3 modes bad

Classical signatures of competition all involve the redistribution of power (the second harmonic is clamped, new modes appear, etc.) Naturally such signatures only occur above threshold. In contrast, the quantum signatures of competition involve the redistribution of noise, and so can occur both below and above threshold.

NDOPO generates correlated signal and idler fields at frequencies $\nu_{s,i} = \nu_1 \pm \Delta$, where ν_1 is half the pump frequency. Above threshold the signal and idler are bright fields; below threshold they are correlated vacuum fields. As discussed in section 3.1.6, correlated quantum noise implies squeezing, and correlated amplitudes imply squeezing of the phase quadrature. Accordingly, Polzik et. al. [8] have suggested pumping the TROPO below threshold and examining the reflected fundamental field. If phase squeezing is observed in a region around the difference frequency Δ, then the presence of competition can be inferred, even though the NDOPO is below threshold. For the QROPO case, where the second harmonic is also resonant, the threshold will be lower but the signature will be the same. In our experiment the free spectral range of the monolith, (which sets the minimum value of Δ), is much larger than the maximum bandwidth of the detectors (5.4 GHz and 100 MHz, respectively), ruling out any observation of this signature.

Above threshold the QROPO and TROPO cases have very different quantum signatures. The QROPO case has been considered in a series of papers by Marte [10]. We briefly list the chief results here.

In Chapter 4 it was shown that, for high interaction strengths, the modes in doubly resonant second harmonic generation (DRSHG) experience a strong phase oscillation of frequency, ν_{dip}. The amplitude squeezing is improved at and around ν_{dip}. As the fundamental power is increased, the phase oscillation becomes larger, pushing the amplitude squeezing to zero. Above this power, the oscillation becomes real and the system undergoes a transition to the self-pulsing regime. QROPO has a notable effect: the frequency of perfect squeezing increases with increasing fundamental power; excess power is drained off to the signal and idler modes and the self-pulsing oscillation is damped out - the system remains stable. Another feature is that the quadrature of the squeezing rotates from amplitude to phase as the NDOPO comes to dominate the SHG.

The signal and idler modes are similar to those produced by normal NDOPO: they are perfectly correlated so that the subtracted intensity fluctuations of both beams is perfectly squeezed; and each individual beam can be amplitude squeezed up to 50% at high interaction. In a normal NDOPO, however, the added intensity fluctuations of both beams is Poissonian if the pump beam is Poissonian. In the QROPO case however, the added intensity fluctuations are squeezed, i.e. sub-Poissonian. This reflects the amplitude squeezing of the second harmonic that drives the NDOPO. Thus perfectly correlated signal and idler photons arrive at predictable intervals.

However in our system the second harmonic is not resonant, and the quantum signature of competition is very different: above threshold the squeezing degrades. To see this, we start with the QROPO case as given by Marte [10]. Recalling the equations of motion 2.45:

$$\begin{aligned}
\dot{\alpha}_1 &= -(\gamma_1 + i\Delta_1)\,\alpha_1 + \kappa_1\alpha_3\alpha_1^* + \sqrt{2\gamma_1^c}\epsilon_1 \\
\dot{\alpha}_3 &= -(\gamma_3 + i\Delta_3)\,\alpha_3 - \frac{\kappa_1^*}{2}\alpha_1^2 - \kappa_2^*\alpha_s\alpha_i \\
\dot{\alpha}_{s,i} &= -(\gamma_{s,i} + i\Delta_{s,i})\,\alpha_{s,i} + \kappa_2\alpha_3\alpha_{i,s}^*
\end{aligned} \tag{7.1}$$

where α_1, α_2, α_s , α_i are the fundamental, second harmonic, signal, and idler field amplitudes, respectively; and κ_1 and κ_2 are the respective nonlinear interaction rates for SHG and NDOPO. We redefine eqns 2.49 so that:

$$\bar{\gamma} = \sqrt{\gamma_s\gamma_i}$$

$$\mathcal{R} = \kappa_1/\kappa_2 \tag{7.2}$$

For a quantum noise limited fundamental pump, $V_{X_1}^{\nu_1} = 1$, and perfect outcoupling efficiency, $\gamma_1^c = \gamma_1$, the second harmonic spectrum is given by:

$$V_{\hat{X}_1}^{2\nu_1} = 1 - 4\gamma_2|\epsilon_2|\frac{\omega^2|\epsilon_1|^2 - |\epsilon_0|^2\Gamma_+^2(\omega)(1/\mathcal{R})}{\omega^2\mathcal{N}_+^2(\omega) + |\epsilon_0|^2\mathcal{M}_+(\omega)} \tag{7.3}$$

where:

$$\begin{aligned}
\epsilon_2 &= \mathcal{R}\bar{\gamma} \\
\epsilon_1 &= \sqrt{2N\mathcal{R}\bar{\gamma}\gamma_2} \\
\epsilon_0 &= \sqrt{2(N-1)\mathcal{R}\bar{\gamma}\gamma_2} \\
\Gamma_+^2(\omega) &= \omega^2 + (\gamma_1 + |\epsilon_2|)^2 \\
\mathcal{N}_+(\omega) &= \omega^2 - \gamma_2(\gamma_1 + |\epsilon_2|) - |\epsilon_1|^2 \\
\mathcal{M}_+(\omega) &= -2\omega^2[\Gamma_+^2(\omega) - |\epsilon_1|^2] + |\epsilon_1|^2\Gamma_+^2(\omega)
\end{aligned} \tag{7.4}$$

We can examine the TROPO case by adiabatically eliminating the second harmonic, i.e. $\gamma_2 \to \infty$. After straightforward, albeit somewhat tedious algebra the spectrum becomes [4]:

$$V_2 = 1 + \frac{2(N-1)B(\omega) - 2NA(\omega)}{(N-1)^2B(\omega) + \omega^2(\gamma_f/2\bar{\gamma})^2 + NA(\omega)C(N)/\mathcal{R} + (\omega^2/2\bar{\gamma})^2} \tag{7.5}$$

where N is the number of times above threshold (N> 1):

$$N = \frac{P_1}{P_1^{thr}} \tag{7.6}$$

and:

$$\begin{aligned}
\gamma_f &= \gamma_1 + \epsilon_2 \\
A(\omega) &= \mathcal{R}^2\omega^2 \\
B(\omega) &= \gamma_f^2 + \omega^2 \\
C(N) &= \gamma_1/\bar{\gamma} + \mathcal{R}(N+1) + 2(N-1)
\end{aligned} \tag{7.7}$$

If we assume the minimum threshold for competition, P_1^{min}, then $\gamma_s = \gamma_i = \gamma_1$ and $\mu_1 = \mu_2$ and equation 7.5 simplifies to [11]:

$$V_2 = 1 + \frac{2(N - 1 - \hat{\omega}^2)}{4N^2\hat{\omega}^2 + (N - 1 - \hat{\omega}^2)^2} \tag{7.8}$$

where $\hat{\omega} = \omega/(2\gamma_1)$. Both eqn 7.5 and eqn 7.8 are obviously very different to the description of the second harmonic spectrum in singly resonant SHG, c.f. eqn 6.25:

$$V_{X_1}^{2\nu_1}(\omega) = 1 + 8\gamma_{nl}\frac{\gamma_1^c(V_{X_i}^{in1}(\omega) - 1) - \gamma_{nl}}{(\gamma_1 + 3\gamma_{nl})^2 + \omega^2} \tag{7.9}$$

where the nonlinear loss rate, $\gamma_{nl} = \mu_1 |\alpha_1|^2$ and $V_{X_1}^{in1}$ is the amplitude quadrature spectrum of the pump field.

For the singly resonant doubler, maximum squeezing occurs at zero frequency with a value of V=1/9 (-9.5 dB) when $V_{X_1}^{in1} = 1$ and $\gamma_{nl} >> \gamma_1$, i.e. for high pumping powers. However once competition begins the maximum squeezing occurs at the competition threshold, for powers above threshold the squeezing degrades. For the minimum threshold, P_1^{min}, the maximum squeezing is at zero frequency with a value V=1/2 (-3 dB). For higher thresholds, $P_1^{thr} > P_1^{min}$, the maximum squeezing is still at zero frequency , but with correspondingly larger values. In all cases eqn 7.5 connects to eqn7.9 without discontinuity.

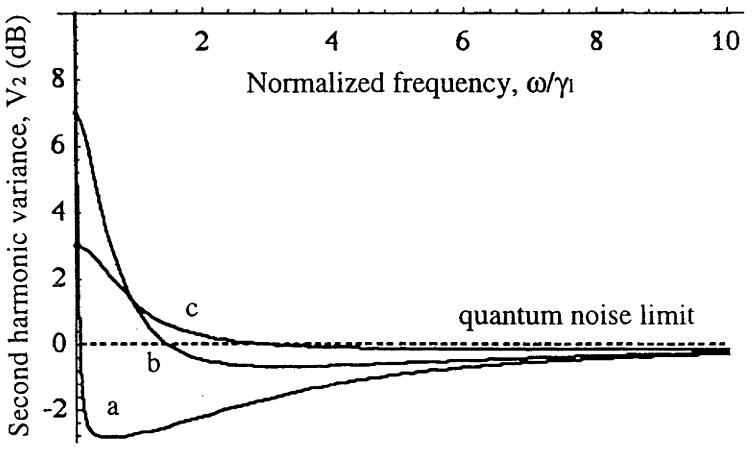

Figure 7.6: Theoretical second harmonic squeezing spectra for the TROPO case when $P_1^{thr} = P_1^{min}$. (a) N = 1.001 (b) N = 1.25 and (c) N = 3.

As Fig. 7.6 shows, for N>1 two effects come into play, both of which degrade the squeezing. The first effect is broadband. As N is increased, the second harmonic power is clamped, and the second harmonic noise is pulled towards the noise set by the second harmonic input field, $V_{X_1}^{in3}$. As this input is a vacuum field, the second harmonic noise is pulled towards the quantum noise limit. This occurs regardless of whether the original second harmonic noise is above (super-Poissonian), or below (sub-Poissonian), shot noise. In the limit N→ ∞ the output is always quantum noise limited, even if the second harmonic amplitude was infinitely noisy (perfectly phase squeezed), or infinitely quiet (perfectly amplitude squeezed).

We label this the *noise-eater effect*. It is analogous to the behaviour of the electro-optic noise-eater: i.e. a feedback loop where a beamsplitter cuts off a proportion of a beam and feeds it to a photodetector; the photocurrent drives an amplitude modulator that is placed before the beamsplitter. (This is an amplitude noise-eater, phase noise-eaters can also be constructed.) The input is the field before the modulator, the output is the field after the beamsplitter. For high gain, the output noise is pulled towards the limit set by the vacuum entering the empty beamsplitter port [12]. As the reflectivity of the beamsplitter is increased, the output power decreases but the output noise becomes dominated by the input vacuum field: in the limit R→ 1 the output is trivially quantum noise limited, as it is simply the perfect reflection of the input vacuum field. The electro-optic noise-eater is not homologous to the TROPO case: in the limit N→ ∞ the second harmonic field still contains power (P_2 (see eqn 2.55). This noise-eating behaviour is expected to occur in other nonlinear optical systems. It has been predicted for the optical limiter [13], i.e. a degenerate OPO that clamps the 2ν field (see section 2.4.1); and from simple physical

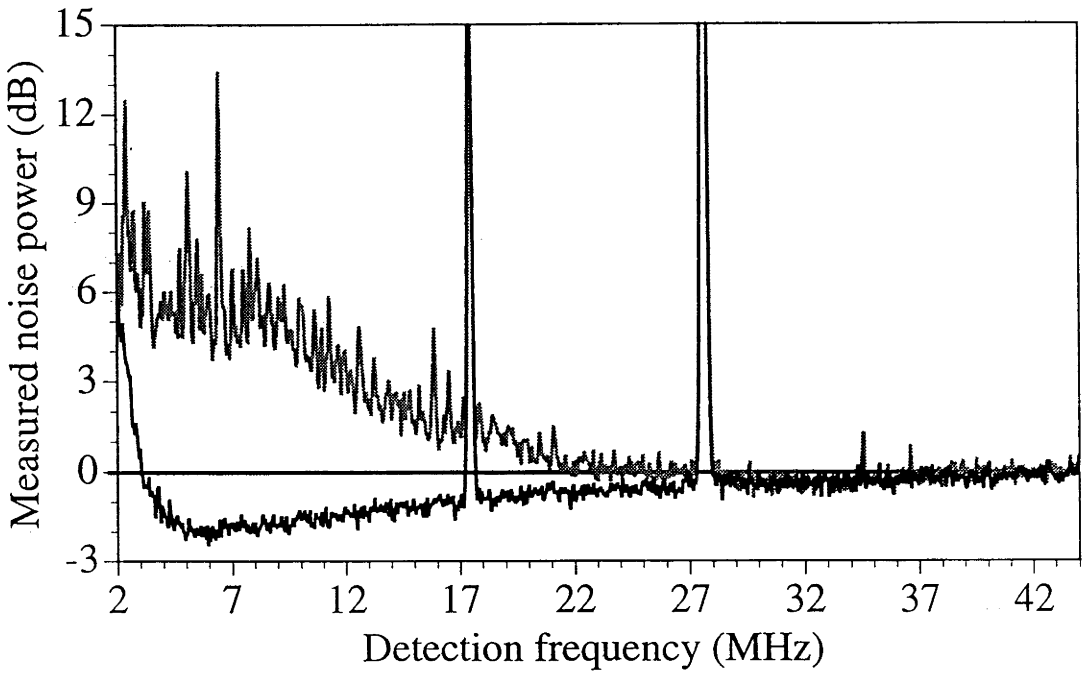

Figure 7.7: (a) Squeezing spectra. (a) Without competition, $P_1 = 74$ mW (b) With competition, $P_1 = 60$ mW.

arguments it is expected to occur in the saturated laser amplifier [14].

The additional squeezing degradation evident at low frequencies on the second harmonic is due to a second, more subtle, effect. In a conventional OPO, the amplitude quadratures of the signal & idler are very noisy above threshold, as the phase quadratures are quite strongly squeezed. (For a DOPO the amplitude only becomes shot noise limited at $P = 4P_{thr}$ and eventually becomes 50% squeezed for $P > 25P_{thr}$ [15]). This low frequency amplitude noise is transmitted from the signal and idler to the second harmonic, degrading the squeezing at low frequencies. However as N is increased this noise decreases, easing the low-frequency squeezing degradation, as can be seen from curves (b) & (c) in Fig. 7.6.

Fig. 7.7(a) shows the experimentally observed squeezing a pump power of 74 mW, competition is suppressed via detuning as discussed earlier. Below 6 MHz the squeezing degrades due to laser pump noise, as discussed in the last Chapter, above 6 MHz the squeezing is as expected from theory with $V_1^{in} = 1$. The spikes at 17 and 27 MHz are from the locking signals. With competition, even at the lower pump power of 60 mW, the squeezing degrades notably as shown in Fig. 7.7(b). As predicted, there is considerable excess noise at low frequencies, whilst the degradation at higher frequencies is more gradual. The excess noise at low frequencies is greater than that shown in Fig. 7.6 due to the presence of numerous, overlapping, noise spikes. It is believed that these spikes are due to a locking instability in the modecleaner which is driven by competing locking signals; with the modecleaner absent, these spikes disappear.

It is clear that even a small amount of χ^2 competition leads to a marked degradation in the squeezing. This previously unexpected limit to second squeezing can be avoided in one of two ways. This weakness can be turned into a strength if the second harmonic

is made resonant: however experimentally this is a more complicated setup. (With this in mind, "4 modes good, 1 mode better"). Alternatively the system can be designed so that competition is suppressed when the pump power is greater than the maximum conversion efficiency power. One solution is a cavity with high dispersion, so that the signal and idler modes are unable to become simultaneously resonant with the fundamental. The cavity used by Tsuchida [16] was highly dispersive , with many air/material interfaces, and the high value of second harmonic squeezing, -5.2 dB inferred, suggests that the system was well above its minimum threshold.

7.4 Summary of TROPO signatures

Competition between SHG and NDOPO in a monolithic cavity has been observed to cause generation of new frequencies in both the visible and infrared fields, clamping of the second harmonic power, and degradation of the second harmonic squeezing. Competition imposes a previously unsuspected limit to squeezing and power generation. These signatures are expected to be commonly observed in efficient, low dispersion systems, unless explicit steps are taken to avoid competition.

Chapter 7 bibliography

[1] S. Schiller and R. L. Byer, J. Opt. Soc. Am. B **10**, no. 9, p. 1696, 1993. *Quadruply resonant optical parametric oscillation in a monolithic total-internal-reflection resonator*

[2] S. Schiller, G. Breitenbach, S. F. Pereira, R. Paschotta, A. G. White and J. Mlynek, Proc. SPIE **2378**, Y. Shevy ed., p. 91, 1995. *"Generation of continuous-wave bright squeezed light", in Laser Frequency Stabilization and Noise Reduction*

[3] S. Schiller, G. Breitenbach, R. Paschotta, and J. Mlynek, Appl. Phys. Lett. **68**, no. 24, p. 3374, 1996. *Subharmonic-pumped continuous-wave parametric oscillator*

[4] A. G. White, P. K. Lam, M. S. Taubman, M. A. M. Marte, S. Schiller, D. E. McClelland and H.-A. Bachor, submitted to Physics Review A, 1996. *Classical and quantum signatures of competing $\chi^{(2)}$ nonlinearities*

[5] K. Schneider and S. Schiller, Opt. Lett., (in press 1997)

[6] G. Breitenbach, Universität Konstanz, Germany, (private communication)

[7] A. E. Siegman, Appl. Opt. **1**, no. 6, p. 739, 1962. *Nonlinear Optical Effects: An Optical Power Limiter*

[8] J. Sorensen, E. Polzik, and J. Ostergaard, Aarhus University, Denmark, (private communication), 1995

[9] F. G. Colville, M. H. Dunn, and M. Ebrahimzadeh, submitted to Opt. Lett., 29 Aug. 1996. *Continuous-Wave, Singly-Resonant, Intra-Cavity Optical Parametric Oscillator*

[10] M. A. M. Marte, Phys. Rev. Lett. **74**, no. 24, p. 4815, 1995. *Sub-Poissonian Twin Beams via Competing Nonlinearities;*

M. A. M. Marte, Acta Physica Slovaca **45**, no. 3, p. 253, 1995. *Mutual influence of two $\chi^{(2)}$-nonlinearities and the generation of sub-Poissonian twin beams;*

M. A. M. Marte, J. Opt. Soc. Am. B **12**, no. 11,, p. 2296, 1995. *Nonlinear dynamics and quantum noise for competing $\chi^{(2)}$ nonlinearities*

[11] S. Schiller, R. Bruckmeier, and A. G. White, Optics Communications, to appear, 1997. *Classical and quantum properties of the subharmonic-pumped parametric oscillator*

[12] M. S. Taubman, H. Wiseman, D. E. McClelland and H.-A. Bachor, J. Opt. Soc. Am. B **12**, p. 1792, 1995. *Effects of intensity feedback on quantum noise*

[13] M. Collett, Auckland University, New Zealand (unpublished), 1995.

[14] M. Gray, Australian National University, Australia (private communication), 1997.

[15] J. J. Slosser and G. J. Milburn, Phys. Rev. A, **50**, no. 1, p. 793, 1994. *Noise reduction in the nondegenerate parametric oscillator with direct detection feedback"*

[16] H. Tsuchida, Opt. Lett., **20**, no. 21, p. 2240, 1995. *Generation of amplitude-squeezed light at 431 nm from a singly resonant frequency doubler*

Chapter 8

Cooperating nonlinearities: Kerr effect

Oh Kerr, Occur!

Sign on laboratory door at Konstanz Universität, courtesy of Robert Bruckmeier

Third order, or $\chi^{(3)}$, nonlinear optical nonlinearities are of considerable importance in modern optics. In signal processing and communications they offer the potential to realize all-optical switching [1, 2]; in quantum optics they may be employed to manipulate the quantum fluctuations of light, in particular to generate nonclassical states of light [3, 4, 5] and perform quantum nondemolition measurements [6, 7].

Central to these applications is the search for materials exhibiting large nonlinearities; in addition they must be enviromentally stable and resistant to optical power. For quantum optical use the media must also have a large ratio of nonlinearity to loss in order to suppress the influence of vacuum fluctuations. A variety of $\chi^{(3)}$ media has been investigated, including vitreous silica, semiconductors, organic compounds, atomic beams, and cold atoms [3, 4, 5, 6, 7]. Because of the limitations (complexity and stability) of these systems, the possibility [8, 9] of using well known second order nonlinear materials for the same purposes sparked a new direction of research [10]. A number of studies [11] have discussed or demonstrated various aspects of cooperating effects in second harmonic generation.

In this chapter we investigate the strong Kerr effect that occurs in singly resonant SHG due to cooperating second order nonlinearities. Phase mismatch is central to this, so in the first section we investigate the phase matching curve for our experiments. Previous investigations that have seen strong third order effects in second order systems have been performed with single pass geometries, and used pulsed lasers with high peak intensities to attain a strong interaction. In the second section we report observation of optical bistability with low power, continuous wave light. In the third section we derive a quantum model for the Kerr effect via the Heisenberg approach, and briefly investigate its behaviour. In the fourth section we report preliminary observations of noise reduction due to the Kerr effect and in the fifth section we summarise our results.

The classical behaviour of the Kerr effect was presented in section 2.5. To recap, the phase matching in singly resonant SHG is tuned so that the second harmonic generated on the forward trip through the cavity is backconverted to fundamental on the return leg. The light is phase shifted during both processes, the processes are nonlinear, thus the fundamental experiences a nonlinear phase shift. The conceptual layout is shown in Fig 8.1. The basic experimental setup is as discussed in the previous chapters [1].

[1] The locked cavity results in this chapter were obtained with the ANU monolith ("the log"); the scanned cavity results in this chapter were obtained when the author was at Universität Konstanz, using "Kristall #19".

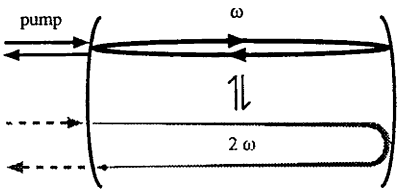

Figure 8.1: Conceptual layout of Kerr in nominally singly resonant SHG. Gray lines represent vacuum inputs, i.e. zero average power.

8.1 Phasematching

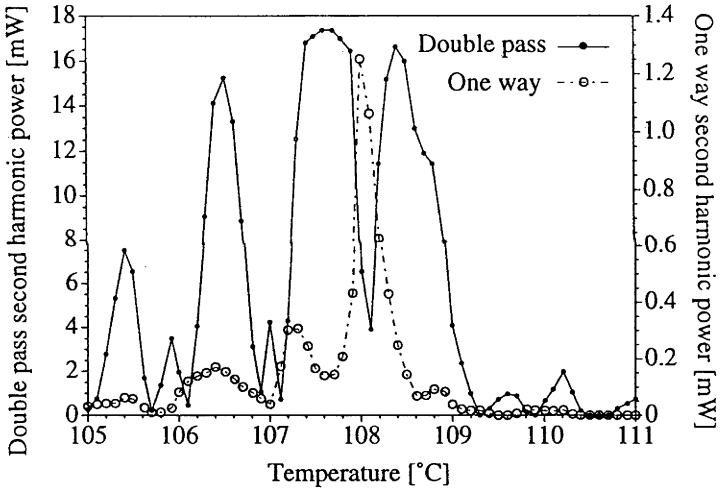

Figure 8.2: Phasematching curve for second harmonic (SH) generation. *double pass*: total SH power leaving the crystal through the AR side; *single pass*: fraction of SH power generated on the first half of the round trip and transmitted through the nominally high-reflectivity mirror. Modematched input 1064 nm power was 33 mW. Lines are guides for the eye.

To map out the phase matching curve the second harmonic power was measured as a function of crystal temperature. The cavity was repeatedly scanned through resonance: under these conditions for crystal # 19 the TROPO threshold was 49 mW; to avoid TROPO the cavity was driven at 33 mW. The power of both the single pass (residual second harmonic that is transmitted through the high reflector) and the double pass (second harmonic that exits the monolith through the AR coated face) beams was measured. Fig. 8.2 plots the observed results. Two points are striking: the double pass curve does not, even remotely, resemble a sinc function; and the single and double pass curves do not have the same shape.

Why is this? A major reason for the difference between the double pass curve and single pass curves is the differential phaseshift between the fundamental and second harmonic waves that occurs at the high reflector [12]. For an ideal singly resonant doubler

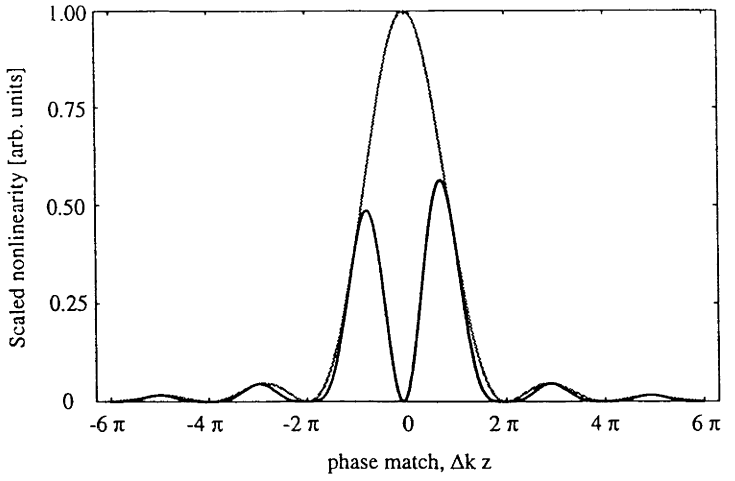

Figure 8.3: Nonlinear interaction, $g(\Delta kz)$, versus phase match: a) with no differential phase shift between fundamental and second harmonic waves $\Delta\phi = 0$; b) large differential phase shift, $\Delta\phi = 170°$.

with interference solely at the back mirror, this interference is described by [13]:

$$g(\Delta kz)_{int} = g(\Delta kz)\left[\frac{\sin(\Delta\phi + \Delta kz)}{2\sin(\Delta\phi + \Delta kz/2)}\right]^2 \tag{8.1}$$

where $\Delta\phi$ is the differential phase shift between the fundamental and the second harmonic at the back mirror. Fig. 8.3 plots $g(\Delta kz)$ versus phase match without and with a differential phase shift. The effect of the interference is clear: the strength of the nonlinearity is greatly reduced and the width of the phase matching peaks is narrowed. (Experimentally this is undesirable, as narrowed phase matching peaks require higher precision temperature locking.) Clearly something like this is occurring in our system, however it is not the entire story.

If the back reflector is the only cause of degradation then the single pass curve should be a sinc function. However in our system it is a distorted, asymmetric curve version of a sinc function (distinctly "sinc-ish", but not a sinc). This distortion is due to physical and temperature inhomogeneities in the crystal, that leads, even for a single pass, to interference effects between the fundamental and second harmonic. It is well known that MgO doped $LiNbO_3$ has many more inhomogeneities than pure $LiNbO_3$, and thus has a distorted phase matching curve [14]. For pure $LiNbO_3$ the FWHM of the phase matching curve has been measured to be 0.55 K [13]; from Fig. 8.3 we see that for our single pass curve the FWHM is 0.3 K. From this, and the distorted single and double pass curves, we conclude that the effective nonlinearity of our material is well below the optimum available with pure $LiNbO_3$.

8.2 Optical bistability

Recalling eqn 2.66, the classical equation of motion for a phase mismatch of $\Delta kz = 2\pi$ in a singly resonant doubler is:

$$\dot{\alpha}_1 = -(\gamma_1 + i\Delta_1)\,\alpha_1 \pm \frac{\mu}{\pi}|\alpha_1|^2\alpha_1 + \sqrt{2\gamma_1^c}\epsilon_1 \tag{8.2}$$

That is, the system acts exactly as a Kerr medium, where $i\,(^{\mu}/_{\pi})|\alpha_1|^2$ is the nonlinear phase shift and $i\Delta_1$ is the linear phase shift. High cavity finesse increases the field α and thus enhances the nonlinear interaction. As shown earlier, significant nonlinear behaviour occurs when the linear detuning, Δ_1, is of the order (but opposite in sign to) the nonlinear detuning, $(^{\mu}/_{\pi})|\alpha_1|^2$. Loss thus play a critical role in the experimental realisation of this system, as both the enhancement and the relative detuning scale inversely with cavity losses.

Figs 8.4 & 8.5 show the behaviour of the line shape of the cavity mode at high input power (125 mW) as the laser is detuned back and forth. The data was obtained by recording the 1064 nm power transmitted through the nominally highly reflecting mirror, which is proportional to $|\alpha|^2$. The wavevector mismatch ΔkL was controlled by varying the temperature (T) of the crystal relative to the phasematching peak at about 108°C, with a tuning coefficient $\partial\Delta k/\partial T$=7.5 rad/(cm K).

In scanned operation the linewidth of crystal # 19 was measured to be 9.0 MHz: from this a total, cold cavity, decay rate of $\gamma_1^c = 2.8 \times 10^7 s^{-1}$ (i.e. $T^c = 0.33\%$). From the linewidth and the incoupling at resonance the cavity loss was inferred to be $\gamma_1^\ell = 1.3 \times 10^7 s^{-1}$ (i.e. $T^\ell = 0.30\%$): the crystal is relatively lossy. Note that the round-trip conversion efficiency at the phasematching peak of $53 \pm 1\%$ agrees well with the predicted maximum conversion efficiency of $\eta_{nl} = T^c/(T^c + T^\ell) = 53\%$. A SHG coefficient $\Gamma_{SHG} \simeq 2/\text{kW}$ is inferred from this result.

From the plane wave analysis in section 2.5.2, the minimum optical bistability threshold is expected when the external conversion efficiency is near zero. The measured double pass SHG efficiency in Fig. 8.3 exhibits near zero minima, which were therefore chosen as the operating points for the observation of the cascading effect. Assuming the idealised calculations of section 2.5.2 to be valid, we calculate that the minimum power for optical bistability is $P_1^{\text{bi thr}} \simeq 45$ mW.

Irrespective of crystal temperature and Δk, absorption of circulating power causes the cavity to heat and expand, resulting in the cavity lineshapes leaning to negative detunings (see section 2.5.4). To attenuate the influence of this thermal effect, the laser was scanned through resonance relatively quickly (11.8 MHz/μs). Fig. 8.4 shows the lineshape when the doubler is operated at room temperature where the phase mismatch is extremely large. No significant asymmetry due to the thermal effect is observed. With the crystal temperature adjusted for maximum SHG efficiency, a significant broadening due to the conversion loss $\mu \text{Re}\mathcal{J}_2'|\alpha|^2$ is observed and a corresponding reduction in circulating subharmonic power. However there is still no significant scanning asymmetry. From this we conclude that the thermal effects have been effectively attenuated, and will only play a minor role, if any, in what follows.

With the temperature changed slightly from the phasematching peak so as to give nearly zero double pass conversion efficiency (see Fig. 8.2), the scans change dramatically as shown in Fig. 8.5. At the high input power level used the scans display hysteresis and are strongly asymmetric. For opposite phase mismatches, the bistability occurs at opposite detuning, as predicted in section 2.5.2. The Kerr effect caused by the cooperating

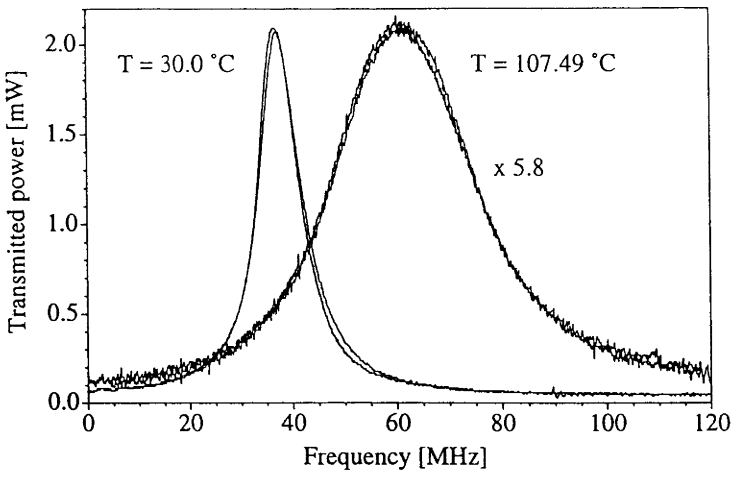

Figure 8.4: Lineshapes of the TEM_{00} resonator mode, 1064 nm input power was 125 mW. The phase matching for both curves is such that there nonlinearities do not cooperate. For $T = 30.0°C$ there is effectively zero nonlinear loss, the linewidth is due solely to mirror and cavity loss decay rates. For $T = 107.49°C$ the nonlinear loss is large, and the linewidth is accordingly broadened. No significant scanning asymmetries can be seen for either case: the thermal effect has been attenuated. The horizontal positions of the lineshapes are arbitrary.

nonlinearities is clearly present. Another signature that this is due to cooperating nonlinearities, and not some other mechanism such as thermal absorption, is that the nonlinear detuning can be changed by altering the phase mismatch: the thermal bistability can never be so affected.

Small thermal effects are still present, as can be seen from the fact that the bistability is greater for negative wavevector mismatch. In the scans shown in Fig. 8.5, second harmonic power production was minimal (a few mW), which is also borne out by the fact that the peak subharmonic circulating power was nearly the same as for the cold cavity case (Fig. 8.4).

Threshold was observed to occur for a pump power of $\approx$ 70 mW, which does not compare well to the predicted value. This is unsurprising, given that $P_1^{\text{bi thr}}$ was calculated using the assumptions of plane waves, a homogeneous nonlinear material and the absence of interference effects, which as Fig. 8.2 shows, is not even approximately true.

For crystal #19 TROPO was observed at pump powers above 49 mW, even when the crystal was phase matched to produce little or no second harmonic. As discussed in the last chapter, if there is sufficient power in the intracavity second harmonic field, TROPO can occur. (That is, even if $\text{Re}\mathcal{J}_2' = 0$). It can be suppressed by changing the phase match, however we were constrained in this by the need to be at a phase match value suitable for a strong Kerr bistability, i.e. little or no second harmonic production. The fast scanning of the cavity also suppresses TROPO to an extent: there appears to be a thermal effect where the signal and idler can pull themselves into resonance via heating if they are not quite on a favourable resonance. Scanning quickly through such resonances (12 MHz/μS) does not give the signal and idler the time they need to establish themselves. A combination of both these methods was used to avoid TROPO: this became increasingly difficult at higher fundamental powers.

Fig. 8.5 is the first observation of optical bistability due to cooperating (or cascaded)

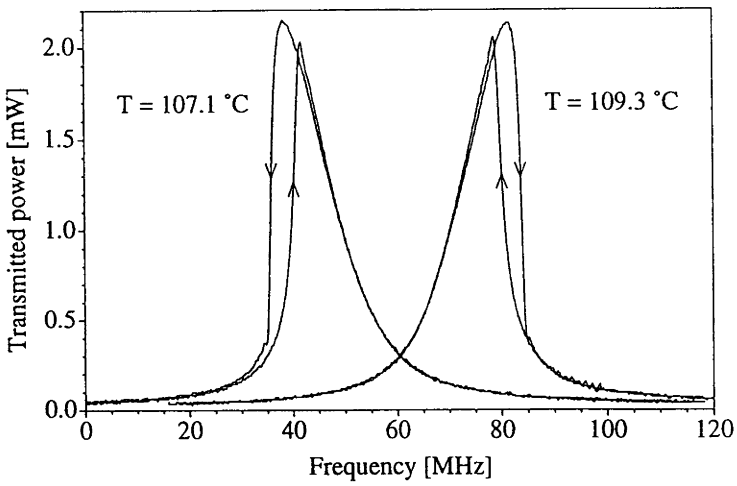

Figure 8.5: Lineshapes of the TEM_{00} resonator mode, 1064 nm input power was 125 mW. T = 107.1°C and T = 109.3°C are points of opposite and roughly equal phase mismatch: the nonlinear loss was minimal at both temperatures. The distinctly different forward and backward scans are evidence for optical bistability due to a cascaded $\chi^{(2)}$ nonlinearity. The horizontal positions of the lineshapes are arbitrary.

$\chi^{(2)}$ nonlinearities [3]. As discussed at the end of the chapter, cooperating nonlinearities offer a powerful technique for the next generation of experiments that require large $\chi^{(3)}$nonlinearities.

8.3 Quantum theory of the Kerr effect

The classical models of the Kerr effect presented in Chapter 2 did not consider the noise properties of the light. There have been various treatments of the noise behaviour of a Kerr cavity [16, 17, 18, 5]. The treatments have varied in both approach (microscopic versus macroscopic) and detail (phenomenological versus rigorous). However all have considered only the case of a quantum noise limited driving field, and are thus of limited utility for modelling experiments. Accordingly in this section we derive, via the Heisenberg approach, our own model to explore the noise reduction behaviour in a Kerr cavity.

8.3.1 Deriving the interaction term

To quantise the doubler acting as a Kerr medium, we replace the complex numbers, α, in eqn 8.2 with operators â. In the classical treatment (see sections 2.2.3 and 2.5.2) the extra term $\mathcal{J}_1'\sqrt{2\mu}\mathcal{A}_3^{in}$ is omitted from eqn 8.2 as there is no seed second harmonic field, i.e. $\mathcal{A}_3^{in} = 0$. In the quantum treatment there is a second harmonic vacuum field: however as at $\Delta kz = 2\pi$ the function $\mathcal{J}_1' = 0$, the second harmonic vacuum has no effect. Even at the

[3] Z.Y. Ou [15]) observed an intensity dependent phase shift in a cw pumped $KNbO_3$ doubler. No bistability was observed, and theory and experiment did not agree very well. However for high Δkz the theory does asymptote to that presented in this thesis. Several, unexplained power features were observed in [15]: these appear similar to the signatures of TROPO or of an avoided crossing between the orthogonal polarisation modes of the fundamental. The latter are typically frequency nondegenerate, power is exchanged between the two when they are not.

quantum level, the phase mismatched singly resonant doubler does not respond to the second harmonic input.

The adiabatic elimination also gives us the ordering of the interaction term, it is $\hat{a}^\dagger\hat{a}\hat{a}$, as opposed to $\hat{a}\hat{a}^\dagger\hat{a}$ or $\hat{a}\hat{a}\hat{a}^\dagger$ (remember, ordering is important with operators). Is this the same ordering as for the $\chi^{(3)}$based Kerr effect? Consider the classical, interaction Hamiltonian for a nonlinear optical system:

$$\mathcal{H}_{int} = -\int_{\text{crystal}} \vec{d}\cdot\vec{E}dV \tag{8.3}$$

$\vec{d}$ can be expanded in a Taylor series:

$$d_i = \chi_{ij}E_j + \chi_{ijk}E_jE_k + \chi_{ijk\ell}E_jE_kE_\ell + \ldots \tag{8.4}$$

For an isotropic material, the classical Hamiltonian then becomes:

$$\mathcal{H}_{int} = \acute{\chi}^{(1)}\int_{\text{crystal}} E^2dV + \acute{\chi}^{(2)}\int_{\text{crystal}} E^3dV + \acute{\chi}^{(3)}\int_{\text{crystal}} E^4dV \tag{8.5}$$

Consider a single optical field, of optical frequency ν. Using the interaction picture electric field (eqn 3.1), and quantising ($a_\nu \rightarrow \hat{a}_\nu$) we obtain:

$$\hat{E} = i\varepsilon_\nu\left[\hat{a}_\nu e^{-i2\pi\nu t} + \hat{a}^\dagger{}_\nu e^{+i2\pi\nu t}\right] \tag{8.6}$$

Substituting this into eqn 8.5 we find that the slowly varying parts of the Hamiltonian (i.e. terms independent of $e^{\pm n\,2\pi t}$) are:

$$\begin{aligned}\mathcal{H}_{int} &= \acute{\chi}^{(1)}\int_{\text{crystal}} \varepsilon_\nu^2(1+2\hat{a}^\dagger{}_\nu\hat{a}_{nu})dV + \acute{\chi}^{(2)}\int_{\text{crystal}} 0dV \\ &+\acute{\chi}^{(3)}\int_{\text{crystal}} \varepsilon_\nu^4(1+4\hat{a}^{\dagger 2}_\nu\hat{a}^2_{nu})dV\end{aligned} \tag{8.7}$$

Evaluating the spatial integrals, and suitably defining $\grave{\chi}^{(3)}$ we find the interaction Hamiltonian for the third order effect is:

$$\hat{\mathcal{H}}_{int} = i\hbar\grave{\chi}^{(3)}(1+4\hat{a}^{\dagger 2}_\nu\hat{a}^2_{nu}) \tag{8.8}$$

The equation of motion interaction term is thus, using eqn 3.57:

$$\begin{aligned}\dot{\hat{a}} &= 1/(i\hbar)[\hat{a},\hat{\mathcal{H}}_{int}] \\ &= (\hat{a}\hat{\mathcal{H}}_{int} - \hat{\mathcal{H}}_{int}\hat{a}) \\ &= \grave{\chi}^{(3)}(\hat{a}\hat{a}^{\dagger 2}\hat{a}^2 - \hat{a}^{\dagger 2}\hat{a}^2\hat{a}) \\ &\vdots \\ &= 8\grave{\chi}^{(3)}\hat{a}^\dagger\hat{a}\hat{a} = \chi^{(3)}\hat{a}^\dagger\hat{a}\hat{a}\end{aligned} \tag{8.9}$$

So the form of the interaction for the $\chi^{(3)}$Kerr effect is $\hat{a}^\dagger\hat{a}\hat{a}$, the same as the $\chi^{(2)}$based Kerr effect. We conclude that the phase mismatched singly resonant doubler (where $\Delta kz = \pm 2n\pi$) is identical in every aspect, both quantum and classical, to a Kerr cavity.

8.3.2 Quantising the Kerr cavity

Using the interaction term discussed in the last section, we can write the equations of motion for the Kerr effect as:

$$\dot{\hat{a}}_1 = -(\gamma_1 + i\Delta_1)\hat{a}_1 \pm i\mu\hat{a}^\dagger{}_1\hat{a}_1\hat{a}_1 + \sqrt{2\gamma_1^c}\hat{A}_1^{in1} + \sqrt{2\gamma_1^\ell}\hat{A}_1^{in2} \tag{8.10}$$

and its conjugate equation. Note that we have absorbed the the factor of π into μ. As normal, we explicitly consider non-perfect escape efficiency, $\eta = \gamma_1^c/\gamma_1$.

Once again we consider two ports for the cavity, the pumping port, in1 and an "other" (loss, transmission, etc.) port in2. Linearising (see sections 3.1.5 & 3.3.2) we obtain the fluctuation equations of motion:

$$\dot{\delta\hat{a}}_1 = -(\gamma_1 + i\Delta_1)\delta\hat{a}_1 + i\mu(2|\alpha_1|^2\delta\hat{a}_1 + \alpha_1^2\delta\hat{a}^\dagger{}_1) + \sqrt{2\gamma_1^c}\hat{A}_1^{in1} + \sqrt{2\gamma_1^\ell}\hat{A}_1^{in2} \tag{8.11}$$

and its complex conjugate. We consider the rotated quadrature operators, $\hat{Y}_1$ & $\hat{Y}_2$, where:

$$\begin{aligned}\hat{Y}_1 &= \hat{a}e^{-i\theta} + \hat{a}^\dagger e^{+i\theta} \\ \hat{Y}_2 &= \hat{a}e^{-i(\theta+\pi/2)} + \hat{a}^\dagger e^{+i(\theta+\pi/2)} \\ &= -i(\hat{a}e^{-i\theta} - \hat{a}^\dagger e^{+i\theta})\end{aligned} \tag{8.12}$$

where θ is the quadrature angle. For $\theta = 0$, $\hat{Y}_1 = \hat{X}_1$ & $\hat{Y}_2 = \hat{X}_2$. The quadrature fluctuation equations of motion are (see section 3.1.3):

$$\dot{\delta\hat{Y}}_i = G\delta\hat{Y}_i + H_i\delta\hat{Y}_j + J_i \tag{8.13}$$

where the subscripts $i = 1, 2$ and $j = 2, 1$ denote the quadrature and its complement; G is:

$$G = -(\gamma_1 - i\frac{\mu}{2}\left[\alpha_1^2 e^{-i\theta} - \alpha_1^{*2} e^{+i\theta}\right]) \tag{8.14}$$

and H_i is:

$$H_i = \pm(\Delta_1 - 2\mu|\alpha_1|^2) + \frac{\mu}{2}\left[\alpha_1^2 e^{-i\theta} + \alpha_1^{*2} e^{+i\theta}\right]) \tag{8.15}$$

where the "+" sign is used for H_1 and the "−" sign is used for H_2. J_i is the coupling term:

$$J_i = \sqrt{2\gamma_1^c}\delta\hat{Y}_i^{in1} + \sqrt{2\gamma_1^\ell}\delta\hat{Y}_i^{in2} \tag{8.16}$$

Fourier transforming (see section 3.3.3) eqn 8.12 becomes:

$$\begin{aligned}\delta\tilde{Y}_i &= \frac{H_i\delta\tilde{Y}_j + J_i}{-(G + i\omega)} \\ \delta\tilde{Y}_j &= \frac{H_j\delta\tilde{Y}_i + J_j}{-(G + i\omega)}\end{aligned} \tag{8.17}$$

Eliminating the cross terms we obtain the expressions:

$$\delta\tilde{Y}_i = \frac{H_iJ_j - J_i(G + i\omega)}{(G + i\omega)^2 - H_iH_j} \tag{8.18}$$

The boundary condition for the reflected fundamental is (see eqns 2.32):

$$\tilde{\mathrm{Y}}_i^{\mathrm{out1}} = \sqrt{2\gamma_1^c}\tilde{\mathrm{Y}}_i - \tilde{\mathrm{Y}}_i^{\mathrm{in1}} \tag{8.19}$$

Thus we obtain:

$$\delta\tilde{\mathrm{Y}}_i^{\mathrm{out1}} = \frac{\sqrt{2\gamma_1^c}H_iJ_j - 2\sqrt{\gamma_1^c\gamma_1^\ell}(G+i\omega)\delta\tilde{\mathrm{Y}}_i^{\mathrm{in2}} - ((G+i\omega)(2\gamma_1^c+(G+i\omega)) - H_iH_j)\tilde{\mathrm{Y}}_i^{\mathrm{in1}}}{(G+i\omega)^2 - H_iH_j} \tag{8.20}$$

Using eqns 8.16 we take the self correlations (see section 3.3.5) to obtain the noise spectrum for the reflected fundamental:

$$V_{\mathrm{Y}_i}^{\mathrm{out1}}(\omega) = \frac{|(G+i\omega)(2\gamma_1^c+(G+i\omega)) - H_iH_j|^2V_{\mathrm{Y}_i}^{\mathrm{in1}}(\omega) + 4\gamma_1^{c\,2}|H_i|^2V_{\mathrm{Y}_j}^{\mathrm{in1}}(\omega) 4\gamma_1^c\gamma_1^\ell(|G|^2+\omega^2)V_{\mathrm{Y}_i}^{\mathrm{in2}}(\omega) + |H_i|^2V_{\mathrm{Y}_j}^{\mathrm{in2}}(\omega))}{|(G+i\omega)^2 - H_iH_j|^2} \tag{8.21}$$

The port *in2* is a vacuum input, so $V_{\mathrm{Y}_i}^{\mathrm{in2}}(\omega) = 1$.

8.3.3 Limits to noise reduction

Teasing out the limits analytically for the Kerr case is a little harder than in the SHG case, as the final expression contains terms like α_1 & α_1^* as well as $|\alpha_1|$.

Fortunately we can use an algebraic trick to simplify analysis. The complex number, α, can be expressed in terms of its magnitude and argument as $\alpha = |\alpha|e^{i\psi}$. From some straightforward mathematics, we find the following:

θ	$2\psi - \pi/2$	2ψ	$2\psi + \pi/2$	$2\psi + \pi$
$\alpha_1^2e^{-i\theta} - \alpha_1^{*\,2}e^{+i\theta}$	$+i\,2\lvert\alpha_1\rvert^2$	0	$-i\,2\lvert\alpha_1\rvert^2$	0
$\alpha_1^2e^{-i\theta} + \alpha_1^{*\,2}e^{+i\theta}$	0	$2\lvert\alpha_1\rvert^2$	0	$-2\lvert\alpha_1\rvert^2$

That is, observing the light at certain quadratures allows us to only consider the absolute magnitude of the field. This simplifies the analysis tremendously, and we find:

θ	$2\psi - \pi/2$	2ψ	$2\psi + \pi/2$	$2\psi + \pi$
G	$-\gamma_1 - \mu\lvert\alpha_1\rvert^2$	$-\gamma_1$	$-\gamma_1 + \mu\lvert\alpha_1\rvert^2$	$-\gamma_1$
H_1	$+(\Delta_1 - 2\mu\lvert\alpha_1\rvert^2)$	$+(\Delta_1 - \mu\lvert\alpha_1\rvert^2)$	$+(\Delta_1 - 2\mu\lvert\alpha_1\rvert^2)$	$+(\Delta_1 - 3\mu\lvert\alpha_1\rvert^2)$
H_2	$-H_1$	$-(\Delta_1 - 3\mu\lvert\alpha_1\rvert^2)$	$-H_1$	$-(\Delta_1 - \mu\lvert\alpha_1\rvert^2)$

It is clear that we do not need to consider $\theta = 2\psi \pm \pi/2$ any further as at those quadrature angles $H_1 = -H_2$ so that $V_{\mathrm{Y}_1} = V_{\mathrm{Y}_2}$ and so we will not observe squeezing.

Consider the spectra of the two quadratures, Y_1 & Y_2 when observed at the quadrature angle $\theta = 2\psi$. We introduce the scaled quantities:

$$\acute{\omega} = \frac{\omega}{\gamma_1} \quad \acute{\Delta} = \frac{\Delta_1}{\gamma_1} \quad \acute{n} = \frac{\mu|\alpha_1|^2}{\gamma_1} \quad \acute{c} = \frac{\gamma_1^c}{\gamma_1} \quad \acute{\ell} = \frac{\gamma_1^\ell}{\gamma_1} \tag{8.22}$$

where $\acute{n}$ is the number of times above threshold and $\acute{c}$ is the coupling ratio. The spectra

are now written as:

$$
\begin{aligned}
V_{Y_1}^{2\psi}(\omega) &= \frac{\left[\omega^2 - (2\acute{c}+1) - (\acute{\Delta}-\acute{n})(\acute{\Delta}-3\acute{n})\right]^2 V_{Y_1}^{in1}(\omega) + 4\acute{\omega}^2(\acute{c}+1)^2 V_{Y_1}^{in1}(\omega)}{+4\acute{c}^2(\acute{\Delta}-\acute{n})^2 V_{Y_2}^{in1}(\omega) + 4\acute{c}\acute{\ell}(\acute{\omega}^2+1)V_{Y_1}^{in2}(\omega) + (\acute{\Delta}-\acute{n})^2 V_{Y_2}^{in2}(\omega))} \\
&\qquad \overline{\left[(\acute{\Delta}-\acute{n})(\acute{\Delta}-3\acute{n}) - \omega^2 + 1\right]^2 + 4\omega^2} \\
V_{Y_2}^{2\psi}(\omega) &= \frac{\left[\omega^2 - (2\acute{c}+1) - (\acute{\Delta}-\acute{n})(\acute{\Delta}-3\acute{n})\right]^2 V_{Y_2}^{in1}(\omega) + 4\acute{\omega}^2(\acute{c}+1)^2 V_{Y_2}^{in1}(\omega)}{+4\acute{c}^2(\acute{\Delta}-3\acute{n})^2 V_{Y_1}^{in1}(\omega) + 4\acute{c}\acute{\ell}(\acute{\omega}^2+1)V_{Y_2}^{in2}(\omega) + (\acute{\Delta}-3\acute{n})^2 V_{Y_1}^{in2}(\omega))} \\
&\qquad \overline{\left[(\acute{\Delta}-\acute{n})(\acute{\Delta}-3\acute{n}) - \omega^2 + 1\right]^2 + 4\omega^2}
\end{aligned}
\tag{8.23}
$$

As always, optimum squeezing occurs when the intracavity squeezed field is output through only one port, i.e. $\gamma_1^c = \gamma_1$ and $\acute{c} = 1$, $\acute{\ell} = 0$. For these quadratures, the best squeezing occurs at zero frequency, $\omega = 0$. Under these conditions, the spectra simplify to:

$$
\begin{aligned}
V_{Y_1}^{2\psi}(\omega) &= \frac{\left[3 + (\acute{\Delta}-\acute{n})(\acute{\Delta}-3\acute{n})\right]^2 V_{Y_1}^{in1}(\omega) + 4(\acute{\Delta}-\acute{n})^2 V_{Y_2}^{in1}(\omega)}{\left[(\acute{\Delta}-\acute{n})(\acute{\Delta}-3\acute{n}) + 1\right]^2 + 4\omega^2} \\
V_{Y_2}^{2\psi}(\omega) &= \frac{\left[3 + (\acute{\Delta}-\acute{n})(\acute{\Delta}-3\acute{n})\right]^2 V_{Y_2}^{in1}(\omega) + 4(\acute{\Delta}-3\acute{n})^2 V_{Y_1}^{in1}(\omega)}{\left[(\acute{\Delta}-\acute{n})(\acute{\Delta}-3\acute{n}) + 1\right]^2 + 4\omega^2}
\end{aligned}
\tag{8.24}
$$

From eqn 8.24 is is clear that when $(\acute{\Delta}-\acute{n})(\acute{\Delta}-3\acute{n}) = -1$ both quadratures are infinitely noisy. As a general rule, the vicinity of such points is where maximum squeezing occurs. This can be seen from the numerators, which are a minimum (and thus the squeezing is maximum) when $(\acute{\Delta}-\acute{n})(\acute{\Delta}-3\acute{n}) = -3$. In the limit that $\mu|\alpha_1|^2$, $\Delta_1 \gg \gamma_1$ both the Y_1 & Y_2 quadratures can be strongly squeezed (at different values of the nonlinearity naturally), as shown in Fig. 8.6. However as $\mu|\alpha_1|^2$, Δ_1 approach γ_1 the squeezing is less robust, and only the squeezing at the Y_2 quadrature survives, as shown in Fig. 8.7.

Fig. 8.8 plots the spectra for both quadratures for parameters where one of the quadratures is squeezed. Even under these ideal conditions, the squeezing linewidth is relatively narrow (less than half the cavity linewidth), and there is considerable additional noise on the other quadrature. It is clear the Kerr squeezed states are not even close to minimum uncertainty states.

Compared to SHG squeezing, Kerr squeezing is unusual in that even for optimum squeezing of the output, *both* quadratures of the input field are coupled together. Indeed, this nonlinear coupling is the heart of the squeezing mechanism. Consider the following argument. It is clear from equation 8.2 the Kerr effect acts as an intensity dependent phase shift. That is, the stronger the field, the proportionately larger the phase shift. Now consider the ball-on-stick picture for the fundamental field inside the cavity, Fig. 8.9. The stick is rotated by an angle proportional to the square of the length of the stick ($\mu\alpha_1^2$). The ball at the end of the stick is also affected. The "top" of the ball (the point furtherest from the origin) is rotated further than the "bottom" of the ball (the point closest to the origin) as it is of greater power. The ball is thus smeared out into a banana or teardrop shape

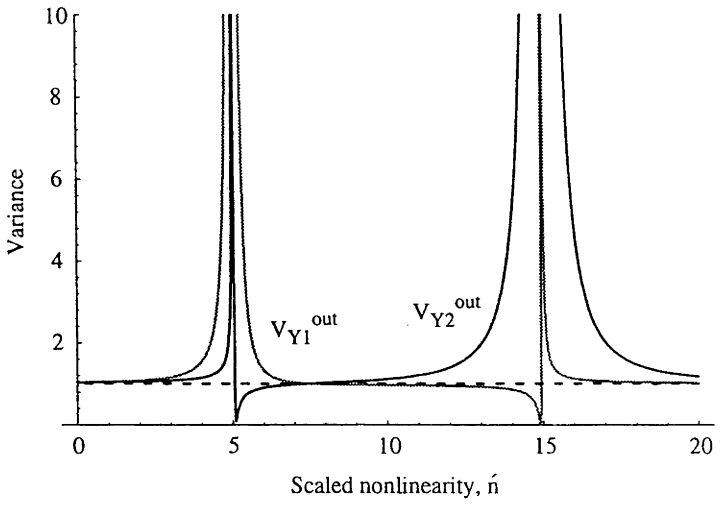

Figure 8.6: Y_1 & Y_2 quadratures versus scaled nonlinearity, $\acute{n} = \mu|\alpha_1|^2/\gamma_1$. The pump is quantum noise limited $V_{Y_1}^{in1}(\omega) = V_{Y_2}^{in1}(\omega) = 1$, the squeezing is observed at zero frequency, $\omega = 0$ for scaled detuning $\acute{\Delta} = \Delta_1/\gamma_1 = 15$, and perfect outcoupling, $\acute{c} = \gamma_1^c/\gamma_1 = 1$. Note that both quadratures are strongly squeezed, but at different nonlinearities.

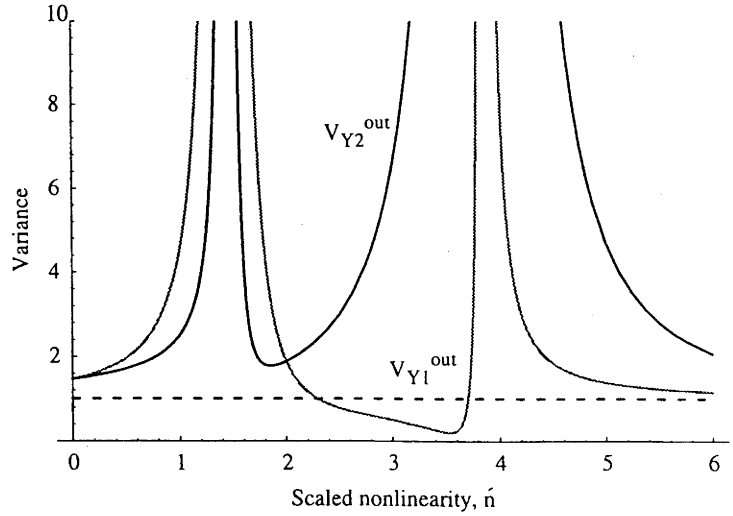

Figure 8.7: As for Fig. 8.6 except for a smaller detuning, $\acute{\Delta} = 5$. Now only one quadrature is strongly squeezed.

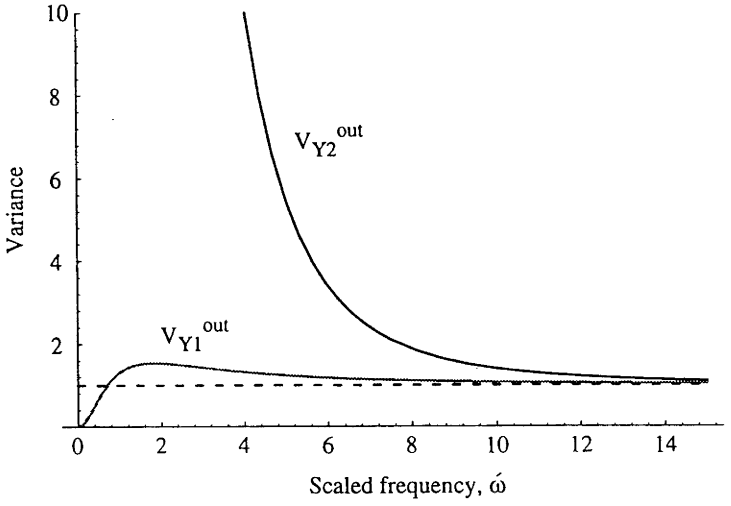

Figure 8.8: Theoretical Kerr squeezing spectra for Y_1, Y_2 quadratures. Scaled frequency, $\acute{\omega} = \omega/\gamma_1$; perfect outcoupling, $\acute{c} = 1$; scaled detuning $\acute{\Delta} = 15$; scaled nonlinearity such that $(\acute{\Delta} - \acute{n})(\acute{\Delta} - 3\acute{n}) = -3$; and quantum noise limited pump $V_{Y_1}^{in1}(\omega) = V_{Y_2}^{in1}(\omega) = 1$. Note the relatively narrow squeezing linewidth.

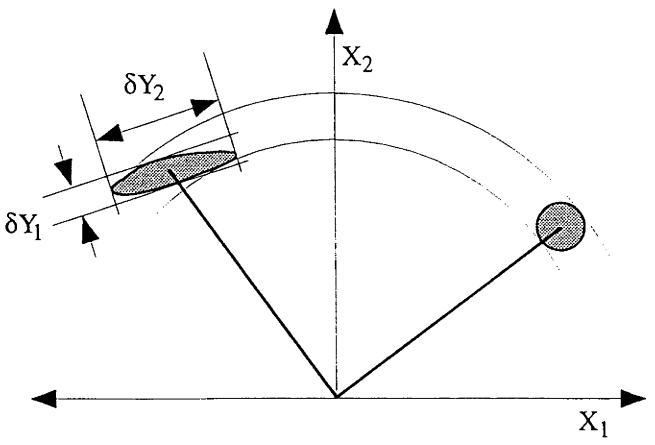

Figure 8.9: Intuitive explanation of Kerr squeezing. Phasor diagrams for an intracavity fundamental field: *right hand side* without Kerr effect; *left hand side* with Kerr effect. The top of the uncertainty area is more intense than the bottom, and so is phase shifted further by the Kerr effect.

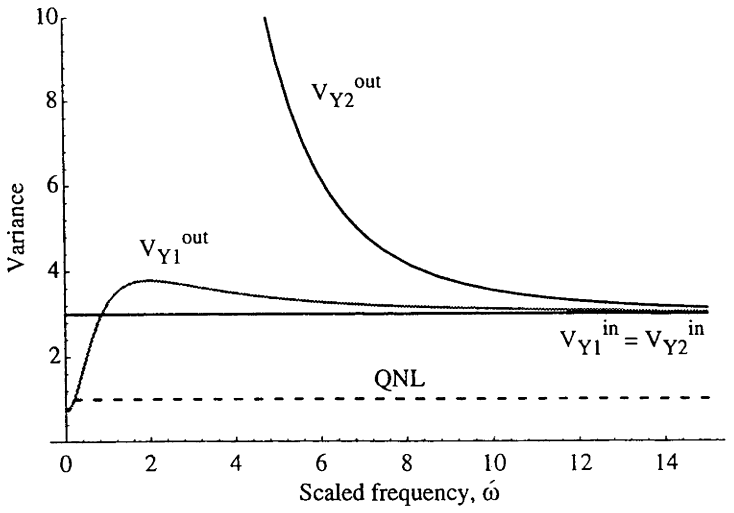

Figure 8.10: Theoretical Kerr squeezing spectra for Y_1, Y_2 quadratures. Scaled frequency, $\acute{\omega} = \omega/\gamma_1$; outcoupling, $\acute{c} = 0.6$; scaled detuning $\acute{\Delta} = 15$; scaled nonlinearity such that $(\acute{\Delta} - \acute{n})(\acute{\Delta} - 3\acute{n}) = -3$; and noisy pump $V_{Y_1}^{in1}(\omega) = V_{Y_2}^{in1}(\omega) = 3$. The squeezing is strongly degraded, but the output beam is still less noisy than the input beam on the Y_1 quadrature. This noise reduction is sometimes known as "classical squeezing".

as shown in Fig. 8.9. Note that at some quadrature axis the banana is narrower than the original ball - the light is now squeezed.

As a source of bright squeezing, the Kerr effect is inherently less practical than SHG as it is sensitive to both the amplitude *and* the phase quadrature of the input light beam. In practice, the phase quadrature of laser light is even noisier than the amplitude (at some frequencies many 10's of dB more). In addition to noise from the same sources that contribute to the amplitude noise (RRO, pump noise, spontaneous emission noise, etc) the phase quadrature has additional noise due to the high phase diffusion of the laser. What is the effect of extra phase noise on Kerr squeezing? No equation for the phase quadrature (equivalent to eqn 6.32 for the amplitude spectrum of a 4 level laser) has yet been published or tested against experiment. However we can tease out the effects of unequal quadratures fairly simply. The quadratures Y_1 & Y_2, are related to the amplitude and phase quadratures, X_1 & X_2, by:

$$\begin{aligned} V_{Y_1}^{in1} &= \cos^2(\theta)V_{X_1}^{in1} + \sin^2(\theta)V_{X_2}^{in1} \\ V_{Y_2}^{in1} &= \sin^2(\theta)V_{X_1}^{in1} + \cos^2(\theta)V_{X_2}^{in1} \end{aligned} \tag{8.25}$$

where θ is the quadrature observation angle. Normally $V_{Y_1}^{in1}$, $V_{Y_1}^{in1}$ will be different to $V_{X_1}^{in1}$, $V_{X_2}^{in1}$. However for the case $V_{X_1}^{in1} = V_{X_2}^{in1}$, then $V_{Y_1}^{in1} = V_{Y_2}^{in1} = V_X^{in1}$ regardless of the value of the quadrature angle. Fig. 8.10 shows the effect of such a uniformly noisy pump, $V_{Y_1}^{in1}(\omega) = V_{Y_2}^{in1}(\omega) = 3$, and nonperfect output coupling, $\acute{c} = 0.6$. The squeezing is considerably degraded, but for the Y_1 quadrature the output is quieter than the input over the same frequency range that it was squeezed in the quantum noise limited case. Thus this noise reduction is sometimes known as "classical squeezing". At high frequencies both quadratures asymptote to the input noise levels: this is expected, as discussed in section 3.4.2 well away from resonance the cavity simply acts a mirror. When the pump is noisier in the phase quadrature than the amplitude, the input values of the quadra-

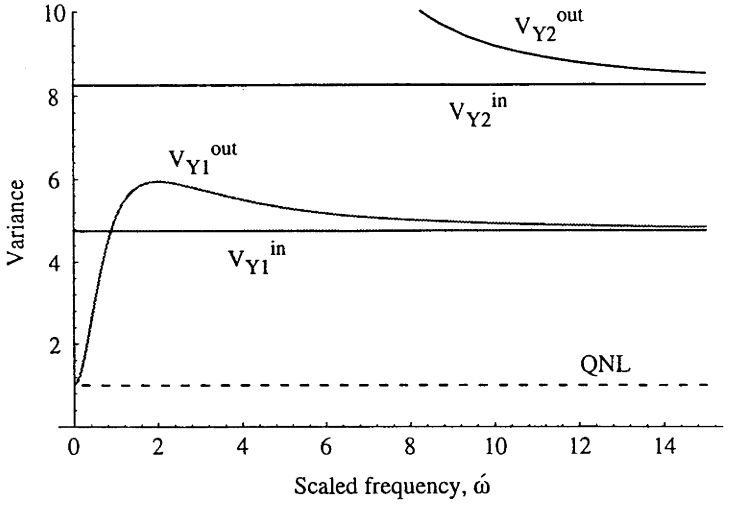

Figure 8.11: Theoretical Kerr squeezing spectra for Y_1, Y_2 quadratures. Scaled frequency, $\acute{\omega} = \omega/\gamma_1$; outcoupling, $\acute{c} = 0.6$; scaled detuning $\acute{\Delta} = 15$; scaled nonlinearity such that $(\acute{\Delta} - \acute{n})(\acute{\Delta} - 3\acute{n}) = -3$; and noisy pump $V_{X_1}^{in1}(\omega) = 3$, $V_{X_2}^{in1}(\omega) = 10$ observed at a quadrature angle $\theta = \pi/6$. The squeezing is destroyed, but the output beam is still less noisy than the input beam on the Y_1 quadrature.

tures Y_1 & Y_2 depend on the quadrature angle. Fig. 8.10 considers the case $\theta = \pi/6$: the squeezing is now totally destroyed. The classical noise reduction occurs over the same frequency range as previously. (It is apparently stronger, as the input noise level has been raised, however in absolute terms it is reducing the noise to approximately the same level as previously.) Very large differences between the two quadratures quickly swamp the squeezing.

In principle, the Kerr medium offers a strong source of squeezed light. In practice, considerable care will need to be taken to reduce the doubly deleterious effect of pump noise.

8.4 Experimental Kerr noise reduction

As is clear from the above theory, the noise is reduced on a quadrature that varies as a function of power, detuning and nonlinearity. Observation of this noise reduction would seem to require an extended experimental setup, so that the quadrature of the light could be examined at will. Ideally this would be done with an external local oscillator (which would, however, have to be much stronger than the signal beam) or by using a single-ended analysing cavity as a phase-sensitive detector (see section 3.4.4).

Due to financial and time constraints, neither option was available during this thesis. However a preliminary experimental investigation was carried out using the Kerr cavity itself as the single ended cavity to form a phase sensitive detector. The trick is to vary the detuning whilst examining the reflected beam from the monolithic cavity. As discussed earlier, frequencies away from the carrier are rotated in quadrature with respect to the carrier, which is by definition the amplitude. Of course using the cavity as both phase sensitive detector and nonlinear medium is not ideal, as the detuning used to change the observed quadrature also changes the nonlinear process. Nevertheless, the experimen-

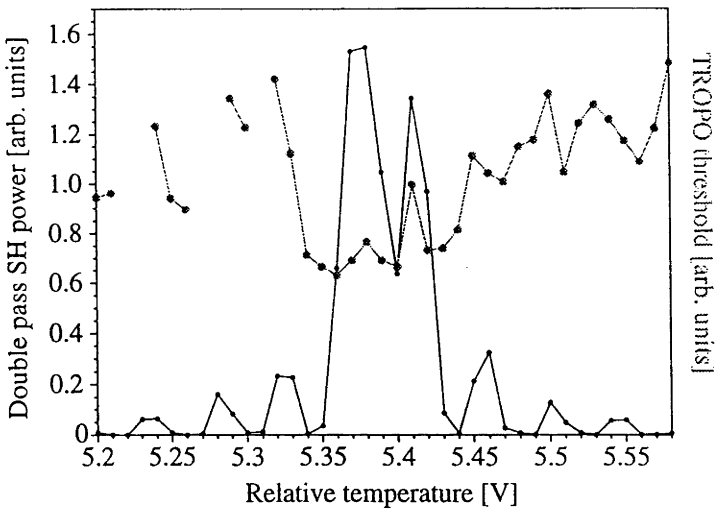

Figure 8.12: TROPO threshold and second harmonic power versus crystal temperature for ANU crystal. Temperature scale has not been calibrated. *double pass*: total SH power leaving the crystal through the AR side. Modematched input 1064 nm power was 33 mW. Lines are guides for the eye, but have been omitted when spanning temperatures where TROPO thresholds were not recorded.

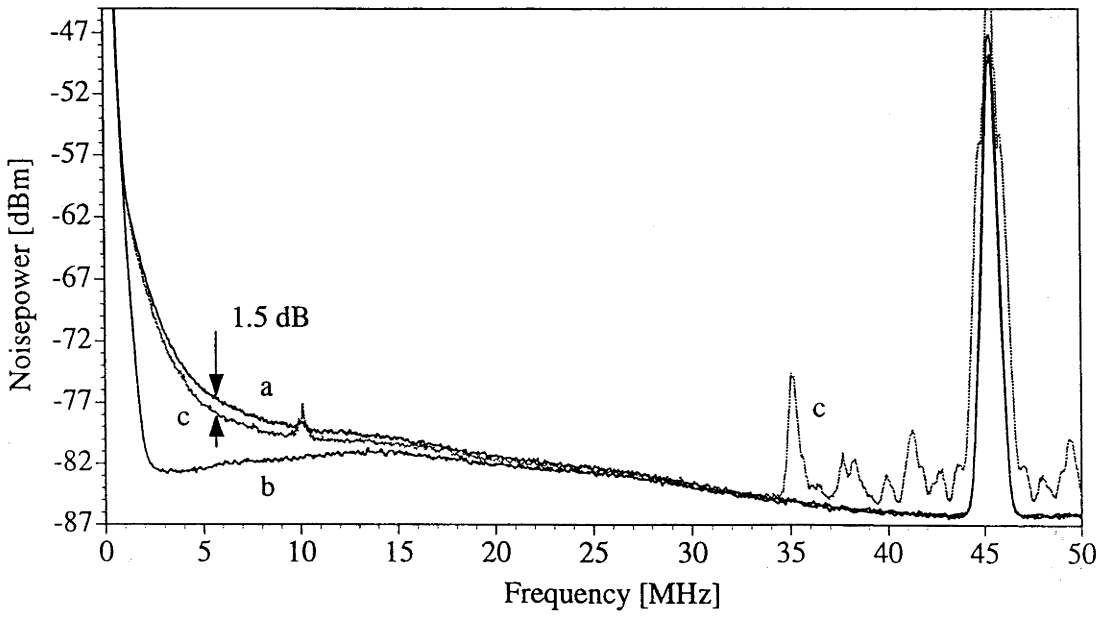

Figure 8.13: Reflected fundamental noisepower versus frequency for Kerr cavity. a) Noise from laser: measured on light reflected from cavity when laser is not locked, and detuned well away from resonance. The cavity thus acts as a simple mirror, R> 99%. b) quantum noise for traces a & c. c) Noise on reflected beam at optimum detuning when crystal set to a Kerr point, i.e. phase match conditions s.t. minimal second harmonic production, strongly asymmetric cavity scans, etc. For this plot, T = 5.34 V, where the optimum SHG squeezing occurred at T = 5.38 V.

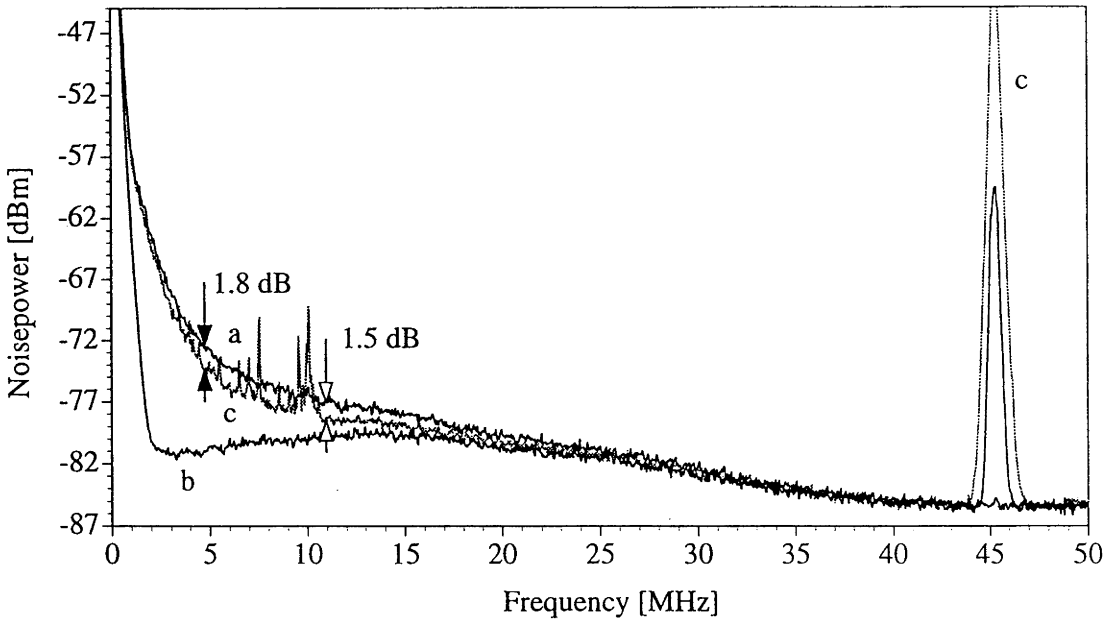

Figure 8.14: Reflected fundamental noisepower versus frequency for Kerr cavity. a) Noise from laser: measured on light reflected from cavity when laser is not locked, and detuned well away from resonance. The cavity thus acts as a simple mirror, R> 99%. b) quantum noise for traces a & c. c) Noise on reflected beam at optimum detuning when crystal set to a Kerr point, i.e. phase match conditions s.t. minimal second harmonic production, strongly asymmetric cavity scans, etc. For this plot, T = 5.44 V, where the optimum SHG squeezing occurred at T = 5.38 V.

tal results obtained to date are intriguing, and suggest that the phase mismatched Kerr system does bear further examination.

The experimental setup is basically that discussed in Chapters 5, 6, & 7. The reflected beam was extracted via a Faraday isolator and sent to a balanced infrared detector pair, of photodetector quantum efficiency 80%. The propagation efficiency through the isolator and associated optics was approximately 63% so that the total quantum efficiency of the detection setup was approximately 50%. The detuning was varied sinusoidally by modulating the locking point of the locking loop. The modecleaner was removed (for simplicity) and the cavity was driven at 30 mW at 1064 nm. Above this TROPO occurred (of which, more later).

The monolith temperature was decreased from the optimum SHG squeezing point to a Kerr point (i.e. minimal second harmonic production, strongly asymmetric cavity scans, see section 8.2.) Fig. 8.12 shows the phase matching curve for the ANU crystal. Note that no effort has been made to absolutely calibrate the temperature scale, as we were chiefly interested in relative measurements. The phase matching curve is symmetrical and less distorted than that of the Konstanz crystal. The outcoupling ratio of the ANU crystal was also some 10% higher (as inferred from the conversion efficiency, see Chapter 6): from these data we infer than the ANU crystal suffered from far less material inhomogeneity than the Konstanz crystal. We operated at the two Kerr points, T = 5.34 V & T = 5.44 V, where the SH production was near zero; optimum SH squeezing occurred at T = 5.38 V.

The crystal was set to T = 5.34 V. When the laser was neither locked nor scanned,

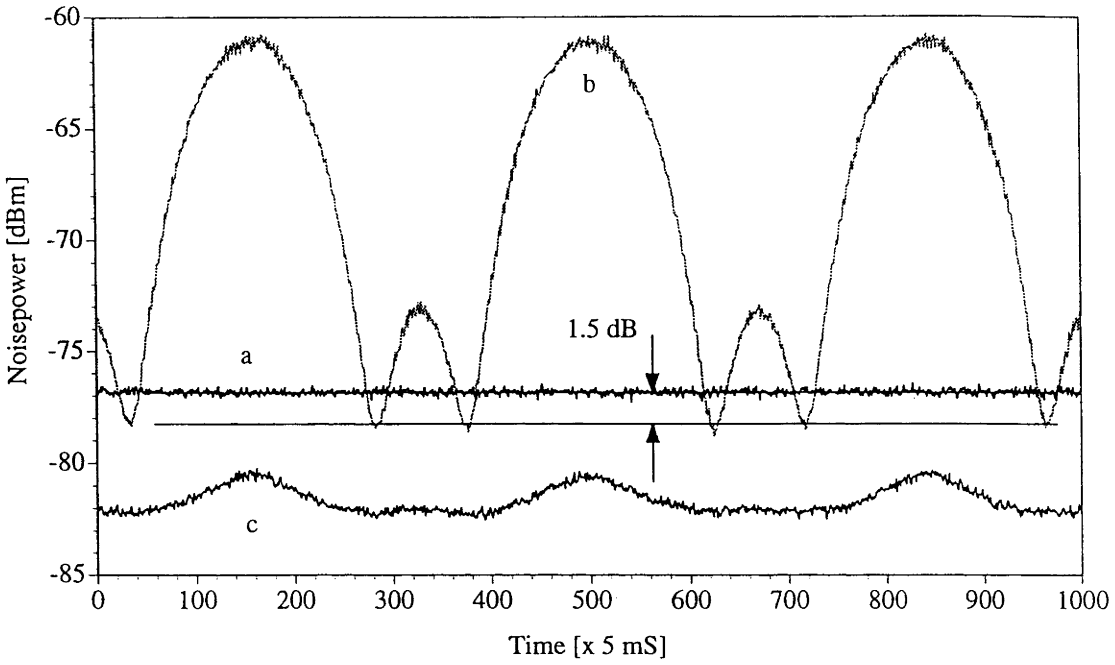

Figure 8.15: Reflected fundamental noisepower versus frequency for Kerr cavity. a) Noise from laser: measured on light reflected from cavity when laser is not locked, and detuned well away from resonance. The cavity thus acts as a simple mirror, R> 99%. b) Noise on reflected beam at 5.98 MHz as a function of detuning. T = 5.34 V, c.f. Fig. 8.13. c) quantum noise as a function of detuning, c.f. trace b.

and detuned well away from the cavity resonance, the cavity acted as a simple reflector (R> 99%). The spectrum of the reflected fundamental for this case is shown in Fig. 8.13a (obtained from the sum port of the detector); Fig. 8.13b is the quantum noise (obtained from the difference port of the detector). Considerable amplitude noise, due to the tail of the RRO of the laser, is evident. The peak at 45 MHz is the residual amplitude noise from the phase modulation used in to the Pound-Drever locking scheme (see Chapter 5).

The laser was then brought onto resonance, and locked. As the cavity was manually detuned the power of the reflected beam did not appreciably change (and the quantum noise trace was identical to trace b). However the spectrum varied considerably: for most of the detuning range it was well above the original noise (as represented by trace a). However for a narrow range of detunings the observed spectrum was quieter than the original light. Fig. 8.13b shows the spectrum for the optimum detuning. The reflected light is not squeezed (it is well above shot noise) but at low frequencies it is quieter than the original light by up to 1.5 dB. The extra structure around the locking peak highlights that we are no longer observing the amplitude quadrature: we are somewhat rotated into the phase quadrature, and are thus seeing more of the phase modulation. The noise reduction increased with increasing power, however the power could not be increased past 30 mW as a strong TROPO occurred.

This noise reduction only occurred in the vicinity of Kerr points. It was not observed when the crystal was set to the point of optimum SHG production nor to a temperature well away from phase match where no second harmonic was produced nor Kerr bistability observed (the "cold" cavity regime). However noise reduction was observed for the

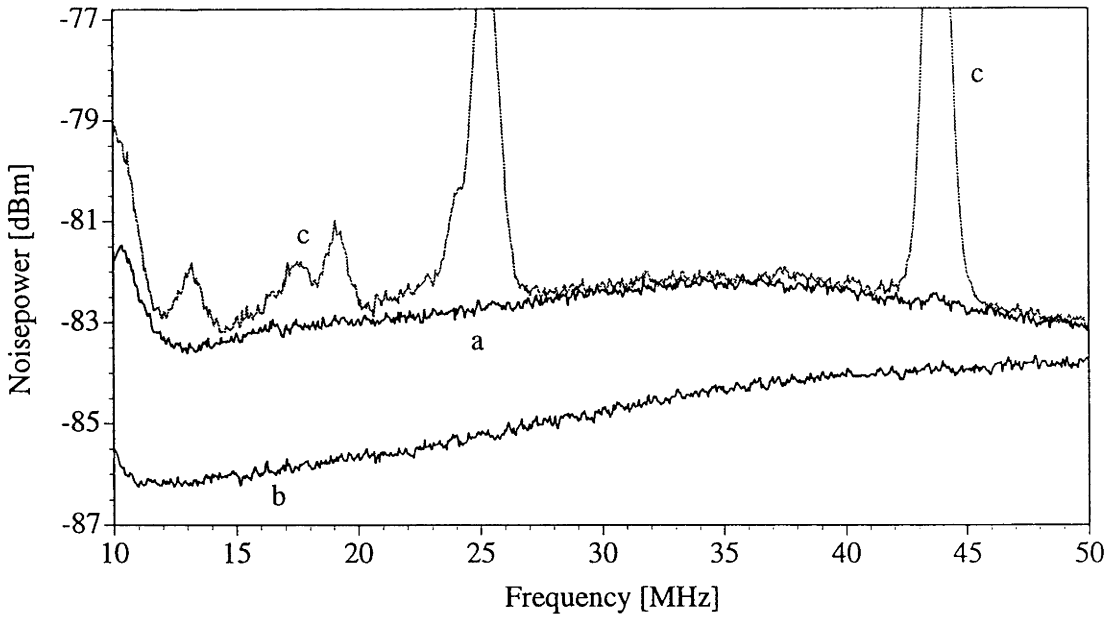

Figure 8.16: As for Fig. 8.13 but with modecleaner in place. No squeezing is seen, but there is considerable additional phase noise.

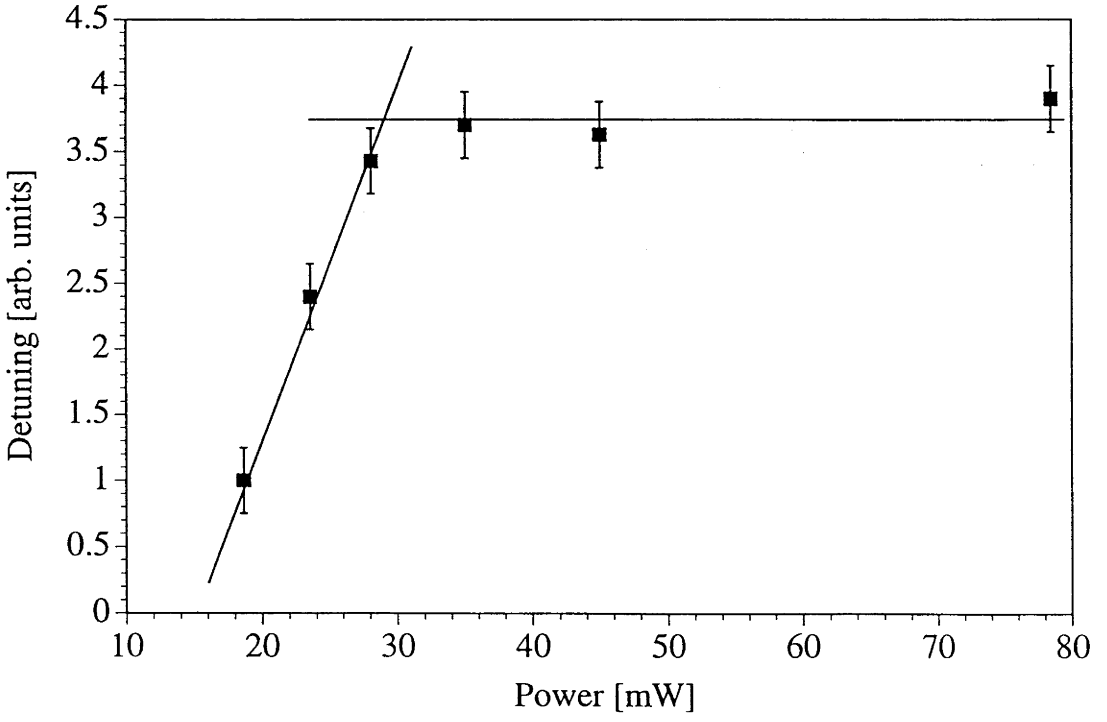

Figure 8.17: Optimum Kerr detuning (point of minimum noise) versus power, for T = 5.34 V. Above TROPO threshold the detuning is clamped.

opposite Kerr point, T = 5.44 V. Fig. 8.14 shows the spectrum : optimum reduction was observed for a detuning of opposite sign to that of Fig. 8.13. This is a typical signature of a Kerr mechanism (see section 8.2), but is not in itself conclusive. There is additional noise evident at low frequencies that was repeatedly present for this phase match: it is currently unexplained but may be linked to the locking system. The detectors were re-balanced between taking Figs 8.13 & 8.14 so to achieve better cancellation of the peak at 45 MHz. The residual amplitude modulation was observed to be 25.9 dB above the shot noise for the simply reflected case; for the rotated quadrature the peak increased by 17.8 dB (clipped on the plot shown here).

To gain a feel for the detuning and quadrature dependence of the noise reduction the noisepower was examined as the cavity was slowly detuned around zero detuning whilst locked (the locking point was scanned at 298 mHz). Of course the cavity could not be symmetrically detuned as one side of the lineshape is bistable. On the stable side of the lineshape the cavity was detuned far enough that more than 90° of quadrature rotation was observed (the noise began to drop again). This suggests that the cavity was detuned on the order of 1 linewidth on that side of the lineshape (see section 3.4.4). Fig. 8.15 is the noisepower versus detuning at $f = 5.98$ Mhz and T = 5.34 V. Trace a is the simply reflected noise; trace b is the reflected noise as a function of detuning and trace c is the shot noise of the reflected light. The optimum noise reduction occurs near, but not at, the peak of the lineshape (i.e. at the minimum power for the reflected beam). As seen from the optical bistability measurement, this peak is shifted in detuning from the nominal zero detuning point of the cavity. Beyond these simple statements, interpretation must be necessarily proscribed as both the observed quadrature and degree of nonlinearity are affected by the detuning.

Given such a strong effect on the classical noise, it was natural to reintroduce the modecleaner so that the input noise was quantum noise limited, and look for squeezing. None was found. There appear to be two reasons for this, both specific to our system. Firstly, the TROPO intruded severely. As discussed in chapters 5, a locking instability exists when both the modecleaner and monolith are locked together. In the last chapter is was seen that this had a deleterious effect on the noise, apparently seeding the TROPO. This effect was quite strong at the Kerr points: with the modecleaner in place the monolith could not be driven above 20 mW without strong TROPO occurring. This limited the power. Secondly the locking instability also appears to introduce considerable additional phase noise, as can be seen from Fig. 8.16. This is the quietest spectra, observed at the optimum detuning. The features at 45 and 27 MHZ are the locking spikes for the monolith and modecleaner, respectively. The other features are beat signals and noise introduced by the dual locking loop. Clearly although quantum noise limited in the amplitude, the same is not true of the phase quadrature. This must be addressed if squeezing is to be observed.

A final observation on the relationship between TROPO and Kerr. The presence of TROPO (at powers above 30 mW) was detected via the infrared optical spectrum analyser, as discussed in the last chapter. However there was an additional signature: above the TROPO threshold the detuning at which the minimum noise spectra was observed, and thus approximately the peak of the lineshape, did not change very much with power. This can be seen in Fig. 8.17, where the optimum detuning is plotted versus power.

8.5 Summary of Kerr effects

Cooperating $\chi^{(2)}$ nonlinearities offer a powerful method for obtaining $\chi^{(3)}$ effects with comparatively low cw powers. As the method is solid state based, it is far simpler than previous methods based on atomic media. Furthermore, a large variety of nonlinear solid state media are available that cover a very large spectral range. Indeed, even media that are not normally considered as phase matchable for SHG may be used, since cooperation is effective even for relatively large phase mismatchs due to the linear, rather than quadratic dependence of the bistability threshold on Δk.

Optical bistability was observed with a relatively low power cw pump beam. For cavity systems the bistability threshold can be lowered in several ways. Resonating the second harmonic significantly reduces the threshold, but at the expense of a more complicated (i.e. doubly resonant) experiment. Now that engineered high nonlinearity materials (QPM materials, such as PPLN) are commercially available it should be possible to significantly lower the threshold simply by virtue of the higher nonlinearity. (Unlike MgO:$LiNbO_3$, the phasematching curves for these materials also correspond closely to the theoretical optimum, another bonus.)

Since several cavity quantum-optical effects such as squeezing [17, 18, 19], quantum nondemolition measurements [20], and noiseless amplification [21], have been predicted assuming self- or cross-Kerr interactions [22], an important extension of the present work is the demonstration that cooperation can lead not only to a self-interaction, as studied here, but also, in phase mismatched sum-frequency generation or type-II SHG, to an effective cross-Kerr coupling between two waves of different wavelength or polarization, respectively.

Our model for Kerr squeezing shows that pump noise plays a doubly critical role as the noise on both quadratures of the pump is coupled into the cavity. When the singly resonant doubler was phase mismatched to the Kerr points, classical noise reduction (1.5-1.8 dB) was observed on the reflected fundamental field. The reduction increased with power, was strongly detuning dependent, and the sign of the optimum detuning changed when the sign of the phase mismatch changed. No squeezing was observed, we believe due to excess phase noise of the laser.

Chapter 8 bibliography

[1] H. Gibbs, Controlling Light with Light (Academic, 1985).

[2] G.I. Stegeman and A. Miller in: Photonics in switching, Vol.1, J.E. Midwinter, ed., (Academic, 1993), p. 81.

[3] M.G. Raizen, L.A. Oroczo, M. Xiao, T.L. Boyd, and H.J. Kimble, Physical Review Letters, 59, p. 198, 1987.

[4] D.M. Hope, H.-A. Bachor, P.J. Manson, D.E. McClelland, and P.T.H. Fisk, Physical Review A, **46**, no. 3, p. R1181, 1992. *Observation of quadrature squeezing in a cavity-atom system*

[5] A. Lambrecht, J.M. Courty, S.Reynaud and E. Giacobino, Applied Physics B **60**, no. ?, p. 129, 1995. *Cold atoms : a new medium for quantum optics;*

A. Lambrecht, T. Coudreau, A. M. Steinberg and E. Giacobino, Europhysics Letters **36**, no. 2, p. 93, 1996. *Squeezing with cold atoms*

[6] G.J. Milburn, M.D. Levenson, R.M. Shelby, S.H. Perlmutter, R.G. DeVoe and D.F. Walls, Journ. Opt. Soc. Am. B, **4**, no. ?, p. 1476, 1987. *??*

[7] J.-F. Roch, G. Roger and P. Grangier, Nonlinear Optics, Principles, Materials, Phenomena and Devices, 5, no. ?, p. 499, 1993.

J.-Ph. Poizat and P. Grangier, Physics Review Letters, **70**, no. ?, p. 71, 1993. ??;

P. Grangier, J.-Ph. Poizat and J.-F. Roch, Physica Scripta, **51**, no. ?, p. 51, 1994. ??;

[8] L.A. Ostrovskii, Journ. Exp. Theor. Phys. Lett., **5**, p. 272, 1967. *Self-action of light in crystals*

[9] J.-M. R. Thomas and J.-P. E. Taran, Optics Communications, **4**, p. 329, 1972. *Pulse distortions in mismatched second harmonic generation*

[10] R. DeSalvo, D.J. Hagan, M. Sheik-Bahae, G. Stegeman, E.W. Van Stryland and H. Vanherzeele, Optics Letters, **17**, p. 28, 1992. *Self-focusing and self-defocusing by cascaded second-order effects in KTP*

[11] See references in: G. Assanto, G.I. Stegeman, M. Sheik-Bahae and E. VanStryland, Journ. Quant. Elec., **31**, p. 673, 1995. *Coherent Interactions for All-Optical Signal Processing via Quadratic Nonlinearities*

[12] R. Paschotta, K. Fiedler, P. Kürz, R. Henking, S. Schiller and J. Mlynek, Optics Letters, **19**, p. 1325, 1994. *82% efficient continuous-wave frequency doubling of 1.06 μm using a monolithic $MgO:LiNbO_3$ resonator;*

[13] S. Schiller, PhD thesis, Edward L. Ginzton Laboratory, Stanford University, Stanford, California, USA, 1993. *Principles and applications of optical monolithic total-internal-reflection resonators*

[14] J. L. Nightingale, W. J. Silva, G. E. Reade, A. Rybicki, W. J. Kozlovsky and R. L. Byer, Proceedings of the SPIE, **681** Laser and Nonlinear optical materials, p. 20, 1986. *Fifty percent conversion efficiency second harmonic generation in magnesium oxide doped lithium niobate*

[15] Z. Y. Ou, Optics Communications, **124**, p. 430, 1996. *Observation of nonlinear phase shift in CW harmonic generation*

[16] P. D. Drummond and D.F. Walls, J. Phys. A, **13**, p. 725, 1980. *Quantum theory of optical bistability. I: Nonlinear polarisability model*

[17] M.J. Collett and D.F. Walls, Physical Review A, **32**, p. 2887, 1985. *Squeezing spectra for nonlinear optical systems*

[18] S. Reynaud, C. Fabre, E. Giacobino and A. Heidmann, Physical Review A, **40**, p. 1440, 1989. *Photon noise reduction by passive optical bistable systems*

[19] C. Fabre and R.J. Horowicz, Optics Communications, **107**, p. 420, 1994. *Self-stabilization of twin beams by a passive Kerr medium*

[20] A.N. Chaba, M.J. Collett and D.F. Walls, Physical Review A, **46**, p. 1499, 1992. *Quantum nondemolition-measurement scheme using a Kerr medium*

[21] I.E. Protsenko and L.A. Lugiato, Optics Communications, **109**, p. 304, 1994. *Noiseless amplification in the optical transistor*

[22] For traveling-wave cascaded quantum effects, see e.g. R.D. Li and P. Kumar, Physical Review A, **49**, p. 2157, 1994.

Chapter 9

Conclusions

His face was that of one who has undergone a long journey.

Epic of Gilgamesh

Cheer up lad, I see land!

Diogenes, on seeing a reader approach the bottom of a parchment scroll

In this thesis we have studied the classical and quantum dynamics of optical frequency conversion, constructing a second harmonic generator to use as our conceptual and experimental testbed.

Classically we confined our attention to steady state behaviours. We found that instead of a single second order nonlinear process ($\chi^{(2)}$nonlinearity), our system could support multiple processes. To unify the various outcomes, we introduced the concept of interacting $\chi^{(2)}$nonlinearities, and classified the interactions as either competing and cooperating. Competing nonlinearities are those where all the up and down conversion processes do not share the same modes; cooperating nonlinearities are this where they do share the same modes.

We observed and modelled competition between second harmonic generation (SHG) and non-degenerate optical parametric oscillation (NDOPO). As the cavity supports three modes, this competition is labelled triply resonant optical parametric oscillation (TROPO). Observed power signatures of TROPO included clamping of the second harmonic power and nondegenerate frequency production in both the visible and infrared. We found that our system could generate light up to 31 nm from degeneracy in the infrared; multiple modes were also observed, which supports the previously suggested idea of cascaded second, sum-, and difference- frequency generation. Given its simplicity, TROPO appears to be a particularly promising method for nondegenerate frequency production. We showed that the second harmonic power is strongly clamped to its competition threshold value (the first observation of clamping since its prediction in 1962) and advised on how to avoid this clamping if strong second harmonic generation is desired.

We developed a set of cavity equations that showed cooperating second order nonlinearities lead to a wide range of third order effects, including self phase modulation (SPM or Kerr effect); cross phase modulation (CPM or cross-Kerr effect); two photon absorption (2PA, this is the effect of singly resonant SHG) and Raman absorption. A cooperating $\chi^{(2)}$system is not a full third order system, as neither four wave mixing (FWM) or third harmonic generation (THG) are predicted. In our experiment we observed (and modelled) a strong optical bistability due to the Kerr effect, showing that in principle and practice a second order cavity can act as a strong third order medium.

For systems with large numbers of photons (linearisable systems), the quantum dynamics of the system can be seen in the behaviour of the quantum noise. We emphasised an intuitive interpretation of quantum noise, the sideband picture, and explored the limits of this interpretation showing that is is valid for any linearisable system. We discussed the Heisenberg approach to modelling linearisable systems, the output of which is quantum noise transfer functions that allow a modular approach to modelling experiments.

Theoretically we considered the effect of laser noise for various configurations of both active (occurs within a laser cavity) and passive (occurs external to a laser cavity) second harmonic generation. We concluded that squeezing via active SHG is not feasible with practicable systems, as the inherent dephasing of lasers totally destroys the squeezing. We highlighted the critical role of laser noise in passive SHG: experimentally pump noise was shown to obscure the squeezing (this is true for all bright squeezing processes). We improved the squeezing by reducing the pump noise with a modecleaning cavity and, unlike previous bright squeezing experiments, obtained perfect agreement between theory and experiment. The simplicity of the modular approach of the theory was highlighted.

The effect of TROPO on the second harmonic squeezing was observed and modelled. In contrast to the predicted outcome for the related quadruply resonant case, the squeezing was found to degrade. We showed that this was due to two effects: a noise eating effect linked to the power clamping, and the effect of the noise of the nondegenerate modes. It was shown that maximum SH squeezing is limited to the value that occurs at TROPO threshold: TROPO must be avoided if strong SH squeezing is to be observed.

We predicted that for certain phase match values the SHG cavity would act exactly as a Kerr cavity, even at the quantum level. We developed a quantum theory that allowed consideration of the pump noise and found that as the Kerr effect ties together the amplitude and phase quadratures, it is sensitive to the pump noise of both. Experimentally, we observed classical noise reduction (1.5-1.8 dB) due to the Kerr effect, but no squeezing. We speculated that the squeezing may be obscured by excess phase noise from the laser.

In conclusion, the work in this thesis has provided definitive limits for classical and quantum behaviour of a frequency doubler. Systems can now be tailored to exclude or include interacting $\chi^{(2)}$nonlinearities as desired. The quantum noise behaviour is now well understood, with the effects of pump noise and interacting nonlinearities all considered and investigated. Squeezing via second harmonic generation is currently the most reliable and well characterised source of bright, continuous wave, squeezed light.

9.1 Future research

There is no doubt that with the advent of tailored nonlinear materials (PPLN, PPLT, etc.) solid state frequency conversion will undergo another renaissance (the last occurring with the introduction of the NPRO laser). The interacting nonlinearity phenomena considered in this thesis may prove to be of technological, as well as fundamental, interest: nondegenerate frequency production via TROPO; optical switching via the Kerr effect. In particular TROPO and the associated cascaded second, sum-, and difference-frequency generation, may be a valuable technique in optical frequency chains, as the nondegenerate modes can be directly seeded by appropriate modulation (at $\pm n$ FSR) of the fundamental.

The new materials also make possible experiments in quantum optics that up to now we have only been able to dream about. Some of these are: squeezing via single pass SHG, which will occur on both the fundamental and second harmonic beams and have a very broad bandwidth as it is not cavity limited; strong squeezing from ring cavity SHG, which allows us to ignore pump noise (see next section); quantum non demolition measurements via SHG, which are simpler than the equivalent OPO experiments; more than 1/9th squeezing via singly resonant SHG (see next section); and double-passing squeezed vacuum through ring OPO cavities to produce very strongly squeezed vacuum.

The technology developed for this thesis is already in the process of becoming obsolete. Given this, and the design knowledge gained from our experiments, it is clear that the current "best" numbers for SHG squeezing will be surpassed quite soon. In the longer term, the question is not so much as to how far the technology can be pushed, but rather whether a technological use will be found for bright squeezing. It is this that will decide the long term relevance of the field.

9.2 Some random ideas

This section contains a number of ideas and approaches that have arisen during the the course of the thesis. Of course, it's much easier to generate ideas than to model them all (let alone test them experimentally!) and for one reason or another these ideas have never quite made it to the publication stage. They are listed here as starting points for discussion - and who knows? one of them may eventually get turned into an experiment. At any rate I hope the reader enjoys considering and discussing them as much as I did (there were more, but these I omitted on grounds of length and humanity).

9.2.1 Resurrecting buried squeezing

There are two methods to evade pump noise. The first, as discussed in Chapter 6, is to try very hard to ensure that there is minimal pump noise, for example, by using a mode cleaning cavity to produce a quantum noise limited pump. An alternative method is to let the squeezing be buried under the pump noise, and resurrect it later in the experiment via optical cancellation [1]-[5].

To do this requires two independent sources of quantum noise. Consider a bright quantum noise limited beam incident on a 50/50 beamsplitter. The two outputs, $\tilde{c}$ & $\tilde{d}$, are superpositions of the two inputs, $\tilde{a}$ & $\tilde{b}$, where (from eqn 3.98):

$$\begin{aligned} \tilde{c} &= \sqrt{0.5}\,\tilde{a} - \sqrt{0.5}\,\tilde{b} \\ \tilde{d} &= \sqrt{0.5}\,\tilde{a} + \sqrt{0.5}\,\tilde{b} \end{aligned} \tag{9.1}$$

and in this sense the output beams are clearly dependent on the input fields. The sum of the two outputs is the noise on the bright input, the difference of the two beams is the noise of the vacuum input (see section 3.4.5). Experimentally, two sources are defined as uncorrelated if the added and subtracted signals are identical. When both beamsplitter input fields are quantum noise limited, the added and subtracted signals are identical (see section 3.4.5): by definition the beamsplitter outputs are uncorrelated. Now let the bright input beam have considerable classical noise: the added signal is noise of the input beam; the difference signal is still quantum noise. The added signal is greater than the subtracted, from which we conclude that the classical noise on the output beams is correlated. However one can still regard the quantum noise of the two output beams, which is buried deep under the classical noise and not directly detectable, as uncorrelated.

Now consider driving two identical squeezing experiments with the two noisy outputs of the beam splitter. As the inputs to the squeezers are far above quantum noise, the outputs are far above quantum noise - any squeezing is buried under the classical noise. However, if the two outputs are subtracted (optically or electronically) then the correlated classical noise will removed, but the uncorrelated quantum noise, which is now squeezed, will not be. The squeezing is resurrected. If the outputs are optically subtracted then the output is a vacuum squeezed beam, even if the squeezing processes are

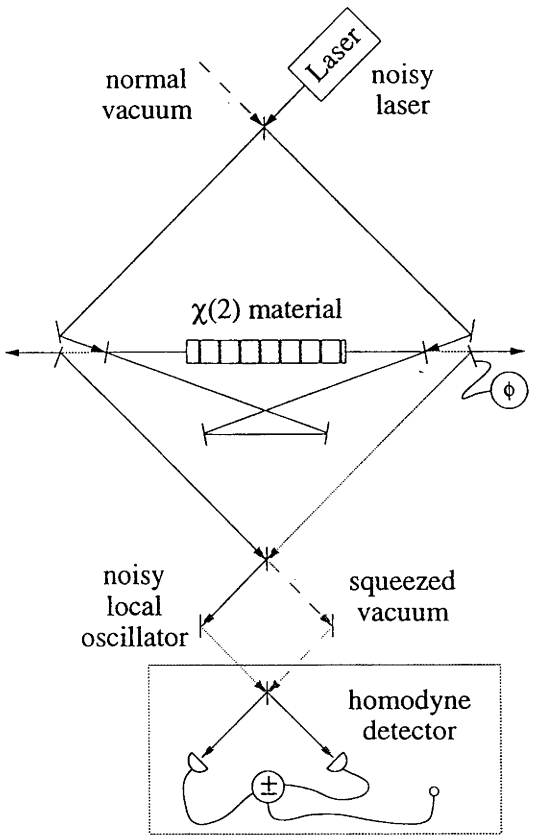

Figure 9.1: Resurrecting buried squeezing. The two counterpropagating modes of a singly resonant, ring frequency doubler are pumped with noisy fundamental beams of identical power. The detected spectrum of either the SH outputs is noisy, no squeezing is present. However if the two SH outputs are subtracted (optically or electronically), then the ideal SH squeezing spectrum is retrieved. Optical subtraction is illustrated, this produces a squeezed vacuum at 532 nm. The bright noisy beam from the sum port of the beamsplitter can be used as a local oscillator in a homodyne detection scheme to detect the vacuum squeezing. All beamsplitters are 50/50.

intrinsically bright (such as SHG).

Optical subtraction to retrieve squeezing was first proposed by Shirasaki & Haus in 1990, who considered the case of pulsed Kerr squeezing [1]. Proof of the principle was provided in 1991 by Bergman and Haus [2] in a remarkable experiment where 5 dB of pulsed Kerr squeezing, generated in a Sagnac interferometer, was observed between 35-85 kHz. This was notable as previous attempts had been plagued by the addition of fibre induced classical noise, which in this experiment was largely cancelled out by the optical subtraction. The experiment was repeated with a 1 GHz pump, and squeezing was observed between 10-30 MHz that deviated from the ideal only due to imperfect temporal mode matching and detector quantum efficiency [3]. The cancellation had removed all sensitivity to the pump noise.

Lai et. al [4] extended the idea to the CW regime, proposing (using chiefly phenomenological arguments) two systems for generating squeezed vacuum. Both systems were based on injection locking squeezed laser diode(s), the common classical noise imposed by the master laser being optically subtracted to leave a squeezed vacuum output. Ralph et. al. considered optical cancellation of the outputs of two identically pumped SHG systems [5]. Using the then recently developed cascaded system formalism, they

presented a rigorous analysis which included the effects of possible experimental limitations (such as asymmetric pumping, detuning, and unbalanced detection) and found that laser noise obscured squeezing could be retrieved. However their theory is based on the Schrödinger approach, and is not particularly elegant. In Appendix 1 we present a simpler, but equivalent treatment, based on the intuitive Heisenberg formalism favoured in this thesis.

Experimentally, optical cancellation works best when the two squeezing systems are identical. For the case of SHG this could be arranged (at least in the first instance) by dual pumping a ring SHG cavity and examining the SH outputs from the counterpropagating modes, as illustrated in Fig. 9.1. Any technical noise induced by the cavity would be identical for both modes and thus removed at the difference port. This scheme is experimentally attractive, as it avoids the need for a modecleaner, and with the advent of significant squeezing from ring SHG cavities [6], it appears experimentally feasible. (If a doubly resonant SHG system is to used to provide fundamental squeezing, then the layout is even simpler. The reflected fundamental beams are retroreflected onto the cavity and squeezed vacuum exits from the first beamsplitter.) In the longer term it is clearly worth considering construction of Sagnac frequency doubling cavities, so that the cancellation is intrinsic, as has been demonstrated with pulsed Kerr squeezing.

9.2.2 Breaking the 1/9th barrier

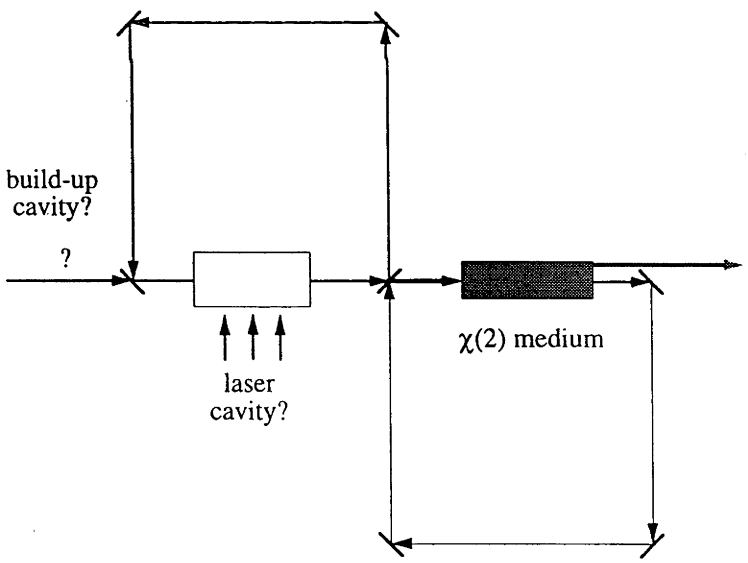

Figure 9.2: Speculative design to beat 1/9th limit to SH squeezing. Based on the proposal of Maeda and Kikuchi [8]. Explanation in text.

All the models presented in this thesis used the mean field approximation (MFA), i.e. intracavity loss is sufficiently low that a mean field is established and maintained within the cavity. The experiments conformed with this model. (Do not be mislead by the figure of 65% conversion efficiency: this is with respect to the pump field, not the intracavity field. The intracavity conversion efficiency, and thus loss, were still quite low.) Experiments are rapidly approaching the point where this will no longer be true: Stanford recently reported a single pass conversion efficiency of 40% using PPLN [7]. If a cavity is built around such a crystal, then the fundamental field will experience very

large loss, and no mean field as such will be built up.

Maeda and Kikuchi have considered this situation for a singly resonant doubler, and examined the squeezing of the second harmonic [8]. The residual fundamental light is not built up as such, acting more as an optical negative feedback beam. Although it does not contribute much power per circulation, it is strongly anti-correlated to the second harmonic and this information is fed back each circulation. The result is the second harmonic light is squeezed beyond the 1/9th limit discussed in Chapter 6. For arbitrarily large interaction and total feedback the second harmonic squeezing in principle becomes perfect.

The key is a high reflectivity coupling mirror, to feed as much of the anticorrelated residual fundamental back into the process each circulation. Unfortunately this raises the pump power required to unfeasible levels, as most of the power simply reflects from the front mirror. Fig. 9.2 shows the beginning of an idea that may help this experiment. Either a build-up cavity or laser cavity could be built in around the coupling mirror, so that the high circulating power is used to pump the SHG cavity. This may bring the experiment into the feasible regime. I feel the laser is more attractive, as it will tend to be injection locked by the very small component of residual fundamental, and so a locking loop will not be required to keep the front cavity resonant.

9.2.3 Kerr in QPM

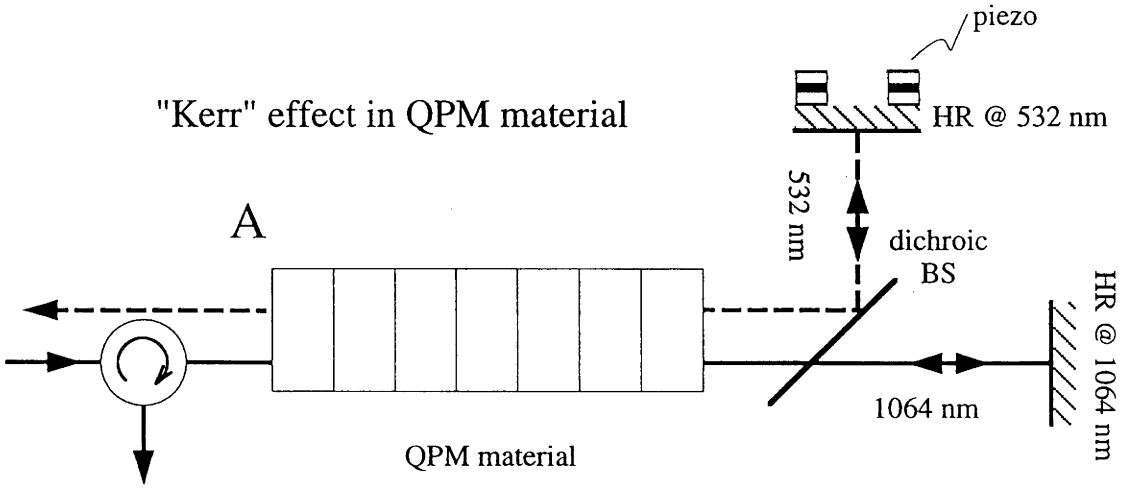

Figure 9.3: System to study the SHG and Kerr behaviour of a $\chi^{(2)}$medium. By varying the phase difference between the reflected fundamental and second harmonic beams, the system behaviour smoothly varies between pure SHG and pure Kerr. Compared with temperature tuning the phase match, this is quick and convenient.

There remains much fruitful research to be done on the interaction between pure SHG and pure Kerr behaviour in a $\chi^{(2)}$system. One of the frustrating features of investigating this using the experimental layout in this thesis was that the phase matching could only be changed via the crystal temperature, which was very slow.

We propose here a more convenient design. Fig. 9.3 shows the core idea. A piece of QPM material (for example, PPLN) is pumped with fundamental light. For the moment we assume that the nonlinear interaction is strong enough that some SHG occurs in a single pass. The phase matching at point "A" depends not only on the crystal tempera-

ture (as per normal) but on the position of the second harmonic mirror with respect to the fundamental mirror: this sets the phase difference $\Delta\phi$. If the external mirrors are adjusted so that $\Delta\phi = 0$ then the reflected SH light is perfectly in phase with the SH light produced on the backward leg by the reflected fundamental. This is a pure SHG case. Adjusting the piezo we can also go towards the Kerr situation: the reflected SH light interferes destructively with the SH produced by the forward leg. If the beams interfere totally (as is possible in the low conversion limit) then the material acts as a perfect Kerr medium. The Kerr phase shift can be detected interferometrically, or may be observed as a Z-scan effect due to the intensity gradient of the Gaussian beam. For high nonlinear interactions, optical switching may occur if a weak beam is injected at the second harmonic or fundamental.

All kinds of tricks are now possible. Scanning quickly between the Kerr and SHG limits while observing the quantum noise properties being just one. As $\Delta\phi$ is scanned both the quadrature and wavelength of the optimum squeezing will vary. Of course this is just the kernel of an idea. A cavity for the fundamental can be built up around the crystal by placing an appropriate mirror at A (a high finesse is probably not necessary). The cavity has the advantage of making the forward and pump beams equal in intensity so that perfect SH cancellation, and thus a perfect Kerr effect, is possible. With a cavity the Kerr effect can be observed directly as optical bistability.

Chapter 9 bibliography

[1] M. Shirasaki and H. A. Haus, Journ. Opt. Soc. Am. B, 7, no. 1, p. 30, 1990. *Squeezing of pulses in a nonlinear interferometer*

[2] K. Bergman and H. A. Haus, Optics Letters, **16**, no. 9, p. 663, 1991. *Squeezing in fibers with optical pulses*

[3] K. Bergman, H. A. Haus, E. P. Ippen and M. Shirasaki **19**, no. 4, p. 290, 1994. *Squeezing in a fiber interferometer with a gigahertz pump*

[4] Y. Lai, H. A. Haus and Y. Yamamoto, Optics Letters, **16**, no. 19, p. 1517, 1991. *Squeezed vacuum from amplitude squeezed states*

[5] T. C. Ralph and A. G. White, Journ. Opt. Soc. Am. B, **12**, no. 5, p. 833, 1995. *Retrieving squeezing from classically noisy light in second-harmonic generation*

[6] H. Tsuchida, Opt. Lett., **20**, no. 21, p. 2240, 1995. *Generation of amplitude-squeezed light at 431 nm from a singly resonant frequency doubler*

[7] E. Gustafson, Stanford University, *private communication*, 1996.

[8] J. Maeda and K. Kikuchi, Opt. Lett., **21**, no. 11, p. 821, 1996. *Bright squeezing by singly resonant harmonic generation: effect of fundamental depletion and feedback*

Appendix A

Resurrecting buried squeezing

Consider two fundamental vacuum fields $\delta\hat{a}$ & $\delta\hat{b}$, incident into two separate SHG systems. From eqn 6.22 the the second harmonic amplitude fluctuations for the two fields are, respectively:

$$\delta\tilde{X}_i^{\text{out3a,b}} = 2\alpha_1\sqrt{\mu}\left[\frac{D_i^{a,b}+E_i^{a,b}}{F_i}\right] - \delta\tilde{X}_i^{\text{in3}a,\,b} \tag{A.1}$$

where D_i, E_i and F_i are defined in eqns 6.17-6.19. The added and subtracted amplitude fluctuations, $\delta\tilde{X}_1^{\pm}$, are defined as:

$$\delta\tilde{X}_1^{\pm} = \delta\tilde{X}_1^{\text{out3a,b}} \pm \delta\tilde{X}_1^{\text{out3a,b}} \tag{A.2}$$

Substituting eqn A.1 and eqns 6.17-6.19 into eqn A.2 we find:

$$\delta\tilde{X}_i^{\pm} = \frac{2\alpha_1\sqrt{2\mu\gamma_1^c}\left[\delta\tilde{X}_1^{\text{in1}b} \pm \delta\tilde{X}_1^{\text{in1}a}\right] + (\mu|\alpha_1|^2 - \gamma_1 + i\omega)\left[\delta\tilde{X}_1^{\text{in3}b} \pm \delta\tilde{X}_1^{\text{in3}a}\right]}{\gamma_1 + 3\mu|\alpha_1|^2 - i\omega} \tag{A.3}$$

Let the two fields a & b be the outputs of a 50/50 beamsplitter illuminated by a laser las and a vacuum vac, i.e.:

$$\begin{aligned}\delta\tilde{X}_1^{\text{in1}a} &= \sqrt{1/2}(\delta\tilde{X}_1^{las} + \delta\tilde{X}_1^{vac})\\ \delta\tilde{X}_1^{\text{in1}b} &= \sqrt{1/2}(\delta\tilde{X}_1^{las} - \delta\tilde{X}_1^{vac})\end{aligned} \tag{A.4}$$

Using these definitions we write:

$$\delta\tilde{X}_i^{\pm} = \frac{4\alpha_1\sqrt{\mu\gamma_1^c}\left[\delta\tilde{X}_1^{las,vac}\right] + (\mu|\alpha_1|^2 - \gamma_1 + i\omega)\left[\delta\tilde{X}_1^{\text{in3}b} \pm \delta\tilde{X}_1^{\text{in3}a}\right]}{\gamma_1 + 3\mu|\alpha_1|^2 - i\omega} \tag{A.5}$$

Taking the self correlations we find the added and subtracted spectra are:

$$V_{X_1}^{\pm} = \frac{16\mu|\alpha_1|^2\gamma_1^c V_{X_1}^{las,vac} + \left[(\mu|\alpha_1|^2 - \gamma_1)^2 + \omega^2\right]\left[V_{X_1}^{\text{in3}b} + V_{X_1}^{\text{in3}a}\right]}{(\gamma_1 + 3\mu|\alpha_1|^2)^2 + \omega^2} \tag{A.6}$$

Or, recalling that $V_{X_1}^{\text{in3}b} = V_{X_1}^{\text{in3}a} = 1$:

$$V_{X_1}^{\pm} = 2\left[1 + 8\mu|\alpha_1|^2\frac{\gamma_1^c(V_{X_1}^{las,vac} - 1) - \mu|\alpha_1|^2}{(\gamma_1 + 3\mu|\alpha_1|^2)^2 + \omega^2}\right] \tag{A.7}$$

As $V_{X_1}^{vac} = 1$, the added and subtracted spectra are identical only if the laser is quantum noise limited, i.e. $V_{X_1}^{las} = 1$. Irrespective of the laser noise, the subtracted spectrum is

always:

$$V_{X_1}^{\pm} = 2V_{X_1}^{\text{idealSHG}} \tag{A.8}$$

where $V_{X_1}^{\text{idealSHG}}$ is the ideal second harmonic squeezing spectrum (as defined in eqn 6.25 with $V_{X_1}^{\text{in1}} = 1$). Experimentally it is actually the photon number spectra that are detected, i.e:

$$V_n^{\pm} = \alpha_1^2 V_{X_1}^{\pm} \tag{A.9}$$

For the sum port, the average detected photon number is $\bar{n}^+ = 2\alpha_1^2$. From this we see that the photon number spectrum for the difference port is directly proportional to the ideal second harmonic squeezing spectrum:

$$V_n^- = \bar{n}^+ V_{X_1}^{\text{idealSHG}} \tag{A.10}$$

Thus regardless of the pump noise of the laser the difference port always gives the ideal squeezing spectrum. Theoretically, it does not matter whether the difference port is electronic (two second harmonic beams separately detected, photocurrents added and subtracted) or optical (two second harmonic beams optically combined with a 50/50 beamsplitter so that all the power exits via one port only; the dark port is vacuum squeezing). Experimentally of course the latter is of more interest.